Frontier Materials & Technologies

Founded in 2008
№ 3
2023
16+
Quarterly
Scientific Journal

The Founder is
Togliatti State University

Editor-in-Chief
Mikhail M. Krishtal, DSc (Physics and Mathematics), Professor

Deputy Editor-in-Chief
for Metallurgy and Materials Science
Dmitry L. Merson, DSc (Physics and Mathematics), Professor

Deputy Editor-in-Chief
for Mechanical Engineering and Machine Science
Aleksandr P. Shaikin, DSc (Engineering), Professor

Deputy Editor-in-Chief
for Welding and Allied Processes and Technologies
Aleksandr I. Kovtunov, DSc (Engineering), Associate Professor

Editors:
Petr Yu. Bochkarev, DSc (Engineering), Professor
Boris M. Brzhozovskiy, DSc (Engineering), Professor
Aleksandr F. Denisenko, DSc (Engineering), Professor
Yuri Z. Estrin, DSc (Physics and Mathematics), Professor
Sergey S. Gavryushin, DSc (Engineering), Professor
Gregory Gerstein, DSc (Engineering)
Fedor V. Grechnikov, Academician of the Russian Academy of Sciences, DSc (Engineering), Professor
Mikhail I. Karpov, Corresponding Member of the Russian Academy of Sciences, DSc (Engineering), Professor
Aleksandr V. Katsman, PhD (Physics and Mathematics)
Aleksandr A. Kazakov, DSc (Engineering), Professor
Leonid V. Khudobin, DSc (Engineering), Professor
Aleksandr V. Kudrya, DSc (Engineering), Professor
Sergey V. Kuzmin, Corresponding Member of the Russian Academy of Sciences, DSc (Engineering), Professor
Aleksey V. Makarov, Corresponding Member of the Russian Academy of Sciences, DSc (Engineering)
Radik R. Mulyukov, Corresponding Member of the Russian Academy of Sciences, DSc (Physics and Mathematics), Professor
Oleg B. Naimark, DSc (Physics and Mathematics), Professor
Nikolay V. Nosov, DSc (Engineering), Professor
Aleksandr V. **Pilinsky**, PhD (Engineering), Associate Professor
Aleksey E. Romanov, DSc (Physics and Mathematics), Professor
Vasili V. Rubanik, Corresponding Member of the National Academy of Sciences of Belarus, DSc (Engineering)
Vladimir A. Shishkov, DSc (Engineering)
Rudolf N. Starobinski, DSc (Engineering), Professor
Ramasubbu Sunder, Fellow of the Indian Academy of Sciences, PhD (Engineering)
Vladimir P. Tabakov, DSc (Engineering), Professor
Alexey Yu. Vinogradov, DSc (Engineering), PhD (Physics and Mathematics), Professor

© Togliatti State University, 2023

Until December 2021,
the journal was published under
the title
**"Science Vector
of Togliatti State University".**

Indexed in Scopus.
Included in the List of HAC,
RSCI core, DOAJ, CNKI,
"White List".
Available in Crossref,
Google Scholar

Registered by the Federal
Service for Supervision
of Communications,
Information Technology
and Mass Media
(Registration Certificate
ПИ No. ФС77-83040
dated March 31, 2022).

Desktop publishing:
Natalya A. Nikitenko

*Responsible/technical
editor:*
Natalya A. Nikitenko

Mailing Address:
14, Belorusskaya St.,
Togliatti,
Russia, 445020
Phone: **(8482) 44-91-74**
E-mail:
vektornaukitgu@yandex.ru

Website:
https://vektornaukitech.ru

Passed for printing
29.09.2023.
Published 15.12.2023.
Format 60×84 1/8.
Digital printing.
Conventional printed sheets 15.6.
Circulation is 30 copies.
Order 3-482-23
The price is free.

Togliatti State University
Publishing
14, Belorusskaya St.,
Togliatti, Russia, 445020

EDITORIAL BOARD INFORMATION

Editor-in-Chief
Mikhail M. Krishtal, Doctor of Sciences (Physics and Mathematics), Professor, Rector (Togliatti State University, Togliatti, Russia).
Scopus AuthorID: 14634063100
ResearcherID: AAD-7707-2019
ORCID: https://orcid.org/0000-0001-7189-0002

Deputy Editor-in-Chief for Metallurgy and Materials Science
Dmitry L. Merson, Doctor of Sciences (Physics and Mathematics), Professor, Director of the Research and Development Institute of Advanced Technologies (Togliatti State University, Togliatti, Russia).
Scopus AuthorID: 6603449333
ResearcherID: M-7210-2016
ORCID: https://orcid.org/0000-0001-5006-4115

Deputy Editor-in-Chief for Mechanical Engineering and Machine Science
Aleksandr P. Shaikin, Doctor of Sciences (Engineering), Professor, Professor at the Department of the Energy-Converting Machines and Control Systems (Togliatti State University, Togliatti, Russia).
Scopus AuthorID: 6602779899
ORCID: https://orcid.org/0000-0002-9832-4753

Deputy Editor-in-Chief for Welding and Allied Processes and Technologies
Aleksandr I. Kovtunov, Doctor of Sciences (Engineering), Associate Professor, Professor at the Department of Welding, Pressure Treatment of Materials and Allied Processes (Togliatti State University, Togliatti, Russia).
Scopus AuthorID: 36761987000
ResearcherID: B-4545-2016
ORCID: https://orcid.org/0000-0002-7705-7377

Editorial board:
Petr Yu. Bochkarev, Doctor of Sciences (Engineering), Professor, Professor of Chair "Mechanical Engineering Technology and Applied Mechanics" (Kamyshin Technological Institute (Branch) of Volgograd State Technical University, Kamyshin, Russia), Professor of Chair "Technical Support of Agro-Industrial Complex" (Saratov State Vavilov Agrarian University, Saratov, Russia).
Scopus AuthorID: 57189893110
Boris M. Brzhozovskiy, Doctor of Sciences (Engineering), Professor, chief researcher of Laboratory of Theory of Mechanisms and Machine Structure (Institute of Machines Science named after A.A. Blagonravov of the Russian Academy of Sciences, Moscow, Russia).
Scopus AuthorID: 55683317200
Alexander F. Denisenko, Doctor of Sciences (Engineering), Professor, Professor of Chair "Technology of Mechanical Engineering, Machines and Tools" (Samara State Technical University, Samara, Russia).
Scopus AuthorID: 36131150100
Yuri Z. Estrin, Doctor of Sciences (Physics and Mathematics), Professor, Professor of Chair of Engineering Materials (Monash University, Melbourne, Australia).
Scopus AuthorID: 7005031984
Sergey S. Gavryushin, Doctor of Sciences (Engineering), Professor, Head of the Department of Computer Systems of Production Automation (Bauman Moscow State Technical University, Moscow, Russia).
Scopus AuthorID: 6507067486
ResearcherID: AAT-8610-2020
ORCID: https://orcid.org/0000-0002-6547-1351
Gregory Gerstein, DSc (Engineering), Laboratory Head (Leibniz University Hannover, Hanover, Germany).
Scopus AuthorID**:** 55001912200
Fedor V. Grechnikov, Academician of the Russian Academy of Sciences, Doctor of Sciences (Engineering), Professor, Head of the Department of Forming Processes (Samara National Research University, Samara, Russia).
Scopus AuthorID: 6506174877
ResearcherID: P-2319-2016
ORCID: https://orcid.org/0000-0002-3767-4004
Mikhail I. Karpov, Corresponding Member of the Russian Academy of Sciences, Doctor of Sciences (Engineering), Professor, Head of the Laboratory of Materials Science (Institute of Solid State Physics RAS, Chernogolovka, Russia).
Scopus AuthorID: 7004130343
ResearcherID: Q-9288-2016
Aleksandr V. Katsman, PhD (Physics and Mathematics), Senior Research Associate (Technion – Israel Institute of Technology, Haifa, Israel).
Scopus AuthorID: 7004225554
Aleksandr A. Kazakov, Doctor of Sciences (Engineering), Professor, Professor at the Department of Metallurgy and Casting Technologies, Head of the Metallurgy Expertise Laboratory (Peter the Great Saint-Petersburg Polytechnic University, St. Petersburg, Russia).
Scopus AuthorID: 56037035400
ResearcherID: E-6090-2014
ORCID: https://orcid.org/0000-0001-6511-1228

Leonid V. Khudobin, Doctor of Sciences (Engineering), Professor, Professor of Chair "Innovative Technologies in Mechanical Engineering" (Ulyanovsk State Technical University, Ulyanovsk, Russia).
Scopus AuthorID: 6701859584
Aleksandr V. Kudrya, Doctor of Sciences (Engineering), Professor, Professor at the Department of Physical Metallurgy and Physics of Strength (National University of Science and Technology MISiS, Moscow, Russia).
Scopus AuthorID: 6603628218
Sergey V. Kuzmin, Corresponding Member of the Russian Academy of Sciences, Doctor of Sciences (Engineering), Professor, First Prorector, Professor of Chair "Equipment and Technology of Welding Production" (Volgograd State Technical University, Volgograd, Russia).
Scopus AuthorID: 57217278342
ResearcherID: I-7424-2012
ORCID: https://orcid.org/0000-0003-2802-8497
Aleksey V. Makarov, Corresponding Member of the Russian Academy of Sciences, Doctor of Sciences (Engineering), Chief Research Associate, Head of the Department of Materials Science, Head of the Laboratory of Mechanical Properties (M.N. Mikheev Institute of Metal Physics of Ural Branch of Russian Academy of Sciences, Ekaterinburg, Russia).
Scopus AuthorID: 36889178900
Scopus AuthorID: 57195590138
ResearcherID: D-5663-2016
ORCID: https://orcid.org/0000-0002-2228-0643
Radik R. Mulyukov, Corresponding Member of the Russian Academy of Sciences, Doctor of Sciences (Physics and Mathematics), Professor, Director (Institute for Metals Superplasticity Problems of the Russian Academy of Sciences, Ufa, Russia).
Scopus AuthorID: 7003520439
ResearcherID: B-3800-2016
ORCID: https://orcid.org/0000-0002-0452-3816
Oleg B. Naimark, Doctor of Sciences (Physics and Mathematics), Professor, Head of the Laboratory of Physical Foundations of Strength (Institute of Continuous Media Mechanics of Ural Branch of Russian Academy of Sciences, Perm, Russia).
Scopus AuthorID: 6701720806
Nikolay V. Nosov, Doctor of Sciences (Engineering), Professor, Professor of Chair "Technology of Mechanical Engineering, Machines and Tools" (Samara State Technical University, Samara, Russia).
Scopus AuthorID: 6602506825
Aleksandr V. Pilinsky, PhD (Engineering), Associate Professor, MSME (Master of Science in Mechanical Engineering), Manager (Raymer Metals, Inc., Los Angeles, USA).
Aleksey E. Romanov, Doctor of Sciences (Physics and Mathematics), Professor, Professor of the Institute of Advanced Data Transfer Systems (ITMO University, St. Petersburg, Russia).
Scopus AuthorID: 7202768874
Vasili V. Rubanik, Corresponding Member of the National Academy of Sciences of Belarus, Doctor of Sciences (Engineering), Head of the Laboratory of Metal Physics (Institute of Technical Acoustics of the National Academy of Sciences of Belarus, Vitebsk, Belarus).
Scopus AuthorID: 57215218253
Vladimir A. Shishkov, Doctor of Sciences (Engineering), Head of the Technical Department (Palladio LLC, Togliatti, Russia).
Rudolf N. Starobinski, DSc (Engineering), Professor, Scientific Consultant (Silencers. Consulting and Engineering, Hamburg, Germany).
Scopus AuthorID: 6602638504
Ramasubbu Sunder, Fellow of the Indian Academy of Sciences, PhD (Engineering), Director (BISS (P) Ltd, Bangalore, India).
Scopus AuthorID: 7003530245
ResearcherID: H-6740-2016
ORCID: https://orcid.org/0000-0001-6143-0723
Vladimir P. Tabakov, Doctor of Sciences (Engineering), Professor, Head of Chair "Innovative Technologies in Mechanical Engineering" (Ulyanovsk State Technical University, Ulyanovsk, Russia).
Scopus AuthorID: 6701501345
ResearcherID: E-1832-2017
ORCID: https://orcid.org/0000-0002-2568-9401
Alexey Yu. Vinogradov, Doctor of Sciences (Engineering), PhD (Physics and Mathematics), Professor, Professor of Faculty of Mechanical and Industrial Engineering (Norwegian University of Science and Technology, Trondheim, Norway).
Scopus AuthorID: 7402889776
ResearcherID: A-7175-2009
ORCID: https://orcid.org/0000-0001-9585-2801

СВЕДЕНИЯ О ЧЛЕНАХ РЕДКОЛЛЕГИИ

Главный редактор
Криштал Михаил Михайлович, доктор физико-математических наук, профессор, ректор (Тольяттинский государственный университет, Тольятти, Россия).
Scopus AuthorID: 14634063100
ResearcherID: AAD-7707-2019
ORCID: https://orcid.org/0000-0001-7189-0002

Заместитель главного редактора по направлению «Металлургия и материаловедение»
Мерсон Дмитрий Львович, доктор физико-математических наук, профессор, директор Научно-исследовательского института перспективных технологий (Тольяттинский государственный университет, Тольятти, Россия).
Scopus AuthorID: 6603449333
ResearcherID: M-7210-2016
ORCID: https://orcid.org/0000-0001-5006-4115

Заместитель главного редактора по направлению «Машиностроение и машиноведение»
Шайкин Александр Петрович, доктор технических наук, профессор, профессор кафедры «Энергетические машины и системы управления» (Тольяттинский государственный университет, Тольятти, Россия).
Scopus AuthorID: 6602779899
ORCID: https://orcid.org/0000-0002-9832-4753

Заместитель главного редактора по направлению «Сварка, родственные процессы и технологии»
Ковтунов Александр Иванович, доктор технических наук, доцент, профессор кафедры «Сварка, обработка материалов давлением и родственные процессы» (Тольяттинский государственный университет, Тольятти, Россия).
Scopus AuthorID: 36761987000
ResearcherID: B-4545-2016
ORCID: https://orcid.org/0000-0002-7705-7377

Редакционная коллегия:
Бочкарев Петр Юрьевич, доктор технических наук, профессор, профессор кафедры «Технология машиностроения и прикладная механика» (Камышинский технологический институт (филиал) Волгоградского государственного технического университета, Камышин, Россия), профессор кафедры «Техническое обеспечение АПК» (Саратовский государственный аграрный университет имени Н.И. Вавилова, Саратов, Россия).
Scopus AuthorID: 57189893110
Бржозовский Борис Максович, доктор технических наук, профессор главный научный сотрудник лаборатории теории механизмов и структуры машин (Институт машиноведения им. А.А. Благонравова РАН, Москва, Россия).
Scopus AuthorID: 55683317200
Виноградов Алексей Юрьевич, доктор технических наук, кандидат физико-математических наук, профессор факультета механической и промышленной инженерии (Норвежский университет науки и технологии, Тронхейм, Норвегия).
Scopus AuthorID: 7402889776
ResearcherID: A-7175-2009
ORCID: https://orcid.org/0000-0001-9585-2801
Гаврюшин Сергей Сергеевич, доктор технических наук, профессор, заведующий лабораторией компьютерных систем автоматизации производства и цифровых технологий (Московский государственный технический университет имени Н.Э. Баумана (национальный исследовательский университет), Москва, Россия).
Scopus AuthorID: 6507067486
ResearcherID: AAT-8610-2020
ORCID: https://orcid.org/0000-0002-6547-1351
Герштейн Грегори, доктор технических наук, заведующий лабораторией (Ганноверский университет имени Готфрида Вильгельма Лейбница, Ганновер, Германия).
Scopus AuthorID**:** 55001912200
Гречников Федор Васильевич, академик РАН, доктор технических наук, профессор, заведующий кафедрой обработки металлов давлением (Самарский национальный исследовательский университет имени академика С.П. Королева, Самара, Россия).
Scopus AuthorID: 6506174877
ResearcherID: P-2319-2016
ORCID: https://orcid.org/0000-0002-3767-4004
Денисенко Александр Федорович, доктор технических наук, профессор, профессор кафедры «Технология машиностроения, станки и инструменты» (Самарский государственный технический университет, Самара, Россия).
Scopus AuthorID: 36131150100
Казаков Александр Анатольевич, доктор технических наук, профессор, профессор кафедры «Металлургические и литейные технологии», руководитель научно-испытательной лаборатории «Металлургическая экспертиза» (Санкт-Петербургский политехнический университет Петра Великого, Санкт-Петербург, Россия).
Scopus AuthorID: 56037035400
ResearcherID: E-6090-2014
ORCID: https://orcid.org/0000-0001-6511-1228
Карпов Михаил Иванович, член-корреспондент РАН, доктор технических наук, профессор, заведующий лабораторией материаловедения (Институт физики твердого тела Российской академии наук, Черноголовка, Россия).
Scopus AuthorID: 7004130343
ResearcherID: Q-9288-2016

Кацман Александр Владимирович, кандидат физико-математических наук, PhD, старший научный сотрудник (Технион – Израильский технологический институт, Хайфа, Израиль).
Scopus AuthorID: 7004225554
Кудря Александр Викторович, доктор технических наук, профессор, заместитель заведующего кафедрой металловедения и физики прочности (Национальный исследовательский технологический университет «МИСиС», Москва, Россия).
Scopus AuthorID: 6603628218
Кузьмин Сергей Викторович, член-корреспондент РАН, доктор технических наук, профессор, первый проректор, профессор кафедры «Оборудование и технология сварочного производства» (Волгоградский государственный технический университет, Волгоград, Россия).
Scopus AuthorID: 57217278342
ResearcherID: I-7424-2012
ORCID: https://orcid.org/0000-0003-2802-8497
Макаров Алексей Викторович, член-корреспондент РАН, доктор технических наук, главный научный сотрудник, заведующий отделом материаловедения и лабораторией механических свойств (Институт физики металлов имени М.Н. Михеева Уральского отделения Российской академии наук, Екатеринбург, Россия).
Scopus AuthorID: 36889178900
Scopus AuthorID: 57195590138
ResearcherID: D-5663-2016
ORCID: https://orcid.org/0000-0002-2228-0643
Мулюков Радик Рафикович, член-корреспондент РАН, доктор физико-математических наук, профессор, директор (Институт проблем сверхпластичности металлов Российской академии наук, Уфа, Россия).
Scopus AuthorID: 7003520439
ResearcherID: B-3800-2016
ORCID: https://orcid.org/0000-0002-0452-3816
Наймарк Олег Борисович, доктор физико-математических наук, профессор, заведующий лабораторией «Физические основы прочности» (Институт механики сплошных сред Уральского отделения Российской академии наук, Пермь, Россия).
Scopus AuthorID: 6701720806
Носов Николай Васильевич, доктор технических наук, профессор, профессор кафедры «Технология машиностроения, станки и инструменты» (Самарский государственный технический университет, Самара, Россия).
Scopus AuthorID: 6602506825
Пилинский Александр Вениаминович, кандидат технических наук, доцент, MSME (Master of Science in Mechanical Engineering), менеджер («Реймер Металс Корпорейшн», Лос-Анджелес, США).
Романов Алексей Евгеньевич, доктор физико-математических наук, профессор Института перспективных систем передачи данных, руководитель научно-исследовательского центра перспективных функциональных материалов и лазерных коммуникационных систем (Национальный исследовательский университет ИТМО, Санкт-Петербург, Россия).
Scopus AuthorID: 7202768874
Рубаник Василий Васильевич, член-корреспондент Национальной академии наук Беларуси, доктор технических наук, заведующий лабораторией физики металлов (Институт технической акустики Национальной академии наук Беларуси, Витебск, Республика Беларусь).
Scopus AuthorID: 57215218253
Старобинский Рудольф Натанович, доктор технических наук, профессор, научный консультант (консалтинг-бюро “Prof. Starobinski. Silencers. Consulting and Engineering”, Гамбург, Германия).
Scopus AuthorID: 6602638504
Сундер Рамасуббу, член Индийской академии наук, кандидат технических наук, директор (“BISS (P) Ltd”, Бангалор, Индия).
Scopus AuthorID: 7003530245
ResearcherID: H-6740-2016
ORCID: https://orcid.org/0000-0001-6143-0723
Табаков Владимир Петрович, доктор технических наук, профессор, заведующий кафедрой «Инновационные технологии в машиностроении» (Ульяновский государственный технический университет, Ульяновск, Россия).
Scopus AuthorID: 6701501345
ResearcherID: E-1832-2017
ORCID: https://orcid.org/0000-0002-2568-9401
Худобин Леонид Викторович, доктор технических наук, профессор, профессор кафедры «Инновационные технологии в машиностроении» (Ульяновский государственный технический университет, Ульяновск, Россия).
Scopus AuthorID: 6701859584
Шишков Владимир Александрович, доктор технических наук, начальник технического отдела (ООО «Палладио», Тольятти, Россия).
Эстрин Юрий Захарович, доктор физико-математических наук, профессор, профессор кафедры инженерных материалов (Университет им. Монаша, Мельбурн, Австралия).
Scopus AuthorID: 7005031984

CONTENT

СОДЕРЖАНИЕ

doi: 10.18323/2782-4039-2023-3-65-1

The profile physical coefficient and its application for modelling the machined surface texture

© 2023

Igor N. Bobrovskij, Doctor of Sciences (Engineering), researcher
Togliatti State University, Togliatti (Russia)

E-mail: bobri@yandex.ru ORCID: https://orcid.org/0000-0002-9513-7936

Received 28.07.2022 *Accepted 14.04.2023*

Abstract: Current trends in the development of mechanical engineering impose increasingly stringent requirements for the performance characteristics of manufactured goods. The main parameters characterizing the quality of a product as a whole are the physical, mechanical, and geometric indicators of the working surfaces of the compound units. In domestic practice, a machined surface is mainly characterized by a rather limited number of parameters (no more than 6), such as the average microroughness height, the microroughness height at 10 points, etc. However, their use is not enough to manufacture competitive products in the modern conditions. For example, international ISO/ASME/DIN standards include a much broader set of parameters required to accurately describe the performance properties of a surface. The paper analyzes the approaches to the formation of requirements for the microgeometry of the working surfaces of parts used in modern mechanical engineering. Based on the analysis, the author proposed and mathematically substantiated a general approach to modelling surface texture characteristics, which allows describing adequately the surface using a new parameter – the profile physical coefficient, since it is virtually impossible to directly compare the technologies developed in Russia with foreign analogues based on the current standards. First, the profile physical coefficient was determined at the section level. Next, it was decomposed into a Fourier series for the two-dimensional and three-dimensional cases. The paper presents the analysis of the new parameter applicability on the example of a product obtained by honing. The author concluded about the applicability of this parameter and the necessity to develop a comprehensive methodology based on it for evaluating the surface after machining.

Keywords: mechanical engineering technology; machining; surface; profile physical coefficient; rough layer; surface texture.

Acknowledgements: The research was supported by a grant from the Russian Science Foundation (Project No. 20-79-00233, https://rscf.ru/project/20-79-00233/).

For citation: Bobrovskij I.N. The profile physical coefficient and its application for modelling the machined surface texture. *Frontier Materials & Technologies*, 2023, no. 3, pp. 9–17. DOI: 10.18323/2782-4039-2023-3-65-1.

INTRODUCTION

The characteristics and surface texture of products are regulated by the international standards, such as ISO/TR 14638, as well as by the chain of standards for surface texture. By now, the roughness profile and the parameters defining it represent but a few characteristics of the surface texture, which are clearly normalised. Surface texture parameters – a primary profile, waviness, and roughness are defined by the ISO 4287:1997 International Standard, as well as by the ISO 3274:1996 Geometrical Product Specification (GPS). Surface structure. Profile method. Rated characteristics of contact (stylus) instruments. The terminology used in mathematical modelling corresponds to the list of accepted international standards:

– ISO 4288:1996 Geometrical Product Characteristics (GPP). Surface structure. Profile method. Rules and procedures for assessing surface structure;

– ISO 11562:1996 Geometrical Product Specification (GPS). Surface structure. Profile method. Metrological characteristics of filters with phase correction;

– ASME B46.1-2009. Surface Texture (Surface Roughness, Waviness, and Lay).

Basic terms:

– profile filter – according to ISO 21920-2 and ISO 16610-21, divides the profile into long-wave and short-wave components;

– real surface – limits the body, separating it from the environment;

– surface profile – is formed as a result of the intersection of a real surface with a special plane parallel to the *XOZ* and *YOZ* coordinate planes;

– primary profile – is regulated by ISO 3274 and serves as the basis for obtaining quantitative evaluation characteristics;

– surface profile – is formed from the primary profile by suppressing a long-wave component and serves as the basis for obtaining the surface profile parameters;

– waviness profile – is obtained by suppressing the long-wave and short-wave components, it is used to obtain the waviness parameters;

– geometrical parameters of the *P*, *R*, *W* groups – are calculated based on the primary profile, surface profile, and waviness profile, respectively.

In the design-engineering practice, a very limited list of parameters is used at the enterprises in the machine-building sector [1–3]. The parameters of the *R* and *W* groups are mainly used [4; 5], in particular, the *Ra*, *Rz* parameters, etc. At the same time, among the parameters little used in practice, *Ra* is one of the promising ones.

The analysis of publications on honing showed that when describing the requirements for surface roughness of parts, in most studies in the field of mechanical engineering, only the *Ra* parameter is given [6–8]. In some publications,

tp or *tp* and *Rz* are added to it [9]. In rare cases, *R*max and *Sm* are added to the above parameters [9]. In the literature, there are practically no parameters from new standards or specific parameters for describing the surface after honing from the less recent DIN standards of the 1980s. In recent years, the alternative methods for obtaining parameters have been actively developed, for example, new algorithms for correlating the parameters of a reflected beam from a microrelief [1]. These methods are being developed to detect all the same *Ra* type standard parameters [2].

Most of publications on honing associate the solution of the optimisation task with the application of theoretical and empirical models. The most common method is the Taguchi method [3]. The indicators of this method are used as an optimisation criterion [4]. An alternative method to achieve the same goal is the neural network method [5]. The authors also use the response surface analysis methods to determine the interrelation between the processing modes and technological parameters [6]. In these publications, only *Ra* was considered as a basic parameter.

The authors of [8] investigated the honing treatment using a magneto-rheological fluid. Interestingly, in this case, the meaning of the term "honing" no longer implies the use of a hone (tool for processing), but primarily the surface formed by this method. Similarly, there is a laser honing process that does not involve mechanical stock removal, but only energy impact. The authors state that the coincidence in the surface texture for the traditional method and the proposed one was 5.88 %. When describing the surface roughness, the authors give the *Ra* parameter. No other parameters were considered, despite the availability of a measuring device (Surftest SJ-400, Mitutoyo) sufficient for their evaluation.

In [9], the authors analyzed how to determine the surface texture using the widely known acoustic emission method. The authors propose two new parameters: *Sf* (calculated as the ratio of signals when applying high and low frequencies) and *Sh* (energy parameter). In this case, these parameters are correlated with the typical *Ra* parameters and the three-dimensional version of the *Ra* parameter – the *Sa* parameter. The work [9] confirms that interest in other methods for determining surface characteristics is high. However, this method will require the purchase of extra equipment for texture evaluation.

In [10], the authors give the reasoning of the theory of a new finishing process proposed as a functional replacement for honing. The surface was considered only from the point of view of the *Ra* parameter. In the paper [11], which describes the influence of changing a honing angle on the roughness and tribological properties, the *Ra* parameter and the *Rk* group (*Rpk, Rk, Rvk*) parameters are given. It is interesting, that the authors concluded that the *Rk* group parameters reflect the tribological characteristics more than the *Ra* parameter. The *Rk* group parameters were developed exactly for this. At the same time, in the conclusions, the authors carried out comparison according to the quantitative values not of *Rk*, but of *Ra* (the optimal value of the *Ra* parameter was 0.85).

The authors of the work [12], related to the evaluation of the tribological properties of a rough honed surface, by changing the contact pressure, evaluated the formed plateau-surface tribologically, dividing it qualitatively into two types: high and low. The basis for division was the authors' classification by the surface decomposed according to the frequencies with given (not variable) parameters over the *Rk* group.

The work [13] studied the influence of the hone radius on technological parameters (cutting force, surface integrity, etc.). The *Ra* parameter served as an estimate of the surface topography. In the conclusions, the smallest numerical value of the *Ra* parameter was considered as a criterion for the best surface.

The paper [14] examined multi-response optimisation to ensure the surface quality and performance. The authors do not directly name the parameters, they indicate the "maximum roughness" (probably *R*max) and "average roughness" (probably *Ra*). As a result, the authors built three models: for average and maximum roughness and for operation time. It was found that the grain size has the most influence on the average *Ra* value. As in the source [13], this conclusion is again obvious considering the mechanics of the process. At the same time, the authors position the presented three-factor optimisation model (two roughness parameters and operation time) as the most complete one.

The paper [15] presents an indirect neural network for modelling roughness during honing. The *Rk* group parameters are used. Using this model, the authors were able to predict the grain size, linear and tangential velocities, and pressure to obtain the specified values of the *Rk* group parameters. Reference [16] uses the results obtained from test honing machines for industrial application. In this paper, the authors supplement the *Rk* group parameters with the *Rz* parameter as necessary for industrial application.

In [17], the honing tool roughness was analyzed. Using two theories of roughness generation, the authors compared the calculated *Ra* parameter with the experimental one. An extensive analysis of the process kinematics (different angles, rotation speeds) was carried out; however, no other parameters except this one were considered.

New parameters are used to a small extent in the literature (Table 1). This is also typical for other studies of machining technologies that consider roughness [18].

Thus, there is a small quantity of parameters used in practice (no more than 6). The parameters available in international standards will allow determining the surface texture more accurately. In this work, the author proceeded with the development of the proposed earlier ideas on the development of a new method for determining the surface texture [19]. It is proposed to introduce into practice a little-used parameter – the profile physical coefficient. To assess the validity of the application of this approach, it is required to study the surface texture of the product according to the method proposed below for the parameter under consideration – the profile physical coefficient. Within this conception, the authors proposed to determine the most significant parameters and then find the range of optimal values for them, and not proceed from a specified limited list of parameters.

The proposed "profile physical coefficient" parameter can be denoted as $P_{mr(c)}$, $T_{mr(c)}$, and $W_{mr(c)}$ depending on the source of the initial data, and is calculated in general form by the following formula:

$$P_{mr(c)}, T_{mr(c)}, W_{mr(c)} = \frac{Ml(c)}{l_n}.$$

Table 1. *Texture parameters applied in the literature*
Таблица 1. *Применяемые в литературе параметры текстуры*

Specified texture parameters				Papers, where the structure parameters under consideration were applied
Ra	***R*max**	***Rk***	***Sa***	
+	–	–	–	[6]
+	–	–	–	[15]
+	–	–	+	[8]
+	–	–	–	[10]
+	–	+	–	[11]
–	–	+	–	[12]
+	–	–	–	[13]
+	+	–	–	[14]
+	+	+	+	[9]

The goal of the research is to develop a general approach to the application of the "profile physical coefficient" parameter and its testing.

METHODS

The technique is based on the assessment of the surface microprofile by the "profile physical coefficient" parameter.

First, the profile physical coefficient was determined at the sectional level. Next, it was expanded into a Fourier series for the two-dimensional and three-dimensional cases. As a result, the complexity of the presented parameter was shown.

Based on the geometrical representation of probability, the profile physical coefficient represents the probability of density of filling with a material in the selected section *c*.

The $P_{mr(c)}$, $T_{mr(c)}$, $W_{mr(c)}$ relative physical coefficient is determined at the sectional level of the $R\delta c$ profile relative to the starting point C_0:

$$P_{mr'}, T_{mr'}, W_{mr} = P_{mr'}, T_{mr'}, W_{mr}(C_1),$$

where $C_1 = C_0 - R_{\delta c}$ (or $P_{\delta c}$, or $W_{\delta c}$);
$C_0 = (CP_{mr0}, T_{mr0}, W_{mr0})$.

The difference between the profile relative physical coefficient $P_{mr(c)}$, $T_{mr(c)}$, $W_{mr(c)}$ and the widely known ones is that not filtered data are used (the parameters of the *R* – roughness group, such as *Ra, tp*), but the primary surface profile (hence the name of the group of parameters *P* – primary).

The profile of the surface relief obtained geometrically in two-dimensional space in the form of a profilogram can be represented analytically in the form of a trigonometric Fourier series:

$$Z(x) = \frac{a_0}{2} + \sum_{n=1}^{\infty} a_n \cos\frac{n\pi x}{l} + b_n \sin\frac{n\pi x}{l},$$

where

$$a_0 = \frac{1}{l}\int_{-l}^{l} Z(x)dx,$$

$$a_n = \frac{1}{l}\int_{-l}^{l} Z(x)\cos\frac{n\pi x}{l}dx,$$

$$b_n = \frac{1}{l}\int_{-l}^{l} Z(x)\sin\frac{n\pi x}{l}dx.$$

$$Z(x) = \begin{cases} Z_1(x), -l \le x \le -l + X_{S_1} \\ Z_2(x), -l + X_{S_1} \le x \le -l + X_{S_1} + X_{S_2} \\ \ldots \\ Z_\gamma(x), -l + \sum_{i=1}^{\gamma-1} X_{S_i} \le x \le -l + \sum_{i=1}^{\gamma}\left(-l + \sum_{i=1}^{\gamma} X_{S_i}\right) \\ Z_k(x), -l + \sum_{i=1}^{k-1} X_{S_i} \le x \le l \end{cases}.$$

In three-dimensional space, the surface topography is specified using a function of two variables $z = f(x,y)$, which can be expanded into a double trigonometric Fourier series in terms of a system of trigonometric functions. These functions represent a trigonometric system for two variables *x* and *y*, each of which is periodic with a period of 2π, both in *x* and *y*.

Each function of the system is orthogonal to any other in square $D(-\pi \le x \le \pi, -\pi \le y \le \pi)$. The specified property takes place in any other square of the form $a \le x \le a + 2\pi, -b \le y \le b + 2\pi$. The orthogonality property follows from the correlations

$$C_1 = C_0 - R_{\delta c}\iint_D 1\cdot\cos mx dxdy = \int_{-\pi}^{\pi} dy\int_{-\pi}^{\pi}\cos mx dx =$$
$$= \int_{-\pi}^{\pi}\left(\frac{1}{m}\left|\sin mx_{-\pi}^{\pi}\right.\right)dy = \frac{1}{m}\int_{-\pi}^{\pi}\left(\sin m\pi - \sin(-m\pi)\right)dy = 0 .$$

In a similar manner

$$\iint_D 1\cdot\sin mx dxdy = \int_{-\pi}^{\pi} dy\int_{-\pi}^{\pi}\sin mx dx =$$
$$= \int_{-\pi}^{\pi}\left(\frac{1}{m}\left|\cos mx_{-\pi}^{\pi}\right.\right)dy = \frac{1}{m}\int_{-\pi}^{\pi}\left(\cos m\pi - \cos(-m\pi)dy\right) = ,$$
$$= -\frac{1}{m}\int_{-\pi}^{\pi}\left(\cos m\pi - \cos m\pi\right)dy = 0$$

as the cos$n\pi$ function is even, then $\cos(-n\pi) = \cos(n\pi)$. As a consequence,

$$\int_D (\cos mx\cos ny)(\cos rx\cos px)\,dxdy =$$
$$= \int_{-\pi}^{\pi}\cos mx\cos rx\left(\int_{-\pi}^{\pi}\cos nx\cos pydy\right)dx =$$
$$= \int_{-\pi}^{\pi}\cos mx\cos rxdx\int_{-\pi}^{\pi}\cos nx\cos pydy = ,$$
$$= \frac{1}{4}\int_{-\pi}^{\pi}\left[\cos(m+r)x + \cos(m-r)x\right]\times$$
$$\times\int_{-\pi}^{\pi}\left[\cos(n+p)x + \cos(n-p)y\right]dy = 0$$

where r and p are integers, at $m \neq r$, $n \neq p$.

It was proved above that the integral in the symmetric region of an even function vanishes when $m = r$ и $n = p$, then the original integral takes the form

$$\int_{-\pi}^{\pi}\cos^2 mxdx\cdot\int_{-\pi}^{\pi}\cos^2 nydy =$$
$$= \frac{1}{2}\int_{-\pi}^{\pi}(1+\cos 2mx)dx\cdot\frac{1}{2}\int_{-\pi}^{\pi}(1+\cos 2ny)dy =$$
$$= \frac{1}{2}\left[2\pi + \frac{1}{2}\left|\sin 2mx_{-\pi}^{\pi}\right.\right]\cdot\frac{1}{2}\left[2\pi + \frac{1}{2}\left|\sin 2ny_{-\pi}^{\pi}\right.\right] =$$
$$= \frac{1}{4}\cdot 4\pi^2 = \pi^2$$

Here, $\sin 2mx_{-\pi}^{\pi} = \sin 2m\pi - \sin(-2m\pi) = 0$ since $\sin m\pi = 0$.

The orthogonality of any pair of different functions of the original trigonometric system is proved similarly.

We define the norms of the elements of the presented trigonometric system:

$$\|1\| = \sqrt{\iint_D dxdy} = \sqrt{4\pi^2} = 2\pi ,$$

$$\|\cos mx\| = \|\sin mx\| = \|\cos ny\| = \|\sin ny\| = \sqrt{2}\pi ,$$

$$\|\cos mx\| = \sqrt{\iint_D \cos^2 mdxdy} = \sqrt{\int_{-\pi}^{\pi} dy\int_{-\pi}^{\pi}\cos^2 mxdx} =$$
$$= \sqrt{\int_{-\pi}^{\pi}\frac{1}{2}(1+)\left|\cos m_{-\pi}^{\pi}dy\right.} = \sqrt{\frac{1}{2}\cdot 2\pi\cdot 2\pi} = \sqrt{2}\pi ,$$

$$\|\cos mx\cdot\cos ny\| = \|\sin mx\cdot\cos ny\| =$$
$$= \|\cos my\cdot\sin ny\| = \|\sin nx\cdot\sin ny\| = \pi ,$$

$$\|\cos mx\cdot\cos ny\| = \sqrt{\int_D \cos^2 mx\cdot\cos^2 ny\cdot dxdy} =$$
$$= \sqrt{\int_{-\pi}^{\pi}\cos^2 mxdx\int_{-\pi}^{\pi}\cos^2 nydy} = \sqrt{\frac{1}{4}\cdot\frac{\pi^2}{4}} = \pi .$$

As in the case of a one-variable function $z = f(x)$, the Fourier coefficients for a two-variable function $z = f(x;y)$ defined in the domain D are found from the correlations [3]:

$$A_{00} = \frac{\iint_D f(x;y)dxdy}{\|1\|^2} = \frac{1}{4\pi^2}\iint_D f(x;y)dxdy ,$$

$$A_{m0} = \frac{\iint_D [f(x;y)\cos mx]dxdy}{\|\cos mx\|^2} =$$
$$= \frac{1}{2\pi^2}\iint_D [f(x;y)\cos mx]dxdy, m = 1, 2, ..., \infty ,$$

$$A_{0n} = \frac{\iint_D [f(x;y)\cos ny]dxdy}{\|\cos ny\|^2} =$$
$$= \frac{1}{2\pi^2}\iint_D [f(x;y)\cos ny]dxdy, n = 1, 2, ..., \infty ,$$

$$B_{m0} = \frac{\iint_D [f(x;y)\sin mx]dxdy}{\|\sin mx\|^2} =$$
$$= \frac{1}{2\pi^2}\iint_D [f(x;y)\sin mx]dxdy, m = 1, 2, ..., \infty ,$$

$$B_{0n} = \frac{\iint_D [f(x;y)\sin ny]dxdy}{\|\sin ny\|^2} =$$
$$= \frac{1}{2\pi^2}\iint_D [f(x;y)\sin ny]dxdy, n = 1, 2, ..., \infty .$$

If m and n both possess the values $m = 1, 2, ..., \infty$, $n = 1, 2, ..., \infty$, then:

$$a_{m.n} = \frac{1}{\pi^2}\iint_D [f(x;y)\cos mx\cdot\cos ny]dxdy ,$$

$$b_{m.n} = \frac{1}{\pi^2}\iint_D [f(x;y)\sin mx\cdot\cos ny]dxdy ,$$

$$c_{m.n} = \frac{1}{\pi^2}\iint_D [f(x;y)\cos mx \cdot \sin ny]dxdy ,$$

$$d_{m.n} = \frac{1}{\pi^2}\iint_D [f(x;y)\sin mx \cdot \sin ny]dxdy .$$

In practical problems, instead of A_{00}, it is advisable to denote $\frac{a_{00}}{4}$, where a_{00} is found from am,n at $m = 0$ and $n = 0$. Similarly, instead of $Am,0$, $A0,n$, $Bm,0$, $B0,n$, we write $\frac{a_{m,0}}{2}, \frac{a_{0,n}}{2}, \frac{b_{m,0}}{2}, \frac{b_{0,n}}{2}$, which are calculated from the expressions am,n , bm,n, cm,n, dm,n when given $m = 1, 2, \ldots, \infty$, $n = 0$ or $n = 1, 2, \ldots, \infty$, $m = 0$. As a result, the double trigonometric series is written as:

$$z = f(x;y) = \sum_{m=0}^{\infty}\sum_{n=0}^{\infty}\lambda_{m.n}\begin{bmatrix} a_{m.n}\cos mx \cdot \cos ny + \\ + b_{m.n}\sin mx \cdot \cos ny + \\ + c_{m.n}\cos mx \cdot \sin ny + \\ + d_{m.n}\sin mx \cdot \sin ny \end{bmatrix},$$

here

$$\lambda = \begin{cases} \frac{1}{4}, \text{ при } m = n = 0 \\ 1, \text{ при } m > 0, n > 0 \\ \frac{1}{2}, \text{ при } m > 0, n = 0 \text{ или } m = 0, n > 0 \end{cases},$$

in this case m and n are positive integers.

In the case when the domain D_Ξ is represented by a rectangle that meets the conditions D_Ξ ($-lx < x < lx$, $-ly < y < ly$) (Fig. 1), the double Fourier series takes the form:

$$z = f(x;y) = \sum_{m=0}^{\infty}\sum_{n=0}^{\infty}\lambda_{m.n}\begin{bmatrix} a_{m.n}\cos m\frac{\pi}{l_x}x \cdot \cos n\frac{\pi}{l_y}y + \\ + b_{m.n}\sin \frac{\pi}{l_x}mx \cdot \cos n\frac{\pi}{l_y}y + \\ + c_{m.n}\cos m\frac{\pi}{l_x}x \cdot \sin n\frac{\pi}{l_y}y + \\ + d_{m.n}\sin m\frac{\pi}{l_x}x \cdot \sin n\frac{\pi}{l_y}y \end{bmatrix}.$$

The λ_{mn} parameter is found according to the correlations written above, and the $am.n$, $bm.n$, $cm.n$, $dm.n$ coefficients are calculated using the formulas:

$$a_{m.n} = \frac{1}{l_x l_y}\iint_{D_\Xi}\left[f(x;y)\cos m\frac{\pi}{l_x}x \cdot \cos n\frac{\pi}{l_y}y \right]dxdy ,$$

$$b_{m.n} = \frac{1}{l_x l_y}\iint_{D}\left[f(x;y)\sin m\frac{\pi}{l_x}x \cdot \cos n\frac{\pi}{l_y}y \right]dxdy ,$$

$$c_{m.n} = \frac{1}{l_x l_y}\iint_{D}\left[f(x;y)\cos m\frac{\pi}{l_x}x \cdot \sin n\frac{\pi}{l_y}y \right]dxdy ,$$

$$d_{m.n} = \frac{1}{l_x l_y}\iint_{D}\left[f(x;y)\sin m\frac{\pi}{l_x}x \cdot \sin n\frac{\pi}{l_y}y \right]dxdy .$$

In the special case when $lx = ly = \pi$, the previous expressions for the square domain D_Ξ are obtained from the written expressions. In the case when the function $z(x; y)$ is specified as piecewise smooth in the domains Di, $i = 1, 2, \ldots, n$:

$$z(x;y) = \begin{cases} f_1(x,y), \text{ при } (x;y) \subset D_1 \\ f_2(x,y), \text{ при } (x;y) \subset D_2 \\ \ldots \\ f_k(x,y), \text{ при } (x;y) \subset D_k \end{cases},$$

the double trigonometric series will be analogous to the Fourier series of similar one-variable functions.

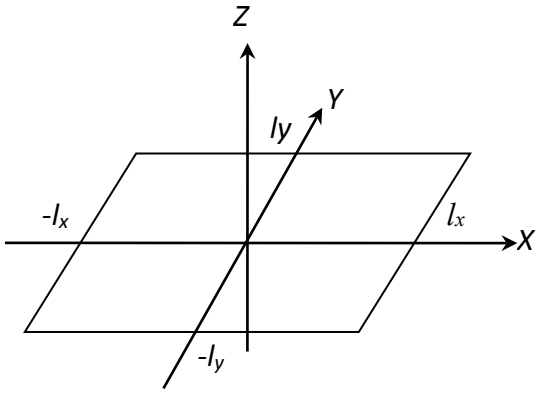

Fig. 1. *Rectangular area D_Ξ in the XOY plane*
Рис. 1. *Прямоугольная область D_Ξ в плоскости XOY*

Surface texture characteristics are predominantly geometric. However, when processing and operating the machine parts and mechanisms, physical indicators are used, such as material removal in various technologies, wear, friction, elasticity, and the rough layer plastic deformation caused by the presence of the material in it.

The complex parameter for evaluating these phenomena is the analyzed profile physical coefficient regulated by the international standard and representing the probability of density of filling with the material in the z section, i.e. $P(VMc)$, according to the geometric concept of probability.

The probability of material content in a rough layer of width c is determined by the formula

$$P(V_{Mc}) = \int_0^c P_{mr((z))}dz .$$

RESULTS

It is possible to test the considered method on the profillogram of the surface of a honed part.

If a profillogram is obtained for a rough layer, where $c = zk$ measured from the OX axis, then the profile physical coefficient from geometric constructions is determined by the formula

$$P_{mr}(z_k) = \frac{\sum_{i=1}^{k_c} Mli}{\sum_{j=1}^{k_c} Mlj},$$

where kc – is the number of sections of the material in the c section.

Specifically for the present case, Rz = 74 mm is divided into k = 10 parts, ln = 155 mm. The results of measurements and calculations are summarized in Table 2 and presented graphically in Fig. 2. Probability of filling the rough layer with the material

$$P(V_m) = \frac{S_m}{R_k \cdot l_n},$$

where Sm – is the area of the figure enclosed by a curve Ml_{Zk}.

Let us find the value of Sm:

$$S_m = \frac{R_Z}{6m}\left(\frac{Ml_0}{2} + 2\sum_{i=1}^{2m-2} Ml_{2i} + 4\sum_{i=1}^{2m-1} Ml_{2i-1}\right), m = 51,$$

$$S_m = \frac{R_Z}{6 \cdot 5}\left[\begin{matrix}748 + 2(151{,}2 + 128{,}1 + 71{,}2 + 34{,}8) + \\ + 4(153{,}6 + 141{,}8 + 83{,}6 + 51{,}9 + 5{,}5)\end{matrix}\right] =$$

$$= R_Z \cdot 86{,}23$$

$$P(V_m) = \frac{R_Z \cdot 86{,}23}{l_n} = \frac{1}{l_n} 86{,}23 = 0{,}5563.$$

The calculation shows that for a rough layer with a given profillogram, the probability of filling it with the material is equal to 0.5563, i.e., the given rough layer contains 55.63 % of the material. The porosity coefficient λ is the characteristic of voids in the specified layer:

$$\lambda = \frac{S_{сл} - S_h}{S_{сл}} = 1 - \frac{S_m}{S_{сл}} 1 - P(V_m),$$

where $S_{сл}$ – is the total area of a rough layer on the length ln, $S_{сл} = Rz \cdot ln$.

Thus, λ = 1 $-P(V_m)$, oil-absorption is 44.37 %.

Table 2. *Calculation of the probability of the density of filling the rough layer with the material along the zi sections*
Таблица 2. *Расчет вероятности плотности заполнения материалом шероховатого слоя по сечениям zi*

z_i	z_0 **0**	z_1 **7.4**	z_2 **14.8**	z_3 **22.2**	z_4 **29.6**	z_5 **37**	z_6 **44.4**	z_7 **51.8**	z_8 **59.2**	z_9 **66.6**	z_{10} **74**
S_{zi}	155	153.6	151.2	141.1	128.1	83.6	71.2	51.9	34.2	5.5	0
$P(S_{zi})$	1	0.991	0.975	0.910	0.826	0.539	0.459	0.335	0.221	0.035	0

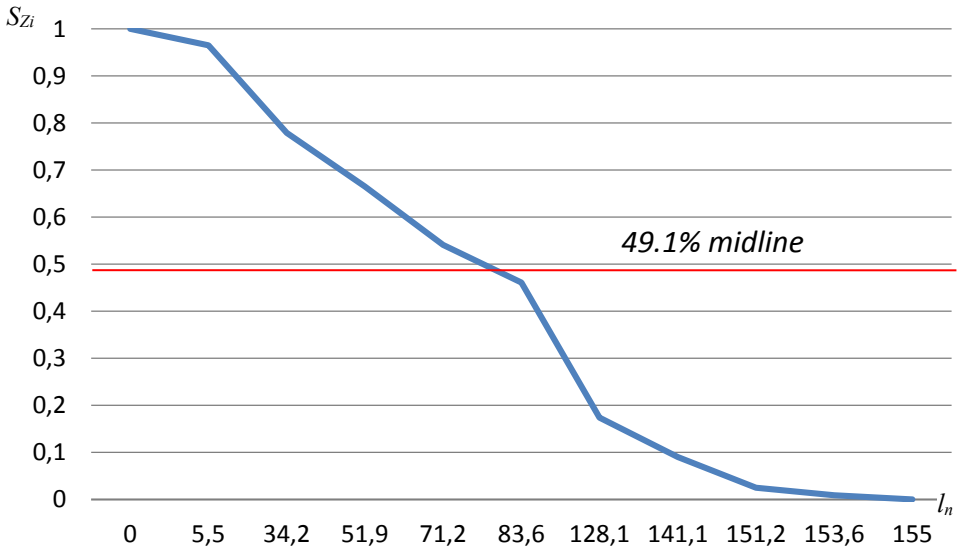

Fig. 2. *The curve of the probability of filling the rough layer with the material along the sections corresponding to the actual profillogram*
Рис. 2. *Кривая вероятности заполнения материалом шероховатого слоя по сечениям, соответствующая реальной профилограмме*

DISCUSSION

Currently, the surface texture parameters used in practice, presented in publications and in production, are insufficient. The use of complex parameters reflecting the operational characteristics of products is required. As part of the work performed, the authors justified the use of the "profile physical coefficient" parameter for estimating the surface texture using a new technique. The use of the profile physical coefficient allows meeting the increasing requirements for the working conditions of the surfaces of parts, especially those operating under friction conditions. Knowledge of the properties of the proposed models will allow recommending the technologies and methods for processing surfaces of interacting parts of machines and mechanisms.

The parameter was tested for a honed surface, and convergence was shown when analyzing the filling of a rough layer with a material along sections, which corresponds to the actual profillogram.

According to the developed technique, the Fourier series expansion of the micro-roughness model profile function given in the interval $(-l; l)$ allows building the entire range of models on a line of selective length according to which the profillogram is reproduced. It is important that in the overall assessment of the working surface microdimensions, it is possible to take into account deviations from a given geometric shape of the part, both regular and random.

A probabilistic assessment of filling the layer with the material from the theoretical reference line or surface to the theoretical equidistant line of the real profile is necessary when developing software for technological equipment operating in automatic control of cutting, grinding, honing, and plastic deformation in the process of forming the texture of the working surface of finished parts.

In future, the developed method for the computational-graphical study of a surface texture can be applied to analyze and evaluate the texture of the surfaces processed by various technologies, including the evaluation of the surface after post-processing of parts obtained additively.

The effect of applying the proposed method for estimating surface texture can be increased when combining it with new processing methods and techniques that contribute to the formation of a given surface texture.

CONCLUSIONS

The author justified the application of the "profile physical coefficient" parameter to set the requirements for the micro-geometry of the working surfaces of the parts.

The analysis of the obtained quantitative parameters found based on profillograms proved that the assessment of the material consumption of a rough layer most completely and comprehensively, compared to the well-known and widely used *Ra* parameter, characterises the geometry of waviness, its shape, flatness, pointedness, relief, performance, wear resistance, and oil absorption of voids and, accordingly, allows innovating the assessment of mixed friction of real surfaces.

REFERENCES

1. Abramov A., Bobrovskij N.M., Nosov N.V., Tabakov V., Galyalieva K. Quasi-optimal correlation algorithm for measuring the parameters of surface microrelief. *Key Engineering Materials*, 2019, vol. 822, pp. 725–730. DOI: 10.4028/www.scientific.net/KEM.822.725.
2. Abramov A., Bobrovskij S.M., Nosov N.V., Tabakov V., Lopatina F. Method for determining texture parameters of processed precision surfaces by correlation. *Key Engineering Materials*, 2019, vol. 822, pp. 731–736. DOI: 10.4028/www.scientific.net/KEM.822.731.
3. Singh R.V., Raghav A.K. Experimental study and modelling of the effect of process parameters on surface roughness during honing process. *Journal of the Institution of Engineers (India). Part PR: Production Engineering Division*, 2010, vol. 90, pp. 3–7.
4. Neagu C., Dumitrescu A. Neural networks modelling of process parameters in honing of thermal engines' cylinders. *Metalurgia International*, 2008, vol. 13, no. 5, pp. 66–78.
5. Feng C.-X.J., Yu Z.-G.S., Kingi U., Pervaiz B.M. Threefold vs. fivefold cross validation in one-hidden-layer and two-hidden-layer predictive neural network modeling of machining surface roughness data. *Journal of Manufacturing Systems*, 2005, vol. 24, no. 2, pp. 93–107. DOI: 10.1016/S0278-6125(05)80010-X.
6. Silva S.P., Brandao L.C., Pimenta P.R.F. Evaluation of quality of steering systems using the honing process and surface response methodology. *Advanced Materials Research*, 2011, vol. 223, pp. 821–825. DOI: 10.4028/www.scientific.net/AMR.223.821.
7. Tripathi B.N., Singh N.K., Vates U.K. Surface roughness influencing process parameters & modeling techniques for four stroke motor bike cylinder liners during honing: Review. *International Journal of Mechanical and Mechatronics Engineering*, 2015, vol. 15, no. 1, pp. 106–112.
8. Paswan S.K., Bedi T.S., Singh A.K. Modeling and simulation of surface roughness in magnetorheological fluid based honing process. *Wear*, 2017, vol. 376-377, pp. 1207–1221. DOI: 10.1016/j.wear.2016.11.025.
9. Buj-Corral I., Álvarez-Flórez J., Domínguez-Fernández A. Acoustic emission analysis for the detection of appropriate cutting operations in honing processes. *Mechanical Systems and Signal Processing*, 2018, vol. 99, pp. 873–885. DOI: 10.1016/j.ymssp.2017.06.039.
10. Span J., Koshy P., Klocke F., Müller S., Coelho R. Dynamic jamming in dense suspensions: Surface finishing and edge honing applications. *CIRP Annals*, 2017, vol. 66, no. 1, pp. 321–324. DOI: 10.1016/j.cirp.2017.04.082.
11. Ma S., Liu Y., Wang Z., Wang Zh., Huang R., Xu J. The Effect of Honing Angle and Roughness Height on the Tribological Performance of CuNiCr Iron Liner. *Metals*, 2019, vol. 9, no. 5, article number 487. DOI: 10.3390/met9050487.
12. Hu Y., Meng X., Xie Y., Fan J. Mutual influence of plateau roughness and groove texture of honed surface on frictional performance of piston ring-liner system. *Proceedings of the Institution of Mechanical Engineers, Part J: Journal of Engineering Tribology*, 2017, vol. 231, no. 7, pp. 838–859. DOI: 10.1177/1350650116682161.
13. Li B., Zhang S., Yan Z., Jiang D. Influence of edge hone radius on cutting forces, surface integrity, and surface oxidation in hard milling of AISI H13 steel. *Inter-*

national Journal of Advanced Manufacturing Technology, 2018, vol. 95, pp. 1153–1164. DOI: 10.1007/s00170-017-1292-z.
14. Nguyen T.-T., Vu T.-C., Duong Q.-D. Multi-responses optimization of finishing honing process for surface quality and production rate. *Journal of the Brazilian Society of Mechanical Sciences and Engineering*, 2020, vol. 42, article number 604. DOI: 10.1007/s40430-020-02690-y.
15. Arantes L.J., Fernandes K.A., Schramm C.R., Leal J.E.S., Piratelli-Filho A., Franco S.D., Arencibia R.V. The roughness characterization in cylinders obtained by conventional and flexible honing processes. *The International Journal of Advanced Manufacturing Technology*, 2017, vol. 93, pp. 635–649. DOI: 10.1007/s00170-017-0544-2.
16. Buj-Corral I., Rodero-De-Lamo L., Marco-Almagro L. Use of results from honing test machines to determine roughness in industrial honing machines. *Journal of Manufacturing Processes*, 2017, vol. 28, pp. 60–69. DOI: 10.1016/j.jmapro.2017.05.016.
17. Yuan B., Han J., Wang D., Zhu Y., Xia L. Modeling and analysis of tooth surface roughness for internal gearing power honing gear. *Journal of the Brazilian Society of Mechanical Sciences and Engineering*, 2017, vol. 39, pp. 3607–3620. DOI: 10.1007/s40430-017-0791-z.
18. Kuznetsov V.P., Voropaev V.V., Skorobogatov A.S. Finishing and hardening of a flat surface ring area of a workpiece by rotary burnishing. *Key Engineering Materials*, 2017, vol. 743, pp. 245–247. DOI: 10.4028/www.scientific.net/KEM.743.245.
19. Bobrovskii I.N. How to Select the most Relevant Roughness Parameters of a Surface: Methodology Research Strategy. *IOP Conference Series: Materials Science and Engineering*, 2018, vol. 302, article number 012066. DOI: 10.1088/1757-899X/302/1/012066.

СПИСОК ЛИТЕРАТУРЫ

1. Abramov A., Bobrovskij N.M., Nosov N.V., Tabakov V., Galyalieva K. Quasi-optimal correlation algorithm for measuring the parameters of surface microrelief // Key Engineering Materials. 2019. Vol. 822. P. 725–730. DOI: 10.4028/www.scientific.net/KEM.822.725.
2. Abramov A., Bobrovskij S.M., Nosov N.V., Tabakov V., Lopatina F. Method for determining texture parameters of processed precision surfaces by correlation // Key Engineering Materials. 2019. Vol. 822. P. 731–736. DOI: 10.4028/www.scientific.net/KEM.822.731.
3. Singh R.V., Raghav A.K. Experimental study and modelling of the effect of process parameters on surface roughness during honing process // Journal of the Institution of Engineers (India). Part PR: Production Engineering Division. 2010. Vol. 90. P. 3–7.
4. Neagu C., Dumitrescu A. Neural networks modelling of process parameters in honing of thermal engines’ cylinders // Metalurgia International. 2008. Vol. 13. № 5. P. 66–78.
5. Feng C.-X.J., Yu Z.-G.S., Kingi U., Pervaiz B.M. Threefold vs. fivefold cross validation in one-hidden-layer and two-hidden-layer predictive neural network modeling of machining surface roughness data // Journal of Manufacturing Systems. 2005. Vol. 24. № 2. P. 93–107. DOI: 10.1016/S0278-6125(05)80010-X.
6. Silva S.P., Brandao L.C., Pimenta P.R.F. Evaluation of quality of steering systems using the honing process and surface response methodology // Advanced Materials Research. 2011. Vol. 223. P. 821–825. DOI: 10.4028/www.scientific.net/AMR.223.821.
7. Tripathi B.N., Singh N.K., Vates U.K. Surface roughness influencing process parameters & modeling techniques for four stroke motor bike cylinder liners during honing: Review // International Journal of Mechanical and Mechatronics Engineering. 2015. Vol. 15. № 1. P. 106–112.
8. Paswan S.K., Bedi T.S., Singh A.K. Modeling and simulation of surface roughness in magnetorheological fluid based honing process // Wear. 2017. Vol. 376-377. P. 1207–1221. DOI: 10.1016/j.wear.2016.11.025.
9. Buj-Corral I., Álvarez-Flórez J., Domínguez-Fernández A. Acoustic emission analysis for the detection of appropriate cutting operations in honing processes // Mechanical Systems and Signal Processing. 2018. Vol. 99. P. 873–885. DOI: 10.1016/j.ymssp.2017.06.039.
10. Span J., Koshy P., Klocke F., Müller S., Coelho R. Dynamic jamming in dense suspensions: Surface finishing and edge honing applications // CIRP Annals. 2017. Vol. 66. № 1. P. 321–324. DOI: 10.1016/j.cirp.2017.04.082.
11. Ma S., Liu Y., Wang Z., Wang Zh., Huang R., Xu J. The Effect of Honing Angle and Roughness Height on the Tribological Performance of CuNiCr Iron Liner // Metals. 2019. Vol. 9. № 5. Article number 487. DOI: 10.3390/met9050487.
12. Hu Y., Meng X., Xie Y., Fan J. Mutual influence of plateau roughness and groove texture of honed surface on frictional performance of piston ring-liner system // Proceedings of the Institution of Mechanical Engineers, Part J: Journal of Engineering Tribology. 2017. Vol. 231. № 7. P. 838–859. DOI: 10.1177/1350650116682161.
13. Li B., Zhang S., Yan Z., Jiang D. Influence of edge hone radius on cutting forces, surface integrity, and surface oxidation in hard milling of AISI H13 steel // International Journal of Advanced Manufacturing Technology. 2018. Vol. 95. P. 1153–1164. DOI: 10.1007/s00170-017-1292-z.
14. Nguyen T.-T., Vu T.-C., Duong Q.-D. Multi-responses optimization of finishing honing process for surface quality and production rate // Journal of the Brazilian Society of Mechanical Sciences and Engineering. 2020. Vol. 42. Article number 604. DOI: 10.1007/s40430-020-02690-y.
15. Arantes L.J., Fernandes K.A., Schramm C.R., Leal J.E.S., Piratelli-Filho A., Franco S.D., Arencibia R.V. The roughness characterization in cylinders obtained by conventional and flexible honing processes // The International Journal of Advanced Manufacturing Technology. 2017. Vol. 93. P. 635–649. DOI: 10.1007/s00170-017-0544-2.
16. Buj-Corral I., Rodero-De-Lamo L., Marco-Almagro L. Use of results from honing test machines to determine roughness in industrial honing machines // Journal of Manufacturing Processes. 2017. Vol. 28. P. 60–69. DOI: 10.1016/j.jmapro.2017.05.016.
17. Yuan B., Han J., Wang D., Zhu Y., Xia L. Modeling and analysis of tooth surface roughness for internal

gearing power honing gear // Journal of the Brazilian Society of Mechanical Sciences and Engineering. 2017. Vol. 39. P. 3607–3620. DOI: 10.1007/s40430-017-0791-z.
18. Kuznetsov V.P., Voropaev V.V., Skorobogatov A.S. Finishing and hardening of a flat surface ring area of a workpiece by rotary burnishing // Key Engineering Materials. 2017. Vol. 743. P. 245–247. DOI: 10.4028/www.scientific.net/KEM.743.245.
19. Bobrovskii I.N. How to Select the most Relevant Roughness Parameters of a Surface: Methodology Research Strategy // IOP Conference Series: Materials Science and Engineering. 2018. Vol. 302. Article number 012066. DOI: 10.1088/1757-899X/302/1/012066.

Физический коэффициент профиля и его применение для моделирования текстуры механически обработанной поверхности

© 2023

Бобровский Игорь Николаевич, доктор технических наук, научный сотрудник
Тольяттинский государственный университет, Тольятти (Россия)

E-mail: bobri@yandex.ru ORCID: https://orcid.org/0000-0002-9513-7936

Поступила в редакцию 28.07.2022 *Принята к публикации 14.04.2023*

Аннотация: Современные тенденции развития машиностроения задают всё более жесткие требования к эксплуатационным характеристикам готовой продукции. Основными параметрами, характеризующими качество изделия в целом, являются физико-механические и геометрические показатели рабочих поверхностей составных деталей. Поверхность, полученная в результате механической обработки, в отечественной практике в основном характеризуется весьма ограниченным числом параметров (не более 6), таких как средняя высота микронеровностей, высоты микронеровностей по 10 точкам и др. Однако их применение недостаточно для производства конкурентоспособной продукции в современных условиях. Например, международные стандарты ISO/ASME/DIN включают гораздо более широкий набор параметров, необходимых для точного описания эксплуатационных свойств поверхности. В статье проанализированы подходы к формированию требований к микрогеометрии рабочих поверхностей деталей, используемых в современном машиностроении. На основе проведенного анализа предложен и математически обоснован общий подход к моделированию характеристик текстуры поверхности, который позволяет адекватно описывать поверхность с использованием нового параметра – физического коэффициента профиля, поскольку прямое сравнение технологий, разработанных в России, с иностранными аналогами с опорой на действующие стандарты практически невозможно. Сначала был определен физический коэффициент профиля на секционном уровне. Далее было выполнено его разложение на ряд Фурье для двухмерного и трехмерного случаев. Приведен анализ применимости нового параметра на примере изделия, полученного с помощью хонингования. Сделан вывод о целесообразности применения данного параметра и необходимости разработки комплексной методики оценки поверхности после механической обработки на его основе.

Ключевые слова: технология машиностроения; механическая обработка; поверхность; физический коэффициент профиля; шероховатый слой; текстура поверхности.

Благодарности: Исследование выполнено за счет гранта Российского научного фонда № 20-79-00233, https://rscf.ru/project/20-79-00233/.

Для цитирования: Бобровский И.Н. Физический коэффициент профиля и его применение для моделирования текстуры механически обработанной поверхности // Frontier Materials & Technologies. 2023. № 3. С. 9–17. DOI: 10.18323/2782-4039-2023-3-65-1.

doi: 10.18323/2782-4039-2023-3-65-2

Development and airworthiness certification of state of art additively manufactured AlSi10Mg mission critical selector valve body part for aerospace

© 2023

Ponnusamy Vignesh*[1], Ph.D., Junior Specialist-1
K.V. Praveen, Bachelor of Engineering, Technical Assistant
Subbulakshmi Krishnakumar, Bachelor of Engineering, Technical Assistant
Mohanrao Chembu Bhuvaneswari, Bachelor of Engineering, Regional Director (Sc 'F')
Shirish Sharad Kale, Ph.D., Director (Sc 'G')
Theagarajan Ram Prabhu, Ph.D., Joint Director (Sc 'E')
RCMA (F&F), CEMILAC, Defence R&D Organization, Bangalore (India)

***E-mail: vigneshpt3532@gmail.com** [1]ORCID: https://orcid.org/0000-0003-4487-2030

Received 22.06.2023 *Accepted 15.08.2023*

Abstract: Aerospace applications can benefit from additive manufacturing (AM), which is highly advantageous for prototyping and rapid manufacturing. It also offers cost and weight savings, as well as integrated design capabilities. As of now, there are only a few AM standards available, many materials and equipment are involved, resulting in many variables that hinder certification and adoption. As a result, nonstandard testing is making AM in the airborne materials less appealing due to its costly and time-consuming nature. The main objective of this work is to manufacture the Selector Valve Body parts of military and civil aircraft through Laser Powder Bed Fusion (LPBF) process using AlSi10Mg powder. Further, this paper has been carried out the metallurgical properties, non-destructive and destructive testing as well as the clear explanation about the certification procedures. Moreover, this underscores the need for the developing guidelines, and standards that cover all aspects of manufacturing from design to manufacturing to operation. A comprehensive analysis from liquid penetration test shows defects are within the permissible level. In addition, it exhibits higher yield strength, ultimate strength, and elongation of (259±4) MPa, (323±4) MPa, and (12.5±1.5) % respectively, along with factual evidence that the precipitation hardened AlSi10Mg indigenously developed and produced is equal in properties to the equivalent precipitation hardening aluminium alloys produced by internationally renowned manufacturers.

Keywords: additive manufacturing; AlSi10Mg; Al alloy; precipitate hardening; development and certification.

For citation: Vignesh P., Praveen K.V., Krishnakumar S., Bhuvaneswari M.C., Kale S.S., Ram Prabhu T. Development and airworthiness certification of state of art additively manufactured AlSi10Mg mission critical selector valve body part for aerospace. *Frontier Materials & Technologies*, 2023, no. 3, pp. 19–30. DOI: 10.18323/2782-4039-2023-3-65-2.

INTRODUCTION

Aerospace, military, biomedical, and automotive parts are made of traditional high-strength aluminium alloys. There are two predominant conventional Al alloys used in aerospace: a precipitation-hardened (Al–Mg–Si) alloy and aluminium 6061 (Al6061) from the 6000 series. Laser additive manufacturing of high-performance alloys like Al6061 has gained significant interest, due to producing high-strength in lightweight structures. AlSi10Mg is a close-eutectic aluminium alloy with high melt fluidity and low shrinkage, and hence has traditionally been the most suitable for laser additive processing [1; 2]. In conventional casting (gravity casting), the hypoeutectic alloy AlSi10Mg is commonly used. Because of its lightweight and excellent mechanical properties, this alloy is widely used in the automotive and aerospace sectors. Meanwhile age hardening, Mg is crucial to its functionality because it facilitates the precipitation of the β′- and β-phases (Mg_2Si) [3; 4]. Numerous investigations have previously been conducted on the additive manufacturing (AM) produced precipitation-hardened (AlSi10Mg) alloy [5]. Generally, they address microstructure, process parameter setup, and mechanical properties, although some address heat treatment as well [6; 7]. AM Al–Si alloys are being optimised by studying their microstructural evolution as they are built, and after heat treatment [8]. Due to melt pool formation, the alloy showed "fish-scale" patterns in the directions of build, and columnar grains in the perpendicular directions [9; 10]. Grain refinement of Al–Si alloys leads to enhance mechanical properties [11]. According to [12], high cooling rates can generate fine grains Al with nano-sized Si, which has higher mechanical characteristics. AM Al–Si–Mg alloys were modified, by altering their morphology and coarsening by using a particular heat treatment [13; 14]. Al alloys after precipitation hardened, especially 6xxxx Al alloys, emerged to study comprehensively for precipitates and mechanical properties [15; 16]. It has been observed that the precipitates occurred in the following order: (Al) GP zones; β"→β'→β. In the GP zones, the clusters of Mg and Si are perfectly coherent with those of the Al matrix. The metastable (β" and β') with different Mg–Si stoichiometry, whereas stable (β) with different Mg_2Si stoichiometry [17; 18]. Peak hardening usually occurs when the GP zones coexist [19]. Aging at various temperatures resulted in varied ageing kinetics, although with equal hardness magnitudes [20]. Sha et al. [21] described a comparable precipitation sequence for Al–7Si–0.6Mg, a composition identical to alloys accessible for Powder Bed Fusion (PBF) AM. In AlSi10Mg alloys, precipitation hardening is still widely used [22]. The peak hardness throughout the ageing process, on the other hand, has seldom been documented.

Given the present relevance about AlSi10Mg alloy for Lazer Powder Bed Fusion (LPBF), a greater knowledge of the precipitation hardening on the microstructure and characteristics is necessary.

The research aim is fabricating the part through LPBF process and evaluation of material as per ASTM F3318. Mechanical properties, of heat-treated LPBF AlSi10Mg alloys (T6). The precipitate development was meticulously studied concerning better comprehension of the mechanical behaviour of the Al alloy formed by LPBF.

METHODS

Powder Details

The Aluminum powder designated (ASTM F3318) was available from Carpenter in the form of a powder (Table 1). The Al powders were gas atomised having an amorphous morphology, as shown in Fig. 1. A laser diffraction study was carried out according to ASTM B822-17, to determine the particle size distribution (PSD) of powder. Fig. 2 shows the D10, D50, and D90 particle diameters in the cumulative distribution at 10, 50, and 90 %. The powder bulk density of 2.3 g/cm^3, D10, D50, and D90 values of 29.89, 41.63, and 53.95 μm, respectively.

Parameters of Laser Powder Bed Fusion

A similar set of processing parameters is used for all parts produced by the EOS M290 machine, under an inert atmosphere. We processed the parts using aluminium-specific processing parameters, which include an Yb-fibre laser with 400 W of power, a scanning rate of 7 m/s, a layer thickness of 0.03 mm, a focus diameter of 80 to 100 mm, hatch distance 0.19 mm, and a recoater type HSS.

Heat Treatment

The body parts of the alloy produced by LPBF subjected: 1) stress relieving at 270±20 °C and soak for 90±15 min and air-cooling; 2) solutionising temperature 530±14 °C and soak for 30±10 min, followed by water quenching. Aging cycle 165±10 °C for 360±15 min followed by air-cooling.

Characterisation

The elements were analysed chemically as per ASTM E3061 using optical emission spectrometers. Microstructural characteristics and grain size were determined as per ASTM E3 & ASTM E407. X-ray radiography test performed on the body parts as per ASTM E1742/E1742M. Liquid (florescence) penetrant testing performed on the body parts as per ASTM E1417. X-ray diffraction (XRD) was carried out to measure the residual stress as per ASTM E2860 in four locations as shown in Fig. 3. In XRD experiments, the voltage, scanning rate, 2θ range, radiation type, and step size were set as 40 kV, 5 deg/min, 10–90°, Cu–Kα, and 0.028°.

Mechanical Properties

In order to test for Brinell hardness on the specimen cross-section, an ASTM E10 hardness test was performed. By applying the load at three different locations, the mean value of hardness (HBW) can be calculated. According to tensile curves, we can determine ultimate strength (UTS), yield strength (YS), and elongation. Tensile tests were conducted in all three directions (XY, Z & 45°) using an ASTM E8 standard (a sample).

RESULTS

Chemical composition

As shown in Table 2, the chemical composition of selector valve body parts, in LPBF as-build, was obtained over two samples of the AlSi10Mg alloy. Noticeably from these results, the alloy's chemical composition is within ASTM F3318 allowable limits. Additionally, oxygen, nitrogen, and hydrogen gas levels were measured and found to be 0.0862, 0.001, and 0.004 wt. %, respectively.

Microstructure of AlSi10Mg in T6 condition

The microstructure of the AlSi10Mg alloy prepared by the LPBF technique after the precipitation hardening is shown in Fig. 4. The precipitated hardened samples (Fig. 4 a), molten pool's edge was not clearly visible, and numerous tiny flakes with elliptical shapes were found on the surface. These irregular flakes, which are elliptical in shape, are scattered throughout the specimens and associate the accumulation zones of precipitates at each end of the long molten pool. This characteristic suggests that in the sample that underwent heat treatment, the precipitate's aggregation region was eroded. Precipitates it is visible in the magnified pictures (Fig. 4 b) that dispersed along the margins of the molten pool, with a limited width of band. After the precipitation hardening, elongated molten pool lost its approximately spherical precipitate bands. Precipitation hardening has significantly coarsened Si particles, which has eliminated distinctive columnar grains. Therefore, T6 heat treatment can help to attain superior mechanical properties by promoting grain refinement and homogenous microstructure.

Mechanical Properties AlSi10Mg in T6 condition

The engineering stress-strain curve showing precipitation hardening's effect on mechanical properties shown in Fig. 5. A summary of selected properties can be found in Table 3. The AlSi10Mg alloy is distinguished by high YS (259±6 MPa) and UTS (324±4 MPa) values, which are typically larger than those achieved by traditional manufacturing process.

Experimental Evaluation of the Inspection Techniques

X-ray testing, and liquid penetrant inspection were applied in order to detect the samples defects. The as-built selector value body parts are subjected to an X-ray radiography examination for the purpose of evaluating defects throughout the specimen (maximum permissible level, as shown in Table 4). The samples with LPBF have been found to be free from any visible weld defects like porosity, lack of penetration, and cracking defects.

Liquid penetrant (LP) examinations are one of the fastest and most common methods of checking LPBF inspections for discontinuities and subsurface openings. Initially, a cleaner is used to clean the surface of the samples, and then penetrant is applied and allowed to dwell for a sufficient period. In order to examine the surface of the sample,

Table 1. *Chemical composition of AlSi10Mg powder wt. %*
Таблица 1. *Химический состав порошка AlSi10Mg, мас. %*

Elements	Cu	Fe	Mg	Mn	Ni	Si	Zn	Ti	Pb	Sn	Others-total	Al
Limits	0.05 max	0.55 max	0.20–0,45	0.45 max	0.05 max	9–11	0.10 max	0.15 max	0.05 max	0.05 max	0.15 max	Bal

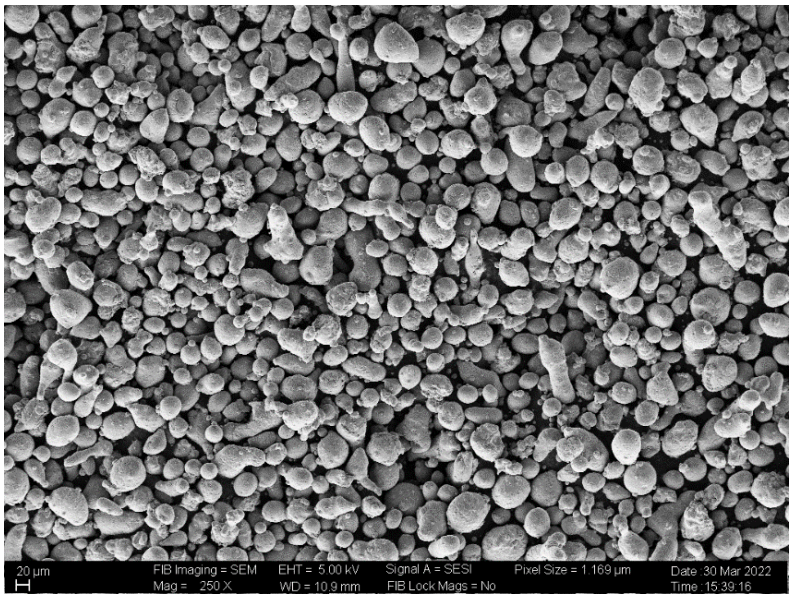

Fig. 1. *AlSi10Mg powder material as seen in SEM images*
Рис. 1. *Порошковый материал AlSi10Mg на РЭМ-изображениях*

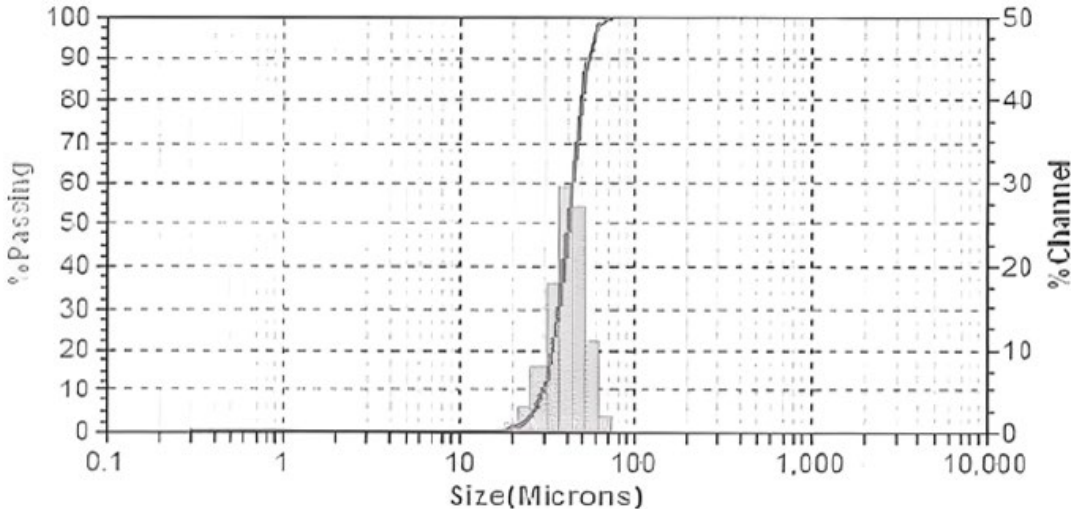

Fig. 2. *Distribution of particle sizes in AlSi10Mg powder*
Рис. 2. *Распределение по размерам частиц в порошке AlSi10Mg*

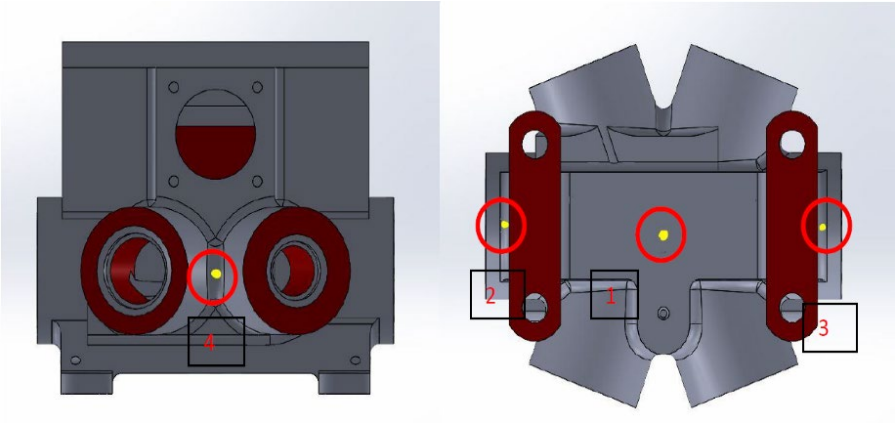

Fig. 3. *Measurement of residual stress in marked areas*
Рис. 3. *Измерение остаточного напряжения в выделенных областях*

Table 2. *Chemical composition of AlSi10Mg in as-developed condition, wt. %*
Таблица 2. *Химический состав AlSi10Mg в исходном состоянии, мас. %*

Elements	Cu	Fe	Mg	Mn	Ni	Si	Zn	Ti	Pb	Sn	Others-total	Al
Limits	0.05 max	0.55 max	0.20–0.45	0.45 max	0.05 max	9–11	0.10 max	0.15 max	0.05 max	0.05 max	0.15 max	Bal
Sample 1	0.028	0.215	0.329	0.046	0.035	10.31	0.032	0.020	0.015	0.024	0.048	Bal
Sample 2	0.032	0.223	0.327	0.046	0.036	10.21	0.035	0.020	0.016	0.024	0.048	Bal

excess penetrant must be removed from the specimen before developer is applied. As shown in Fig. 6, the selector valve body parts were fabricated by additive manufacturing. Fluorescent penetrant inspection was performed on these parts to verify that they met the acceptance criteria listed in Table 5. The selector value body parts were subjected to a liquid penetrant examination. There are no indications of discrete cracks or microcracks on the surfaces of the AM parts. A noteworthy feature of the surface is the absence of inclusions, stringers, cracks, seams, laps, undercuts, flakes, and laminations. As far as airworthiness is concerned, the two non-destructive tests listed above are of great importance. The selector valve body parts cannot be deployed in the hydraulic system if they fail these two tests.

Residual stress

The residual stress of AlSi10Mg in the T6 condition is shown in Fig. 7. There are different points at which residual stress measurements can be made, so a residual stress value is the average of them all. As a result of plastic deformation, materials usually generate residual stresses. In spite of this, no plastic deformation has occurred in the LPBF specimens. A repeating rapid heating and cooling of the molten phase accumulates residual thermal stresses in the solidified layer. The specimen 1 is clearly subjected to compressive residual stress (location 1), which gradually increases (locations 2 and 3). The specimen 1 is clearly subjected to compressive residual stress (location 1), which gradually increases (locations 2 and 3). In contradictory location 4, the residual stress turns into tensile stress. Specimen 2 is initially subjected to compressive stress, steep increases in residual stress, which turned into a tensile test in location 2, and then back to compressive stress in locations 3 and 4.

Airworthiness certification

This section describes the typical airworthiness certification (AWC) process of aerospace LPBF with an example of selector valve body parts. AWC of Selector Valve Body Parts LPBF has three phases: (1) process design evaluation, (2) development trials and testing, and (3) certification documentation.

The component under examination is categorized for functionality and process criticality while evaluating process designs. In the current study, selector valve body parts that are typically modelled before beginning trials were examined. In the model, the component is LPBF for various process parameter combinations and is analysed for the degree of ease and comfort in the LPBF contours and sharp information, as well as the defect evolution. After finalising the process parameters, trials simulate the modelling constraints to verify the model's accuracy. Following that, airworthiness authorities review and certify the design

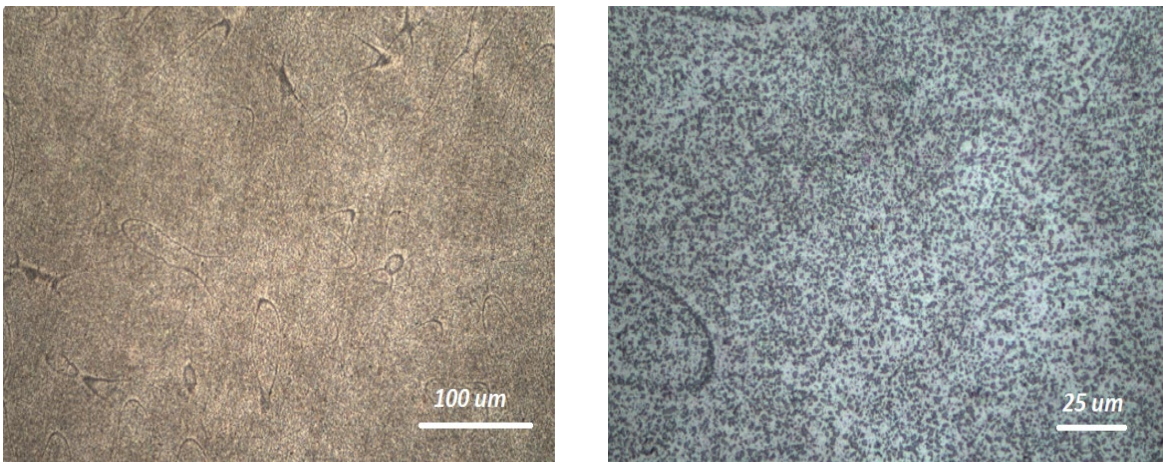

a *b*

Fig. 4. *Optical microstructure of AlSi10Mg at T6 condition* ***(a)*** *and higher magnification* ***(b)***
Рис. 4. *Оптическое изображение микроструктуры AlSi10Mg в режиме T6* ***(a)*** *и увеличенное изображение* ***(b)***

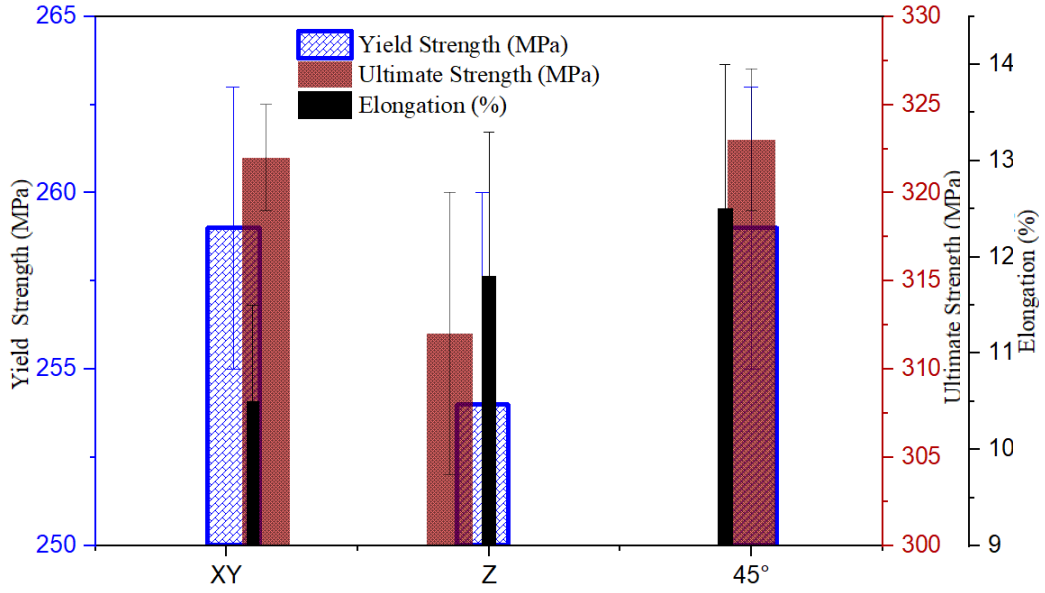

Fig. 5. *Tensile properties of T6 condition AlSi10Mg test samples*
Рис. 5. *Свойства при растяжении испытательных образцов AlSi10Mg в режиме T6*

Table 3. *Mechanical properties of selector valve body parts in T6 conditions*
Таблица 3. *Механические свойства деталей корпуса переключателя в режиме T6*

Specimen direction	Yield Strength, MPa	Ultimate Strength, MPa	Elongation, %	Hardness, HBW
XY	259±4	322±3	10.5±1	88.8±2
Z	254±6	312±8	11.8±1.5	
45°	259±4	323±4	12.5±1.5	

Table 4. *Maximum permissible radiography severity levels for discontinuity*
Таблица 4. *Максимально допустимые уровни радиографической интенсивности для неоднородности*

Discontinuity	Severity Level – Grade B	
	¼	¾
Gas Holes	1	1
Gas Porosity, Round	1	1
Gas Porosity, Elongated	1	2
Foreign Material	1	1
Keyhole porosity	<0.152 mm	
Cracks	None	
Surface irregularity	Not to exceed drawing tolerance	
Overlaps	None	
Incomplete Fusion	None	

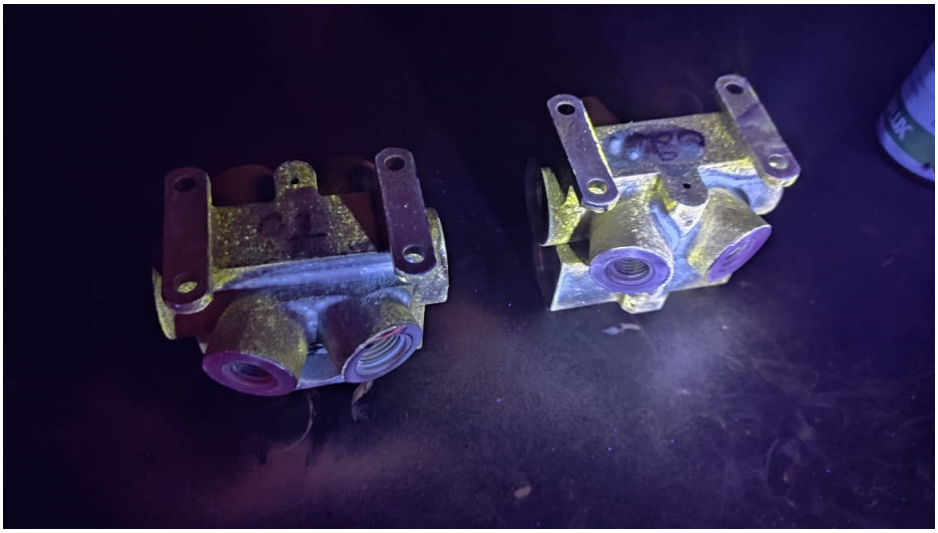

Fig. 6. *Result Dye penetrant test of selector valve body parts*
Рис. 6. *Результат цветной дефектоскопии деталей корпуса переключателя*

parameters. Finally, the drawing, and design validation report are developed and subjected to airworthiness qualification testing. Additionally, the qualification tests necessary to verify the airworthiness of Selector valve body parts are created based on the components functioning, operating conditions, and interactions with other parts. In this example, selector valve body parts (LPBF) have been subjected to post-heat treatment, during which, structure property correlations were carried out. Selector valve body components are a line replaceable unit (LRU), thus the fault tolerance level is extremely restrictive since any flaws larger than the critical size seriously impair hydraulic system performance. As a standard practise for surface defect inspection, radiography testing (ASTM E1742) and fluorescence penetrant inspection (ASTM E1417) are recommended.

A thorough test plan that includes testing requirements in accordance with aerospace material and testing standards, component geometry, and designer-specific testing needs, is created based on the aforementioned inputs, and certified by airworthiness agencies. The sample strategy is designed, based on the testing method, designer specifications, and part criticality. Non-destructive and destructive testing are typically performed on a single sample per batch and in parts produced. The qualification of the test schedule of the LPBF in the presence of airworthiness agencies is carried out in development batches. After testing,

Table 5. *Maximum discontinuity sizes (in mm) and distributions are allowed*
Таблица 5. *Максимальные допустимые размеры (в мм) и распределения неоднородностей*

Type of discontinuity	Max size of discontinuity allowed
Inclusion rounded: surface	1.193 dia D-3*
Inclusion rounded: subsurface	1.6 dia D-3*
Inclusion stringers: surface	9.52 long DD-1**
Inclusion stringers: subsurface	12.7 long DD-1**
Laps or seams (unmachined surfaces)	25.4 long DD-1**
Laps or seams or (machined surfaces)	0
Propagating discontinuities (laminations, flakes, cracks, etc.)	0
Unmelted particle, balling, porosity	None

Note. The following is a list of distribution designations.
** D-3 – there should be no more than three times the maximum distance between discontinuities.*
*** DD-1 – linear discontinuities cannot be closer than 12.7 mm and parallel discontinuities cannot be closer than 6.35 mm.*
*Примечание. * D-3 – между неоднородностями должно быть не более трех максимальных расстояний.*
*** DD-1 – расстояние между линейными неоднородностями не может быть меньше, чем 12,7 мм, а между параллельными неоднородностями – меньше, чем 6,35 мм.*

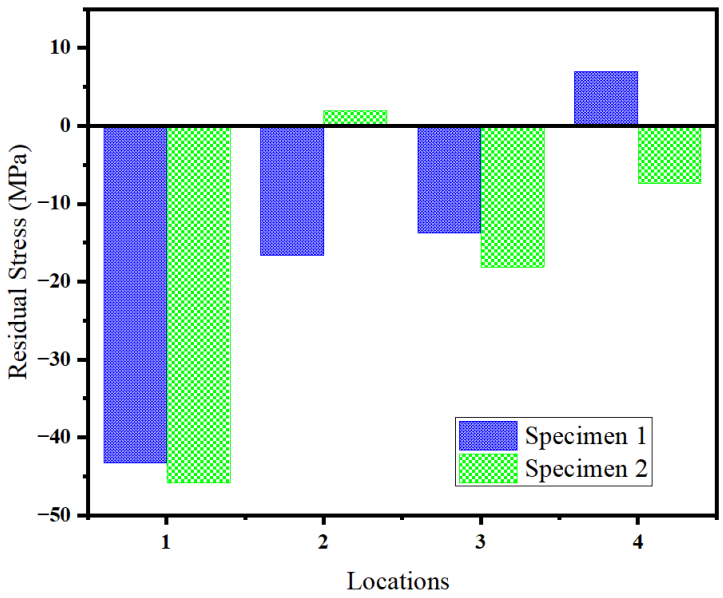

Fig. 7. *Residual stress in precipitation hardened AlSi10Mg specimens*
Рис. 7. *Остаточное напряжение в образцах дисперсионно-твердеющего AlSi10Mg*

the reports are prepared and submitted to airworthiness agencies for review.

Before certification by airworthiness agencies, the testing reports are rigorously checked and validated for correctness in the final step of certification which is shown in the Fig. 8. Following a thorough review of the reports, Selector valve body parts is granted permission to continue manufacturing on the specific platform. Part machining, fitting, functional tests simulating real hydraulic operating conditions, and prototype hydraulic units trials are all part of the selector valve body parts.

Certification includes the process and product validation against the test schedule. The tests that must be performed to qualify the Selector valve body components are determined by the material specification and operating conditions. Working conditions include things like operational temperature and contact condition. The following tests must be performed in order to certify

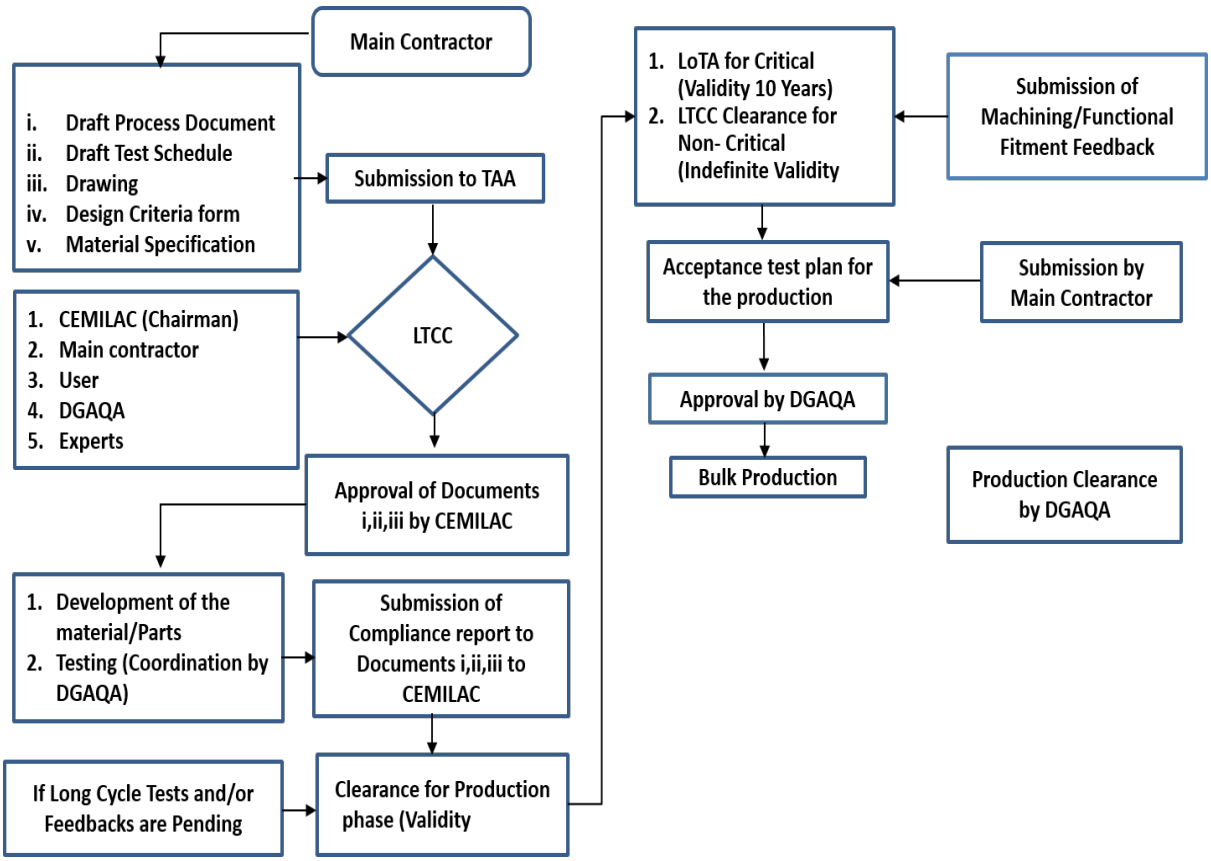

Fig. 8. *An overview of the certification process*
Рис. 8. *Общее представление процесса сертификации*

the process and product: (1) chemical composition to correspond to the material specification; (2) NDT (X-ray and Dye penetrant testing) to validate the defect level within a reasonable range; (3) microstructure to confirm the heat treatment procedure; and (4) a tensile test at room temperature on a specimen in the independently required condition.

The foregoing tests are performed, and the test reports are checked for conformity to the AM (LPBF) test schedule. These are provisionally certified for component-level LRU performance based on good compliance. Following successful completion of the aforesaid tests, the selector valve body parts is type certified for five years by the Indian military airworthiness certification organization (CEMILAC).

DISCUSSION

The alloy's extremely fine grains microstructure, which is developed by rapid solidification. On the other hand, AM parts have low elongation (12.5 %). A material's strength significantly enhanced by the formation and homogenous distribution of precipitates due to artificial aging. During the aging process, precipitation occurs as a result of the reaction of Mg with Si, where fine grains of precipitate interact with dislocations which leads to strengthening of the material. The precipitation hardening process involves several stages. As a first step, Mg and Si atoms form small clusters (GP zones). Mg_2Si then precipitates nucleate in metastable and coherent β″ phases. These progressively transition into metastable and semi coherent β′ phases, which have the greatest strengthening effect. As-fabricated LPBF samples are generally much harder than heat-treated T4 materials. In T4 conditions fine-grained recrystallisation microstructure created during a solid solution is the cause of this reduced hardness. LPBF specimen can exhibit high hardness values due to their cellular dendritic microstructures, dislocation structures, and fine dispersion of eutectic Si in the Al matrix [12]. The solutionising treatment, on the other hand, dissolves these secondary phases and significantly reduces hardness [13], the following artificial ageing can cause metastable phases such as Mg_2Si precipitate. This change may have a minor impact on the hardness values. As a result, the precipitation hardening has an effect on increasing hardness, however, it may be necessary to reduce stress and obtain other mechanical qualities. As a result of plastic deformation, materials usually generate residual stresses. In spite of this, no plastic deformation has occurred in the LPBF specimens. A repeating rapid heating and cooling of the molten phase accumulates residual thermal stresses in the solidified layer. Laser beams can result in complex stresses on specimens during Laser Additive Manufacturing (LAM), processing because the underlying layer is remelted and reheated. Heat gradients along the building direction cause alternating tensile and compressive residual stresses between the underlying and

subsequent layers. Because of the large scale and low quantity of grain boundaries in the T6 specimen, dislocations glide and climb easily (Fig. 4). In order to improve mechanical properties and increase service life, tensile residual stress must be reduced or eliminated from a material.

CONCLUSIONS

LPBF has been used for the development and testing of selector valve body parts, and the process is well suited to fabricate selector valve body parts using additive manufacturing. The preferred material for selector valve body parts is AlSi10Mg. There have been discussions regarding the potential application of different service areas throughout the AM process, including design, materials, pre-processing, 3D-printing and manufacturing, post-processing, testing and inspection, verification, and certification. This novel certification pathway will provide the hydraulic system of aircraft and its supply chain ecosystem, with a novel approach to identify the most efficient path to building trust and confidence in the adoption of this emerging technology, which would otherwise not be possible because of its novel approach.

REFERENCES

1. Bradford R.L., Cao L., Klosterman D., Herman F., Forman L., Browning C. A metal–metal powder formulation approach for laser additive manufacturing of difficult-to-print high-strength aluminum alloys. *Materials Letters*, 2021, vol. 300, article number 130113. DOI: 10.1016/j.matlet.2021.130113.
2. Bajakke P.A., Malik V.R., Deshpande A.S. Particulate metal matrix composites and their fabrication via friction stir processing – a review. *Materials and Manufacturing Processes*, 2018, vol. 34, no. 8, pp. 833–881. DOI: 10.1080/10426914.2019.1605181.
3. Matilainen V., Piili H., Salminen A., Syvänen T., Nyrhilä O. Characterization of process efficiency improvement in laser additive manufacturing. *Physics Procedia*, 2014, vol. 56, pp. 317–326. DOI: 10.1016/j.phpro.2014.08.177.
4. Fousová M., Dvorský D., Michalcová A., Vojtěch D. Changes in the microstructure and mechanical properties of additively manufactured AlSi10Mg alloy after exposure to elevated temperatures. *Materials Characterization*, 2018, vol. 137, pp. 119–126. DOI: 10.1016/j.matchar.2018.01.028.
5. Tradowsky U., White J., Ward R.M., Read N., Reimers W., Attallah M.M. Selective laser melting of AlSi10Mg: Influence of post-processing on the microstructural and tensile properties development. *Materials & Design*, 2016, vol. 105, pp. 212–222. DOI: 10.1016/j.matdes.2016.05.066.
6. Zhou L., Mehta A., Schulz E., McWilliams B., Cho K., Sohn Y. Microstructure, precipitates and hardness of selectively laser melted AlSi10Mg alloy before and after heat treatment. *Materials Characterization*, 2018, vol. 143, pp. 5–17. DOI: 10.1016/j.matchar.2018.04.022.
7. Li X.P., Wang X.J., Saunders M., Suvorova A., Zhang L.C., Liu Y.J., Fang M.H., Huang Z.H., Sercombe T.B. A selective laser melting and solution heat treatment refined Al–12Si alloy with a controllable ultrafine eutectic microstructure and 25% tensile ductility. *Acta Materialia*, 2015, vol. 95, pp. 74–82. DOI: 10.1016/j.actamat.2015.05.017.
8. Andersen S.J., Zandbergen H.W., Jansen J., TrÆholt C., Tundal U., Reiso O. The crystal structure of the β″phase in Al–Mg–Si alloys. *Acta Materialia*, 1998, vol. 46, no. 9, pp. 3283–3298. DOI: 10.1016/S1359-6454(97)00493-X.
9. Rometsch P.A., Schaffer G.B. An age hardening model for Al–7Si–Mg casting alloys. *Materials Science and Engineering: A*, 2002, vol. 325, no. 1-2, pp. 424–434. DOI: 10.1016/S0921-5093(01)01479-4.
10. Montero-Sistiaga M.L., Mertens R., Vrancken B., Wang X., Van Hooreweder B., Kruth J.P., Van Humbeeck J. Changing the alloy composition of Al7075 for better processability by selective laser melting. *Journal of Materials Processing Technology*, 2016, vol. 238, pp. 437–445. DOI: 10.1016/j.jmatprotec.2016.08.003.
11. Li W., Li S., Liu J., Zhang A., Zhou Y., Wei Q., Yan C., Shi Y. Effect of heat treatment on AlSi10Mg alloy fabricated by selective laser melting: Microstructure evolution, mechanical properties and fracture mechanism. *Materials Science and Engineering: A*, 2016, vol. 663, pp. 116–125. DOI: 10.1016/j.msea.2016.03.088.
12. Takata N., Kodaira H., Sekizawa K., Suzuki A., Kobashi M. Change in microstructure of selectively laser melted AlSi10Mg alloy with heat treatments. *Materials Science and Engineering: A*, 2017, vol. 704, pp. 218–228. DOI: 10.1016/j.msea.2017.08.029.
13. Reunova K.A., Astafurova E.G., Moskvina V.A., Astafurov S.V., Panchenko M.Y., Melnikov E.V., Kolubaev E.A. Microstructure and Phase Composition of a Gradient Material "Stainless Steel/Cr-Ni Alloy" Produced by Electron-Beam Additive Manufacturing. *Russian Physics Journal*, 2022, vol. 65, pp. 771–777. DOI: 10.1007/s11182-022-02696-0.
14. Astafurova E.G., Panchenko M.Yu., Moskvina V.A. et al. Microstructure and grain growth inhomogeneity in austenitic steel produced by wire-feed electron beam melting: The effect of post-building solid-solution treatment. *Journal of Materials Science*, 2020, vol. 55, no. 22, pp. 9211–9224. DOI: 10.1007/s10853-020-04424-w.
15. Moskvina V.A., Melnikov E.V., Zagibalova E.A. Characteristics of a gradient material based on chromium-nickel stainless steel and Cr20Ni80 alloy produced by electron-beam 3D-printing. *Vektor nauki Tolyattinskogo gosudarstvennogo universiteta*, 2021, no. 3, pp. 57–66. DOI: 10.18323/2073-5073-2021-3-57-66.
16. Khalikova G.R., Zakirova G.R., Farkhutdinov A.I., Korznikova E.A., Trifonov V.G. The structure and mechanical properties of the AK12D (Al-Si-Cu-Ni-Mg) aluminum alloy subjected to friction stir processing. *Frontier Materials & Technologies*, 2022, no. 3-2, pp. 99–108. DOI: 10.18323/2782-4039-2022-3-2-99-108.

17. Torubarov I.S., Drobotov A.V., Gushchin I.A., Vdovin D.S., Plotnikov A.L., Yakovlev A.A. Additive manufacturing of parts with three-dimensional continuous fiber reinforcement. *Frontier Materials & Technologies*, 2022, no. 2, pp. 92–104. DOI: 10.18323/2782-4039-2022-2-92-104.
18. Vetkasov N.I., Kapustin A.I., Sapunov V.V. The development and application of the process of preliminary formation of the high-homogeneous dry mixture “Aluminum powder – single-wall CNT” in the technology ofproduction of the aluminium matrix composites. *Vektor nauki Tolyattinskogo gosudarstvennogo universiteta*, 2018, no. 3, pp. 14–21. DOI: 10.18323/2073-5073-2018-3-14-21.
19. Raja A., Cheethirala S.R., Gupta P., Vasa N.J., Jayaganthan R. A review on the fatigue behaviour of AlSi10Mg alloy fabricated using laser powder bed fusion technique. *Journal of Materials Research and Technology*, 2022, vol. 17, pp. 1013–1029. DOI: 10.1016/j.jmrt.2022.01.028.
20. Limbasiya N., Jain A., Soni H., Wankhede V., Krolczyk G., Sahlot P. Comprehensive review on the effect of process parameters and post-process treatments on microstructure and mechanical properties of selective laser melting of AlSi10Mg. *Journal of Materials Research and Technology*, 2022, vol. 21, pp. 1141–1176. DOI: 10.1016/j.jmrt.2022.09.092.
21. Sha G., Möller H., Stumpf W.E., Xia J.H., Govender G., Ringer S.P. Solute nanostructures and their strengthening effects in Al–7Si–0.6 Mg alloy F357. *Acta Materialia*, 2012, vol. 60, no. 2, pp. 692–701. DOI: 10.1016/j.actamat.2011.10.029.
22. Zhao L., Song L., Macías J.G.S., Zhu Y., Huang M., Simar A., Li Z. Review on the correlation between microstructure and mechanical performance for laser powder bed fusion AlSi10Mg. *Additive Manufacturing*, 2022, vol. 56, article number 102914. DOI: 10.1016/j.addma.2022.102914.

СПИСОК ЛИТЕРАТУРЫ

1. Bradford R.L., Cao L., Klosterman D., Herman F., Forman L., Browning C. A metal–metal powder formulation approach for laser additive manufacturing of difficult-to-print high-strength aluminum alloys // Materials Letters. 2021. Vol. 300. Article number 130113. DOI: 10.1016/j.matlet.2021.130113.
2. Bajakke P.A., Malik V.R., Deshpande A.S. Particulate metal matrix composites and their fabrication via friction stir processing – a review // Materials and Manufacturing Processes. 2018. Vol. 34. № 8. P. 833–881. DOI: 10.1080/10426914.2019.1605181.
3. Matilainen V., Piili H., Salminen A., Syvänen T., Nyrhilä O. Characterization of process efficiency improvement in laser additive manufacturing // Physics Procedia. 2014. Vol. 56. P. 317–326. DOI: 10.1016/j.phpro.2014.08.177.
4. Fousová M., Dvorský D., Michalcová A., Vojtěch D. Changes in the microstructure and mechanical properties of additively manufactured AlSi10Mg alloy after exposure to elevated temperatures // Materials Characterization. 2018. Vol. 137. P. 119–126. DOI: 10.1016/j.matchar.2018.01.028.
5. Tradowsky U., White J., Ward R.M., Read N., Reimers W., Attallah M.M. Selective laser melting of AlSi10Mg: Influence of post-processing on the microstructural and tensile properties development // Materials & Design. 2016. Vol. 105. P. 212–222. DOI: 10.1016/j.matdes.2016.05.066.
6. Zhou L., Mehta A., Schulz E., McWilliams B., Cho K., Sohn Y. Microstructure, precipitates and hardness of selectively laser melted AlSi10Mg alloy before and after heat treatment // Materials Characterization. 2018. Vol. 143. P. 5–17. DOI: 10.1016/j.matchar.2018.04.022.
7. Li X.P., Wang X.J., Saunders M., Suvorova A., Zhang L.C., Liu Y.J., Fang M.H., Huang Z.H., Sercombe T.B. A selective laser melting and solution heat treatment refined Al–12Si alloy with a controllable ultrafine eutectic microstructure and 25% tensile ductility // Acta Materialia. 2015. Vol. 95. P. 74–82. DOI: 10.1016/j.actamat.2015.05.017.
8. Andersen S.J., Zandbergen H.W., Jansen J., TrÆholt C., Tundal U., Reiso O. The crystal structure of the β″ phase in Al–Mg–Si alloys // Acta Materialia. 1998. Vol. 46. № 9. P. 3283–3298. DOI: 10.1016/S1359-6454(97)00493-X.
9. Rometsch P.A., Schaffer G.B. An age hardening model for Al–7Si–Mg casting alloys // Materials Science and Engineering: A. 2002. Vol. 325. № 1-2. P. 424–434. DOI: 10.1016/S0921-5093(01)01479-4.
10. Montero-Sistiaga M.L., Mertens R., Vrancken B., Wang X., Van Hooreweder B., Kruth J.P., Van Humbeeck J. Changing the alloy composition of Al7075 for better processability by selective laser melting // Journal of Materials Processing Technology. 2016. Vol. 238. P. 437–445. DOI: 10.1016/j.jmatprotec.2016.08.003.
11. Li W., Li S., Liu J., Zhang A., Zhou Y., Wei Q., Yan C., Shi Y. Effect of heat treatment on AlSi10Mg alloy fabricated by selective laser melting: Microstructure evolution, mechanical properties and fracture mechanism // Materials Science and Engineering: A. 2016. Vol. 663. P. 116–125. DOI: 10.1016/j.msea.2016.03.088.
12. Takata N., Kodaira H., Sekizawa K., Suzuki A., Kobashi M. Change in microstructure of selectively laser melted AlSi10Mg alloy with heat treatments // Materials Science and Engineering: A. 2017. Vol. 704. P. 218–228. DOI: 10.1016/j.msea.2017.08.029.
13. Reunova K.A., Astafurova E.G., Moskvina V.A., Astafurov S.V., Panchenko M.Y., Melnikov E.V., Kolubaev E.A. Microstructure and Phase Composition of a Gradient Material “Stainless Steel/Cr-Ni Alloy” Produced by Electron-Beam Additive Manufacturing // Russian Physics Journal. 2022. Vol. 65. P. 771–777. DOI: 10.1007/s11182-022-02696-0.
14. Astafurova E.G., Panchenko M.Yu., Moskvina V.A. et al. Microstructure and grain growth inhomogeneity in austenitic steel produced by wire-feed electron beam melting: The effect of post-building solid-solution

treatment // Journal of Materials Science. 2020. Vol. 55. № 22. P. 9211–9224. DOI: 10.1007/s10853-020-04424-w.
15. Москвина В.А., Мельников Е.В., Загибалова Е.А. Особенности градиентного материала на основе нержавеющей хромоникелевой стали и сплава Х20Н80, изготовленного методом электронно-лучевой 3D-печати // Вектор науки Тольяттинского государственного университета. 2021. № 3. С. 57–66. DOI: 10.18323/2073-5073-2021-3-57-66.
16. Халикова Г.Р., Закирова Г.Р., Фархутдинов А.И., Корзникова Е.А., Трифонов В.Г. Структура и механические свойства алюминиевого сплава АК12Д, подвергнутого обработке трением с перемешиванием // Frontier Materials & Technologies. 2022. № 3-2. С. 99–108. DOI: 10.18323/2782-4039-2022-3-2-99-108.
17. Торубаров И.С., Дроботов А.В., Гущин И.А., Вдовин Д.С., Плотников А.Л., Яковлев А.А. Аддитивное производство изделий с пространственным армированием непрерывным волокном // Frontier Materials & Technologies. 2022. № 2. С. 92–104. DOI: 10.18323/2782-4039-2022-2-92-104.
18. Веткасов Н.И., Капустин А.И., Сапунов В.В. Разработка и применение процесса предварительного формирования высокооднородной сухой смеси «Алюминиевый порошок – одностенные УНТ» в технологии получения алюмоматричных композитов // Вектор науки Тольяттинского государственного университета. 2018. № 3. С. 14–21. DOI: 10.18323/2073-5073-2018-3-14-21.
19. Raja A., Cheethirala S.R., Gupta P., Vasa N.J., Jayaganthan R. A review on the fatigue behaviour of AlSi10Mg alloy fabricated using laser powder bed fusion technique // Journal of Materials Research and Technology. 2022. Vol. 17. P. 1013–1029. DOI: 10.1016/j.jmrt.2022.01.028.
20. Limbasiya N., Jain A., Soni H., Wankhede V., Krolczyk G., Sahlot P. Comprehensive review on the effect of process parameters and post-process treatments on microstructure and mechanical properties of selective laser melting of AlSi10Mg // Journal of Materials Research and Technology. 2022. Vol. 21. P. 1141–1176. DOI: 10.1016/j.jmrt.2022.09.092.
21. Sha G., Möller H., Stumpf W.E., Xia J.H., Govender G., Ringer S.P. Solute nanostructures and their strengthening effects in Al–7Si–0.6 Mg alloy F357 // Acta Materialia. 2012. Vol. 60. № 2. P. 692–701. DOI: 10.1016/j.actamat.2011.10.029.
22. Zhao L., Song L., Macías J.G.S., Zhu Y., Huang M., Simar A., Li Z. Review on the correlation between microstructure and mechanical performance for laser powder bed fusion AlSi10Mg // Additive Manufacturing. 2022. Vol. 56. Article number 102914. DOI: 10.1016/j.addma.2022.102914.

Разработка и сертификация летной годности современной ответственной детали корпуса переключателя для аэрокосмических систем, изготовленной из сплава AlSi10Mg с помощью аддитивной технологии

© 2023

Вигнеш Поннусами*[1], доктор наук, младший специалист-1
Правин К.В., бакалавр технических наук, технический помощник
Кришнакумар Суббулакшми, бакалавр технических наук, технический помощник
Бхуванесвари Моханрао Чембу, бакалавр технических наук, региональный директор (сектор 'F')
Кейл Шириш Шарад, доктор наук, директор (сектор 'G')
Рам Прабху Тэгараджан, доктор наук, содиректор (сектор 'E')
Региональный центр военной полетопригодности (F&F), Центр боевой полетопригодности и сертификации, Организация оборонных исследований и разработок, Бангалор (Индия)

***E-mail: vigneshpt3532@gmail.com**

[1]ORCID: https://orcid.org/0000-0003-4487-2030

Поступила в редакцию 22.06.2023 *Принята к публикации 15.08.2023*

Аннотация: Аддитивные технологии (АТ) очень эффективны для макетирования и быстрого производства, поэтому их применение выгодно для аэрокосмической отрасли. Они позволяют сэкономить средства, а также облегчить конструкции, подходят для комплексного проектирования. Однако на данный момент доступно лишь несколько стандартов аддитивных технологий, требуется много материалов и оборудования, что приводит к возникновению затруднений с сертификацией и внедрением АТ. Нестандартные испытания приводят к тому, что АТ в аэрозольных материалах оказываются менее привлекательными из-за их дороговизны и трудоемкости. Целью работы является изготовление деталей корпуса переключателя военных и гражданских самолетов методом лазерного сплавления порошкового слоя (LPBF) с применением порошка AlSi10Mg. Выявлены физико-химические свойства материала, проведены неразрушающие и разрушающие испытания, а также даны четкие разъяснения процедур сертификации. Сделан упор на необходимости разработки руководств и стандартов, охватывающих все аспекты производства – от проектирования до изготовления и эксплуатации продукта. Комплексный анализ испытаний на проникновение жидкости показывает, что дефекты находятся в пределах допустимого уровня. AlSi10Mg демонстрирует более высокие показатели предела текучести, предела прочности и относительного

удлинения, равные (259±4) МПа, (323±4) МПа и (12,5±1,5) % соответственно. Показано, что дисперсионно-твердеющий AlSi10Mg, разработанный и производящийся в Индии, по свойствам не уступает аналогичным дисперсионно-твердеющим алюминиевым сплавам всемирно известных производителей.

Ключевые слова: аддитивное производство; AlSi10Mg; алюминиевый сплав; дисперсионное твердение; разработка и сертификация.

Для цитирования: Вигнеш П., Правин К.В., Кришнакумар С., Бхуванесвари М.Ч., Кейл Ш.Ш., Рам Прабху Т. Разработка и сертификация летной годности современной ответственной детали корпуса переключателя для аэрокосмических систем, изготовленной из сплава AlSi10Mg с помощью аддитивной технологии // Frontier Materials & Technologies. 2023. № 3. С. 19–30. DOI: 10.18323/2782-4039-2023-3-65-2.

doi: 10.18323/2782-4039-2023-3-65-3

Simulation of contact thermal resistance when designing processing equipment

© 2023

Aleksandr F. Denisenko*[1], Doctor of Sciences (Engineering), Professor,
professor of Chair "Mechanical Engineering Technology, Machines and Tools"
Lyubov Yu. Podkruglyak[2], postgraduate student
of Chair "Mechanical Engineering Technology, Machines and Tools"
Samara State Technical University, Samara (Russia)

***E-mail: sammortor@yandex.ru**

[1]ORCID: https://orcid.org/0000-0001-6393-2831
[2]ORCID: https://orcid.org/0009-0006-6735-4454

Received 24.05.2023 *Accepted 26.06.2023*

Abstract: Analysis of the processing equipment structures when designing according to the temperature criterion is a necessary guarantee of ensuring the required performance characteristics. The presence of a significant number of parts in the processing equipment units and mechanisms requires, when designing, the prediction of the heat flow passage through the joints. When simulating contact thermal resistance, the variety of requirements for a joint can be taken into account by introducing a pseudolayer into the contact zone. The paper presents test results of the proposed regression dependence of the temperature change when the heat flow goes through the pseudolayer obtained considering four significant factors: the pseudolayer thickness, the nominal pressure, the material yield strength, and the actual contact zone location. The adequacy of the specified regression dependence was verified experimentally and applying numerical simulation using large-block finite elements. To describe the process of heat transfer in the thermal model elements, the authors determined contact thermal resistances for several conditions for the heat flow propagation: from one finite element to another within one part; from one finite element to another located in an adjacent part; heat flow passing through closed cavities; heat flow propagation into the environment for finite elements located on the outer (free) contour of the part. The experiments showed a good agreement between the experimental data and the simulation results. The application of large-block finite elements based on the proposed contact thermal resistance model allowed bringing the FE simulation technique to engineering use without complex software.

Keywords: processing equipment; heat flow; simulation of contact thermal resistance; contact thermal resistance; pseudolayer; large-block finite elements; thermal conductivity ratio.

For citation: Denisenko A.F., Podkruglyak L.Yu. Simulation of contact thermal resistance when designing processing equipment. *Frontier Materials & Technologies*, 2023, no. 3, pp. 31–42. DOI: 10.18323/2782-4039-2023-3-65-3.

INTRODUCTION

Modern mechanical engineering is impossible without using technological equipment (TE), which has high reliability, accuracy, and productivity. Reducing the time for TE design requires simultaneous consideration of all criteria (strength, rigidity, dynamic, thermal, etc.) that the created equipment must meet. The implementation of the design criteria requirements is largely based on the models used, which allow assessing the operational capabilities of the created TE even at the design stage.

A special role in the design is given to the analysis of the temperature factor influence, since the internal heat generated by the operating equipment leads to changes in the temperature of its assembly units and, as a result, to thermal errors [1; 2]. Thermal effects can contribute more than 50 % to the total error [3].

With the expansion of the use of numerically controlled equipment, the problem of heat resistance of TE structures has become significantly more complicated due to an increase in the energy saturation of equipment, and the intensification of its operation [4; 5]. Determination of temperature deformations of technological equipment units significantly affecting the operational characteristics is carried out based on the construction of a temperature field. The researchers paid special attention to determining the thermal deformations of the spindle assemblies of metal-cutting machine tools as the most complex TE assembly unit, the operation of which primarily influences the output accuracy characteristics of the equipment [6–8].

The problems of creating mathematical models that allow predicting the temperature field pattern, even at the stage of equipment design, have been largely solved by the widespread use of numerical simulation using finite element models. There are numerous examples of successful use of the finite element method (FEM) when solving thermal problems [6; 9].

Numerical simulation using the FEM made it possible, first of all, to remove one of the significant problems: the maximum consideration of the configuration of the parts included in the TE, earlier, when using analytical dependencies, as a rule, was provided by a significant simplification (often unreasonable) of the geometry of the parts.

However, even with the extensive experience gained during FEM testing, when designing technological equipment, there remains a problem associated with a significant number of parts included in the equipment, determined by the functional purpose of the equipment and its configuration [10]

(for example, in a metal-cutting machine there are more than 3000 parts), connected to each other in a certain way. Thus, to construct the TE temperature field, it is necessary to simulate the heat flow propagation both through solid parts (modern software tools make it quite easy to do), and through their connections.

The heat flow passage through parts and their connections can be simulated taking into account thermal resistance [11]. For solid parts, thermal resistance is determined based on the introduction of thermal conductivity coefficients, the values of which for various materials are widely presented in the literature [12; 13]. A multi-analysis of the formation of contact thermal resistance (CTR) is given in [14; 15].

The complexity of CTR simulation is associated with the presence of a temperature jump during the heat flow passage through the contact zone. As noted in [16], an attempt to use the classical FEM for modelling encounters difficulties associated with the creation of a FE mesh corresponding to neighbouring contacting parts, which is very difficult for complex geometries. The authors propose to build a modelling principle in the representation of a contact with an intermediate thin material, in which two materials are mixed. However, the dependencies for determining the characteristics of the specified intermediate layer are not given in the work.

The works of a number of researchers [17–19] cover the obtaining of the dependences for determining CTR, based on the experimental data approximation. However, these dependencies are difficult to use in engineering practice, since they, as a rule, have a narrowly focused practical significance, and require a large amount of initial data, such as the profile standard deviation; surface hardness (microhardness); average tangent of the roughness slope angle; maximum corner radius of the protrusions; a parameter characterising the degree of mechanical loading of contact irregularities, etc. [14]. In this regard, the issue of CTR simulation is still very relevant.

The purpose of this study is to develop a technique for simulating contact thermal resistance, which allows estimating the temperature change in the contact zone, based on identifying, and taking into account the most significant design and technological factors available when used in engineering practice.

METHODS

The complexity of taking into account a significant number of influencing factors for engineering practice when assessing the CTR can be resolved by modelling a joint in the form of a pseudolayer, the characteristics of which are determined by the contact conditions [20; 21]. The research methods involve a reasonable selection of the most significant factors affecting the contact thermal resistance based on the one-factor numerical experiments, using the FEM, and a full factorial experiment (FFE) to obtain a regression dependence, describing the temperature change in the contact zone. The efficacy of the obtained model should be confirmed by the results of full-scale and numerical experiments.

Previous studies [20] allowed distinguishing four significant factors: pseudolayer thickness h, nominal pressure q_a, material yield strength σ_T, and location of the actual contact zone l. Based on the use of the ELCUT package, when planning a full factorial experiment of the 2^4 type, a regression model was obtained in the following form

$$\Delta T = 0{,}055 + 7{,}403\cdot 10^{4} h - 2{,}216\cdot 10^{-10} q_a + \\ + 5{,}25\cdot 10^{-11}\sigma_T + 6{,}112 l - 7{,}257\cdot 10^{-4} h q_a + \\ + 2{,}05\cdot 10^{-5} h\sigma_T + 2{,}892\cdot 10^{6} h l + 0{,}736\cdot 10^{-18} q_a\sigma_T - \\ - 2{,}048\cdot 10^{-8}\sigma_T l + 8{,}276\cdot 10^{-13} h\sigma_T q_a .$$

Further analysis [22] showed that it is possible to simplify the obtained regression model, leaving only two factors as the most significant ones: the pseudolayer thickness determined by the roughness of the contacting surfaces and the nominal pressure, which depends on the normal force and the nominal contact area:

$$\Delta T = 0{,}055 + 7{,}403\cdot 10^{4} h - 2{,}216\cdot 10^{-10} q . \qquad (1)$$

The pseudolayer thickness can be taken as an average thickness of the gap in the joint [23; 24]:

$$h = R_{p1} + R_{p2} = 2{,}6\left(R_{a1} + R_{a2}\right),$$

where R_p is the smoothing height;
R_a is the arithmetic average roughness height.

To test the efficacy of the proposed regression dependence, the authors carried out full-scale experiments on the heat flow passage through a flat joint, and performed numerical simulation using large-block finite elements [25].

For a full-scale experiment, steel samples were made from 15 grade steel with dimensions of $L\times B\times H$=40×20×10 mm. In one sample, a hole Ø4.4 mm was drilled to place a temperature source in it (Fig. 1). The surface roughness in the contact zone of the samples was R_a=0.1 μm.

To assess the influence of contact pressure on CTR, a pair of specimens was fixed in the jaws, which created a compression force (Fig. 2).

To reduce the convection heat emission, the samples were placed in a thermal protection created using a three-layer winding of an asbestos cord Ø3 mm glued with liquid glass. The thermal protection left two sections 10 mm long open, where the temperature could be subsequently recorded in the source location area, and at the end of the flow propagation in the samples (Fig. 2). The jaws were thermally insulated from the specimens with sheet cloth laminate, and plywood 10 and 5 mm thick, respectively.

To determine the compression force of the specimens, the jaws were pre-calibrated according to the applied torque on the jaw screws using a DOSM-1 dynamometer, which has the highest limit load of 10 000 N. During the experiments, the maximum Q value (Fig. 2) was 6 550 N.

The temperature measurement in the open areas of the samples was carried out by a non-contact method, using a calibrated DT-8833 pyrometer. During the experiments, the jaws were mounted on the table of a jig-boring machine, and the pyrometer was fixed on a massive stand with a distance of ~15 mm from the measured surface to the sensitive element of the infrared sensor located at the focus of the pyrometer optical system. Since the optical resolution (the sighting factor – the ratio between the distance to

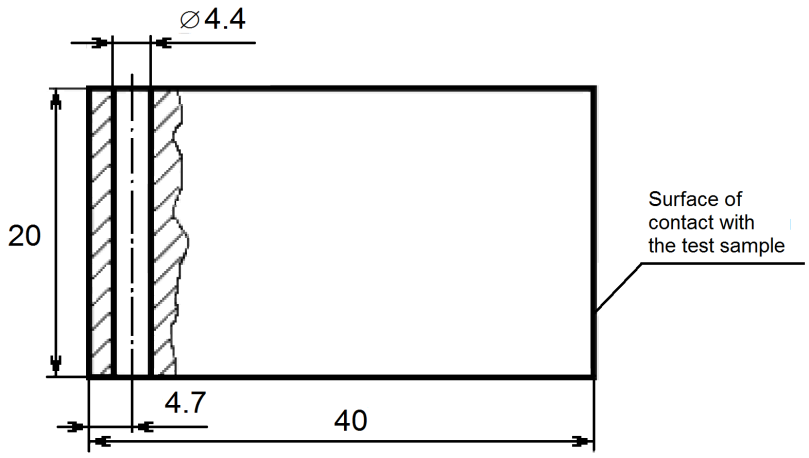

Fig. 1. *Sample for heat source*
Рис. 1. *Образец для теплового источника*

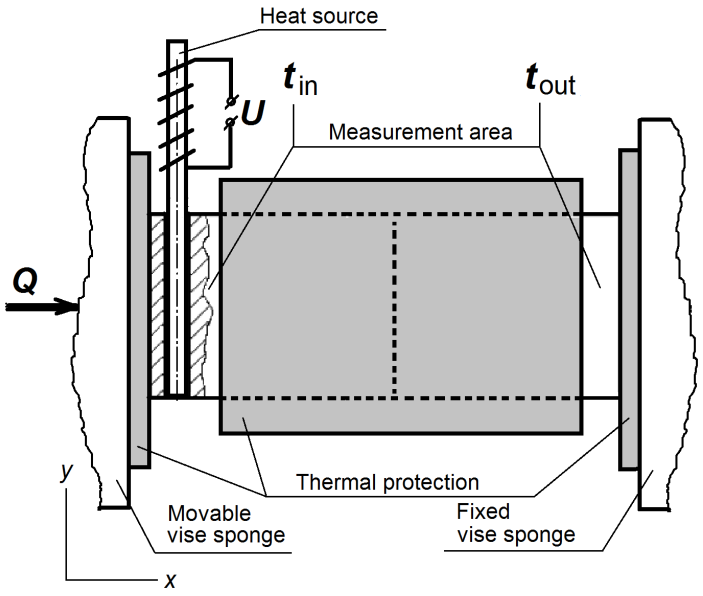

Fig. 2. *The experimental unit scheme*
Рис. 2. *Схема экспериментальной установки*

the measurement object and the measuring spot size), for the DT-8833 pyrometer is 13:1, in this case, the measurement spot had a diameter of ~1 mm. This circumstance was taken into account when selecting the dimensions of the measurement zones (Fig. 2), which, according to the rules for using pyrometers, should be at least 2 times larger than the size of the measuring spot.

During the experiments, the heating element power (W) was determined by fixing the consumed current (I=1.8 A) and voltage (U=12.0 V):

$$P = IU\eta\,. \qquad (2)$$

The value of the efficiency factor η for converting electrical power into a thermal one was estimated considering the following. Since the heat source was removed from the heating zone (Fig. 2), and the heat was transferred to the sample using a copper rod Ø4 mm with a significant length, the value of η was taken equal to 0.35.

Numerical simulation was carried out according to the technique using large-block finite elements (FE), which was earlier tested for flat models [25].

Simulation of thermal processes in the equipment assembly units, using large-block FE, allows reducing the problem of building a temperature field to solving a system of linear equations, and refusing to use complex software products (for example, ANSYS).

The technique for developing a 3D computational model, involves the selection of rectangular parallelepipeds in the parts of assembly units, subject to the condition that eight FE must be connected at the vertices that are not located on free surfaces. At vertices located on free surfaces, there should be up to four such FE.

Since the proposed technique with large-block rectangular elements assumes that the heat flow propagates in the FE in a straight line, the thermal resistance of the element along the corresponding coordinate axis is equal to

$$R_X^T = \frac{\Delta X}{\lambda \cdot \Delta Y \cdot \Delta Z};$$

$$R_Y^T = \frac{\Delta Y}{\lambda \cdot \Delta X \cdot \Delta Z};$$

$$R_Z^T = \frac{\Delta Z}{\lambda \cdot \Delta X \cdot \Delta Y},$$

where ΔX, ΔY, ΔZ are the dimensions of the FE along the corresponding coordinate axis;
λ is the coefficient of thermal conductivity of the material of the element (part).

For each coordinate plane of each FE, the equilibrium equations of heat flows in its nodes located in the FE geometric centers were set up. For example, for element *A* in Fig. 3, the equation can be written as follows:

$$\begin{aligned}&\sigma_{x(C-A)}(t_C - t_A) + \sigma_{x(E-A)}(t_E - t_A) + \\ &+ \sigma_{y(B-A)}(t_B - t_A) + \sigma_{y(D-A)}(t_D - t_A) + \\ &+ \sigma_{z(K-A)}(t_K - t_A) + \sigma_{z(L-A)}(t_L - t_A) = 0\end{aligned}, \qquad (3)$$

where t_i is the temperature at the *i*-th node;
$\sigma_{x(i-j)}=\sigma_{x(j-i)}$, $\sigma_{y(i-j)}=\sigma_{y(j-i)}$, $\sigma_{z(i-j)}=\sigma_{z(j-i)}$ is total (absolute) thermal conductivity between *i* and *j* nodes along the *x, y, z* coordinates respectively, W/K.

The values of thermal conductivity between *i* and *j* nodes along the *x, y, z* coordinates are determined by the formulas:

$$\sigma_{x(i-j)} = \frac{1}{0{,}5R_{xi}^T + R_{x(i-j)}^C + 0{,}5R_{xj}^T};$$

$$\sigma_{y(i-j)} = \frac{1}{0{,}5R_{yi}^T + R_{y(i-j)}^C + 0{,}5R_{yj}^T};$$

$$\sigma_{z(i-j)} = \frac{1}{0{,}5R_{zi}^T + R_{z(i-j)}^C + 0{,}5R_{zj}^T},$$

where $R^C_{x(i-j)}$, $R^C_{y(i-j)}$, $R^C_{z(i-j)}$ are thermal resistance of the joint between *i* and *j* finite elements along the *x, y, z* coordinates, respectively.

The experimental unit model to carry out a numerical experiment using large-block FE was represented as 13 interconnected rectangular parallelepipeds (Fig. 4).

In accordance with the expression (3), to determine the temperature in the thermal model elements, the authors composed the equilibrium equations for heat flows in its nodes located in the geometric centres of the elements:

$$\begin{cases}\sigma_{x(2-1)}(t_2 - t_1) + 2\sigma_{y(B-1)}(t_B - t_1) + \\ + 2\sigma_{z(B-1)}(t_B - t_1) + P = 0; \\ \sigma_{x(3-2)}(t_3 - t_2) + 2\sigma_{y(B-2)}(t_B - t_2) + \\ + 2\sigma_{z(B-2)}(t_B - t_2) + 2\sigma_{x(1-2)}(t_1 - t_2) = 0; \\ \sigma_{x(4-3)}(t_4 - t_3) + \sigma_{x(2-3)}(t_2 - t_3) + \\ + \sigma_{y(6-3)}(t_6 - t_3) + \sigma_{y(8-3)}(t_8 - t_3) + \\ + \sigma_{z(10-3)}(t_{10} - t_3) + \sigma_{z(12-3)}(t_{12} - t_3) = 0; \\ \ldots \\ \ldots \\ \sigma_{x(10-11)}(t_{10} - t_{11}) + \sigma_{z(4-11)}(t_4 - t_{11}) + \\ + \sigma_{z(B-11)}(t_B - t_{11}) + \sigma_{x(B-11)}(t_B - t_{11}) = 0; \\ \sigma_{x(13-12)}(t_{13} - t_{12}) + \sigma_{z(3-12)}(t_3 - t_{12}) + \\ + \sigma_{z(B-12)}(t_B - t_{12}) + \sigma_{x(B-12)}(t_B - t_{12}) = 0; \\ \sigma_{x(12-13)}(t_{12} - t_{13}) + \sigma_{z(4-13)}(t_4 - t_{13}) + \\ + \sigma_{z(B-13)}(t_B - t_{13}) + \sigma_{x(B-13)}(t_B - t_{13}) = 0,\end{cases}$$

where t_A is the ambient temperature;
$\sigma_{x(i-B)}$, $\sigma_{y(i-B)}$, $\sigma_{z(i-B)}$ is the total (absolute) thermal conductivity between *i* node and air along the *x*, *y*, *z* coordinates, respectively, W/K.

The values of thermal conductivity between *i* and *j* nodes (except for the nodes No. 3 and No. 4 along the *x* coordinate) along the *x*, *y*, *z* coordinates are determined by the formulas:

$$\sigma_{x(i-j)} = \frac{1}{0{,}5R_{xi}^T + 0{,}5R_{xj}^T};$$

$$\sigma_{y(i-j)} = \frac{1}{0{,}5R_{yi}^T + 0{,}5R_{yj}^T};$$

$$\sigma_{z(i-j)} = \frac{1}{0{,}5R_{zi}^T + 0{,}5R_{zj}^T}.$$

Thermal conductivity $\sigma^C_{x(3-4)}$ between the nodes No. 3 and No. 4 along the *x* coordinate should take into account the CTR in the joint of the specified elements:

$$\sigma_{x(3-4)} = \frac{1}{0{,}5R_{xi}^T + R_{x(3-4)}^C + 0{,}5R_{xj}^T}.$$

The introduction of a pseudolayer with a thickness *h* to the contact zone when modelling allows representing the actual contact zone (ACZ) (Fig. 5) in the form of the following model (Fig. 6).

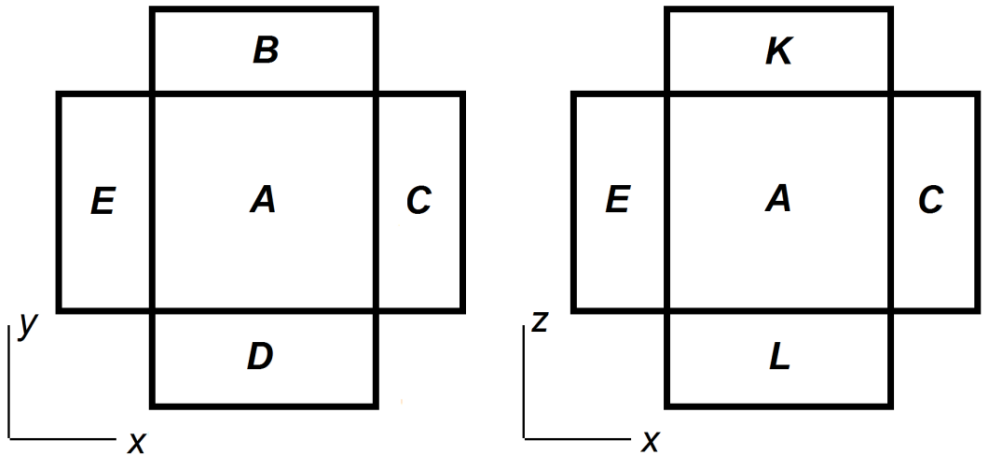

Fig. 3. *For the construction of an equilibrium equation for a finite element A*
Рис. 3. *К составлению уравнения равновесия для конечного элемента А*

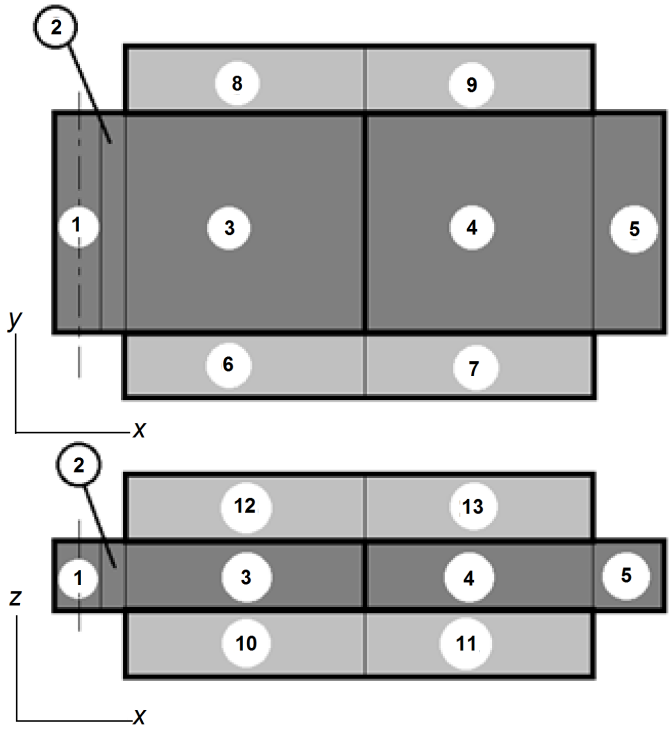

Fig. 4. *Simulation of the experimental unit using large-block FE*
Рис. 4. *Моделирование экспериментальной установки с помощью крупноблочных КЭ*

Considering the parallel passage of heat flows through these zones, we can write that the pseudolayer thermal conductivity will be equal to the sum of the conductivities, through the actual contact zones σ_{ACZ}, and the volumes filled with air (oil) σ_A:

$$\sigma_{PL} = \sum \sigma_{ACZ} + \sum \sigma_A ,$$

where $\sigma_{PL} = \frac{\lambda_{PL} A_a}{h}$;

$\sum \sigma_{ACZ} = \frac{\lambda_{AC} A_r}{h}$;

$\sum \sigma_A = \frac{\lambda_A (A_a - A_r)}{h}$;

A_a is the nominal contact area;
A_r is the actual contact area;
λ_{PL} is the pseudolayer thermal conductivity coefficient;
λ_A is the air thermal conductivity coefficient.

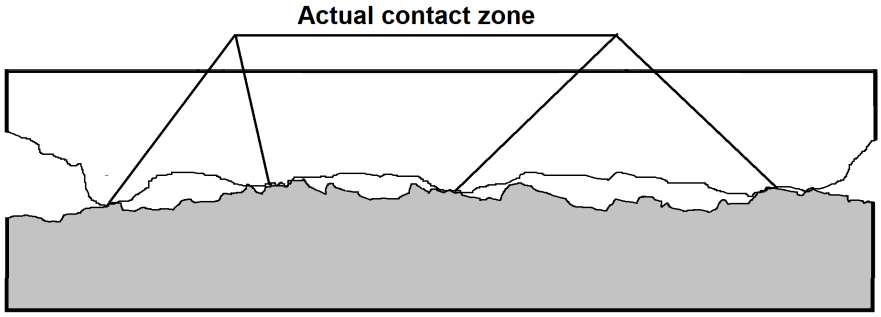

Fig. 5. *The formation of actual contact zones in a flat joint*
Рис. 5. *Формирование зон фактического контакта в плоском стыке*

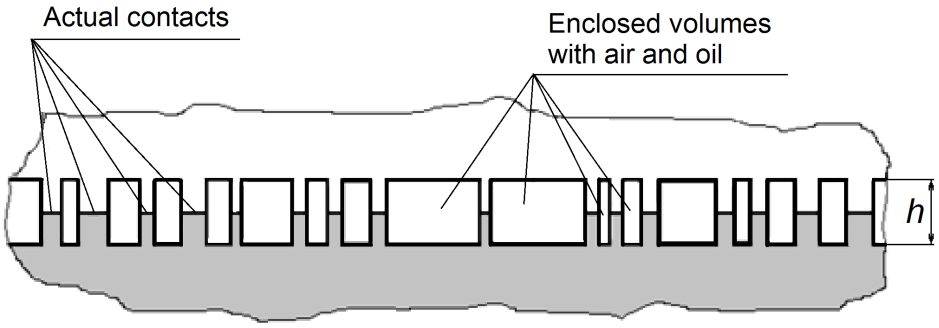

Fig. 6. *Representation of a flat joint in the form of a pseudolayer with a thickness of h*
Рис. 6. *Представление плоского стыка в виде псевдослоя толщиной h*

Not accounting for the influence of oxide films in the actual contact zone on the CTR, it can be assumed that $\lambda_{AC}=\lambda$, where λ is the thermal conductivity coefficient of the contacting materials.

Then, introducing the notation $\eta = \frac{A_r}{A_a}$, we will receive

$$\lambda_{PL} = \eta\left[\lambda + \lambda_A\left(\frac{1}{\eta} - 1\right)\right]. \quad (4)$$

According to the data of the work [21],

$$A_r = \frac{0{,}48075}{\sigma_T} A_a q_a$$

where σ_T is the yield strength of the contacting materials, from which

$$\eta = \frac{0{,}48075}{\sigma_T} q_a .$$

In the case of contact of parts with different physical and mechanical properties, the arithmetic mean of the yield strengths of their materials can be taken as the σ_T value.

Taking into account that due to the presence of macrodeviations, the ACZs are concentrated in the region of contour areas [23], and that ACZs consist of a combination of actual contacts of microroughnesses, and closed volumes filled with air or oil (Fig. 4), the value of $R^C_{x(3-4)}$ is calculated using dependencies (1) and (2):

$$R^C_{x(3-4)} = \frac{\Delta T}{0{,}01P} \cdot \frac{\lambda}{\lambda_{PL}} = \\ = \frac{0{,}055 + 7{,}403 \cdot 10^4 h - 2{,}216 \cdot 10^{-10} q}{0{,}01 IU\eta} \cdot \frac{\lambda}{\lambda_{PL}}.$$

RESULTS

For numerical simulation for the used sample material (grade 15 steel), the authors accept σ_T=240 MPa, λ=55 W/(m·°K), λ_A=0.028 W/(m·°K).

The results of measuring the temperature difference $t_{in}-t_{out}$ on the stand (Fig. 2) for 6-fold measurements are shown in Fig. 7 by points, and the simulation results estimated by the temperature difference in FE No. 1 and No. 5 are shown by a solid line. The scatter of experimental data relative to the calculated curve can be estimated by a standard deviation equal to 0.192.

Fig. 8 shows the numerical simulation at different roughness of contacting surfaces of the samples.

The influence of filling of closed cavities during the contact of rough surfaces with oil was simulated using the dependence (4), where the value of the thermal conductivity coefficient of oil was substituted for λ_A (Fig. 9). The thermal conductivity coefficient of oil is about 500 times less than the thermal conductivity coefficient of steel, and for mineral oils at a temperature of 20 °C it is 0.104 W/(m·°K) [24]. The value of the thermal conductivity coefficient for oils used in spindle units, equal to 0.143 W/(m·°K), is indicated in [25].

Thus, for closed cavities of the simulation model filled with oil, it is possible to choose the value of the thermal conductivity coefficient from the range of λ=0.1...0.14 W/(m·°K).

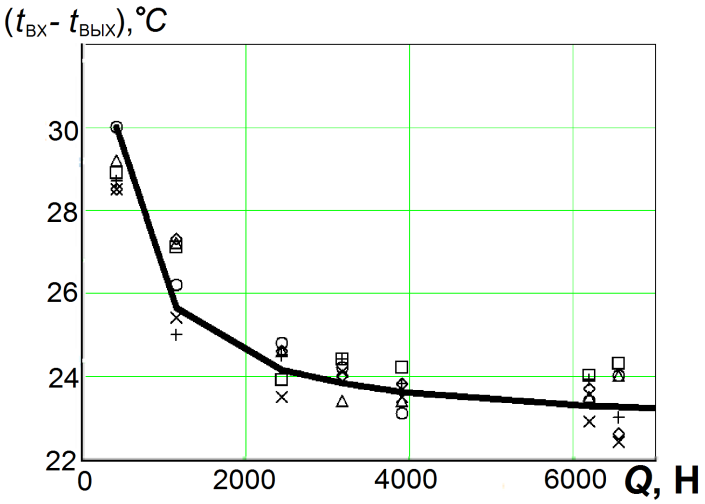

Fig. 7. *The results of field measurements (points) and simulation (solid line) of the temperature difference $t_{вх}$–$t_{вых}$ depending on the compression force of the samples*
Рис. 7. *Результаты натурных измерений (точки) и моделирования (сплошная линия) разницы температур $t_{вх}$–$t_{вых}$ в зависимости от усилия сжатия образцов*

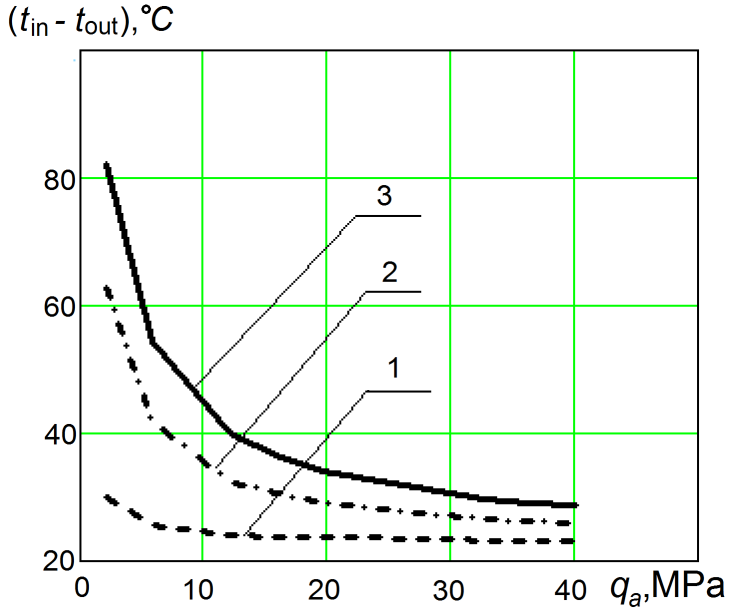

Fig. 8. *The results of numerical simulation of the temperature difference $t_{вх}$–$t_{вых}$ depending on the pressure in the joint at different roughness of the contacting surfaces: 1 – R_{a1}=R_{a2}=0.1 μm; 2 – R_{a1}=0.1 μm, R_{a2}=3.2 μm; 3 – R_{a1}=R_{a2}=3.2 μm*
Рис. 8. *Результаты численного моделирования разницы температур $t_{вх}$–$t_{вых}$ в зависимости от давления в стыке при различной шероховатости контактирующих поверхностей: 1 – R_{a1}=R_{a2}=0,1 мкм; 2 – R_{a1}=0,1 мкм, R_{a2}=3,2 мкм; 3 – R_{a1}=R_{a2}=3,2 мкм*

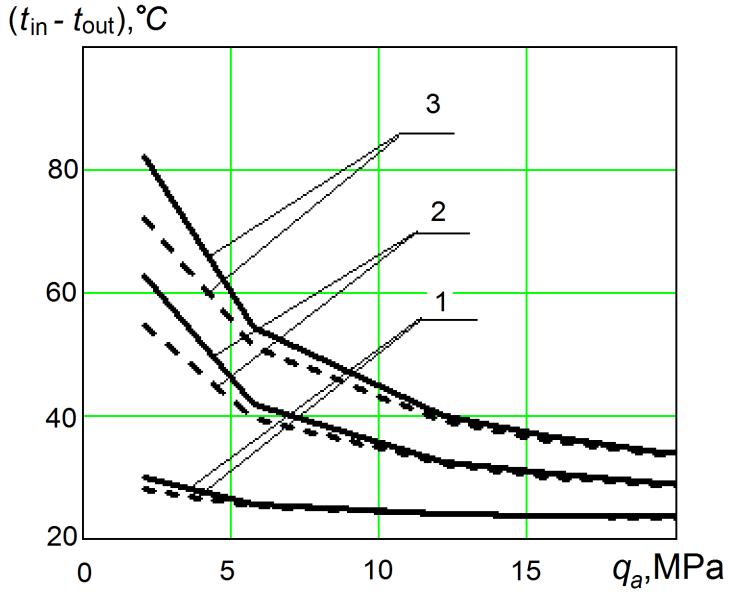

Fig. 9. *The influence of oil in the contact zone on the temperature difference $t_{вх}-t_{вых}$: a solid line – air (λ_B=0.028 W/(m·K)); a dotted line – oil (λ_M=0.12 W/(m·K)); 1 – $R_{a1}=R_{a2}$=0.1 μm; 2 – R_{a1}=0.1 μm, R_{a2}=3.2 μm; 3 – $R_{a1}=R_{a2}$=3.2 μm*

Рис. 9. *Влияние масла в зоне контакта на разницу температур $t_{вх}-t_{вых}$: сплошная линия – воздух (λ_B=0,028 Вт/(м·К)); пунктир – масло (λ_M=0,12 Вт/(м·К)); 1 – $R_{a1}=R_{a2}$=0,1 мкм; 2 – R_{a1}=0,1 мкм, R_{a2}=3,2 мкм; 3 – $R_{a1}=R_{a2}$=3,2 мкм*

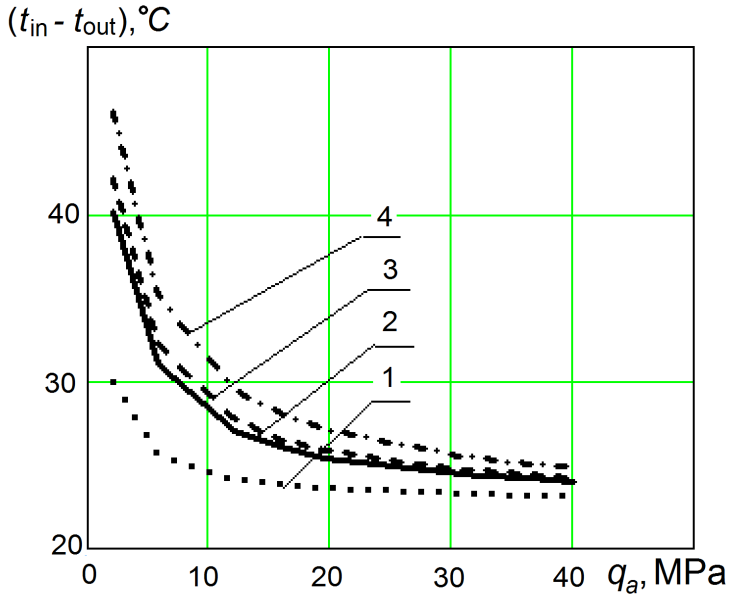

Fig. 10. *The results of numerical simulation of the temperature difference $t_{вх}-t_{вых}$ depending on the pressure in the joint for various steel grades: 1 – Cm.15 steel; 2 – Cm.45 steel; 3 – Cm.40X steel; 4 – Cm.40XH steel*

Рис. 10. *Результаты численного моделирования разницы температур $t_{вх}-t_{вых}$ в зависимости от давления в стыке для различных марок сталей: 1 – Ст.15; 2 – Ст.45; 3 – Ст.40Х; 4 – Ст.40ХН*

The influence of grades of contacting materials was evaluated by numerical experiments, with samples from the grade 15 steel (λ=55 W/(m·°K), σ_T=240 MPa), grade 45 steel (λ=48.1 W/(m·°K), σ_T=680 MPa), 40H steel (λ=46 W/(m·°K), σ_T=775 MPa), and 40HN steel (λ=44 W/(m·°K), σ_T=1050 MPa). The simulation results are shown in Fig. 10.

DISCUSSION

The results of full-scale and numerical experiments, confirm the earlier conclusions of some researchers, about the significant influence of pressure in a joint on CTR [11; 14; 17]. Moreover, this influence is especially manifested in the region of low pressures. This result can be adequately explained by the increase in the actual contact area as the pressure increases.

The influence of the roughness of the contacting surfaces (Fig. 8) affects the entire pressure variation range, which confirms once again the necessity of a reasonable selection of this parameter when designing process equipment.

Simulation showed that the liquid layer (oil) introduction into the contact zone reduces the CTR (Fig. 9). A similar conclusion was obtained in the work [9]. However, one should note that this influence is significant only at a significant roughness of the contacting surfaces, and only at low pressures.

The simulation results for different steel grades (Fig. 10) show that in critical cases it is necessary to consider the material yield strength, the values of which for different steel grades can differ significantly. This is particularly true when using alloyed steels.

The results obtained indicate that the CTR decreases with an increase in the thermal conductivity of the contacting metals, an increase in the force of compression of the samples, and an increase in the surface treatment quality.

CONCLUSIONS

1. The conducted full-scale experiments both qualitatively and quantitatively confirmed the adequacy of the proposed technique for using large-block finite elements and the regression dependence describing the modelling of a flat joint in the form of a pseudolayer during the heat flow passage.

2. The results obtained confirmed the significant contact thermal resistance dependence on the nominal pressure in the joint. This dependence is especially manifested at low pressures (<10...15 MPa), and has a pronounced decreasing characteristic.

3. The influence of lubrication in the contact zone should be considered only for highly rough contacting surfaces (R_a>1 μm).

4. When designing assembly units, with the possibility of varying the grades of steels used, one should pay attention to the values of the material yield strength, with an increase in which the contact thermal resistance increases.

REFERENCES

1. Huang Z., Liu Y., Du L., Yang H. Thermal error analysis, modeling and compensation of five-axis machine tools. *Journal of Mechanical Science and Technology*, 2020, vol. 34, pp. 4295–4305. DOI: 10.1007/s12206-020-0920-y.
2. Mares M., Horejs O., Havlik L. Thermal error compensation of a 5-axis machine tool using indigenous temperature sensors and CNC integrated Python code validated with a machined test piece. *Precision Engineering*, 2021, vol. 66, pp. 21–30. DOI: 10.1016/j.precisioneng.2020.06.010.
3. Week M., Mckeown P., Bonse R., Herbst U. Reduction and compensation of thermal error in machine tools. *CIRP Annals*, 1995, vol. 44, no. 2, pp. 589–598. DOI: 10.1016/S0007-8506(07)60506-X.
4. Zhou H., Hu P., Tan H., Chen J., Liu G. Modelling and compensation of thermal deformation for machine tool based on the real-time data of the CNC system. *Procedia Manufacturing*, 2018, vol. 26, pp. 1137–1146. DOI: 10.1016/j.promfg.2018.07.150.
5. Wei X., Ye H., Miao E., Pan Q. Thermal error modeling and compensation based on Gaussian process regression for CNC machine tools. *Precision Engineering*, 2022, vol. 77, pp. 65–76. DOI: 10.1016/j.precisioneng.2022.05.008.
6. Živković A.M., Zeljković M.V., Mlađenović C.D., Tabaković S.T., Milojević Z.L., Hadžistević M.J. A Study of Thermal Behavior of the Machine Tool Spindle. *Thermal Science*, 2019, vol. 23, no. 3B, pp. 2117–2130. DOI: 10.2298/TSCI180129118Z.
7. Kang C.M., Zhao C.Y., Zhang J.Q. Thermal behavior analysis and experimental study on the vertical machining center spindle. *Transactions of the Canadian Society for Mechanical Engineering*, 2020, vol. 44, no. 3, pp. 344–351. DOI: 10.1139/tcsme-2019-0124.
8. Cheng Y., Zhang X., Zhang G., Jiang W., Li B. Thermal error analysis and modeling for high-speed motorized spindles based on LSTM-CNN. *International Journal of Advanced Manufacturing Technology*, 2022, vol. 121, pp. 3243–3257. DOI: 10.1007/s00170-022-09563-9.
9. Fu C.-B., Tian A.-H., Yau H.-T., Hoang M.-C. Thermal monitoring and thermal deformation prediction for spherical machine tool spindles. *Thermal Science*, 2019, vol. 23, no. 4, pp. 2271–2279. DOI: 10.2298/TSCI1904271F.
10. Denisenko A.F., Grishin R.G. Optimizing the layout of a CNC lathe. *Frontier Materials & Technologies*, 2022, no. 2, pp. 17–27. DOI: 10.18323/2782-4039-2022-2-17-27.
11. Dornyak O.R., Popov V.M., Anashkina N.A. Mathematical modeling of contact thermal resistance for elastostrained solid bodies by the methods of multiphase systems mechanics. *Journal of Engineering Physics and Thermophysics*, 2019, vol. 92, no. 5, pp. 1117–1129. EDN: RUNKGS.
12. Kuznetsov A.P. *Teplovoy rezhim metallorezhushchikh stankov* [Thermal regime of machine tools]. Moscow, Yanus-K Publ., 2013. 480 p.

13. Alferov V.I. Calculation of heat resistance in the design of metal-cutting machines. *STIN*, 2006, no. 4, pp. 7–10. EDN: KTURXZ.
14. Mesnyankin S.Y., Vikulov A.G., Vikulov D.G. Solid-solid thermal contact problems: current understanding. *Physics-Uspekhi*, 2009, vol. 52, no. 9, pp. 891–914. EDN: MWUFBJ.
15. Madhusudana C.V. *Thermal Contact Conductance*. 2nd ed. Sydney, Springer Publ., 2014. 260 p. DOI: 10.1007/978-3-319-01276-6.
16. Aalilija A., Gandin C.-A., Hachem E. A simple and efficient numerical model for thermal contact resistance based on diffuse interface immersed boundary method. *International Journal of Thermal Sciences*, 2021, vol. 166, article number 106817. DOI: 10.1016/j.ijthermalsci.2020.106817.
17. Ivanov A.S., Izmailov V.V. Thermal conductivity of a plane joint. *Russian Engineering Research*, 2009, vol. 29, no. 7, pp. 671–673. EDN: LLSSLZ.
18. Popov V.M., Dornyak O.R., Latynin A.V., Lushnikova E.N. Heat exchange in the area of surface contact with shape deviations. *Voronezhskiy nauchno-tekhnicheskiy vestnik*, 2020, vol. 4, no. 4, pp. 64–69. DOI: 10.34220/2311-8873-2021-4-4-64-69.
19. Xian Y., Zhang P., Zhai S., Yuan P., Yang D. Experimental characterization methods for thermal contact resistance: A review. *Applied Thermal Engineering*, 2018, vol. 130, pp. 1530–1548. DOI: 10.1016/j.applthermaleng.2017.10.163.
20. Denisenko A.F., Podkruglyak L.Yu. Construction of a regression model of thermal resistance of a contact pseudo medium. *Izvestiya Samarskogo nauchnogo tsentra Rossiyskoy akademii nauk*, 2021, vol. 23, no. 3, pp. 47–54. DOI: 10.37313/1990-5378-2021-23-3-47-54.
21. Denisenko A.F., Grishin R.G., Podkruglyak L.Y. Formation of Contact Thermal Resistance Based on the Analysis of the Characteristics of the Pseudo-Medium. *Lecture Notes in Mechanical Engineering*, 2022, pp. 221–229. DOI: 10.1007/978-3-030-85233-7_26.
22. Dmitriev V.A., Denisenko A.F., Podkruglyak L.Yu. Determination of the significance of factors in the modeling of contact thermal resistance. *Mekhatronika, avtomatika i robototekhnika*, 2023, no. 11, pp. 169–172. DOI: 10.26160/2541-8637-2023-11-169-172.
23. Khokhlov V.M. Calculation of contour contact areas and pressures. *Izvestiya vysshikh uchebnykh zavedeniy. Mashinostroenie*, 1990, no. 4, pp. 20–24. EDN: TNZQKP.
24. Khokhlov V.M. Roughness of surfaces of elastically contacting bodies. *Izvestiya vysshikh uchebnykh zavedeniy. Mashinostroenie*, 1990, no. 10, pp. 109–113.
25. Denisenko A.F., Podkruglyak L.Yu. Development of the heat model of the spindle support metal cutting machine. *Izvestiya Samarskogo nauchnogo tsentra Rossiyskoy akademii nauk*, 2020, vol. 22, no. 3, pp. 49–55. DOI: 10.37313/1990-5378-2020-22-3-49-55.

СПИСОК ЛИТЕРАТУРЫ

1. Huang Z., Liu Y., Du L., Yang H. Thermal error analysis, modeling and compensation of five-axis machine tools // Journal of Mechanical Science and Technology. 2020. Vol. 34. P. 4295–4305. DOI: 10.1007/s12206-020-0920-y.
2. Mares M., Horejs O., Havlik L. Thermal error compensation of a 5-axis machine tool using indigenous temperature sensors and CNC integrated Python code validated with a machined test piece // Precision Engineering. 2021. Vol. 66. P. 21–30. DOI: 10.1016/j.precisioneng.2020.06.010.
3. Week M., Mckeown P., Bonse R., Herbst U. Reduction and compensation of thermal error in machine tools // CIRP Annals. 1995. Vol. 44. № 2. P. 589–598. DOI: 10.1016/S0007-8506(07)60506-X.
4. Zhou H., Hu P., Tan H., Chen J., Liu G. Modelling and compensation of thermal deformation for machine tool based on the real-time data of the CNC system // Procedia Manufacturing. 2018. Vol. 26. P. 1137–1146. DOI: 10.1016/j.promfg.2018.07.150.
5. Wei X., Ye H., Miao E., Pan Q. Thermal error modeling and compensation based on Gaussian process regression for CNC machine tools // Precision Engineering. 2022. Vol. 77. P. 65–76. DOI: 10.1016/j.precisioneng.2022.05.008.
6. Živković A.M., Zeljković M.V., Mlađenović C.D., Tabaković S.T., Milojević Z.L., Hadžistević M.J. A Study of Thermal Behavior of the Machine Tool Spindle // Thermal Science. 2019. Vol. 23. № 3B. P. 2117–2130. DOI: 10.2298/TSCI180129118Z.
7. Kang C.M., Zhao C.Y., Zhang J.Q. Thermal behavior analysis and experimental study on the vertical machining center spindle // Transactions of the Canadian Society for Mechanical Engineering. 2020. Vol. 44. № 3. P. 344–351. DOI: 10.1139/tcsme-2019-0124.
8. Cheng Y., Zhang X., Zhang G., Jiang W., Li B. Thermal error analysis and modeling for high-speed motorized spindles based on LSTM-CNN // International Journal of Advanced Manufacturing Technology. 2022. Vol. 121. P. 3243–3257. DOI: 10.1007/s00170-022-09563-9.
9. Fu C.-B., Tian A.-H., Yau H.-T., Hoang M.-C. Thermal monitoring and thermal deformation prediction for spherical machine tool spindles // Thermal Science. 2019. Vol. 23. № 4. P. 2271–2279. DOI: 10.2298/TSCI1904271F.
10. Денисенко А.Ф., Гришин Р.Г. Оптимизация компоновки токарного станка с ЧПУ // Frontier Materials & Technologies. 2022. № 2. С. 17–27. DOI: 10.18323/2782-4039-2022-2-17-27.
11. Дорняк О.Р., Попов В.М., Анашкина Н.А. Математическое моделирование контактного термического сопротивления для упругодеформируемых твердых тел методами механики многофазных систем // Инженерно-физический журнал. 2019. Т. 92. № 5. С. 2155–2167. EDN: DAMSLD.
12. Кузнецов А.П. Тепловой режим металлорежущих станков. М.: Янус-К, 2013. 480 с.

13. Алферов В.И. Расчет теплостойкости при проектировании металлорежущих станков // СТИН. 2006. № 4. С. 7–10. EDN: KTURXZ.
14. Меснянкин С.Ю., Викулов А.Г., Викулов Д.Г. Современный взгляд на проблемы теплового контактирования твердых тел // Успехи физических наук. 2009. Т. 179. № 9. С. 945–970. EDN: LKFJLN.
15. Madhusudana C.V. Thermal Contact Conductance. 2nd ed. Sydney: Springer, 2014. 260 p. DOI: 10.1007/978-3-319-01276-6.
16. Aalilija A., Gandin C.-A., Hachem E. A simple and efficient numerical model for thermal contact resistance based on diffuse interface immersed boundary method // International Journal of Thermal Sciences. 2021. Vol. 166. Article number 106817. DOI: 10.1016/j.ijthermalsci.2020.106817.
17. Иванов А.С., Измайлов В.В. Термическая проводимость плоского стыка // Вестник машиностроения. 2009. № 7. С. 41–43. EDN: MRMJGN.
18. Попов В.М., Дорняк О.Р., Латынин А.В., Лушникова Е.Н. Теплообмен в зоне контакта поверхностей с отклонениями формы // Воронежский научно-технический вестник. 2020. Т. 4. № 4. С. 64–69. DOI: 10.34220/2311-8873-2021-4-4-64-69.
19. Xian Y., Zhang P., Zhai S., Yuan P., Yang D. Experimental characterization methods for thermal contact resistance: A review // Applied Thermal Engineering. 2018. Vol. 130. P. 1530–1548. DOI: 10.1016/j.applthermaleng.2017.10.163.
20. Денисенко А.Ф., Подкругляк Л.Ю. Построение регрессионной модели термического сопротивления контактной псевдосреды // Известия Самарского научного центра Российской академии наук. 2021. Т. 23. № 3. С. 47–54. DOI: 10.37313/1990-5378-2021-23-3-47-54.
21. Denisenko A.F., Grishin R.G., Podkruglyak L.Y. Formation of Contact Thermal Resistance Based on the Analysis of the Characteristics of the Pseudo-Medium // Lecture Notes in Mechanical Engineering. 2022. P. 221–229. DOI: 10.1007/978-3-030-85233-7_26.
22. Дмитриев В.А., Денисенко А.Ф., Подкругляк Л.Ю. Определение значимости факторов при моделировании контактного термического сопротивления // Мехатроника, автоматика и робототехника. 2023. № 11. С. 169–172. DOI: 10.26160/2541-8637-2023-11-169-172.
23. Хохлов В.М. Расчет контурных площадей контакта и давлений // Известия высших учебных заведений. Машиностроение. 1990. № 4. С. 20–24. EDN: TNZQKP.
24. Хохлов В.М. Шероховатость поверхностей упруго контактирующих тел // Известия высших учебных заведений. Машиностроение. 1990. № 10. С. 109–113.
25. Денисенко А.Ф., Подкругляк Л.Ю. Разработка тепловой модели шпиндельной опоры металлорежущего станка // Известия Самарского научного центра Российской академии наук. 2020. Т. 22. № 3. С. 49–55. DOI: 10.37313/1990-5378-2020-22-3-49-55.

Моделирование контактного термического сопротивления при проектировании технологического оборудования

© 2023

Денисенко Александр Федорович*[1], доктор технических наук, профессор,
профессор кафедры «Технология машиностроения, станки и инструменты»
Подкругляк Любовь Юрьевна[2], аспирант кафедры «Технология машиностроения, станки и инструменты»
Самарский государственный технический университет, Самара (Россия)

***E-mail: sammortor@yandex.ru**

[1]ORCID: https://orcid.org/0000-0001-6393-2831
[2]ORCID: https://orcid.org/0009-0006-6735-4454

Поступила в редакцию 24.05.2023 *Принята к публикации 26.06.2023*

Аннотация: Анализ конструкций технологического оборудования при проектировании по температурному критерию является необходимой гарантией обеспечения требуемых эксплуатационных характеристик. Наличие значительного количества деталей в узлах и механизмах технологического оборудования требует при проектировании прогнозирования прохождения теплового потока через соединения. Многообразие требований к соединению при моделировании контактного термического сопротивления может быть учтено введением в зону контакта псевдослоя. Приведены результаты проверки предложенной регрессионной зависимости изменения температуры при прохождении теплового потока через псевдослой, полученной при учете четырех существенных факторов: толщины псевдослоя, номинального давления, предела текучести материала, расположения зоны фактического контакта. Адекватность указанной регрессионной зависимости проверялась экспериментально и с использованием численного моделирования с применением крупноблочных конечных элементов. Для описания процесса теплообмена в элементах тепловой модели были определены контактные термические сопротивления для нескольких условий распространения теплового потока: от одного конечного элемента к другому в пределах одной детали; от одного конечного элемента к другому, расположенному в соседней детали; прохождения теплового потока через замкнутые полости; распространения теплового потока в окружающую среду для конечных элементов, расположенных на наружном (свободном) контуре детали. Проведенные эксперименты показали хорошее совпадение

экспериментальных данных и результатов моделирования. Применение крупноблочных конечных элементов на основе предложенной модели контактного термического сопротивления позволило довести методику конечно-элементного моделирования до инженерного использования без сложного программного обеспечения.

Ключевые слова: технологическое оборудование; тепловой поток; моделирование контактного термического сопротивления; контактное термическое сопротивление; псевдослой; крупноблочные конечные элементы; коэффициент теплопроводности.

Для цитирования: Денисенко А.Ф., Подкругляк Л.Ю. Моделирование контактного термического сопротивления при проектировании технологического оборудования // Frontier Materials & Technologies. 2023. № 3. С. 31–42. DOI: 10.18323/2782-4039-2023-3-65-3.

doi: 10.18323/2782-4039-2023-3-65-4

Control of the dynamic stability of metal-cutting systems in the process of cutting based on the fractality of roughness of the machined surface

© 2023

Yury G. Kabaldin[1,3], Doctor of Sciences (Engineering),
professor of Chair "Technology and Equipment of Machine Building"
Pavel A. Sablin*[2,4], PhD (Engineering), Associate Professor, assistant professor of Chair "Machine Building"
Vladimir S. Schetinin[2,5], Doctor of Sciences (Engineering), Associate Professor, professor of Chair "Machine Building"
[1]*R.E. Alekseev Nizhny Novgorod State Technical University, Nizhny Novgorod (Russia)*
[2]*Komsomolsk-na-Amure State University, Komsomolsk-on-Amur (Russia)*

***E-mail: ikpmto@knastu.ru**

[3]ORCID: https://orcid.org/0000-0003-4300-6659
[4]ORCID: https://orcid.org/0000-0001-5950-9010
[5]ORCID: https://orcid.org/0000-0003-0194-2254

Received 15.06.2023 *Accepted 06.09.2023*

Abstract: The problem of increasing the efficiency of mechanical treatment within modern automated production is relevant for many branches of the processing industry. This problem requires a deep study of the physical processes occurring during cutting. The urgency of the problem increases even more with the development of digital production in our country. Today, in the presence of a wide range of products, enterprises are forced to create conditions for reducing the technological cycle when manufacturing a particular product. To carry out the study, an experiment was conducted in which the U8 carbon steel was used as the processed material, and the T15K6 alloy was used as the tool material. During the experiment, the authors observed a change in the roughness of the machined surface depending on the cutting speed. The paper considers the possibility of assessing the quality of the surface layer during cutting based on fractal and neural network modeling. It is identified that the fractal dimension shows the regularity of the reproduction of the machined surface roughness during cutting. The calculated fractal dimension of the machined surface roughness correlates well with the values of the machined surface roughness (correlation coefficient is 0.8–0.9). A neural network structure has been developed, which allows controlling the machined surface quality depending on the cutting conditions. The authors studied the possibility of using neural network models to control technological systems of cutting treatment. When creating digital twins, it is proposed to take into account factors affecting the quality of the treated surface and processing performance, which are poorly accounted for in modeling, as well as when conducting full-scale experiments during machining. Such factors are wear of the cutting tool, the process of plastic deformation, and cutting dynamics.

Keywords: cutting process; machined surface roughness; neural network; surface layer quality control.
For citation: Kabaldin Yu.G., Sablin P.A., Schetinin V.S. Control of the dynamic stability of metal-cutting systems in the process of cutting based on the fractality of roughness of the machined surface. *Frontier Materials & Technologies*, 2023, no. 3, pp. 43–51. DOI: 10.18323/2782-4039-2023-3-65-4.

INTRODUCTION

Increasing the efficiency of mechanical processing is an important scientific and technical problem that the world's leading scientists have been dealing with for many decades. The concept of "machining efficiency" implies two very important indicators: productivity and quality. In this regard, a number of scientific schools of the Russian Federation use the indicators of mechanical processing quality as the main criterion for assessing its efficiency. Surface roughness is one of the main parameters determining the quality of a machined part.

Within automated production, there is an acute problem of increasing the efficiency of machining based on a more in-depth study of physical processes accompanying cutting. This problem becomes relevant especially for digital production, the creation of which in the country is associated with the Russian Government program "Industry 4.0".

Digital transformation at all levels of machining enterprises is caused by the need both to analyse Big Data coming from equipment, systems, devices using sensors and to use this data to reduce the time for designing technological processes and launching new products increasing production flexibility, product quality and efficiency of production processes.

In the work [1], for high processing rates, a method for the formation of roughness of the machined surface is proposed, taking into account the random nature of their formation based on fractal representations. In the works, the author describes that for the formation of fractals, shock loads are necessary, which create tension–compression waves reflecting the travelling wave of the subsequent separation of the layer, the thickness of which is determined by the properties of the billet material. Such destruction is usually called spalling.

The fractal dimension (D_F) values given in the work [1], although they are fractional, have large values and require clarification. For example, finishing and precision machines have D_F=2.6–3.0, respectively. It is known that high values of D_F correspond to chaotic attractors [2], i. e., unstable regimes.

The quality of processed surfaces of various parts of machines and mechanisms is a complex operational factor that primarily affects the reliability of manufactured

products. Surface quality indicators include such characteristics as roughness, waviness, shape errors, shape position errors, etc. [4–6].

Factors influencing the roughness parameter of the machined surface [7–9] can be presented in the form of three groups:

– factors depending on the geometry of the cutting process;

– factors depending on the plastic deformation of the processed material;

– factors depending on self-oscillations during processing.

In this regard, for example, the total value of the roughness height R_z during cutting can be represented in the following form:

$$R_Z = \Delta R_Z^{\text{H}} + \Delta R_Z^{\text{ПЛ}} + \Delta R_Z^{\text{B}}, \quad (1)$$

where ΔR_Z^{H} is the height of uncut metal;

$\Delta R_Z^{\text{ПЛ}}$ is the roughness altitude gain due to plastic deformations;

ΔR_Z^{B} is the roughness altitude gain due to self-oscillations.

Thus, the roughness of machined surfaces is both the most important characteristic of surface quality and a reflection of the relationships between the processes occurring in the cutting system.

When factors related to the cutting process geometry arise, the process of microroughness occurrence is usually considered as copying the motion trajectory of a cutting tool of a certain shape on the machined surface. In this regard, the microroughness height and the surface shape are determined both by the cutting tool shape and by elements of the cutting modes, which can influence the change in the trajectory of the cutting blades relative to the machined surface.

Plastic deformations of the surface layer of the billet [6] during processing, as well as self-oscillatory processes, violate the reference shape of the future part and the regular distribution of surface irregularities increases by an order of magnitude. As a rule, only one of the three factors has a significant influence on the formation of surface microroughness, which ultimately determines the roughness measure. However, in some situations, all three factors influence the process of formation of the surface layer of the part, and it is very difficult to assess the degree of impact of each factor. The roughness of the machined surface in such cases becomes complex, devoid of clearly defined patterns.

There are a number of statistical relationships linking surface roughness with processing conditions. Currently, there are theoretical and empirical formulas that establish the relationship of one or another surface roughness criterion with the main technological factors. Thus, for example, in [10] the dependence of surface roughness during high-speed and fine turning on cutting conditions is given:

$$R_a = \frac{C_t C_s C_v C_r C_\varphi C_{HB} t^m s^n \varphi^x \varphi^y \alpha^\mu}{v^p r^q HB^w}, \quad (2)$$

where R_a, t, s, r – in μm;

v – in m/min;

angles φ, φ_1, α – in degrees;

HB – processed material hardness;

m, n, p, q, etc. are exponential factors at relevant conditions, which are characterised by the constants C_t ,C_s ,C_v, etc.

For fine boring of steel billets with cutters made of hard T15K6 and T30K4 alloys, formula (2) has the following form:

$$R_a = \frac{t^{0,16} s^{0,45} \varphi^{0,82}}{v^{0,49} r^{0,25}}. \quad (3)$$

As follows from equations (2) and (3), the main technological factors determining the surface roughness during cutting are speed, feed, cutting depth, properties of the material being processed, as well as the cutting edge angle φ and the radius r of the cutter tip rounding. There are other, more complex statistical dependencies. Therefore, an important point when studying the mechanism of formation of roughness during machining is also the study of the physics of processes accompanying cutting in relation to the energy transfer to the processing zone, the nonlinearity of the resulting effects and the inevitable influence of dissipative processes on the roughness height and technological system stability as a whole.

The purpose of the study is to show that the use of approaches of nonlinear dynamics and neural network modelling allows controlling the cutting process at the level of dynamic stability of metal-cutting systems.

METHODS

To carry out experimental studies, a stand was created consisting of:

– a 1K625 model screw-cutting lathe;

– an STD.201-2 model turning dynamometer;

– an NI cDAQ-9174 National Instruments interface unit;

– a PC.

To conduct the experiment, a billet made of U8 carbon steel was prepared. To obtain from the dynamometer more reliable data, this experimental assembly should be calibrated for each material being processed. The dynamometer is supplied with a standard calibration blank (including one made of U8 steel), as well as a verification procedure.

After calibration, according to the Walter calculator recommendations, cutting modes were selected, which were supplemented by others selected based on the requirements of processing efficiency: from gentle modes, but with obtaining maximum surface quality, to high-performance modes with the loss of the machined surface quality.

After processing the billets on the experimental bench, profilograms of the surfaces were taken.

To evaluate the R_a and R_z parameters characterising the roughness of the machined surface, a stand was developed [3], which included a blank fixed in the centers of the lathe, a TR200 profilometer connected via an interface to a PC. The TR200 profilometer allows both obtaining the value of any roughness parameter, in accordance with GOST R ISO 4287-2014, and observing the nature of surface irregularities.

Further, the fractal dimension D_F of the machined surface roughness was calculated using the profilogram attractors. The fractal dimension was calculated according to known techniques, but using original software.

Employees of the Department of Mechanical Engineering Technology of Komsomolsk-on-Amur State Technical University developed a DynAnalyzer computer program, which allows constructing an attractor and calculating the fractal dimension using a numerical series (according to a profilogram or using vibroacoustic emission (VAE) signals, etc.).

The final stage of implementation of the methodology was neural network modelling. In neural network modelling of surface roughness, the search for the optimal artificial neural network (ANN) structure was carried out using the version 6.5 Matlab software, which resulted in an architecture containing 7 neurons in the first hidden layer and 1 neuron in the second hidden layer. The ANN was trained based on the obtained experimental data. The neural network model was also tested on input data different from those on which it was trained.

RESULTS

Fig. 1 shows profilograms of the processed U8 steel surfaces at various cutting modes.

It is known [4] that the fractal dimension characterises the process stability and its reproduction regularity. In this case, this is the regularity of the reproduction of irregularities on the treated surface. Moreover, the smaller the fractal dimension, the more stable the reproduction of irregularities during cutting will be.

Fig. 2 shows that the attractor corresponding to the surface processed at a cutting rate of 50 m/min is the most chaotic (Fig. 2 b). It is known that at low cutting rates an intense build-up forming occurs, which affects the roughness. Based on the fractal dimension of this attractor, one can state that the processes occurring in the machine tool system are irregular, and the system itself is unstable. As a result, the surface roughness is high. The last fifth attractor (Fig. 2 e), on the contrary, indicates that the oscillations occurring in the system are regular and the system is stable.

Fig. 3 shows a model of a fractal rough surface in the form of a Cantor set [2].

This model shows the similarity of surface irregularities associated with repetitive processes during machining. Based on this model, the authors proposed a fractal approach to the formation and control of the roughness of machined surfaces during cutting for automated production conditions.

Fig. 4 shows the dependence of the roughness R_a on the cutting rate V carried out on the described stand when processing U8 steel and the results of assessing the fractal dimension of the roughness R_a profilograms after their processing. The analysis of the results shows that the greatest differences in these types of dependencies are observed in the region of low and high rates.

To assess the possibility of diagnosing the R_a parameter during the cutting process, a correlation analysis of the dependences of R_a on D_{Ra} was carried out. The values of the correlation coefficients turned out to be high (0.7–0.9).

During the development of a cutting process control system, the authors created a neural network (Fig. 5) based on diagnostics by the machined surface fractality.

DISCUSSION

As mentioned above, chip formation processes (plastic deformation), cutting tool wear, processed material properties and cutting dynamics are the main factors determining the roughness height during machining [11].

However, these factors in the literature [12] are considered independently of each other, i.e., they are studied and optimised separately. In particular, when developing methods for reducing the cutting tool wear rate, as well as the machined surface roughness, the type of chips generated and the equipment dynamic state are not taken into account. Studying the interdependence of various parameters of these factors, i.e., a system approach to machining will make it possible to create more accurately, in particular, the models of chip formation, the machined surface roughness, the cutting tool wear and the cutting process itself.

One of the promising research tools that can take into account the interrelation and interdependence of the cutting process output parameters is artificial intelligence approaches. The latter can be achieved based on the creation of digital twins (DT) [13; 14]. Digital twin is a new word in modelling equipment, technological processes and digital production planning. DT is based on a number of mathematical models reliably describing processes and relationships both at an individual facility and within the entire production equipment using the Big Data analysis. In this regard, the development of neural network models and machine learning becomes very important.

Using the existing statistical dependencies and neural network modelling [14; 15] allows both simulating it and assessing the current state of the process equipment as a whole, and, consequently, the processed surface quality.

A digital twin acts as a virtual model of a part, product, process, technology, etc. Such a model is capable, at the micro- and macro-level, of either describing an actual technology object, acting as a duplicate of a finished specific product or process, or serving as a prototype of a future technology object. At the same time, any information that can be obtained when testing a physical object must also be obtained based on testing a digital twin.

The influence of processing modes (V; s; t) and physical and mechanical properties of the processed material (σ_b) on the machined surface roughness is most covered in the literature [4; 6; 9]. The influence of the cutting process dynamics on the machined surface roughness is the least studied (equation (1)).

Currently, it is proved that self-oscillations during cutting are associated with a phase shift of cutting forces [16]. The work [16] shows the relationship r between the phase characteristic of cutting forces and chip shrinkage K_a.

Fig. 6 shows the dependences r of the phase characteristic of cutting forces on the microroughnesses R_z height [16]. It follows from Fig. 6 that self-oscillations have the greatest influence on the machined surface roughness when cutting ductile materials (steel 10). With increasing cutting rate, the influence of self-oscillations on the machined surface roughness decreases [17; 19].

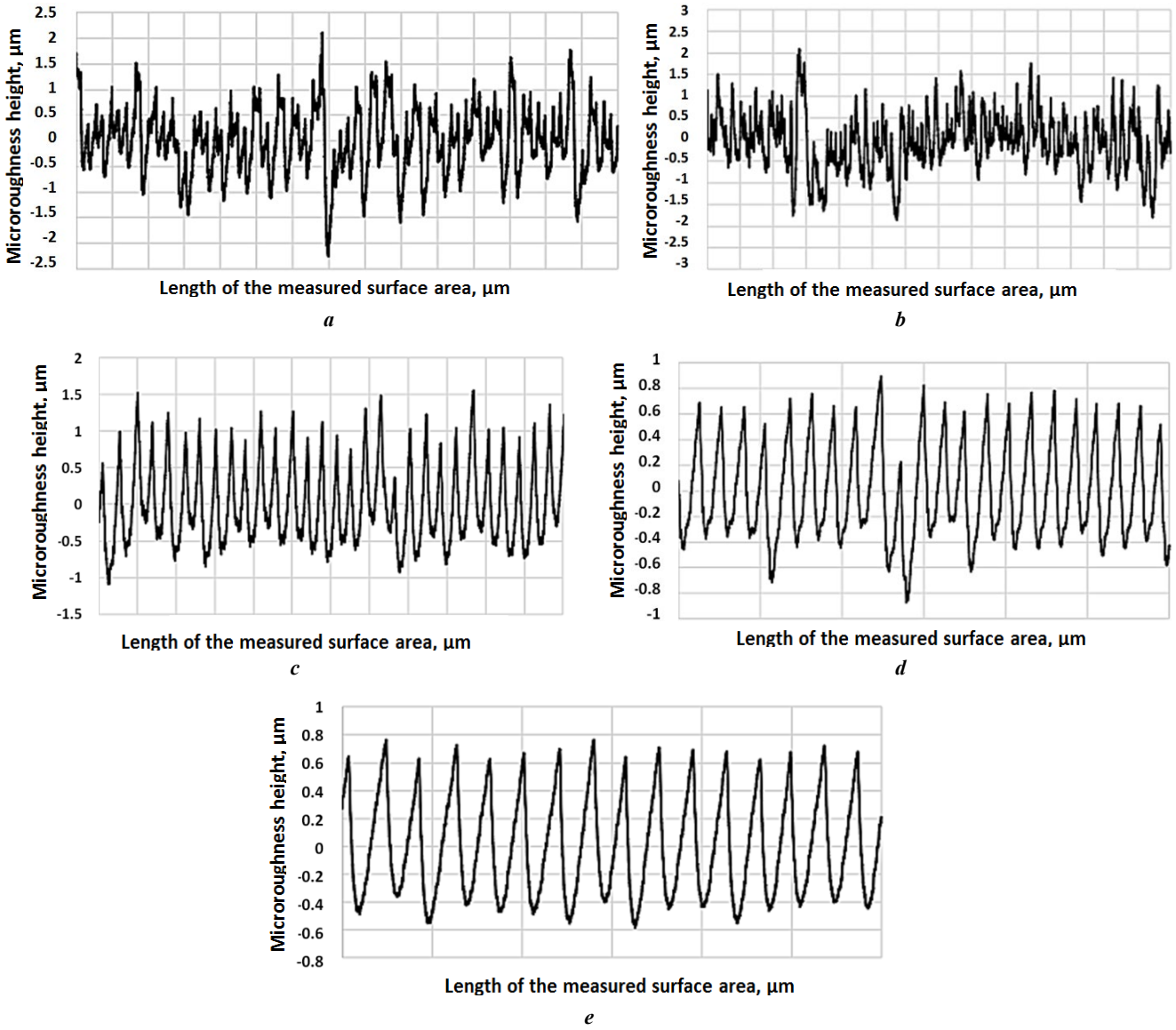

Fig. 1. *Profile records of machined surfaces (У8 steel, T15K6 cutter):*
a *– V_{cut}=20 m/min, Ra 2.32;* ***b*** *– V_{cut}=50 m/min, Ra 2.6;*
c *– V_{cut}=75 m/min, Ra 1.6;* ***d*** *– V_{cut}=105 m/min, Ra 1.25;* ***e*** *– V_{cut}=130 m/min, Ra 1.2*
Рис. 1. *Профилограммы обработанных поверхностей (сталь У8, резец Т15К6):*
a *– $V_{рез}$=20 м/мин, Ra 2,32;* ***b*** *– $V_{рез}$=50 м/мин, Ra 2,6;*
c *– $V_{рез}$=75 м/мин, Ra 1,6;* ***d*** *– $V_{рез}$=105 м/мин, Ra 1,25;* ***e*** *– $V_{рез}$=130 м/мин, Ra 1,2*

The surface roughness digital twin (Fig. 6) allows, at the stage of designing technological processes, to select machining modes providing a given roughness depending on both the dynamic state of the machine equipment and the grade of the processed material and its strength properties (σ_b).

Increasing the number of parameters at the neural network input [14; 15], changing its architecture and accumulating a database about the cutting process allows studying other factors that affect the machined surface roughness, but are difficult to study, in particular, the influence of the corner radius of the cutting blade tip, the cutting angle, etc.

Currently, modern machine tools are considered as a cyber-physical system (CPS), which uses sensors installed on the cutting tool [12; 18; 20] and on other essential controls of the machine, which collect data on the CPS state in real time, after which this information is sent to the digital twin. Constant updating of the database for the digital twin about the cutting process allows increasing the accuracy of modelling the machined surface roughness and the CPS dynamic state control during cutting.

For this purpose, the authors studied the possibility of using neural network models to control technological cutting processing systems and carried out additional experimental studies. In this regard, the authors took a time series of vibroacoustic emission signals picked up during cutting from the machine dynamic system and calculated the VAE signal fractal dimension, which, as studies have shown, correlates well with the fractal dimension of the machined surface roughness. The values of the correlation coefficients turned out to be quite high (0.8–0.9).

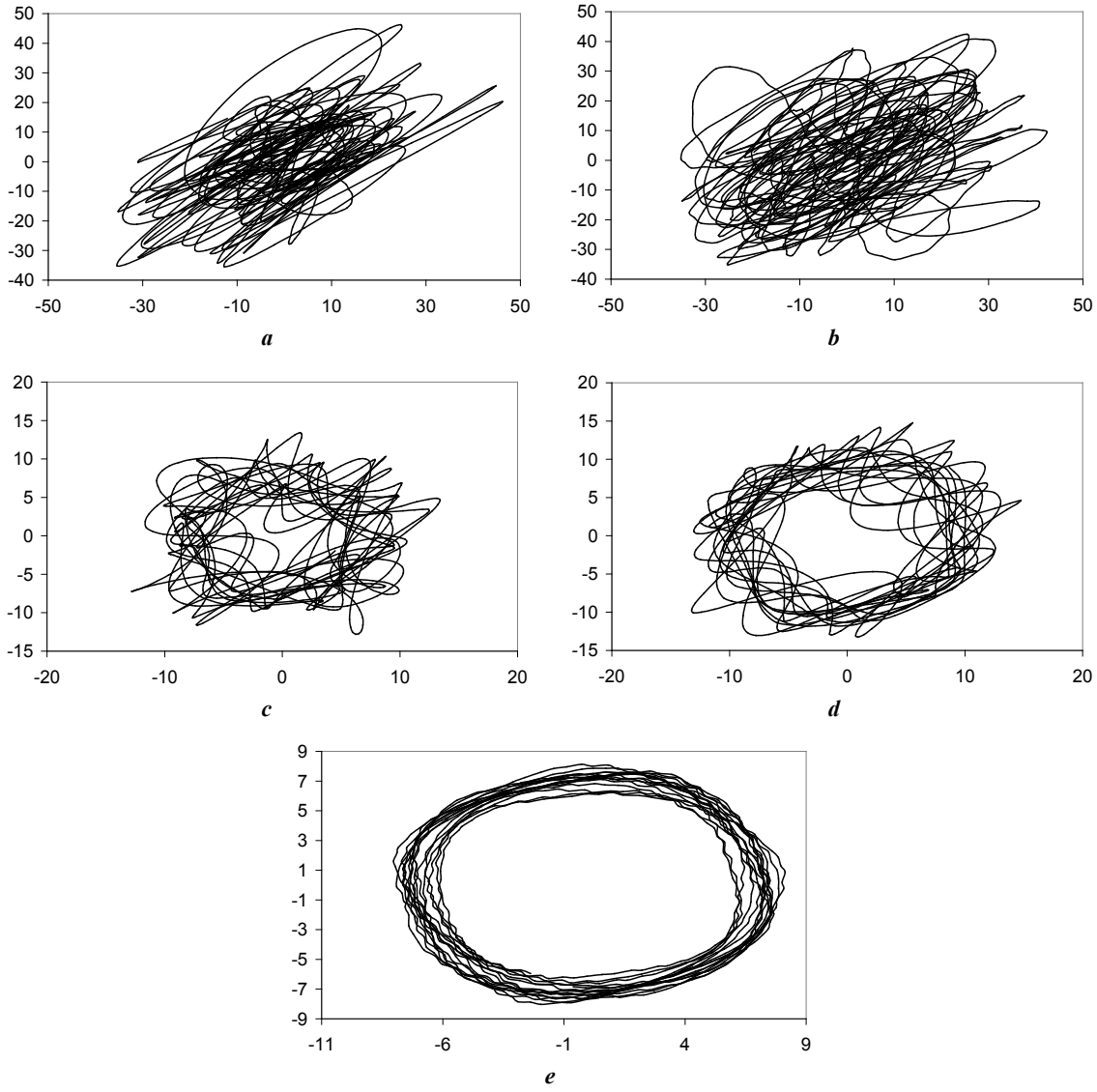

Fig. 2. *Attractors of the machined У8 steel surfaces corresponding to cutting rates:*
a *– V_{cut}=20 m/min, Ra 2.32;* ***b*** *– V_{cut}=50 m/min, Ra 2.6;*
c *– V_{cut}=75 m/min, Ra 1.6;* ***d*** *– V_{cut}=105 m/min, Ra 1.25;*
e *– V_{cut}=130 m/min, Ra 1.2*

Рис. 2. *Аттракторы обработанных поверхностей стали У8, соответствующие скоростям резания:*
a *– $V_{рез}$=20 м/мин, Ra 2,32;* ***b*** *– $V_{рез}$=50 м/мин, Ra 2,6;*
c *– $V_{рез}$=75 м/мин, Ra 1,6;* ***d*** *– $V_{рез}$=105 м/мин, Ra 1,25;*
e *– $V_{рез}$=130 м/мин, Ra 1,2*

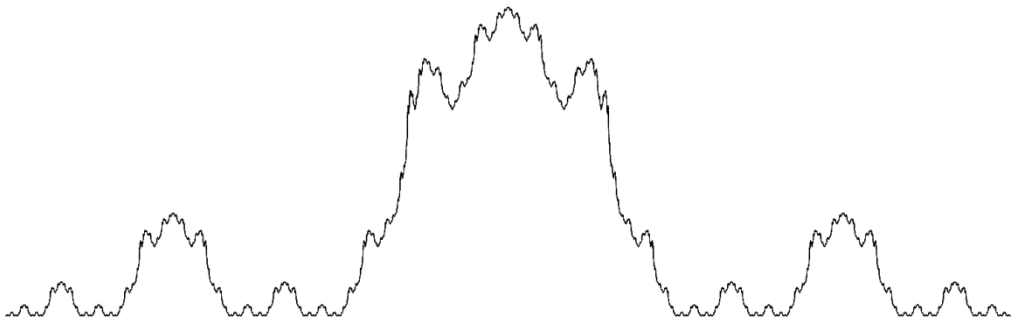

Fig. 3. *The model of Cantor profile of surface roughness*
Рис. 3. *Модель канторовского профиля шероховатости поверхности*

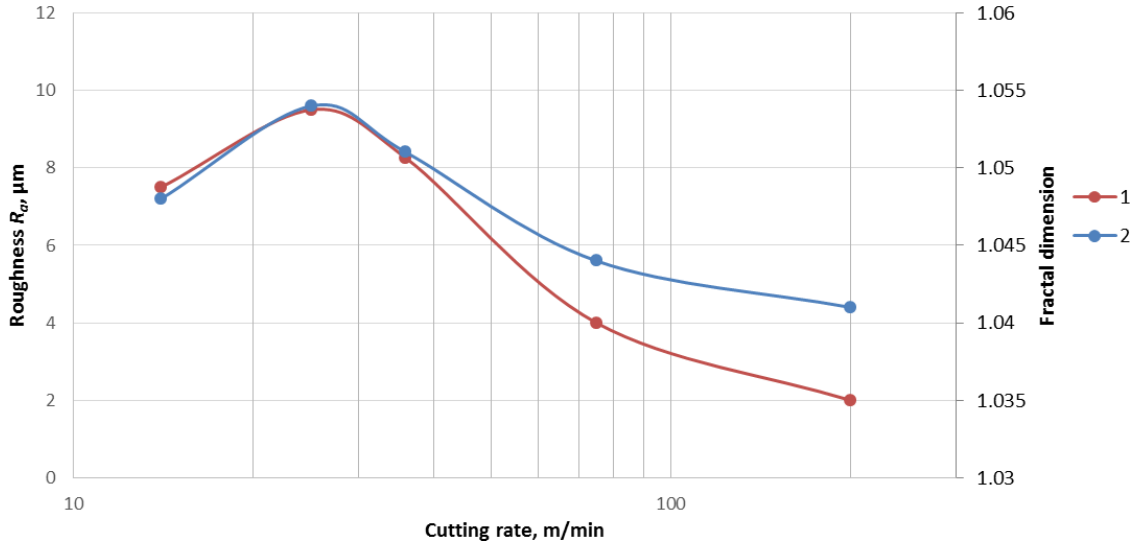

Fig. 4. *The dependence R_a of roughness (1) and D_{Ra} of fractal dimension (2) on the cutting rate (У8 steel, T15K6 cutter; S=0.11 mm/rev, t=1 mm)*
Рис. 4. *Зависимость R_a шероховатости (1) и D_{Ra} фрактальной размерности (2) от скорости резания (сталь У8, резец Т15К6; S=0,11 мм/об, t=1 мм)*

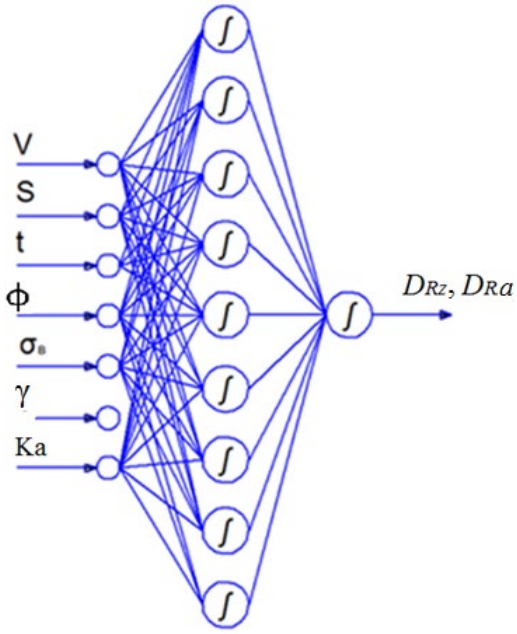

Fig. 5. *The structure of artificial neural network for assessing the fractality of the machined surface based on the cutting conditions*
Рис. 5. *Структура искусственной нейронной сети для оценки фрактальности обработанной поверхности от условий резания*

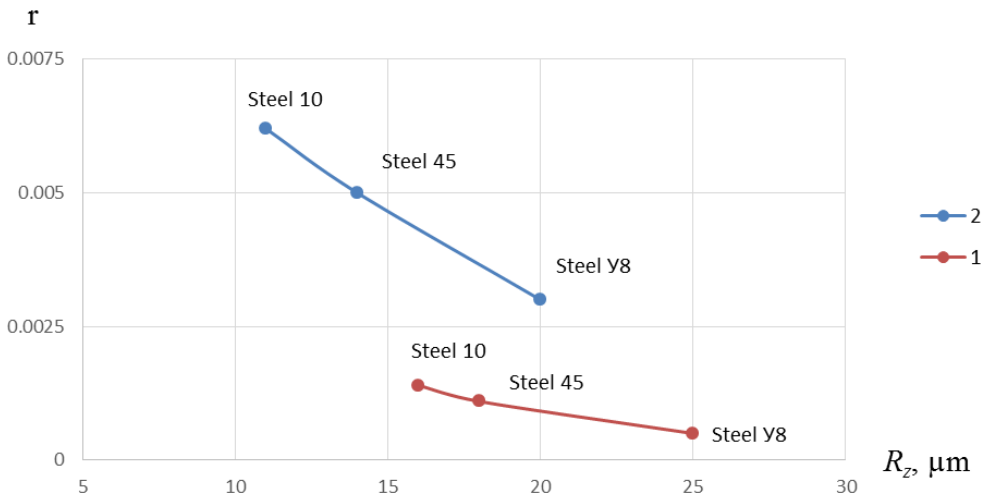

Рис. 6. *Зависимость r фазовой характеристики сил резания от шероховатости обработанной поверхности (1 – 80 м/мин; 2 – 30 м/мин) [16]*

Fig. 6. *The dependence r of phase characteristic of cutting forces on the machined surface roughness (1 – 80 m/min; 2 – 30 m/min) [16]*

CONCLUSIONS

1. A correlation was identified between the machined surface roughness and the fractal dimension D_{Ra}. The correlation coefficient was 0.8–0.9.

2. A system based on artificial intelligence is proposed that allows taking into account a wide range of input parameters affecting the machined surface roughness.

3. The proposed intelligent system is capable of self-learning, which allows increasing the number of input parameters and create a database of virtual models (digital twins).

REFERENCES

1. Kudinov A.V. Fractal approach to the formation of surfaces on metal-cutting machines. *STIN*, 1996, no. 6, pp. 13–16.
2. Feder E. *Fraktaly* [Fractals]. Moscow, Mir Publ., 1991. 260 p.
3. Kabaldin Yu.G., Shatagin D.A., Kolchin P.V. *Upravlenie kiberfizicheskimi sistemami v tsifrovom proizvodstve na osnove iskusstvennogo intellekta i oblachnykh tekhnologiy* [Control of cyber-physical systems in digital production based on artificial intelligence and cloud technologies]. Moscow, Inovatsionnoe mashinostroenie Publ., 2019. 293 p.
4. Isaev A.I. *Protsess obrazovaniya poverkhnostnogo sloya pri obrabotke metallov rezaniem* [The process of formation of the surface layer during metal cutting]. Moscow, Mashgiz Publ., 1950. 358 p.
5. Kabaldin Yu.G. Mechanisms of deformation of the cut layer and chip formation during cutting. *Vestnik mashinostroeniya*, 1993, no. 7, pp. 25–30.
6. Mylnikov V.V., Pronin A.I., Chernyshov E.A. Optimization of the Turning of Quenched Steel by Cutting Ceramic on the Basis of Simplex Planning. *Russian Engineering Research*, 2019, vol. 39, pp. 49–51. DOI: 10.3103/S1068798X19010209.
7. Starkov V.K. *Obrabotka rezaniem. Upravlenie stabilnostyu i kachestvom v avtomatizirovannom proizvodstve* [Cutting processing. Stability and quality management in automated production]. Moscow, Mashinostroenie Publ., 1989. 296 p.
8. Suslov A.G. Technological support of machinery surface roughness parameters at cutter edge machining. *Vestnik mashinostroeniya*, 1988, no. 1, pp. 40–42.
9. Yakobson M.O. *Sherokhovatost, naklep i ostatochnye napryazheniya pri mekhanicheskoy obrabotke* [Roughness, work hardening, and residual stress during machining]. Moscow, Mashgiz Publ., 1986. 292 p.
10. Makarov A.D. *Optimizatsiya protsessov rezaniya* [Optimization of cutting processes]. Moscow, Mashinostroenie Publ., 1976. 277 p.
11. Muravev V.I., Bakhmatov P.V., Lonchakov S.Z., Frolova A.V. Deformation and fracture of strengthened high-carbon steel after treatment in temperature conditions of phase pre-transformation and transformation. *Izvestiya vysshikh uchebnykh zavedeniy. Chernaya metallurgiya*, 2019, vol. 62, no. 1, pp. 62–72. DOI: 10.17073/0368-0797-2019-1-62-72.
12. Zharkov I.G. *Vibratsii pri obrabotke lezviynym instrumentom* [Vibrations during edge-tool treatment]. Leningrad, Mashinostroenie Publ., 1986. 184 p.
13. Sablin P.A., Shchetinin V.S. Influence of the micro profile of the treated surface on the strength and performance characteristics of machine parts. *Uprochnyayushchie tekhnologii i pokrytiya*, 2021, vol. 17, no. 8, pp. 368–370. DOI: 10.36652/1813-1336-2021-17-8-368-370.
14. Amosov O.S., Amosova S.G., Iochkov I.O. Accurate multi-class recognition of defects in rivet joints in aircraft products by their video images using deep neural networks. *Pribory i sistemy. Upravlenie, kontrol, diagnostika*, 2022, no. 5, pp. 30–41. DOI: 10.25791/pribor.5.2022.1339.

15. Medvedev V.S., Potemkin V.G. *Neyronnye seti. MATLAB 6* [Neural networks. MATLAB 6]. Moscow, DIALOG-MIFI Publ., 2001. 630 p.
16. Kabaldin Yu.G., Bashkov A.A. Self-organization and mechanism of friction during cutting. *Vestnik mashinostroeniya*, 2023, no. 2, pp. 167–173. DOI: 10.36652/0042-4633-2023-102-2-167-173.
17. Shchelkunov E.B., Vinogradov S.V., Shchelkunova M.E., Pronin A.I., Samar E.V. Formalized Configurational Calculations of Parallel Mechanisms. *Russian Engineering Research*, 2018, vol. 38, no. 8, pp. 581–584. DOI: 10.3103/S1068798X18080130.
18. Mylnikov V.V., Kondrashkin O.B., Shetulov D.I., Chernyshov E.A., Pronin A.I. Fatigue resistance changes of structural steels at different load spectra. *Steel in Translation*, 2019, vol. 49, no. 10, pp. 678–682. DOI: 10.3103/S0967091219100097.
19. Shchelkunov E.B., Shchelkunova M.E., Ryabov S.A., Glinka A.S. Parallel Mechanisms with Flexible Couplings. *Russian Engineering Research*, 2021, vol. 41, pp. 593–597. DOI: 10.3103/S1068798X21070236.
20. Zakovorotnyy V.L., Gvindzhiliya V.E. Correlation of attracting sets of tool deformations with spatial orientation of tool elasticity and regeneration of cutting forces in turning. *Izvestiya vysshikh uchebnykh zavedeniy. Prikladnaya nelineynaya dinamika*, 2022, vol. 30, no. 1, pp. 37–56. DOI: 10.18500/0869-6632-2022-30-1-37-56.

СПИСОК ЛИТЕРАТУРЫ

1. Кудинов А.В. Фрактальный подход к формированию поверхностей на металлорежущих станках // СТИН. 1996. № 6. С. 13–16.
2. Федер Е. Фракталы. М.: Мир, 1991. 260 с.
3. Кабалдин Ю.Г., Шатагин Д.А., Колчин П.В. Управление киберфизическими системами в цифровом производстве на основе искусственного интеллекта и облачных технологий. М.: Иновационное машиностроение, 2019. 293 с.
4. Исаев А.И. Процесс образования поверхностного слоя при обработке металлов резанием. М.: Машгиз, 1950. 358 с.
5. Кабалдин Ю.Г. Механизмы деформации срезаемого слоя и стружкообразование при резании // Вестник машиностроения. 1993. № 7. С. 25–30.
6. Myl'nikov V.V., Pronin A.I., Chernyshov E.A. Optimization of the Turning of Quenched Steel by Cutting Ceramic on the Basis of Simplex Planning // Russian Engineering Research. 2019. Vol. 39. P. 49–51. DOI: 10.3103/S1068798X19010209.
7. Старков В.К. Обработка резанием. Управление стабильностью и качеством в автоматизированном производстве. М.: Машиностроение, 1989. 296 с.
8. Суслов А.Г. Технологическое обеспечение параметров шероховатости поверхностей деталей машин при обработке лезвийным инструментом // Вестник машиностроения. 1988. № 1. С. 40–42.
9. Якобсон М.О. Шероховатость, наклеп и остаточные напряжения при механической обработке. М.: Машгиз, 1986. 292 с.
10. Макаров А.Д. Оптимизация процессов резания. М.: Машиностроение, 1976. 277 с.
11. Муравьев В.И., Бахматов П.В., Лончаков С.З., Фролова А.В. Особенности деформации и разрушения упрочненных высокоуглеродистых сталей после обработки в температурных условиях фазового предпревращения и превращения // Известия высших учебных заведений. Черная металлургия. 2019. Т. 62. № 1. С. 62–72. DOI: 10.17073/0368-0797-2019-1-62-72.
12. Жарков И.Г. Вибрации при обработке лезвийным инструментом. Л.: Машиностроение, 1986. 184 с.
13. Саблин П.А., Щетинин В.С. Влияние микропрофиля обработанной поверхности на прочностные и эксплуатационные характеристики деталей машин // Упрочняющие технологии и покрытия. 2021. Т. 17. № 8. С. 368–370. DOI: 10.36652/1813-1336-2021-17-8-368-370.
14. Амосов О.С., Амосова С.Г., Иочков И.О. Точное многоклассовое распознавание дефектов заклепочных соединений в авиационных изделиях по их видеоизображениям с использованием глубоких нейронных сетей // Приборы и системы. Управление, контроль, диагностика. 2022. № 5. С. 30–41. DOI: 10.25791/pribor.5.2022.1339.
15. Медведев В.С., Потемкин В.Г. Нейронные сети. MATLAB 6. М.: ДИАЛОГ-МИФИ, 2001. 630 с.
16. Кабалдин Ю.Г., Башков А.А. Самоорганизация и механизм трения при резании // Вестник машиностроения. 2023. № 2. С. 167–173. DOI: 10.36652/0042-4633-2023-102-2-167-173.
17. Shchelkunov E.B., Vinogradov S.V., Shchelkunova M.E., Pronin A.I., Samar E.V. Formalized Configurational Calculations of Parallel Mechanisms // Russian Engineering Research. 2018. Vol. 38. № 8. P. 581–584. DOI: 10.3103/S1068798X18080130.
18. Мыльников В.В., Шетулов Д.И., Кондрашкин О.Б., Чернышов Е.А., Пронин А.И. Изменение показателей сопротивления усталости конструкционных сталей при различных спектрах нагружения // Известия высших учебных заведений. Черная металлургия. 2019. Т. 62. № 10. С. 796–802. DOI: 10.17073/0368-0797-2019-10-796-802.
19. Shchelkunov E.B., Shchelkunova M.E., Ryabov S.A., Glinka A.S. Parallel Mechanisms with Flexible Couplings // Russian Engineering Research. 2021. Vol. 41. P. 593–597. DOI: 10.3103/S1068798X21070236.
20. Заковоротный В.Л., Гвинджилия В.Е. Связь притягивающих множеств деформаций инструмента с пространственной ориентацией упругости и регенерацией сил резания при точении // Известия высших учебных заведений. Прикладная нелинейная динамика. 2022. Т. 30. № 1. С. 37–56. DOI: 10.18500/0869-6632-2022-30-1-37-56.

Управление динамической устойчивостью металлорежущих систем в процессе резания по фрактальности шероховатости обработанной поверхности

© 2023

Кабалдин Юрий Георгиевич[1,3], доктор технических наук, профессор,
профессор кафедры «Технология и оборудование машиностроения»
Саблин Павел Алексеевич*[2,4], кандидат технических наук, доцент,
доцент кафедры «Машиностроение»
Щетинин Владимир Сергеевич[2,5], доктор технических наук, доцент,
профессор кафедры «Машиностроение»
[1]*Нижегородский государственный технический университет им. Р.Е. Алексеева, Нижний Новгород (Россия)*
[2]*Комсомольский-на-Амуре государственный университет, Комсомольск-на-Амуре (Россия)*

***E-mail: ikpmto@knastu.ru**

[3]ORCID: https://orcid.org/0000-0003-4300-6659
[4]ORCID: https://orcid.org/0000-0001-5950-9010
[5]ORCID: https://orcid.org/0000-0003-0194-2254

Поступила в редакцию 15.06.2023 *Принята к публикации 06.09.2023*

Аннотация: Проблема повышения эффективности механической обработки в условиях современного автоматизированного производства является актуальной для многих отраслей перерабатывающей промышленности. Данная проблема требует глубокого изучения физических процессов, происходящих при резании. Ее актуальность еще более возрастает с развитием цифрового производства в нашей стране. Сегодня при наличии широкой номенклатуры изделий предприятия вынуждены создавать условия для сокращения технологического цикла при производстве того или иного изделия. Для проведения исследования был поставлен эксперимент, в котором в качестве обрабатываемого материала использовалась углеродистая сталь У8, а в качестве инструментального материала – Т15К6. В ходе проведения эксперимента наблюдали за изменением шероховатости обработанной поверхности в зависимости от скорости резания. В работе рассмотрена возможность оценки качества поверхностного слоя при резании на основе фрактального и нейронносетевого моделирования. Обнаружено, что фрактальная размерность показывает регулярность воспроизведения неровностей на обработанной поверхности при резании. Рассчитанная фрактальная размерность шероховатости обработанной поверхности хорошо коррелирует со значениями шероховатости обработанной поверхности (коэффициент корреляции 0,8–0,9). Разработана структура нейронной сети, позволяющая управлять качеством обработанной поверхности в зависимости от условий резания. Изучена возможность использования нейронносетевых моделей для управления технологическими системами обработки резанием. Предложено при создании цифровых двойников учитывать факторы, влияющие на качество обработанной поверхности и производительность обработки, которые слабо поддаются учету при моделировании, а также при проведении натурных экспериментов в ходе механической обработки. Такими факторами являются износ режущего инструмента, процесс пластической деформации и динамика резания.

Ключевые слова: процесс резания; шероховатость обработанной поверхности; нейронная сеть; управление качеством поверхностного слоя.

Для цитирования: Кабалдин Ю.Г., Саблин П.А., Щетинин В.С. Управление динамической устойчивостью металлорежущих систем в процессе резания по фрактальности шероховатости обработанной поверхности // Frontier Materials & Technologies. 2023. № 3. С. 43–51. DOI: 10.18323/2782-4039-2023-3-65-4.

doi: 10.18323/2782-4039-2023-3-65-5

The influence of the supply mains parameters on the stability of phase control during resistance welding

© 2023

Aleksey S. Klimov*[1], PhD (Engineering),
assistant professor of Chair "Welding, Pressure Material Treatment, and Allied Processes"
Andrey K. Kudinov[2], senior lecturer of Chair "Industrial Electronics"
Vitaly S. Klimov[3], PhD (Engineering),
assistant professor of Chair "Applied Mathematics and Informatics"
Valery V. Eltsov, Doctor of Sciences (Engineering),
professor of Chair "Welding, Pressure Material Treatment, and Allied Processes"
Denis A. Boldyrev[4], Doctor of Sciences (Engineering),
professor of Chair "Nanotechnologies, Materials Science, and Mechanics"
Togliatti State University, Togliatti (Russia)

***E-mail: KlimovTGU@yandex.ru, klimov@tltsu.ru**

[1]ORCID: https://orcid.org/0009-0003-8679-0882
[2]ORCID: https://orcid.org/0009-0003-3026-2554
[3]ORCID: https://orcid.org/0000-0002-1467-3543
[4]ORCID: https://orcid.org/0000-0002-6951-5825

Received 30.05.2023 *Accepted 09.06.2023*

Abstract: Resistance welding in large-scale manufacturing is carried out with a significant number of disturbances, the cumulative effect of which may exceed the capabilities of modern control equipment. Most resistance welding control systems used in industry to compensate for existing disturbances provide welding current phase control depending on the measured parameters characterizing the process of welded joint formation. The efficiency of such controllers is largely determined by the accuracy of measuring and setting the phase control parameters, which include the opening and conduction angles of welding thyristors. The paper shows that when switching on a contact machine, a phase shift of the mains voltage occurs in the load mode relative to the mains voltage in the idle mode. Using a simplified electric equivalent circuit of a contact welding machine, the paper describes the nature of the phase shift of the mains voltage. Circuit active resistance and inductance are selected as parasitic parameters of the mains. The authors simulated the electrical processes in the contact machine according to the three-loop equivalent circuit. The study shows the influence of mains parasitic parameters on the phase regulation stability, the features of the obtained current and voltage oscillograms. Depending on the mains and contact welding machine parameters, the phase shift magnitude ranges from fractions to units of an electrical degree. With welding current parametric stabilization by the mains voltage, the influence of mains parasitic parameters can be neglected. When the regulator operates in the mode of maintaining the secondary current numerical value, a decrease in the generated current relative to the specified one is observed. The authors proposed and tested a technique for determining the parasitic parameters of the supply mains based on the results of a short circuit test.

Keywords: supply mains parameters; phase control during resistance welding; resistance welding; resistance welding control under disturbances; resistance welding diagnostics; simulation of electric processes; phase control; welding current measurement and control.

For citation: Klimov A.S., Kudinov A.K., Klimov V.S., Eltsov V.V., Boldyrev D.A. The influence of the supply mains parameters on the stability of phase control during resistance welding. *Frontier Materials & Technologies*, 2023, no. 3, pp. 53–60. DOI: 10.18323/2782-4039-2023-3-65-5.

INTRODUCTION

The leading position of resistance welding, when manufacturing sheet parts in mass production is explained by high technical and economic performance. As well as a significant amount of accumulated positive experience, in the field of application and expansion of the technology options of this method. Every year, about 100,000 resistance-welding machines are put into operation in the world for a total amount of about 1.5 billion US dollars, which is 30 % of the welding equipment market. The growing needs of the global industry allow predicting an increase in sales of resistance-welding equipment up to 2 billion US dollars by 2025 [1; 2]. In the Russian Federation, 40 % of resistance-welding equipment has a service life of more than 20 years; updating the stock of welding machines is hindered by an increase in the purchase price for equipment and components, insufficient funding for research and development in the field of welding [3; 4].

In the current economic conditions, the task of improving the quality of welding work, and expanding technology options, should be solved by the several-fold increase in the efficiency of using the equipment already available at the enterprise, without significant costs for its replacement and total redesign. In this case, a significant role is assigned to control systems and techniques of operational diagnostics of the welding equipment state [5; 6].

The concept of welding process control, accepted by most equipment manufacturers, considers the resistance-welding controller as an independent product implementing the preprogrammed control algorithm [7]. A significant quality improvement of the joints, was achieved through

the stabilisation and correction of welding modes, implemented by modern equipment. In this area, such well-known manufacturers of resistance-welding equipment as CJSC Elektrik-MIKS (Russia), Selma (Russia), Bosch Rexroth (Germany), ENTRON Controls (USA), Welding Technology Corporation (USA), Spotron (Japan), Dengensha (Japan), and Tecna (Italy) are developing. The operation of resistance welding machines, in mass production is characterised by a number of disturbances (intensive wear of welding electrodes, compression drive, current-carrying elements, supply network instability). The cumulative effect of which cannot be compensated by modern control systems [8–10]. The issue, of increasing the stability of the resistance welding quality under various disturbances, can be solved by a comprehensive solution of the problems of operational diagnostics of the state of welding equipment, and power supply network. Simulation of electrical processes in the "machine – part" system, searching for feedback parameters, and synthesizing diagnostic and control algorithms [11–13].

In the phase control systems with effective current stabilisation based on negative feedback, the error reduction relative to the set value is achieved by introducing an integrating component into the control law. This provides effective compensation for fluctuations in the operating network voltage relative to the nominal one [14; 15]. The low quality of the supply networks, and their congestion with other consumers distorts the shape of the mains voltage signal. In this case, an error occurs in measuring and setting the time parameters of the supply voltage and current, which reduces the efficiency of phase control, and disrupts the normal operation of resistance welding controllers. The issue of resistance welding diagnostics and control, taking into account the distortion of the mains voltage shape, is not covered in the scientific literature.

The purpose of this study is to increase the reliability of diagnostics and the efficiency of resistance welding control systems, under the conditions of mains voltage fluctuations by simulating electrical processes in the "machine – part" system, and developing the techniques for diagnosing the state of supply networks.

METHODS

Preliminary calculation of the resistance welding electrical parameters, and construction of current and voltage oscillograms were performed using a simplified equivalent circuit shown in Fig. 1 a. The circuit includes series-connected active resistances of the welding transformer primary winding R_{1t}, the secondary circuit R_2, and the load R_{weld}, as well as the secondary circuit inductance L_2 and the transformer primary winding R_{1t}. The operation of the thyristor contactor is simulated by the K key position. The supply network is modelled by an ideal voltage source $E(t)$ of a sinusoidal shape and parasitic resistance R_s and network inductance L_s connected in series with it. At the terminals "1" and "2", the reference voltage U_s is measured equal to $U_{s,oc}$ at idle and $U_{s,weld}$ in the welding mode. When the machine is running in idle mode, a deviation of the mains voltage $U_{s,oc}$ relative to the nominal mains

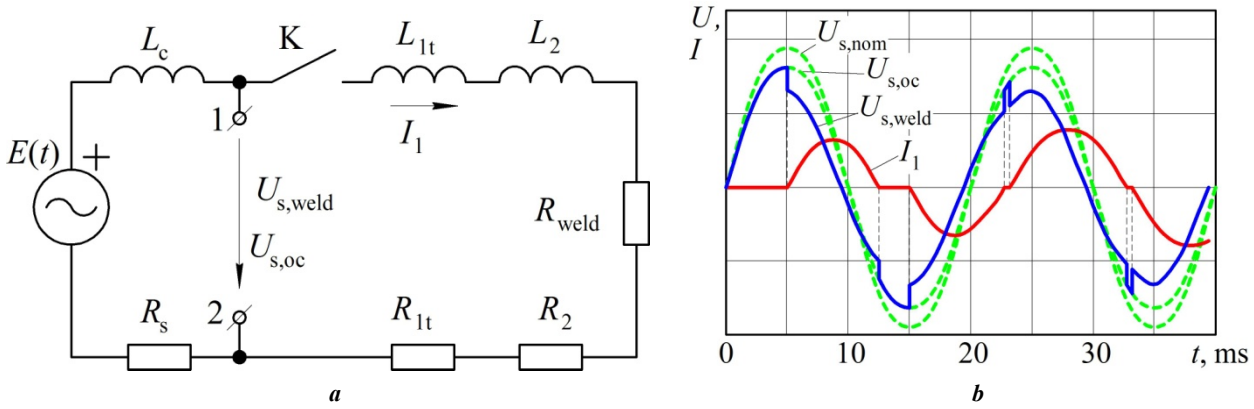

Fig. 1. *A simplified electric equivalent circuit of the contact welding machine when connecting to a non-ideal circuit* ***(a)*** *and oscillograms of the current and voltage* ***(b)****. E(t) – ideal sinusoidal voltage source;*
R_s and L_c – active resistance and inductance of the supply mains;
R_{1m} and L_{1m} – active resistance and inductance of the transformer primary winding;
R_2 and L_2 – active resistance and inductance of the secondary circuit;
R_{weld} – active load resistance (of welded parts);
$U_{s,nom}$, $U_{s,oc}$ and $U_{s,\,weld}$ – mains voltage is nominal, idle, and under the load conditions;
I_1 – the current in the primary circuit of the contact welding machine

Рис. 1. *Упрощенная схема замещения контактной машины при подключении к неидеальной сети* ***(а)*** *и осциллограммы тока и напряжения* ***(b)****.*
E(t) – идеальный источник напряжения синусоидальной формы;
R_s and L_c – активное сопротивление и индуктивность питающей сети;
R_{1m} и L_{1m} – активное сопротивление и индуктивность первичной обмотки трансформатора;
R_2 и L_2 – активное сопротивление и индуктивность вторичного контура;
R_{weld} – активное сопротивление нагрузки (свариваемых деталей);
$U_{s,nom}$, $U_{s,oc}$ and $U_{s,\,weld}$ – напряжение сети номинальное, в режиме холостого хода и в режиме нагрузки;
I_1 – ток в первичном контуре контактной машины

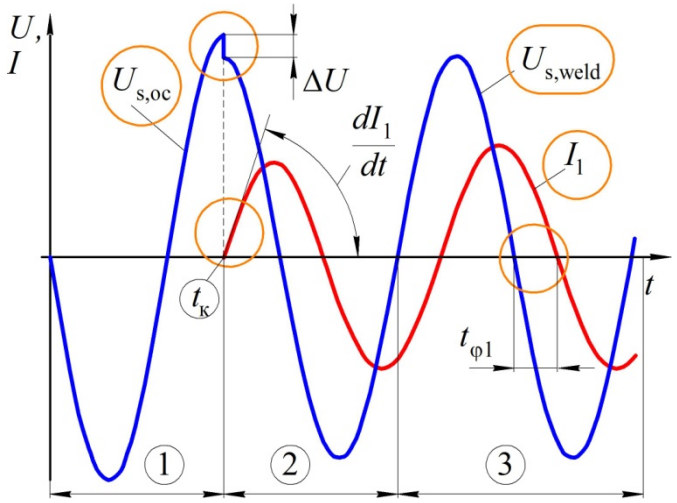

Fig. 2. *Current and voltage oscillograms at full-phase switching-on.*
$U_{s,oc}$ and $U_{s,\,weld}$ – mains voltage in idle mode and in load mode;
I_1 – the current in the primary circuit of the contact welding machine;
ΔU – power failure; $t_к$ – commutation moment of the thyristor contactor;
dI_1/dt – primary current growth rate; $t_{\varphi 1}$ – phase shift
Рис. 2. *Осциллограммы тока и напряжения при полнофазном включении.*
$U_{s,oc}$ and $U_{s,\,weld}$ – напряжение сети в режиме холостого хода и в режиме нагрузки;
I_1 – ток в первичном контуре контактной сварочной машины;
ΔU – провал напряжения; $t_к$ – момент коммутации тиристорного контактора;
dI_1/dt – скорость нарастания первичного тока; $t_{\varphi 1}$ – фазовый сдвиг

voltage $U_{s,nom}$ is observed, which is explained by the network congestion by other electric energy consumers. When the machine operates in the welding mode, an abrupt decrease in the mains voltage $U_{s,weld}$ relative to the idle voltage $U_{s,oc}$ is observed, which manifests itself both by a decrease in the voltage supplied to the contactor and by a voltage phase lag $U_{s,weld}$ relative to the voltage $U_{s,oc}$, which is shown in Fig. 1 b.

The authors proposed to calculate the parasitic parameters of the supply network (resistance R_s and inductance L_s), based on the results of a short circuit test in the full-phase switching on of the welding machine. On the oscillogram of currents and voltages, three characteristic regions can be distinguished, which are shown in Fig. 2. The first one – before switching the thyristor contactor, where the effective mains voltage in the idle mode $U_{s,oc}$ is measured. The second – after switching the thyristor contactor, when the transient processes occur. This area lasts 2…3 half cycles of mains voltage. At the switching moment t_k of the thyristor contactor, the power failure ΔU and the rate of the primary current rise dI_1/dt are measured. The third area characterised by a sinusoidal form of voltage and current is used to measure the effective voltage of the network under load $U_{s,weld}$, the primary current I_1 and the current-voltage lag angle φ_1. It should be noted that the short circuit mode is characterised by the largest phase shift $t_{\varphi 1}$, which allows improving the accuracy of the calculation of parasitic network parameters. The accuracy increases as well with an increase in the primary current I_1, therefore, the maximum stage of the welding transformer was taken for measurements. The maximum suppression of transient processes when the thyristor contactor is turned on is ensured when switching at the moment of the maximum voltage $U_{s,oc}$, therefore, the first switching on of the thyristors was performed at an opening angle of α=90° el.

Since at the switching moment the current I_1 is equal to zero, the observed power failure ΔU is completely caused by the voltage drop on the parasitic inductance of the network L_s and can be calculated according to the formula (1) from the primary current growth rate dI_1/dt:

$$L_s = \frac{\Delta U}{\frac{dI_1}{dt}}. \qquad (1)$$

The active resistance R_s is calculated according to the formula (2) taking into account the supply network frequency f_s:

$$R_s = \sqrt{\left(\frac{U_{s,oc}}{I_1}\right)^2 - \left(\frac{U_{s,weld}}{I_1}\sin\varphi_1 + 2\pi f_s L_s\right)^2} - \frac{U_{s,weld}}{I_1}\cos\varphi_1. \qquad (2)$$

The supply network parasitic parameters were measured in the resistance welding laboratory of Togliatti State University, using an MT-4019 resistance welding machine, an RKDP-0401 welding process recorder, and an RMS-24 welding controller. The thyristor contactor was switched on at the 8th stage of the transformer.

RESULTS

The mains voltage measured at no load was $U_{s,oc}$=380 V. At the time of switching the thyristor contactor, the power failure was ΔU=39 V. The primary current growth rate was dI_1/dt=148 kA/s, the mains voltage measured in the load mode was $U_{s,weld}$=343 V, and the primary current of full-phase switching in the load mode was I_1=258 A. The lag angle of the primary current from the voltage was φ_1=61° el. When calculating according to formulas (1) and (2), the supply network parasitic parameters R_s=0.14 Ohm and L_s=0.26 mH were obtained.

Simulation of electrical processes in welding equipment, taking into account the network parasitic parameters R_s and L_s, was performed using a T-equivalent circuit and bringing the parameters to the transformer primary winding [16]. The supply network is modelled by an ideal sinusoidal voltage source E. The on state of the thyristor contactor is modelled by a jumper strap; the calculated equivalent circuit in this case is shown in Fig. 3 a. The off state of the thyristor contactor is modelled by an electrical circuit break; the calculated equivalent circuit in this case is shown in Fig. 3 b. The scheme additionally takes into account the transformer core parameters R_0 and L_0. The mathematical description of electrical processes was performed using the state-variable approach; the inductance currents L_{1t}+L_s (I_1 current), inductance L_2 (I_2 current), and inductance L_0 (I_0 current) were chosen as state variables. The following systems of differential equations of the first order for the on (3) and off (4) thyristor contactor states are obtained:

$$\frac{d}{dt}\begin{bmatrix} I_1 \\ I_2 \\ I_0 \end{bmatrix} = \begin{bmatrix} -\dfrac{R_0 + R_s + R_{1t}}{L_s + L_{1t}} & \dfrac{R_0}{L_s + L_{1t}} & \dfrac{R_0}{L_s + L_{1t}} \\ \dfrac{R_0}{L_2} & -\dfrac{R_0 + R_2 + R_{weld}}{L_2} & -\dfrac{R_0}{L_2} \\ \dfrac{R_0}{L_0(I_0)} & -\dfrac{R_0}{L_0(I_0)} & -\dfrac{R_0}{L_0(I_0)} \end{bmatrix} \times \begin{bmatrix} I_1 \\ I_2 \\ I_0 \end{bmatrix} + \begin{bmatrix} \dfrac{1}{L_s + L_{1t}} \\ 0 \\ 0 \end{bmatrix} E(t) \quad (3)$$

$$\frac{d}{dt}\begin{bmatrix} I_1 \\ I_2 \\ I_0 \end{bmatrix} = \begin{bmatrix} 0 & 0 & 0 \\ 0 & -\dfrac{R_0 + R_2 + R_{weld}}{L_2} & -\dfrac{R_0}{L_2} \\ 0 & -\dfrac{R_0}{L_0(I_0)} & -\dfrac{R_0}{L_0(I_0)} \end{bmatrix} \times \begin{bmatrix} I_1 \\ I_2 \\ I_0 \end{bmatrix}. \quad (4)$$

Using (3) and (4), the transient process was calculated when the MT-4019 machine was turned on at the thyristor opening angle of α=60° el. for previously found network parasitic parameters R_s=0.14 Ohm, L_s=0.26 mH. The calculated current and voltage curves shown in Fig. 4, have characteristic failures, at the moment of switching of the thyristor contactor, the shape and size of which correspond to the oscillograms obtained using the RKD-0401 recorder. Fig. 4 shows as well, that the zero crossing point of the mains voltage in the idle mode $U_{s,oc}$ does not coincide with the zero-crossing point of the mains voltage in the welding mode $U_{s,weld}$, while the actual opening angle of the thyristors α differs from the specified α_{set}.

DISCUSSION

The analysis of the results of full-scale experiments and mathematical modelling shows that under the conditions of mass production, the supply network imperfection leads to a disruption in the normal course of phase control during resistance welding. The correct setting of the thyristor opening angle α, measured from the zero-crossing point of the idle mains voltage $U_{s,oc}$ is possible only in the first half-cycle of the welding current. On subsequent half-cycles, the $U_{s,oc}$ idle voltage signal is absent. Instead, there is a phase-shifted $U_{s,weld}$ voltage signal in the welding mode. Under the conditions of non-ideal supply network, the actual thyristor opening angle α differs from the α_{set} value, specified by the regulator by the allowance value Δα:

$$\alpha = \alpha_{set} - \Delta\alpha . \quad (5)$$

The allowance value is calculated according to (3)–(5) for predetermined supply network parasitic parameters, and can be represented by a family of curves depending on the actual thyristor, opening angle α, power factor cosφ,

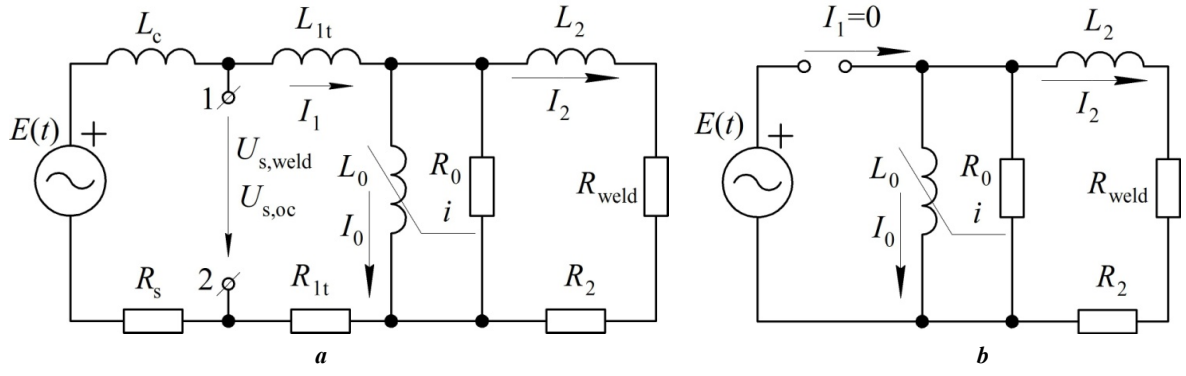

Fig. 3. *Calculated equivalent circuit of the contact welding machine with on* ***(a)*** *and off* ***(b)*** *thyristor contactor*
Рис. 3. *Расчетная схема замещения контактной сварочной машины при включенном* ***(a)*** *и выключенном* ***(b)*** *тиристорном контакторе*

and machine load Q, as shown in Fig. 5. Depending on the parameters of the welding mode and phase control, the allowance Δα ranges from tenths to units of an electrical degree. It grows with a decrease in the power factor (cosφ), and the phase regulation depth (angle α), an increase in the load Q of the welding machine in terms of power.

When using welding regulators that implement parametric stabilisation of the welding current to the mains voltage (RKM-803 and RKM-804 in the parametric stabilisation mode, RVI-801), the influence of the network parasitic parameters on the quality of welding can be neglected. Thus, for the parametric stabilisation algorithm [17] implemented in the RKM-803 and RKM-804 controllers, the actual heating level N (the ratio of the effective current to the full-phase current) differs slightly from the specified heating level N_{set}, moreover upwards, as shown in Fig. 6 a. From this, the authors can conclude that the phase shift of the observed voltage $U_{s,weld}$ relative to the idle voltage $U_{s,oc}$ does not violate the phase regulation when implementing the parametric stabilisation algorithms.

The quantitative setting and maintenance of the welding current value implemented in most modern resistance welding controllers, under the conditions of a phase shift in the welding voltage $U_{s,weld}$ relative to the idle voltage $U_{s,oc}$, can take place with significant violations. When the controller operates in the mode of maintaining the welding current numerical value, the generated current I_2 is equal to the specified current I_{set} only at two key points α_{set}' and α_{set}'', which were used when constructing the regulation characteristic. For intermediate values of the thyristor opening angle α_{set}, the generated current $I_2(\alpha_{set}-\Delta\alpha)$, which corresponds to the actual thyristor opening angle according to (5), is less than the set current I_{set}. The resulting error is shown in Fig. 6 b. Thus, for the MT-3003 and MT-1933 stationary machines, the deviation of generated and set currents during welding of 08Yu steel samples with a thickness of (1.5+1.5) mm was 1.5 and 0.5 kA, respectively.

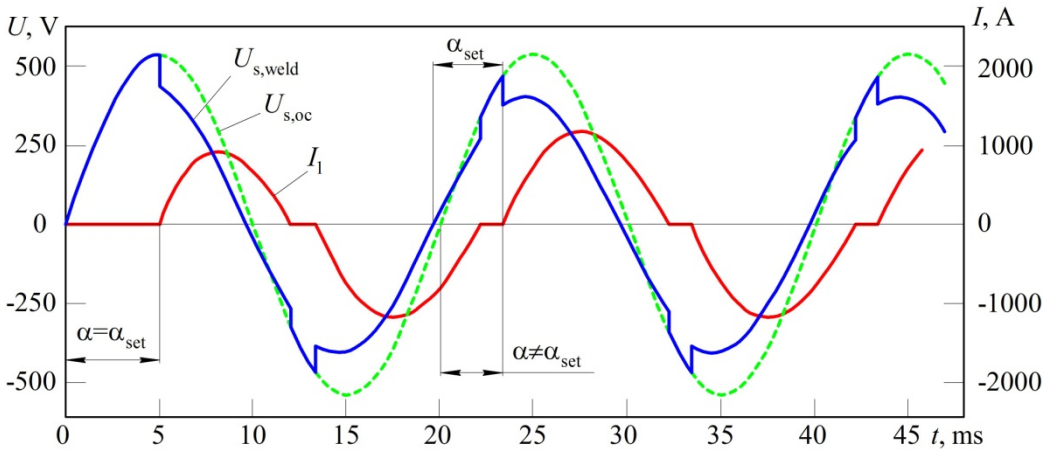

Fig. 4. *Calculated voltage and current curves built taking into account the supply mains parasitic parameters*
Рис. 4. *Расчетные кривые напряжения и тока, построенные с учетом паразитных параметров питающей сети*

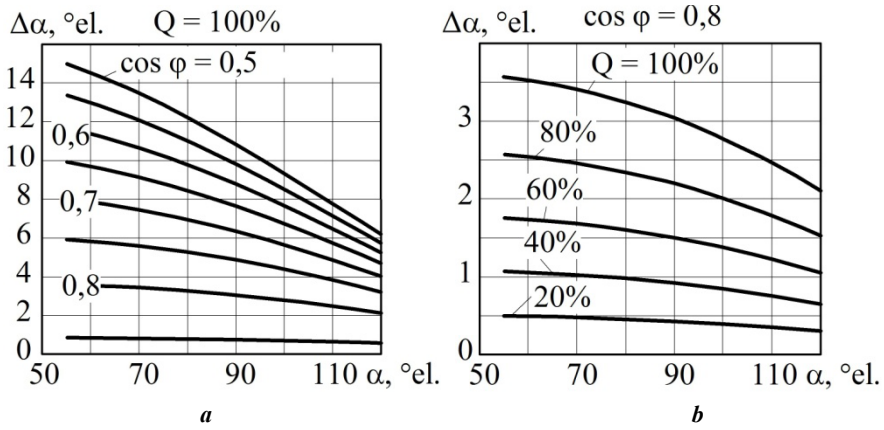

Fig. 5. *The dependence of the allowance Δα on the control angle α at different loads by power Q for cosφ=0.8* ***(a)*** *and at 100 % load of the welding machine* ***(b)***
Рис. 5. *Зависимость поправки Δα от угла регулирования α при различной загрузке по мощности Q для cosφ=0,8* ***(а)*** *и при 100 % загрузке сварочной машины* ***(b)***

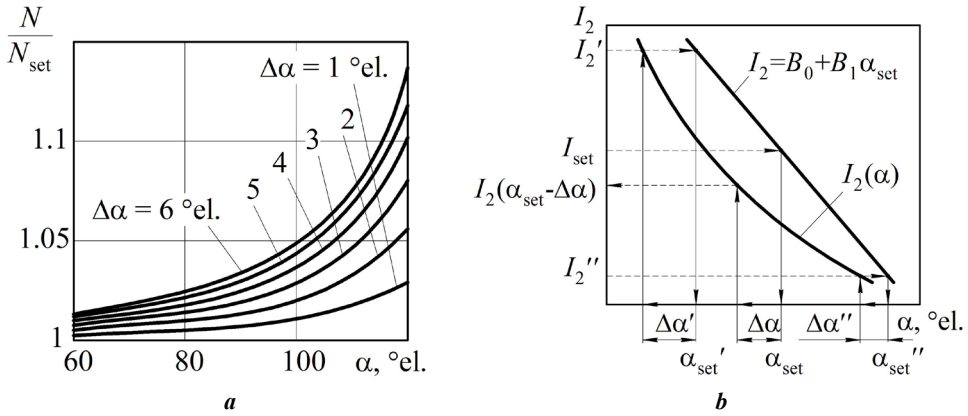

Fig. 6. *The ratio of the actual heating level N to the set heating level N_{set} with parametric stabilization at the parametric stabilization (**a**); current setting error at the quantitative stabilization of welding current (**b**)*

Рис. 6. *Отношение действительного уровня нагрева N к заданному уровню нагрева N_{set} при параметрической стабилизации (**a**); погрешность задания тока при количественной стабилизации сварочного тока (**b**)*

To diagnose resistance welding and predict the quality of joints, an assessment of the time intervals of the thyristor contactor operation is performed with the calculation of the power factor cosφ [18–20]. The error in setting the opening angle of thyristors Δα ranging from fractions to units of an electrical degree disrupts the normal operation of control and diagnostic algorithms. So, at Δα=1° el., the actual value of cosφ turns out to be more than calculated by 1 ... 10 %, and at Δα = 3° el., the error can reach 20 %. Reducing the phase regulation depth, and increasing the value of the power factor cosφ through optimising the welding mode parameters and the design of the resistance machine secondary circuit, can significantly reduce the influence of Δα on the accuracy of control and diagnostics of resistance welding.

CONCLUSIONS

With a phase shift of the mains voltage in the load mode relative to the mains voltage in the idle mode, an error in setting the opening angle of the thyristors occurs, which reaches several electrical degrees.

The study shows that in the case of parametric control of the current by the network voltage, the influence of network parasitic parameters can be neglected. With the secondary current numerical maintenance, the generated current turns out to be less than the specified one due to the occurrence of an error in setting the thyristor opening angle α.

A technique for calculating the supply network parasitic parameters, based on the results of a short circuit test in the full-phase switching mode is proposed.

REFERENCES

1. Ertas A.H., Akbulut M. Experimental Study on Fatigue Performance of Resistance Spot-Welded Sheet Metals. *The International Journal of Advanced Manufacturing Technology*, 2021, vol. 114, pp. 1205–1218. DOI: 10.1007/s00170-021-06822-z.
2. Kang M., Choi W.H., Kim C. Statistical Analysis of Korean Welding Industry. *Journal of Welding and Joining*, 2023, vol. 41, no. 2, pp. 107–111. DOI: 10.5781/JWJ.2023.41.2.4.
3. Oshchepkov F.N. Contemporary market of welding equipment: problems and prospects. *Svarka i diagnostika*, 2013, no. 5, pp. 62–63. EDN: RDYYHT.
4. Lukin M.A. Scientific and technical level of welding production in modern Russia. *Svarochnoe proizvodstvo*, 2015, no. 12, pp. 31–36. EDN: VKSMWL.
5. Zhou B., Pychynski T., Reischl M., Kharlamov E. Machine Learning with Domain Knowledge for Predictive Quality Monitoring in Resistance Spot Welding. *Journal of Intelligent Manufacturing*, 2022, vol. 33, no. 4, pp. 1139–1163. DOI: 10.1007/s10845-021-01892-y.
6. Cho Y., Rhee S. Experimental study of nugget formation in resistance spot welding. *Welding Journal*, 2003, vol. 82, no. 8, pp. 195–201.
7. Gladkov E.A., Klimov A.S., Antsiborov A.N. Experience of contact welding regulators in mass production. *Svarka i diagnostika*, 2021, no. 1, pp. 47–53. DOI: 10.52177/2071-5234_2021_01_47.
8. Wei D., Li D., Tang D., Jiang Q. Deep Learning Assisted Vision Inspection of Resistance Spot Welds. *Journal of Manufacturing Processes*, 2021, vol. 62, no. 8, pp. 262–274. DOI: 10.1016/j.jmapro.2020.12.015.
9. Klimov A.S., Kudinov A.K., Klimov V.S. Influence of Grid Parameters on Control and Diagnostics in Resistance Spot Welding. *Russian Engineering Research*, 2021, no. 9, pp. 813–819. DOI: 10.3103/S1068798X2109015X.
10. Dong J., Hu J., Luo Z. Quality Monitoring of Resistance Spot Welding Based on a Digital Twin. *Metals*, 2023, vol. 13, no. 4, article number 697. DOI: 10.3390/met13040697.
11. Martin O., Ahedo V., Santos J.I., Galan J.M. Comparative Study of Classification Algorithms for Quality Assessment of Resistance Spot Welding Joints From Pre- and Post-Welding Inputs. *IEEE Access*, 2022, no. 10, pp. 6518–6527. DOI: 10.21203/rs.3.rs-645372/v2.
12. Zhao D., Wang Y., Zhang P., Liang D. Modeling and Experimental Research on Resistance Spot Welded Joints for Dual-Phase Steel. *Materials*, 2019, vol. 12, no. 7, article number 1108. DOI: 10.3390/ma12071108.

13. Xia Y.J., Shen Y., Zhou L., Li Y.B. Expulsion intensity monitoring and modeling in resistance spot welding based on electrode displacement signals. *Journal of Manufacturing Science and Engineering*, 2020, vol. 143, no. 3, pp. 1–26. DOI: 10.1115/1.4048441.
14. Yang W.R., Wang C.S. Current Measurement of Resistance Spot Welding Using DSP. *Tamkang Journal of Science and Engineering*, 2011, vol. 14, no. 1, pp. 33–38.
15. Matsushita M., Ikeda R., Oi K. Development of a new program control setting of welding current and electrode force for single-side resistance spot welding. *Welding in the World*, 2015, vol. 59, pp. 533–543. DOI: 10.1007/s40194-015-0228-1.
16. Klimov A.S., Kudinov A.K., Komirenko A.V., Antsiborov A.N. A method for measuring current in resistance welding. *Welding International*, 2013, vol. 27, pp. 830–833. DOI: 10.1080/09507116.2013.796636.
17. Klimov A.S., Antsiborov A.N., Klimov V.S., Kudinov A.K. Current regulation in contact welding. *Russian Engineering Research*, 2019, vol. 39, pp. 766–771. DOI: 10.3103/S1068798X19090119.
18. Zhou M., Zhang H., Hu S.J. Relationships between Quality and Attributes of Spot Welds. *Welding Journal*, 2003, vol. 82, no. 4, pp. 72S–77S.
19. Martin O., De Tiedra P. Advances in the Control and Improvement of Quality in the Resistance Spot Welding Process. *Metals*, 2022, vol. 12, no. 11, article number 1810. DOI: 10.3390/met12111810.
20. Ziyad K., Manohar D. Adaptive control of resistance spot welding based on a dynamic resistance model. *Mathematical and Computation Applications*, 2019, vol. 24, no. 4, article number 86. DOI: 10.3390/mca24040086.

СПИСОК ЛИТЕРАТУРЫ

1. Ertas A.H., Akbulut M. Experimental Study on Fatigue Performance of Resistance Spot-Welded Sheet Metals // The International Journal of Advanced Manufacturing Technology. 2021. Vol. 114. P. 1205–1218. DOI: 10.1007/s00170-021-06822-z.
2. Kang M., Choi W.H., Kim C. Statistical Analysis of Korean Welding Industry // Journal of Welding and Joining. 2023. Vol. 41. № 2. P. 107–111. DOI: 10.5781/JWJ.2023.41.2.4.
3. Ощепков Ф.Н. Современный рынок сварочного оборудования: проблемы и перспективы // Сварка и диагностика. 2013. № 5. С. 62–63. EDN: RDYYHT.
4. Лукин М.А. Научно-технический уровень сварочного производства в современной России // Сварочное производство. 2015. № 12. С. 31–36. EDN: VKSMWL.
5. Zhou B., Pychynski T., Reischl M., Kharlamov E. Machine Learning with Domain Knowledge for Predictive Quality Monitoring in Resistance Spot Welding // Journal of Intelligent Manufacturing. 2022. Vol. 33. № 4. P. 1139–1163. DOI: 10.1007/s10845-021-01892-y.
6. Cho Y., Rhee S. Experimental study of nugget formation in resistance spot welding // Welding Journal. 2003. Vol. 82. № 8. P. 195–201.
7. Гладков Э.А., Климов А.С., Анциборов А.Н. Опыт применения регуляторов контактной сварки в массовом производстве // Сварка и диагностика. 2021. № 1. С. 47–53. DOI: 10.52177/2071-5234_2021_01_47.
8. Wei D., Li D., Tang D., Jiang Q. Deep Learning Assisted Vision Inspection of Resistance Spot Welds // Journal of Manufacturing Processes. 2021. Vol. 62. № 8. P. 262–274. DOI: 10.1016/j.jmapro.2020.12.015.
9. Klimov A.S., Kudinov A.K., Klimov V.S. Influence of Grid Parameters on Control and Diagnostics in Resistance Spot Welding // Russian Engineering Research. 2021. № 9. P. 813–819. DOI: 10.3103/S1068798X2109015X.
10. Dong J., Hu J., Luo Z. Quality Monitoring of Resistance Spot Welding Based on a Digital Twin // Metals. 2023. Vol. 13. № 4. Article number 697. DOI: 10.3390/met13040697.
11. Martin O., Ahedo V., Santos J.I., Galan J.M. Comparative Study of Classification Algorithms for Quality Assessment of Resistance Spot Welding Joints From Pre- and Post-Welding Inputs // IEEE Access. 2022. № 10. P. 6518–6527. DOI: 10.21203/rs.3.rs-645372/v2.
12. Zhao D., Wang Y., Zhang P., Liang D. Modeling and Experimental Research on Resistance Spot Welded Joints for Dual-Phase Steel // Materials. 2019. Vol. 12. № 7. Article number 1108. DOI: 10.3390/ma12071108.
13. Xia Y.J., Shen Y., Zhou L., Li Y.B. Expulsion intensity monitoring and modeling in resistance spot welding based on electrode displacement signals // Journal of Manufacturing Science and Engineering. 2020. Vol. 143. № 3. P. 1–26. DOI: 10.1115/1.4048441.
14. Yang W.R., Wang C.S. Current Measurement of Resistance Spot Welding Using DSP // Tamkang Journal of Science and Engineering. 2011. Vol. 14. № 1. P. 33–38.
15. Matsushita M., Ikeda R., Oi K. Development of a new program control setting of welding current and electrode force for single-side resistance spot welding // Welding in the World. 2015. Vol. 59. P. 533–543. DOI: 10.1007/s40194-015-0228-1.
16. Klimov A.S., Kudinov A.K., Komirenko A.V., Antsiborov A.N. A method for measuring current in resistance welding // Welding International. 2013. Vol. 27. P. 830–833. DOI: 10.1080/09507116.2013.796636.
17. Klimov A.S., Antsiborov A.N., Klimov V.S., Kudinov A.K. Current regulation in contact welding // Russian Engineering Research. 2019. Vol. 39. P. 766–771. DOI: 10.3103/S1068798X19090119.
18. Zhou M., Zhang H., Hu S.J. Relationships between Quality and Attributes of Spot Welds // Welding Journal. 2003. Vol. 82. № 4. P. 72S–77S.
19. Martin O., De Tiedra P. Advances in the Control and Improvement of Quality in the Resistance Spot Welding Process // Metals. 2022. Vol. 12. № 11. Article number 1810. DOI: 10.3390/met12111810.
20. Ziyad K., Manohar D. Adaptive control of resistance spot welding based on a dynamic resistance model // Mathematical and Computation Applications. 2019. Vol. 24. № 4. Article number 86. DOI: 10.3390/mca24040086.

Влияние параметров питающей сети на стабильность фазового регулирования при контактной сварке

© 2023

Климов Алексей Сергеевич*[1], кандидат технических наук,
доцент кафедры «Сварка, обработка материалов давлением и родственные процессы»
Кудинов Андрей Константинович[2], старший преподаватель кафедры «Промышленная электроника»
Климов Виталий Сергеевич[3], кандидат технических наук,
доцент кафедры «Прикладная математика и информатика»
Ельцов Валерий Валентинович, доктор технических наук,
профессор кафедры «Сварка, обработка материалов давлением и родственные процессы»
Болдырев Денис Алексеевич[4], доктор технических наук,
профессор кафедры «Нанотехнологии, материаловедение и механика»
Тольяттинский государственный университет, Тольятти (Россия)

***E-mail: KlimovTGU@yandex.ru,**
klimov@tltsu.ru

[1]ORCID: https://orcid.org/0009-0003-8679-0882
[2]ORCID: https://orcid.org/0009-0003-3026-2554
[3]ORCID: https://orcid.org/0000-0002-1467-3543
[4]ORCID: https://orcid.org/0000-0002-6951-5825

Поступила в редакцию 30.05.2023 *Принята к публикации 09.06.2023*

Аннотация: Контактная сварка в условиях массового производства выполняется при значительном количестве возмущений, совокупное действие которых может превышать возможности современной аппаратуры управления. Большинство систем управления контактной сваркой, применяемых в промышленности для компенсации действующих возмущений, предусматривает фазовое регулирование сварочного тока в зависимости от измеренных параметров, характеризующих процесс формирования сварного соединения. Эффективность работы таких регуляторов в значительной мере определяется точностью измерения и задания параметров фазового регулирования, к которым относят углы открытия и проводимости сварочных тиристоров. В работе показано, что при включении контактной машины происходит фазовый сдвиг напряжения сети в режиме нагрузки относительно напряжения сети в режиме холостого хода. С использованием упрощенной электрической схемы замещения контактной сварочной машины в работе описана природа фазового сдвига напряжения сети. В качестве паразитных параметров сети выделены активное сопротивление и индуктивность сети. Моделирование электрических процессов в контактной машине выполнено согласно трехконтурной схеме замещения. Показано влияние паразитных параметров сети на стабильность фазового регулирования, особенности получаемых осциллограмм тока и напряжения. В зависимости от параметров сети и контактной сварочной машины, величина фазового сдвига составляет от долей до единиц электрического градуса. При параметрической стабилизации сварочного тока по напряжению сети влиянием паразитных параметров сети можно пренебречь. При работе регулятора в режиме поддержания численного значения вторичного тока наблюдается уменьшение создаваемого тока относительно заданного. Предложена и апробирована методика определения паразитных параметров питающей сети по результатам опыта короткого замыкания.

Ключевые слова: параметры питающей сети; фазовое регулирование при контактной сварке; контактная сварка; управление контактной сваркой в условиях возмущений; диагностика контактной сварки; моделирование электрических процессов; фазовое управление; измерение и регулирование сварочного тока.

Для цитирования: Климов А.С., Кудинов А.К., Климов В.С., Ельцов В.В., Болдырев Д.А. Влияние параметров питающей сети на стабильность фазового регулирования при контактной сварке // Frontier Materials & Technologies. 2023. № 3. С. 53–60. DOI: 10.18323/2782-4039-2023-3-65-5.

doi: 10.18323/2782-4039-2023-3-65-6

Formation of a bimetallic Ti–Al material by a wire-feed electron-beam additive manufacturing

© 2023

Andrey V. Luchin*[1], postgraduate student,
research engineer of "Physics of Hierarchical Structures of Metals and Alloys" Laboratory
Elena G. Astafurova[2], Doctor of Sciences (Physics and Mathematics), Associate Professor,
chief researcher of "Physics of Hierarchical Structures of Metals and Alloys" Laboratory
Sergey V. Astafurov[3], PhD (Physics and Mathematics),
senior researcher of "Physics of Hierarchical Structures of Metals and Alloys" Laboratory
Kseniya A. Reunova[4], postgraduate student,
junior researcher of "Physics of Hierarchical Structures of Metals and Alloys" Laboratory
Elena A. Zagibalova[5], student, engineer of "Physics of Hierarchical Structures of Metals and Alloys" Laboratory
Eugeny A. Kolubaev[6], Doctor of Sciences (Engineering), Professor, Director
Institute of Strength Physics and Materials Science of Siberian Branch of Russian Academy of Sciences, Tomsk (Russia)

***E-mail: luchin250398@yandex.ru**

[1]ORCID: https://orcid.org/0000-0003-4020-0755
[2]ORCID: https://orcid.org/0000-0002-1995-4205
[3]ORCID: https://orcid.org/0000-0003-3532-3777
[4]ORCID: https://orcid.org/0000-0002-1318-1010
[5]ORCID: https://orcid.org/0000-0002-2079-7198
[6]ORCID: https://orcid.org/0000-0001-7288-3656

Received 20.06.2023 *Accepted 21.08.2023*

Abstract: Currently, there is a request from aerospace and aircraft for the construction materials with sufficiently high mechanical strength, thermal creep, corrosion and oxidation resistance. The conventional alloys used for these purposes are too heavy. At the same time, alternative light materials such as Ti–Al-based alloys have many flaws, when they are produced by conventional methods. This work considers the possibility to produce the Ti–Al-based alloys by the method of a wire-feed electron-beam additive manufacturing (EBAM). We study the chemical and phase compositions, microstructure and microhardness of a bimetallic Ti–Al alloy, obtained by this method. It is found the formation of five characteristic regions between titanium and aluminum parts of the bimetallic billet. The mixing zone consists of TiAl and $TiAl_3$ intermetallics, that is confirmed by the investigation of microstructure, chemical and phase compositions. According to XRD (X-ray diffraction) and EDS (energy-dispersive X-ray spectroscopy) analyses, it can be assumed that TiAl intermetallic prevails over $TiAl_3$ one. The average microhardness of the mixing zone equals to 450 HV (≈4.4 GPa). This zone has developed dendritic microstructure, and even distribution of the phases without link to dendritic and inter-dendritic zones. The cracks appearing in this area are filled with the material of the upper layers, so the whole material is poreless and defect-free. Thus, the results of this work have shown a fundamental possibility to produce the intermetallic Ti–Al alloys with the use of the EBAM.

Keywords: electron beam additive manufacturing; titanium aluminide; Ti–Al; $TiAl_3$; titanium; aluminum; intermetallics; microstructure; microhardness.

Acknowledgements: The work was supported by the Government research assignment for Institute of Strength Physics and Materials Science SB RAS, project No. FWRW-2022-0005.

The equipment of the "Nanotech" center of the Institute of Strength Physics and Materials Science SB RAS was utilized.

The authors thank V. Rubtsov and S. Nikonov for their assistance with the additive manufacturing of the material.

The paper was written on the reports of the participants of the XI International School of Physical Materials Science (SPM-2023), Togliatti, September 11–15, 2023.

For citation: Luchin A.V., Astafurova E.G., Astafurov S.V., Reunova K.A., Zagibalova E.A., Kolubaev E.A. Formation of a bimetallic Ti–Al material by a wire-feed electron-beam additive manufacturing. *Frontier Materials & Technologies*, 2023, no. 3, pp. 61–70. DOI: 10.18323/2782-4039-2023-3-65-6.

INTRODUCTION

Conventional alloys used for aerospace and turbine engines are superalloys based on Ni, Co, or Fe. They provide sufficient mechanical strength, high thermal creep, corrosion and oxidation resistance [1]. All of these groups of alloys have a quite high value of density, that influences the efficiency in terms of sensible lifting force usage, fuel waste and CO_2 emission as a result [2]. Hence, there is an obvious question about the possibility of obtaining such alternative alloys that would be light enough and have all the aforementioned properties.

Low density (≈3.8 g/cm^3), good resistance to high temperature creep, and oxidation are essential properties of Ti–Al-based alloys, which take note attention of the aerospace, aircraft and automotive industries. These alloys have a significantly higher specific yield strength compared to conventional alloys such as Ti and Ni-based alloys, especially in the temperature range of 600–1000 °C [3]. In addition, TiAl intermetallic has a slight advantage in cost and density

compared to Ti-alloys, which average density is ≈4.5 g/cm^3 [1]. The intermetallic can also compete in value of density, strength and possible exploiting temperatures with traditional Al-based alloys applied in aircraft industry [4]. The main disadvantage of TiAl intermetallic constraining it from widespread usage was low plasticity (less 2 %) at room temperature [5]. Although there were approaches to improve plasticity by severe plastic deformation and thermal treatment, which included: strengthening by nanotwins or precipitates, formation of nanograin gradient structure or a bimodal microstructure [6]. The use of these mechanisms allows to achieve strain to failure of ≈14 % in TiAl intermetallics. Moreover, understanding of phase transformations, and use of thermal treatment enabled the start of application of Ti–Al-based alloys in automobile and aircraft industries [7; 8].

Conventional fabrication and processing of Ti–Al-based alloys have a range of difficulties. The most cost-effective way of fabrication is casting, but this method delivers the coarse-grained lamellar samples with high anisotropy and well-known flaws [9–11]. There is a study where authors overcame the disadvantages of casting by selection of temperatures, cooling rates and crucible materials. They succeed in obtaining a homogeneous structure without macroscopic defects, although some protrusions on the surface have been detected, and there was a need for post processing [12]. Obviously, such quality of products is unacceptable for aircraft and aerospace applications.

Other conventional methods such as powder metallurgy, and wrought processing (rolling, forging, extrusion) have many drawbacks. Their common disadvantage is the large working cycle of machining to obtain the required accuracy and shape of the parts. The additional machining also leads to the need for heat treatments and waste of material. Powder metallurgy is always related to high porosity, oxygen impurities, low plasticity, and additional processing requirement [13].

Currently, researchers try to find the best production way of the intermetallic in the field of additive manufacturing (AM) methods. The main advantages of AM technologies are cost-effectiveness (there is no need for additional machining with waste material), high dimensional accuracy and variability of the shape of the parts. These methods can be divided into three main groups in terms of a feedstock usage: a wire-feed AM, a powder-feed AM, and a powder bed fusion AM [13–15]. The first two allow obtaining parts in the wide size range with high building rates, when the third is not suitable for large parts but has good dimensional accuracy, and lower surface roughness. The last method has an important disadvantage, regardless of which heat source is used (laser or electron beam). The problem is the high temperature gradient, and the cooling rate of the material in the process. This leads to an inhomogeneous structure with a lot of cracks [13–15]. Although some researchers suggest numerical thermokinetic models of a layer growth that allow to optimize the process of powder melting. It is shown that the scanning mode, in particular the electron beam scanning step, most of all affects the quality of the surface layer [16].

The choice of electron beam as a source of energy is optimal in terms of price, stability and control of the AM process in comparison with laser beam and arc. The performance executing in a vacuum, that is necessary during the working of titanium, delivers a high purity of a resulting product [17; 18].

The use of wires as a feedstock allows to minimise the quantity of impurities and pores, and avoid the structural inhomogeneity as a result. This approach also has a bigger potential in terms of its use in industry, because of the assortment, availability and quality of wires are significantly greater than those for powders [19; 20].

The work is aimed to consider the possibility to produce Ti–Al-based alloys by the method of a wire-feed electron-beam additive manufacturing. We study the chemical and phase compositions, microstructure and microhardness of the additively obtained bimetallic material, with the focus on the transition zone between the Ti- and Al-based parts.

METHODS

The bimetallic billet presented in Fig. 1 a was fabricated by the method of a wire-feed electron beam additive manufacturing. The installation for electron-beam additive manufacturing (EBAM) consisted of a vacuum chamber, a wire feeder, an electron beam source and a movable three-axis table. It was engineered in the Institute of Strength Physics and Materials Science (Siberian Branch of the Russian Academy of Sciences). The feedstock was presented by two kinds of wires. The materials of wires were titanium (Grade 2; Ti–0.25Fe–0.2H–0.2O–0.1Si–0.07C–N0.04) and aluminium (EN ISO 18273; 99.8Al–0.13Fe–0.01Cu–0.01Mn–0.02Si–0.01V). A diameter of wires was 1.2 mm for both materials. The billet moved and melted under an electron beam along a substrate made of a mild steel. The chemical composition of the steel was Fe–1.9Mn–0.8Si–0.08C wt. %. The change of Z-coordinate and rotation by 180° occurred for each next layer. The first 14 applied layers were made of titanium wire, and then the material changed and to 14 layers of aluminium were deposited. An approximate height of each layer in the resultant billet was about 0.5 mm. During the process, a beam current was changing from 55 to 33 mA for titanium layers, and from 13 to 16 mA for aluminium ones. A scanning frequency and a wire feed rate were 100 Hz and 5.8 mm/s respectively. The process of EBAM was carried out in a vacuum chamber at a pressure of 10^{-3} Pa. The studied sample with dimensions of 13×7×1 mm in size shown in Fig. 1 b was cut off a billet by electrical discharge machining.

The sample was mechanically ground and polished. The solution consisted of hydrofluoric acid, nitric acid, and water in the proportion of 25:7:3 was used for etching of the sample. Microstructure and surface morphology of the sample were studied on Apreo 2 SEM scanning electron microscope (SEM, Thermo Fisher Scientific, Czech Republic) in back-scattered electrons (BSE) mode. LEO EVO 50 SEM (Zeiss, Germany) with an energy dispersive spectroscopy (EDS) device was used for elemental composition analysis. The definition of phase composition of the specimens was performed by X-ray diffraction on DRON 7 diffractometer (Bourevestnik, Saint Petersburg, Russia) with Co-Kα radiation. XRD analysis was performed for the section cut in parallel to the substrate in the intermediate between Ti and Al regions highlighted with a dashed line in Fig. 2. AFFRI DM8 microhardness tester (Affri, Italy) was applied for rough assessment of mechanical properties. The load on the Vickers indenter was 100 g, and a load time of 10 s was used.

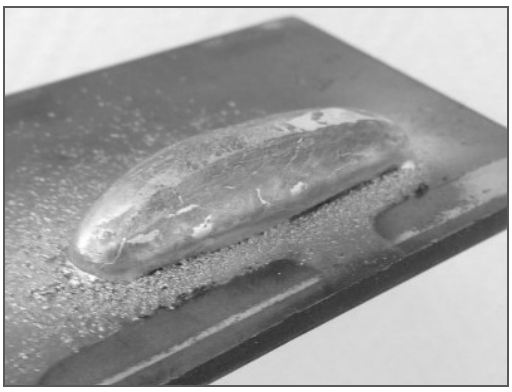

a

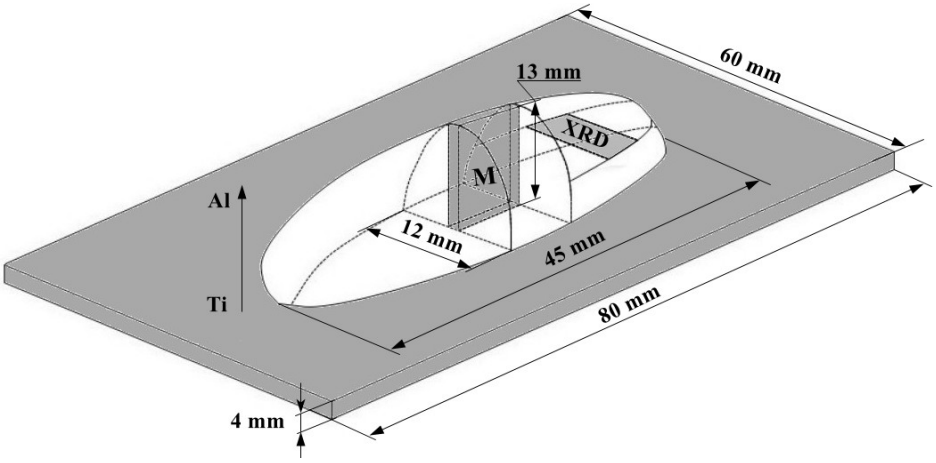

b

Fig. 1. *EBAM-fabricated Ti–Al alloy billet (**a**)*
*and extracted sections for study of the microstructure (M) and phase composition (PCA) (**b**)*
Рис. 1. *Заготовка сплава Ti–Al, полученная методом ЭЛАП (**a**),*
*и сечения, выбранные для исследования микроструктуры (M) и фазового состава (PCA) (**b**)*

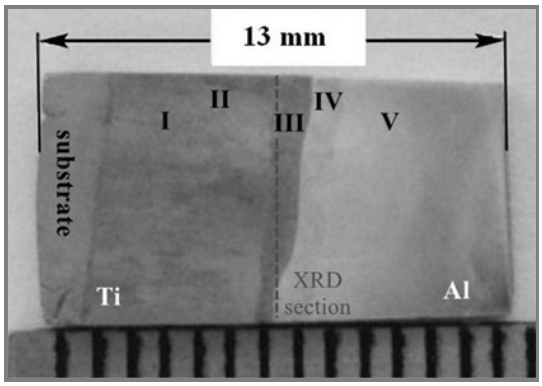

Fig. 2. *The common view of the studied sample extracted from the EBAM-fabricated bimetallic billet as shown in Fig. 1 b.*
Numbers I, II, III, IV, V show characteristic zones revealed by etching of the sample.
I – the zone of the titanium layer near the substrate material where their mixing is realized;
II – the part of the titanium layer located next to the mixing zone of titanium and aluminum;
III – the mixing zone of the Ti and Al components in the melting pool;
IV – the intermediate layer between the mixing zone and the region of pure aluminum; V – the layers of pure aluminum
Рис. 2. *Общий вид исследуемого образца, извлеченного из биметаллической заготовки, полученной методом ЭЛАП*
и показанной на рис. 1 b. Цифры I, II, III, IV, V обозначают характерные зоны, выявленные травлением образца.
I – зона слоя титана вблизи материала подложки, где осуществляется их смешивание;
II – часть титанового слоя, расположенная рядом с зоной смешивания титана и алюминия;
III – зона смешивания компонентов Ti и Al в плавильной ванне;
IV – промежуточный слой между зоной смешивания и областью чистого алюминия; V – слои чистого алюминия

RESULTS

Fig. 2 presents the metallographic image of the studied sample extracted from the EBAM-fabricated bimetallic billet**.** The difference of tones from dark-grey of Ti to light-grey of Al is seen after etching of the sample. Area I is defined as the zone of the titanium layer near the substrate material where their mixing is realised. Area II is the part of the titanium layer located next to the mixing zone of titanium and aluminium. The mixing zone marked as area III corresponds to the mixture of the Ti and Al components in the melting pool. Area IV was defined as the intermediate layer between the mixing zone and the region of pure aluminium. The last region is presented by the layers of pure aluminium and corresponds to area V.

Areas V and I are the furthest regions from the mixing zone, and their compositions correspond to the wire materials made of pure aluminium and titanium, respectively. Since the mixing zone and the nearest regions are the main area of interest, the elemental composition analysis for areas V and I was not performed. According to EDS data, the elemental composition of area VI is presented by aluminium, titanium is almost absent (<1 %) (Table 1). Area III contains high values of Al (≈52 %) and Ti (≈44 %). According to TiAl phase diagram such ratio of components can match γ-TiAl phase. SEM-image of microstructure shows that there are cracks filled with aluminium layers in the mixing zone (Fig. 3 a). It is noticeable that area III has developed dendritic microstructure (Fig. 3 b). The absence of a composition contrast in BSE mode of SEM-imaging shows the even distribution of the phases without link to dendritic and inter-dendritic zones. Thus, area III is more attractive and takes attention in terms of finding Ti–Al compositions. Because of that, the further research is focused on this area. Area II contains the significant volume of titanium (≈90–92 %) and iron (≈7–9 %), but aluminium is almost absent (<1 %).

According to XRD pattern of EBAM-fabricated sample in area III, the phase composition is presented by TiAl and $TiAl_3$ phases (Fig. 4). The small peak corresponded to 41.5° (111) can be explained only by the presence of insignificant quantity of α-Ti phase. The intensity of the peaks, especially the first two most intensive peaks of 45.0° (111) and 52.4° (002), shows that TiAl intermetallic noticeably prevails over $TiAl_3$. In addition, we can not deny the presence of aluminium since it has common peaks with TiAl intermetallic phase.

Since the interfaces between the areas II, III, and IV are not flat, the Ti and Al layers adjacent to area III are in the field of X-ray analysis. Due to this, the α-Ti phase stabilised by aluminium from the upper regions of area IV appears in area III. At the same time, stabilization of the β-Ti phase is observed in area II due to the presence of iron diffusing from the substrate (Fig. 5, Table 1).

Microhardness of EBAM-fabricated bimetallic Ti–Al alloy sample varies throughout the whole billet. This means the significant difference of strength properties of all its areas (Fig. 6).

The microhardness of areas I and II is ≈530 HV (≈5.2 GPa) and ≈390 HV (≈3.8 GPa), respectively. The average value of microhardness for area III is 450 HV (≈4.4 GPa). There is a region related to area IV with deviation from the μH value of pure aluminium where the microhardness is about 70 HV. The value of aluminium layer corresponded to area V equals to 30 HV.

DISCUSSION

As it was shown above in Fig. 2, the EBAM method allowed to obtain the bimetallic billet of Ti–Al system. Various regions can be easily distinguished by their grey shades into five characteristic areas, with different chemical and phase compositions. The microhardness testing results also allow to differ them by the noticeable changes of microhardness along the height of the sample.

The first deposited layers, related to areas I and II, are supposed to the initial phase composition of Grade 2 titanium wire presented by α-Ti phase. But the microhardness values of these areas are significantly higher than usual for Grade 2 pure titanium consisted of α-Ti phase (≈1.5 GPa) [21]. It is shown that, according to the results of XRD analysis, area II is presumably presented by β-Ti solution (Fig. 5). The formation of β-Ti phase in pure titanium is possible, when the temperature of heat treatment achieves the point of phase transformation equal to ≈590 °C, with following quenching [22]. The temperature of melting pool achieved by the EBAM process is significantly higher than 590 °C, but the cooling rate is quite low [23]. This means that the phase composition will be presented by the α-Ti phase as a result. Although, the presence of iron in these areas confirmed by the EDS data is high, and sufficient for preventing of the α-Ti-phase formation, since iron is a strong stabilizer of the β-phase [24]. The increase of microhardness values occurring from area II to area I in the direction of the substrate should be related to the change of chemical and phase composition [25]. According to phase diagram of the Fe–Ti system this can be a result of FeTi-intermetallic appearance [22]. An increase in the concentration of iron, in the direction of the substrate, contributes to an increase in the volume of the intermetallic phase, and hence the strength characteristics.

The EDS data of area III, shows a small deviation from equiatomic ratio between aluminium and titanium components to the side of the former (Table 1). The XRD analysis confirms that obtained alloy in this area is presented by TiAl and $TiAl_3$ intermetallics, Al, and α-Ti phases (Fig. 4). Presumably the presence of aluminium in area III, provides the small appearance of α-Ti phase, since the former contributes stabilisation of α-Ti phase [24]. Moreover, the pure Al can be detected in this area because of filling the cracks with the aluminium (Fig. 3 a). When the layers in the area III solidified, the material of the upper aluminium layer of area IV filled these cracks. Thus, there is the process of the "healing" of these cracks which appear in area III while the following deposition. Due to this, there are no voids or cracks in the mixing zone. It is also obvious that a quantity of the aluminium phase in this area should not be large. This follows from the fact that, according to EDS data, the quantity of titanium is large, and cannot be presented only by the trace amount of α-Ti phase. The average value of microhardness in area III is 450 HV (≈4.4 GPa) and corresponds to the possible range from 3 GPa to 5 GPa for TiAl-based intermetallics (Fig. 6) [26]. This range is quite wide, because the microhardness depends on the microstructure,

Table 1. *EDS data for areas II, III, IV of the EBAM-fabricated Ti–Al alloy sample*
Таблица 1. *Результаты ЭДС для областей II, III, IV сплава Ti–Al, полученного методом ЭЛАП*

Area	Spectrum	Al	Ti	Fe
		Atomic %		
IV	1	99.87	0.11	0.02
	2	99.99	0.01	0.00
	3	99.80	0.11	0.09
III	4	52.55	42.83	4.62
	5	57.07	40.96	1.97
	6	58.15	38.85	3.00
II	7	0.06	90.70	9.24
	8	0.89	91.40	7.71
	9	0.24	92.45	7.31

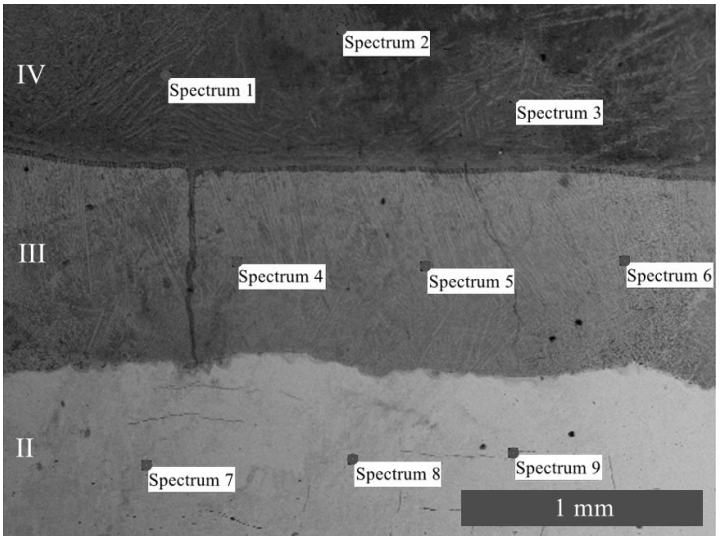

a

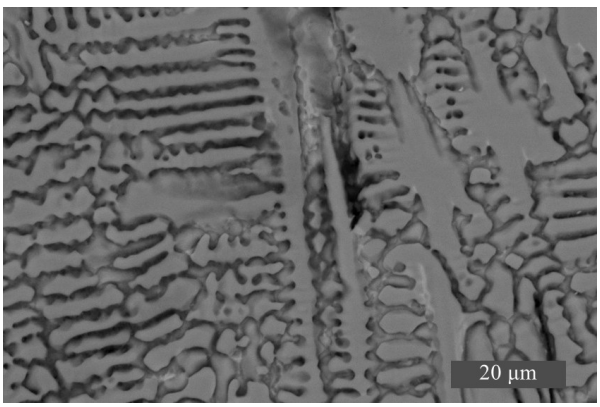

b

Fig. 3. *SEM-image of microstructure and EDS points for areas II, III, IV (**a**) and BSE mode SEM-image of area III (**b**) of the EBAM-fabricated Ti–Al alloy sample*
Рис. 3. *СЭМ-изображение микроструктуры и точек ЭДС для областей II, III, IV (**а**) и СЭМ-изображение в режиме ОРЭ области III сплава Ti–Al, полученного методом ЭЛАП (**b**)*

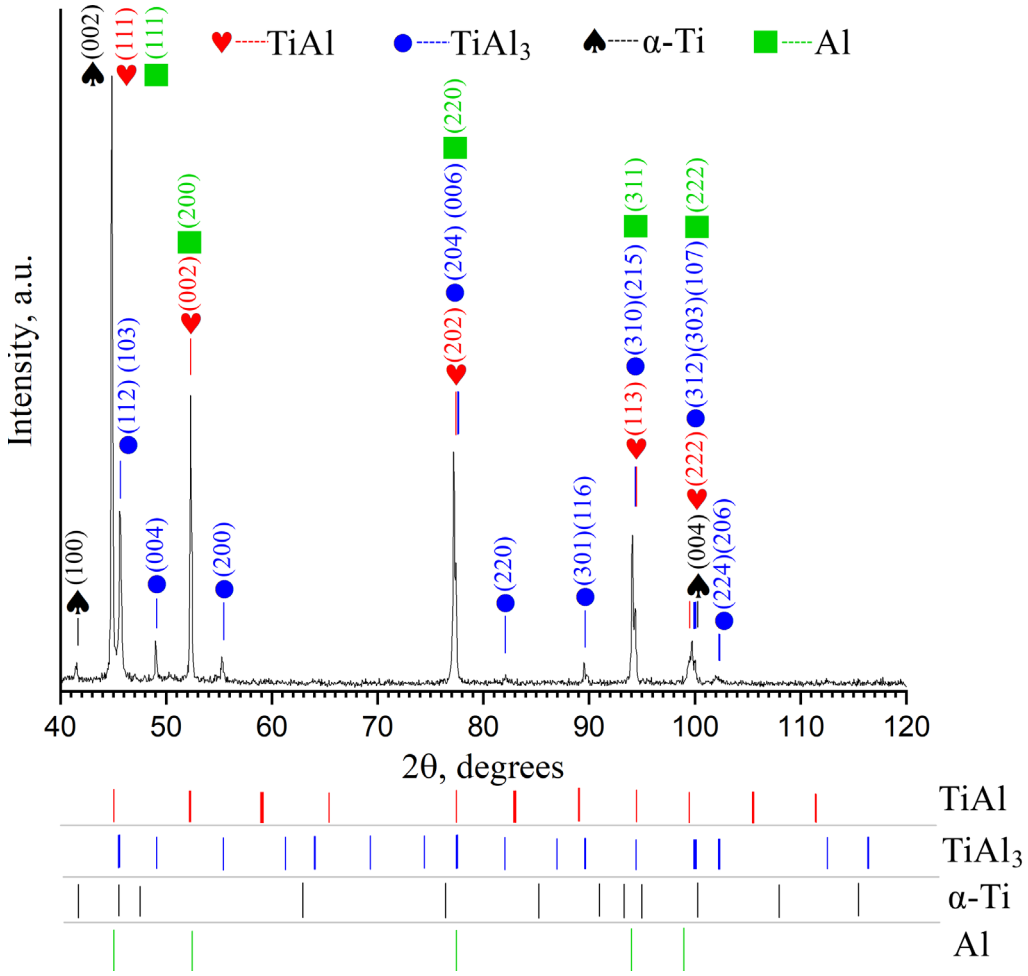

Fig. 4. *XRD pattern of EBAM-fabricated bimetallic Ti–Al alloy sample in area III*
Рис. 4. *РДА-дифрактограмма области III образца биметаллического Ti–Al сплава, полученного методом ЭЛАП*

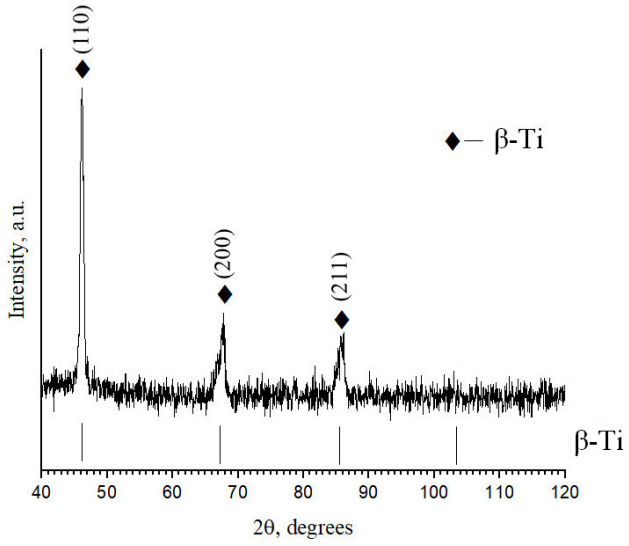

Fig. 5. *XRD pattern of EBAM-fabricated sample in area II*
Рис. 5. *РДА-дифрактограмма области II образца, полученного методом ЭЛАП*

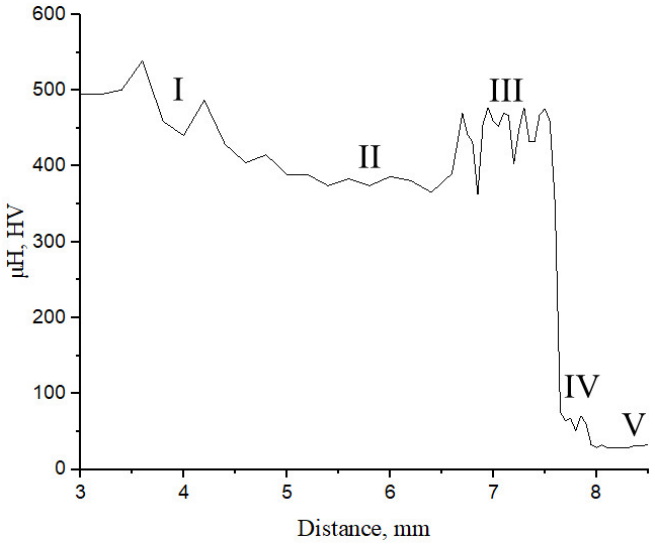

Fig. 6. *Microhardness vs the distance from the substrate of EBAM-fabricated sample*
Рис. 6. *Зависимость микротвердости от расстояния от подложки образца, полученного методом ЭЛАП*

exact phase composition stoichiometry and elemental composition. Moreover, it is extremely difficult to obtain homogenous single phase intermetallic. Thus, the phase composition of this area is commonly presented by the mixture of TiAl and $TiAl_3$ intermetallics, and the former one prevails over the latter.

Area IV was defined as the intermediate layer between the mixing zone and the region of pure aluminium marked as area V. According to EDS data, the elemental composition of area IV is presented by aluminium, titanium is almost absent (<1 %) (Table 1). As it was aforementioned, the microhardness of area IV is higher than typical for pure aluminium (Fig. 6). This can be related to the formation of a small transition zone between area III and pure aluminium layer of area V. Possibly, this zone is the mechanical mixture of pure aluminium and $TiAl_3$ intermetallic and the Al-based solid solution Al (Ti). Although the zone is quite small and, apparently, does not correspond to the EDS data presented for area IV. Thus, this zone requires more precise study of the chemical and phase composition. Since the microhardness of area V equals to that of pure aluminium, it can be suggested that area V has the same chemical composition [27].

CONCLUSIONS

The possibility to produce Ti–Al-based alloys by the method of a wire-feed electron-beam additive manufacturing is presented in this study. The chemical and phase compositions, microstructure and microhardness of the additively obtained bimetallic material Ti–Al system, with the focus on the transition zone between the Ti- and Al-based parts are carried out.

The method allows us to obtain Ti–Al-based alloy presented by the mixture of TiAl, $TiAl_3$ intermetallics and an insignificant amount of pure aluminium and titanium phases. The intensity of XRD peaks, the chemical composition ratio, and the value of microhardness show that TiAl intermetallic noticeably prevails over $TiAl_3$. The average microhardness of the mixing zone is 450 HV (≈4.4 GPa). This zone has developed a dendritic microstructure, and even distribution of the phases without link to dendritic and inter-dendritic zones. The cracks appearing in this area are filled with the material of the upper layers. Thus, the whole material of obtained bimetallic material is defect-free. Although the fact of iron presence from the substrate material in the billet layers requires changing and optimising of EBAM mode for obtaining of a high-quality bimetallic billet.

REFERENCES

1. Gialanella S., Malandruccolo A. Chapter 4. Titanium and Titanium Alloys. *Aerospace alloys*. Switzerland, Springer Publ., 2020, pp. 129–189. DOI: 10.1007/978-3-030-24440-8.
2. Rao K.A. Nickel Based Superalloys – Properties and Their Applications. *International Journal of Management, Technology and Engineering*, 2018, vol. 8, no. V, pp. 268–277.
3. Clemens H., Smarsly W., Güther V., Mayer S. Advanced intermetallic titanium aluminides. *Proceedings of the 13th World Conference on Titanium*, 2016, pp. 1189–1200. DOI: 10.1002/9781119296126.ch203.
4. Dwivedi P., Siddiquee A.N., Maheshwari S. Issues and requirements for aluminum alloys used in aircraft components: state of the art. *Russian Journal of Non-Ferrous Metals*, 2021, vol. 62, pp. 212–225. DOI: 10.3103/S1067821221020048.
5. Bewlay B.P., Nag S., Suzuki A., Weimer M.J. TiAl alloys in commercial aircraft engines. *Materials at High Temperatures*, 2016, vol. 33, no. 4-5, pp. 549–559. DOI: 10.1080/09603409.2016.1183068.
6. Edalati K., Toh S., Iwaoka H., Watanabe M., Horita Z., Kashioka D., Kishida K., Inui H. Ultrahigh strength and high plasticity in TiAl intermetallics with bimodal grain

structure and nanotwins. *Scripta Materialia*, 2012, vol. 67, no. 10, pp. 814–817. DOI: 10.1016/j.scriptamat.2012.07.030.
7. Tetsui T. Application of TiAl in a turbocharger for passenger vehicles. *Advanced Engineering Materials*, 2001, vol. 3, no. 5, pp. 307–310. DOI: 10.1002/1527-2648(200105)3:5<307::AID-ADEM307>3.0.CO;2-3.
8. Jarvis D.J., Voss D. IMPRESS Integrated Project – an overview paper. *Materials Science and Engineering: A*, 2005, vol. 413-414, pp. 583–591. DOI: 10.1016/j.msea.2005.09.066.
9. Clemens H., Kestler H. Processing and applications of intermetallic γ-TiAl-based alloys. *Advanced engineering materials*, 2000, vol. 2, no. 9, pp. 551–570. DOI: 10.1002/1527-2648(200009)2:9<551::AID-ADEM551>3.0.CO;2-U.
10. Wu X. Review of alloy and process development of TiAl alloys. *Intermetallics*, 2006, vol. 14, no. 10-11, pp. 1114–1122. DOI: 10.1016/j.intermet.2005.10.019.
11. Cobbinah P.V., Matizamhuka W.R. Solid-state processing route, mechanical behaviour, and oxidation resistance of TiAl alloys. *Advances in Materials Science and Engineering*, 2019, vol. 2019, pp. 1–21. DOI: 10.1155/2019/4251953.
12. Brotzu A., Felli F., Mondal A., Pilone D. Production issues in the manufacturing of TiAl turbine blades by investment casting. *Procedia Structural Integrity*, 2020, vol. 25, pp. 79–87. DOI: 10.1016/j.prostr.2020.04.012.
13. Soliman H.A., Elbestawi M. Titanium aluminides processing by additive manufacturing – a review. *The International Journal of Advanced Manufacturing Technology*, 2022, vol. 119, no. 9-10, pp. 5583–5614. DOI: 10.1007/s00170-022-08728-w.
14. Emiralioğlu A., Ünal R. Additive manufacturing of gamma titanium aluminide alloys: a review. *Journal of Materials Science*, 2022, vol. 57, no. 7, pp. 4441–4466. DOI: 10.1007/s10853-022-06896-4.
15. Dzogbewu T.C. Additive manufacturing of TiAl-based alloys. *Manufacturing Review*, 2020, vol. 7, no. 35, pp. 1–8. DOI: 10.1051/mfreview/2020032.
16. Kryukova O.N., Knyazeva A.G. Thermokinetic. Model of a Layer Growth on a Substrate During Electron-Beam Cladding. *Russian Physics Journal*, 2023, vol. 66, no. 1, pp. 66–73. DOI: 10.1007/s11182-023-02906-3.
17. Löber L., Biamino S., Ackelid U., Sabbadini S., Epicoco P., Fino P., Eckert J. Comparison off selective laser and electron beam melted titanium aluminides. *International Solid Freeform Fabrication Symposium*, 2011. DOI: 10.26153/tsw/15316.
18. Negi S., Nambolan A.A., Kapil S., Joshi P.S., Karunakaran K.P., Bhargava P. Review on electron beam based additive manufacturing. *Rapid Prototyping Journal*, 2020, vol. 26, no. 3, pp. 485–498. DOI: 10.1108/RPJ-07-2019-0182.
19. Özel T., Shokri H., Loizeau R. A Review on Wire-Fed Directed Energy Deposition Based Metal Additive Manufacturing. *Journal of Manufacturing and Materials Processing*, 2023, vol. 7, no. 1, article number 45. DOI: 10.3390/jmmp7010045.
20. Kolubaev E.A., Rubtsov V.E., Chumaevsky A.V., Astafurova E.G. Micro-, Meso-and Macrostructural Design of Bulk Metallic and Polymetallic Materials by Wire-Feed Electron-Beam Additive Manufacturing. *Physical Mesomechanics*, 2022, vol. 25, no. 6, pp. 479–491. DOI: 10.1134/S1029959922060017.
21. Lim H.S., Hwang M.J., Jeong H.N., Lee W.Y., Song H.J., Park Y.J. Evaluation of surface mechanical properties and grindability of binary Ti alloys containing 5 wt % Al, Cr, Sn, and V. *Metals*, 2017, vol. 7, no. 11, article number 487. DOI: 10.3390/met7110487.
22. Kriegel M.J., Wetzel M.H., Treichel A., Fabrichnaya O., Rafaja D. Binary Ti–Fe system. Part I: Experimental investigation at high pressure. *Calphad*, 2021, vol. 74, article number 102322. DOI: 10.1016/j.calphad.2021.102322.
23. Osipovich K., Kalashnikov K., Chumaevskii A. et al. Wire-Feed Electron Beam Additive Manufacturing: A Review. *Metals*, 2023, vol. 13, no. 2, article number 279. DOI: 10.3390/ma15030814.
24. Bieler T.R., Trevino R.M., Zeng L. Alloys: titanium. *Encyclopedia of Condensed Matter Physics*, 2005, pp. 65–76. DOI: 10.1016/B0-12-369401-9/00536-2.
25. Sujan G.K., Wu B., Pan Z., Li H. In-Situ Fabrication of Titanium Iron Intermetallic Compound by the Wire Arc Additive Manufacturing Process. *Metallurgical and Materials Transactions A*, 2020, vol. 51, pp. 552–557. DOI: 10.1007/s11661-019-05555-9.
26. Chen X.Y., Fang H.Z., Wang Q., Zhang S.Y., Chen R.R., Su Y.Q. Microstructure and microhardness of Ti–48Al alloy prepared by rapid solidification. *China Foundry*, 2020, vol. 17, pp. 429–434. DOI: 10.1007/s41230-020-0090-7.
27. Alshabatat N., Al-qawabah S. Effect of 4 % wt. Cu Addition on the Mechanical Characteristics and Fatigue Life of Commercially Pure Aluminum. *Jordan Journal of Mechanical & Industrial Engineering*, 2015, vol. 9, no. 4, pp. 297–301.

СПИСОК ЛИТЕРАТУРЫ

1. Gialanella S., Malandruccolo A. Chapter 4. Titanium and Titanium Alloys // Aerospace alloys. Switzerland: Springer, 2020. P. 129–189. DOI: 10.1007/978-3-030-24440-8.
2. Rao K.A. Nickel Based Superalloys – Properties and Their Applications // International Journal of Management, Technology and Engineering. 2018. Vol. 8. № V. P. 268–277.
3. Clemens H., Smarsly W., Güther V., Mayer S. Advanced intermetallic titanium aluminides // Proceedings of the 13th World Conference on Titanium. 2016. P. 1189–1200. DOI: 10.1002/9781119296126.ch203.
4. Dwivedi P., Siddiquee A.N., Maheshwari S. Issues and requirements for aluminum alloys used in aircraft components: state of the art // Russian Journal of Non-Ferrous Metals. 2021. Vol. 62. P. 212–225. DOI: 10.3103/S1067821221020048.
5. Bewlay B.P., Nag S., Suzuki A., Weimer M.J. TiAl alloys in commercial aircraft engines // Materials at High Temperatures. 2016. Vol. 33. № 4-5. P. 549–559. DOI: 10.1080/09603409.2016.1183068.
6. Edalati K., Toh S., Iwaoka H., Watanabe M., Horita Z., Kashioka D., Kishida K., Inui H. Ultrahigh strength and high plasticity in TiAl intermetallics with bimodal grain structure and nanotwins // Scripta Materialia. 2012. Vol. 67. № 10. P. 814–817. DOI: 10.1016/j.scriptamat.2012.07.030.
7. Tetsui T. Application of TiAl in a turbocharger for passenger vehicles // Advanced Engineering Materials.

2001. Vol. 3. № 5. P. 307–310. DOI: 10.1002/1527-2648(200105)3:5<307::AID-ADEM307>3.0.CO;2-3.
8. Jarvis D.J., Voss D. IMPRESS Integrated Project – an overview paper // Materials Science and Engineering: A. 2005. Vol. 413-414. P. 583–591. DOI: 10.1016/j.msea.2005.09.066.
9. Clemens H., Kestler H. Processing and applications of intermetallic γ-TiAl-based alloys // Advanced engineering materials. 2000. Vol. 2. № 9. P. 551–570. DOI: 10.1002/1527-2648(200009)2:9<551::AID-ADEM551>3.0.CO;2-U.
10. Wu X. Review of alloy and process development of TiAl alloys // Intermetallics. 2006. Vol. 14. № 10-11. P. 1114–1122. DOI: 10.1016/j.intermet.2005.10.019.
11. Cobbinah P.V., Matizamhuka W.R. Solid-state processing route, mechanical behaviour, and oxidation resistance of TiAl alloys // Advances in Materials Science and Engineering. 2019. Vol. 2019. P. 1–21. DOI: 10.1155/2019/4251953.
12. Brotzu A., Felli F., Mondal A., Pilone D. Production issues in the manufacturing of TiAl turbine blades by investment casting // Procedia Structural Integrity. 2020. Vol. 25. P. 79–87. DOI: 10.1016/j.prostr.2020.04.012.
13. Soliman H.A., Elbestawi M. Titanium aluminides processing by additive manufacturing – a review // The International Journal of Advanced Manufacturing Technology. 2022. Vol. 119. № 9-10. P. 5583–5614. DOI: 10.1007/s00170-022-08728-w.
14. Emiralioğlu A., Ünal R. Additive manufacturing of gamma titanium aluminide alloys: a review // Journal of Materials Science. 2022. Vol. 57. № 7. P. 4441–4466. DOI: 10.1007/s10853-022-06896-4.
15. Dzogbewu T.C. Additive manufacturing of TiAl-based alloys // Manufacturing Review. 2020. Vol. 7. № 35. P. 1–8. DOI: 10.1051/mfreview/2020032.
16. Kryukova O.N., Knyazeva A.G. Thermokinetic. Model of a Layer Growth on a Substrate During Electron-Beam Cladding // Russian Physics Journal. 2023. Vol. 66. № 1. P. 66–73. DOI: 10.1007/s11182-023-02906-3.
17. Löber L., Biamino S., Ackelid U., Sabbadini S., Epicoco P., Fino P., Eckert J. Comparison off selective laser and electron beam melted titanium aluminides // International Solid Freeform Fabrication Symposium. 2011. DOI: 10.26153/tsw/15316.
18. Negi S., Nambolan A.A., Kapil S., Joshi P.S., Karunakaran K.P., Bhargava P. Review on electron beam based additive manufacturing // Rapid Prototyping Journal. 2020. Vol. 26. № 3. P. 485–498. DOI: 10.1108/RPJ-07-2019-0182.
19. Özel T., Shokri H., Loizeau R. A Review on Wire-Fed Directed Energy Deposition Based Metal Additive Manufacturing // Journal of Manufacturing and Materials Processing. 2023. Vol. 7. № 1. Article number 45. DOI: 10.3390/jmmp7010045.
20. Kolubaev E.A., Rubtsov V.E., Chumaevsky A.V., Astafurova E.G. Micro-, Meso-and Macrostructural Design of Bulk Metallic and Polymetallic Materials by Wire-Feed Electron-Beam Additive Manufacturing // Physical Mesomechanics. 2022. Vol. 25. № 6. P. 479–491. DOI: 10.1134/S1029959922060017.
21. Lim H.S., Hwang M.J., Jeong H.N., Lee W.Y., Song H.J., Park Y.J. Evaluation of surface mechanical properties and grindability of binary Ti alloys containing 5 wt % Al, Cr, Sn, and V // Metals. 2017. Vol. 7. № 11. Article number 487. DOI: 10.3390/met7110487.
22. Kriegel M.J., Wetzel M.H., Treichel A., Fabrichnaya O., Rafaja D. Binary Ti–Fe system. Part I: Experimental investigation at high pressure // Calphad. 2021. Vol. 74. Article number 102322. DOI: 10.1016/j.calphad.2021.102322.
23. Osipovich K., Kalashnikov K., Chumaevskii A. et al. Wire-Feed Electron Beam Additive Manufacturing: A Review // Metals. 2023. Vol. 13. № 2. Article number 279. DOI: 10.3390/ma15030814.
24. Bieler T.R., Trevino R.M., Zeng L. Alloys: titanium // Encyclopedia of Condensed Matter Physics. 2005. P. 65–76. DOI: 10.1016/B0-12-369401-9/00536-2.
25. Sujan G.K., Wu B., Pan Z., Li H. In-Situ Fabrication of Titanium Iron Intermetallic Compound by the Wire Arc Additive Manufacturing Process // Metallurgical and Materials Transactions A. 2020. Vol. 51. P. 552–557. DOI: 10.1007/s11661-019-05555-9.
26. Chen X.Y., Fang H.Z., Wang Q., Zhang S.Y., Chen R.R., Su Y.Q. Microstructure and microhardness of Ti–48Al alloy prepared by rapid solidification // China Foundry. 2020. Vol. 17. P. 429–434. DOI: 10.1007/s41230-020-0090-7.
27. Alshabatat N., Al-qawabah S. Effect of 4 % wt. Cu Addition on the Mechanical Characteristics and Fatigue Life of Commercially Pure Aluminum // Jordan Journal of Mechanical & Industrial Engineering. 2015. Vol. 9. № 4. P. 297–301.

Формирование биметаллического материала Ti–Al методом проволочного электронно-лучевого аддитивного производства

© 2023

Лучин Андрей Владимирович*[1], аспирант,
инженер-исследователь лаборатории физики иерархических структур в металлах и сплавах
Астафурова Елена Геннадьевна[2], доктор физико-математических наук, доцент,
главный научный сотрудник лаборатории физики иерархических структур в металлах и сплавах
Астафуров Сергей Владимирович[3], кандидат физико-математических наук,
старший научный сотрудник лаборатории физики иерархических структур в металлах и сплавах
Реунова Ксения Андреевна[4], аспирант,
младший научный сотрудник лаборатории физики иерархических структур в металлах и сплавах
Загибалова Елена Андреевна[5], студент,
инженер лаборатории физики иерархических структур в металлах и сплавах
Колубаев Евгений Александрович[6], доктор технических наук, профессор, директор
Институт физики прочности и материаловедения Сибирского отделения Российской академии наук, Томск (Россия)

***E-mail: luchin250398@yandex.ru**

[1]ORCID: https://orcid.org/0000-0003-4020-0755
[2]ORCID: https://orcid.org/0000-0002-1995-4205
[3]ORCID: https://orcid.org/0000-0003-3532-3777
[4]ORCID: https://orcid.org/0000-0002-1318-1010
[5]ORCID: https://orcid.org/0000-0002-2079-7198
[6]ORCID: https://orcid.org/0000-0001-7288-3656

Поступила в редакцию 20.06.2023 *Принята к публикации 21.08.2023*

Аннотация: В настоящее время в аэрокосмической промышленности и авиастроении существует запрос на новые конструкционные материалы, обладающие достаточно высокой механической прочностью, тепловой ползучестью, стойкостью к коррозии и окислению. Обычные сплавы, используемые для этих целей, слишком тяжелы. В то же время альтернативные легкие материалы, такие как сплавы на основе Ti–Al, имеют множество недостатков при производстве традиционными методами. В данной работе рассмотрена возможность получения сплавов на основе Ti–Al методом проволочного электронно-лучевого аддитивного производства (ЭЛАП). Изучены химический и фазовый составы, микроструктура и микротвердость биметаллического сплава Ti–Al, полученного данным методом. Обнаружено образование пяти характерных областей между титановой и алюминиевой частями биметаллической заготовки. Зона смешивания состоит из интерметаллидов TiAl и $TiAl_3$, что подтверждается исследованием ее микроструктуры, химического и фазового составов. По результатам рентгеновского дифракционного анализа и энергодисперсионной рентгеновской спектроскопии можно предположить, что объемная доля интерметаллида TiAl в зоне смешивания выше, чем доля фазы $TiAl_3$. Средняя микротвердость зоны смешивания составляет 450 HV (≈4,4 ГПа). В зоне смешивания сформировалась развитая дендритная микроструктура и равномерное распределение фаз без привязки к дендритным и междендритным зонам. Трещины, появляющиеся в этой области, заполняются материалом верхних слоев, поэтому материал беспористый и бездефектный. Это показывает принципиальную возможность получения интерметаллидных сплавов Ti–Al с использованием ЭЛАП.

Ключевые слова: электронно-лучевое аддитивное производство; алюминид титана; Ti–Al; $TiAl_3$; титан; алюминий; интерметаллиды; микроструктура; микротвердость.

Благодарности: Работа выполнена в рамках государственного научного задания Института физики прочности и материаловедения СО РАН, проект № FWRW-2022-0005).

Исследования выполнены с использованием оборудования Центра коллективного пользования «Нанотех» Института физики прочности и материаловедения СО РАН.

Авторы благодарят Рубцова В.Е. и Никонова С.Ю. за помощь при аддитивном производстве материала.

Статья подготовлена по материалам докладов участников XI Международной школы «Физическое материаловедение» (ШФМ-2023), Тольятти, 11–15 сентября 2023 года.

Для цитирования: Лучин А.В., Астафурова Е.Г., Астафуров С.В., Реунова К.А., Загибалова Е.А., Колубаев Е.А. Формирование биметаллического материала Ti–Al методом проволочного электронно-лучевого аддитивного производства // Frontier Materials & Technologies. 2023. № 3. С. 61–70. DOI: 10.18323/2782-4039-2023-3-65-6.

doi: 10.18323/2782-4039-2023-3-65-7

The effect of strain rate on mechanical properties and fracture mode of the AZ31 alloy and commercially pure magnesium pre-exposed in a corrosive medium

© 2023

Evgeny D. Merson*[1], PhD (Physics and Mathematics),
senior researcher of the Research Institute of Advanced Technologies
Vitaly A. Poluyanov[2], PhD (Engineering),
junior researcher of the Research Institute of Advanced Technologies
Pavel N. Myagkikh[3], junior researcher of the Research Institute of Advanced Technologies
Dmitry L. Merson[4], Doctor of Sciences (Physics and Mathematics), Professor,
Director of the Research Institute of Advanced Technologies
Togliatti State University, Togliatti (Russia)

***E-mail: Mersoned@gmail.com**

[1]ORCID: https://orcid.org/0000-0002-7063-088X
[2]ORCID: https://orcid.org/0000-0002-0570-2584
[3]ORCID: https://orcid.org/0000-0002-7530-9518
[4]ORCID: https://orcid.org/0000-0001-5006-4115

Received 15.11.2022 *Accepted 02.12.2022*

Abstract: Magnesium alloys are promising materials for aviation, automotive engineering, and medicine, however, due to the low resistance to stress corrosion cracking (SCC), their wide application is limited. To create alloys with high resistance to SCC, a comprehensive study of this phenomenon nature is required. Previously, it was suggested that diffusible hydrogen and corrosion products formed on the magnesium surface can play an important role in the SCC mechanism. However, the contribution of each of these factors to the SCC-induced embrittlement of magnesium and its alloys is understudied. Since the influence of diffusible hydrogen on the mechanical properties of metals increases with the strain rate decrease, the study of the strain rate sensitivity of the SCC-susceptibility of magnesium alloys is a critical task. In this work, the authors studied the effect of the strain rate in the range from $5 \cdot 10^{-6}$ to $5 \cdot 10^{-4}$ s^{-1} on the mechanical properties, the state of the side and fracture surfaces of the as-cast commercially pure magnesium and the AZ31 alloy before and after exposure to a corrosive environment and after removal of corrosion products. The study identified that the preliminary exposure to a corrosive medium leads to the AZ31 alloy embrittlement, but does not affect the mechanical properties and the fracture mode of pure magnesium. The authors found that the AZ31 alloy embrittlement caused by the preliminary exposure to a corrosive medium appears extensively only at the low strain rate and only if the layer of corrosion products is present on the specimens' surface. The study shows that a change in the strain rate has little effect on the mechanical properties of pure magnesium. The authors concluded that the main cause of the AZ31 alloy embrittlement after soaking in a corrosive medium is the corrosion products layer, which presumably contains the embrittling agents such as hydrogen and residual corrosive medium.

Keywords: magnesium alloys; AZ31; pure magnesium; stress corrosion cracking; corrosion; strain rate; mechanical properties.

Acknowledgements: The research is financially supported by the Russian Science Foundation within the scientific project No. 18-19-00592.

For citation: Merson E.D., Poluyanov V.A., Myagkikh P.N., Merson D.L. The effect of strain rate on mechanical properties and fracture mode of the AZ31 alloy and commercially pure magnesium pre-exposed in a corrosive medium. *Frontier Materials & Technologies*, 2023, no. 3, pp. 71–82. DOI: 10.18323/2782-4039-2023-3-65-7.

INTRODUCTION

The impact of a corrosive environment on a metal, to which an external or internal mechanical stress is applied, facilitates the initiation and propagation of cracks. This phenomenon referred to as stress corrosion cracking (SCC) is a common cause of a sudden failure of elements of industrial equipment and structures, as well as other metal goods operating in contact with an aggressive environment. At best, the failure of one or another part causes economic losses, for example, associated with the stoppage of production and repair process, and at worst, it leads to techno-catastrophes often accompanied by human losses. Most structural metals and alloys are suceptible to this harmful phenomenon, including carbon and stainless steels, alloys based on copper, titanium, aluminum, magnesium, and many others.

Recently, special emphasis has been paid to the issue of SCC of magnesium alloys. Since these materials have the highest specific strength among known structural alloys, they are of great interest for the aircraft and automotive industries, as well as for other industries where the product weight is one of the most important parameters. However, the operating conditions of a large number of vehicles, including ground and air transport vehicles, are favorable for the SCC development since these conditions involve the contact of loaded parts with aggressive media, for example, salt water or humid air.

Moreover, the application of magnesium alloys in medical bioresorbable implants that can dissolve in the human body without harming it is actively developing. The use of these products, for example, in the form of plates and screws for fixing bone fragments in fractures, allows avoiding

a repeated operation, which is usually required after the end of treatment to remove traditional insolvable temporary implants made of titanium or stainless steels. Being in the natural internal environment of the human body that is aggressive towards magnesium, an implant constantly experiences static and alternating loads. Since the cross section gradually decreases as the device dissolves, such operating conditions are associated with a particularly high risk of premature brittle fracture of the implant due to SCC.

Thus, the production of magnesium alloys with an increased SCC resistance is a critical task, the solution of which requires a comprehensive study of this phenomenon nature. In the issue of choosing the approaches to the formation of a microstructure with the high SCC resistance, understanding the mechanisms of the crack initiation and propagation in a corrosive environment is of key importance. Many works show that the nucleation of cracks during SCC occurs on elongated corrosion pits, which are formed by the magnesium local anodic dissolution [1; 2]. However, currently, the mechanism of further crack propagation is not unanimous. Most researchers tend to believe that the growth of cracks in magnesium alloys under the SCC conditions is controlled by the diffusible hydrogen, which penetrates into the metal as a result of the cathodic reaction of hydrogen reduction occurring on the magnesium surface in aqueous corrosion solutions [3; 4]. The following arguments are given in favor of this hypothesis. Firstly, using gas analysis, it was experimentally shown that soaking in a corrosive medium leads to an increase in the hydrogen concentration in pure magnesium [5], as well as in the Mg–7.5%Al [6], AZ31, and ZK60 alloys [5; 7]. Secondly, it has been identified that pure magnesium [8], as well as some of magnesium alloys, including AZ31 [7], AZ91 [9], AZ80 [10], ZK21 [11], ZK60 [7], Mg–2Zn–1Nd–0.6Zr [12], and others [13–15] suffer embrittlement, called pre-exposure SCC (PESCC), which manifests itself upon tension in air, if before testing, specimens of these materials were kept in a corrosive environment. Thirdly, the degree of embrittlement as a result of PESCC decreases with increasing strain rate [16], which is one of the characteristic features of hydrogen embrittlement of many metals and alloys, for example, steels and aluminum alloys [17; 18]. Fourthly, as is the case with hydrogen embrittlement, PESCC of magnesium alloys can be partially or completely eliminated by keeping samples in air or in vacuum at room or elevated temperature after exposure to a corrosive environment [19; 20].

At first sight, the specified features of SCC and PESCC of magnesium alloys are actually very similar to the features of hydrogen embrittlement observed in other metals, which invited the researchers' assumption about the analogy of the mechanisms controlling these phenomena. Nevertheless, the results of a number of recent studies have shown that SCC and PESCC of magnesium alloys can also develop in the absence of diffusible hydrogen in their bulk. So, the works [5; 7] identified that the diffusible hydrogen concentration in the samples of pure magnesium, as well as of the AZ31 and ZK60 alloys, which were subject to the PESCC tests or exposure to a corrosive environment, was negligible if the corrosion products were removed from the surface of samples before gas analysis (which was not done in earlier works). Moreover, it was found that the removal of a layer of corrosion products from the samples of the AZ31 and ZK60 alloys exposed to a corrosive environment leads to the complete restoration of their mechanical properties and the elimination of any PESCC signs, including a strain rate dependence of the loss of ductility in the ZK60 alloy [7; 16]. Thus, it was proved that a corrosion products' layer formed on the alloy surface when interacting with a corrosive medium can play a key role in the PESCC mechanism. In [16], it was assumed that this layer acts as a container for "embrittling agents", in particular, hydrogen and residual corrosion medium, which, during the crack growth, can diffuse through the crack volume to its tip contributing to its propagation. The presence of a corrosive medium, as well as hydrogen, in the corrosion products' layer in the ZK60 alloy was experimentally confirmed in the work [20].

At the same time, the suppression of the PESCC of magnesium alloys with an increase in the strain rate probably indicates that the crack growth rate is limited by the rate of diffusion of embrittling agents from the surface to the tip of this crack. However, studies of the strain rate effect on the PESCC of magnesium alloys, especially after the removal of corrosion products, have hardly been carried out. In fact, data of this kind are presented in the literature only for the ZK60 alloy [16]. Therefore, to increase the reliability of the results of previous works and the conclusions about the SCC and PESCC mechanisms based on these results, it is necessary to carry out similar tests for other magnesium alloys, as well as for pure magnesium.

The work was aimed to clarify the PESCC nature of magnesium alloys by studying the effect of the strain rate and corrosion products on the mechanical properties and fracture surface of the AZ31 alloy and technically pure magnesium.

METHODS

The research was carried out using the samples of the as-cast technically pure magnesium and the AZ31 commercial alloy samples in the form of a hot-rolled sheet. The chemical composition of the selected materials shown in Table 1 was identified using the ARL 4460 optical-emission spectrometer (Thermo Fisher Scientific). An average size of a pure magnesium grain and the AZ31 alloy α-phase was 3 mm and 10 μm respectively. The microstructure of the selected materials was considered in previous works [5].

Threaded cylindrical specimens for tensile tests with a working part of 30×6 mm in size were produced by turning blanks. The specimens were cut along the rolling direction (AZ31) or along the cast slab axis (pure magnesium). The working part of prepared specimens was soaked in an aqueous corrosion solution of 4 % NaCl + 4 % $K_2Cr_2O_7$ for 24 hours. The soaking in the corrosion media was carried out at room temperature (24 °C) without applying the external mechanical and electrical stress. After that, the specimens were removed out of the corrosion solution, washed in an ethylic alcohol jet, and then dried with compressed air.

Mechanical tests of specimens pre-exposed to a corrosive environment were carried out in air at room temperature according to the uniaxial tension scheme at constant initial strain rate of $5 \cdot 10^{-6}$ and $5 \cdot 10^{-4}$ s^{-1} (0.01 and 1 mm/min) using the AG-Xplus testing machine (Shimadzu).

Table 1. *Chemical composition of the AZ31 alloy and technically pure magnesium, % wt.*
Таблица 1. *Химический состав сплава AZ31 и технически чистого магния, вес. %*

Material	Mg	Al	Zn	Ca	Zr	Fe	Cu	Mn	Ce	Nd	Si
AZ31	Base	4.473	0.887	0.0015	–	0.002	0.003	0.312	0.017	0.007	0.008
Pure magnesium	Base	0.005	–	0.0002	–	0.067	–	0.002	0.009	0.001	0.003

To compare, similar tests were conducted for specimens in the reference state, previously not subjected to exposure to a corrosive environment, and for specimens pre-exposed to a corrosive environment, from the surface of which corrosion products were removed immediately after exposure. The removal of corrosion products was performed by dipping a specimen for 1 minute to the standard C.5.4 (20 % CrO_3 + 1 % $AgNO_3$) solution according to the GOST R 9.907-2007 standard. After removing the corrosion products, the specimens were washed in alcohol and dried with compressed air. After mechanical tests, the fractures and side surfaces of fractured specimens were analyzed using the JCM-6000 scanning electron microscope (JEOL).

RESULTS

Mechanical properties

As a result of the experiments, it was found that an increase in the strain rate of samples of the AZ31 alloy in the reference state leads to a decrease in their ductility and an increase in strength (Fig. 1 a, 1 b, 2 a). The tests at a low strain rate showed that preliminary holding of samples of this alloy in a corrosive environment leads to a decrease both in its strength and ductility (Fig. 1 a, 1 b, 2 a). However, at a high strain rate, there is no decrease in mechanical properties after corrosion exposure. Moreover, the complete restoration of the alloy mechanical properties occurs if, after soaking in a corrosive environment, corrosion products are removed from the surface of the samples. This effect is observed both at low and high strain rates.

The ductility of the reference pure magnesium samples slightly depends on the strain rate, and the increase in the strength with increasing strain rate is much weaker than that of the AZ31 alloy (Fig. 1 c, 1 d, 2 b). Preliminary exposure to a corrosive environment does not have a significant effect on the pure magnesium ductility, but leads to a slight decrease in its strength, which slightly increases with an increase in the strain rate. Interestingly, the ductility of pure magnesium specimens with the removed corrosion products is significantly lower than that of specimens in the reference state and specimens kept in a corrosive environment, from the surface of which corrosion products were not removed.

The analysis of fractures and side surfaces

On the side surface of the AZ31 alloy specimens (Fig. 3) tested for tension in the initial state, a large number of small ductile cracks oriented across the tension axis are observed (Fig. 3 a, 3 d). These cracks appear along the grooves formed by the cutter on the metal surface during turning. On the surface of the samples that were subjected to soaking in a corrosive environment followed by a tensile test at a low strain rate, there are also many cracks, which, however, are much larger and more brittle compared to cracks on the reference samples (Fig. 3 b). After testing at a high strain rate, there are practically no such large cracks in specimens of a similar type (Fig. 3 e). Large cracks are present on the surface of samples from which the corrosion products were removed before testing, but their quantity is significantly less than that of samples that were tested after holding in the environment without removing the corrosion products (Fig. 3 c).

The fractographic analysis (Fig. 4) showed that the fractures of the AZ31 alloy reference samples are fully-ductile, regardless of the strain rate (Fig. 4 a, 4 d). On the fracture surface of specimens tested at a low strain rate and after pre-exposure to a corrosive medium, together with the dominant ductile component, there are multiple brittle fracture areas, which are always located in the peripheral part of the fracture and directly adjacent to the side surface of the specimen (Fig. 4 b). One of these brittle areas is blocked with a frame ("A" area in Fig. 4 b) and is shown at higher magnification in Fig. 5 a.

On the fracture surface of specimens with the removed corrosion products tested at a low strain rate, there are also a small amount of such brittle fracture areas (Fig. 4 c and 5 b); however, their quantity is significantly less than in specimens from which the corrosion products were not removed. The fractures of all specimens pre-exposed to a corrosive environment and tested at a high strain rate are fully-ductile and do not contain brittle fracture areas, regardless of whether the corrosion products were removed from them or not (Fig. 4 d–f).

On the side surface of pure magnesium specimens tested in the reference state and after soaking in a corrosive environment, including the subsequent removal of corrosion products, there are large cracks and numerous slip bands (Fig. 6). Moreover, a network of small cracks is also observed on the surface of specimens pre-exposed to a corrosive environment (Fig. 6 e and 7 a). Interestingly, there is a large quantity of corrosion pits on the surface of samples with the removed corrosion products (Fig. 6 c, 6 f, and 7 b), which are not observed on the surface of samples tested immediately after soaking in a corrosive environment (without the removal of corrosion products). No critical effect of the strain rate on the appearance of the side surface of pure magnesium specimens in the initial state and after soaking in a corrosive medium was found.

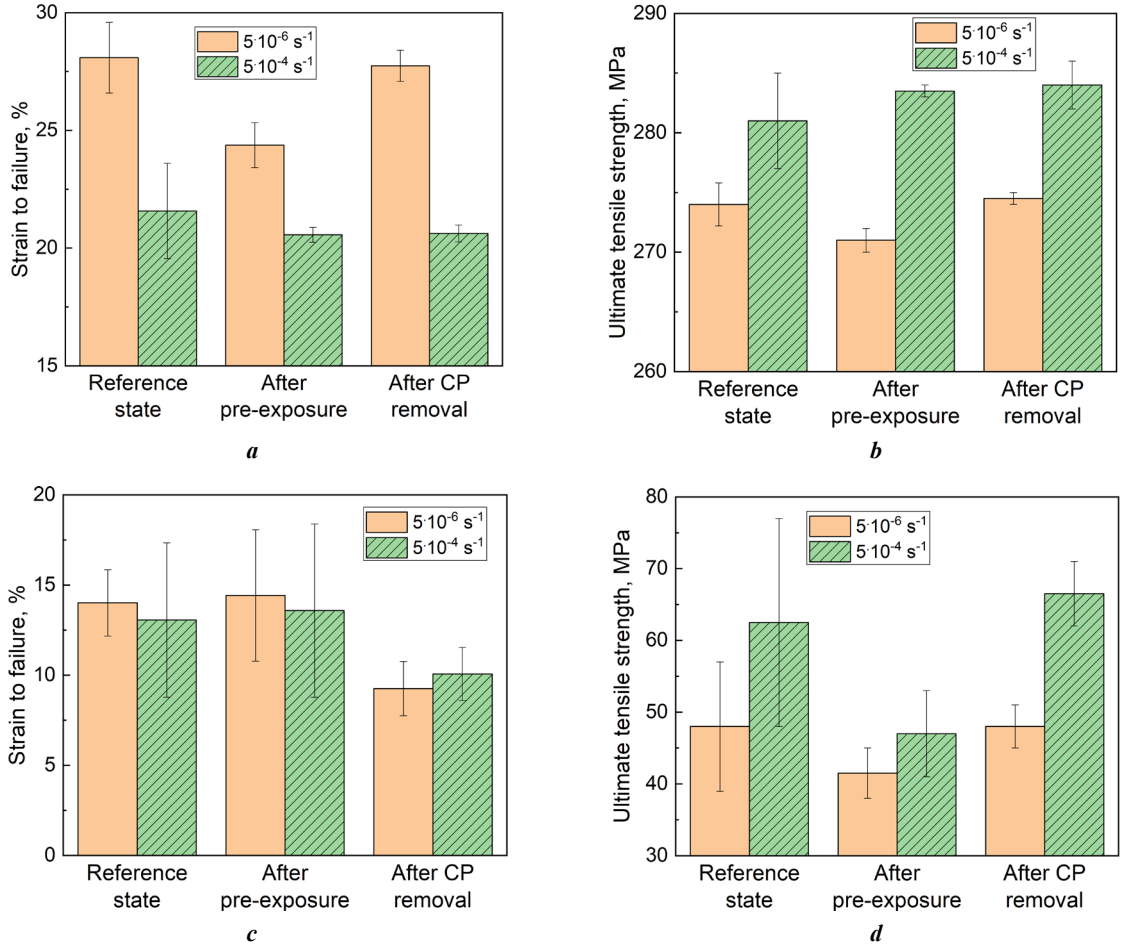

Fig. 1. *The effect of strain rate on elongation to failure (**a**, **c**) and ultimate tensile strength (**b**, **d**) of the AZ31 alloy specimens (**a**, **b**) and technically pure magnesium specimens (**c**, **d**) in the reference state, after the pre-exposure to a corrosive medium, and after the pre-exposure to a corrosive medium followed by the removal of corrosion products*

Рис. 1. *Влияние скорости деформирования на деформацию до разрушения (**a**, **c**) и предел прочности (**b**, **d**) образцов сплава AZ31 (**a**, **b**) и технически чистого магния (**c**, **d**) в исходном состоянии, после выдержки в коррозионной среде и после выдержки в коррозионной среде с последующим удалением продуктов коррозии*

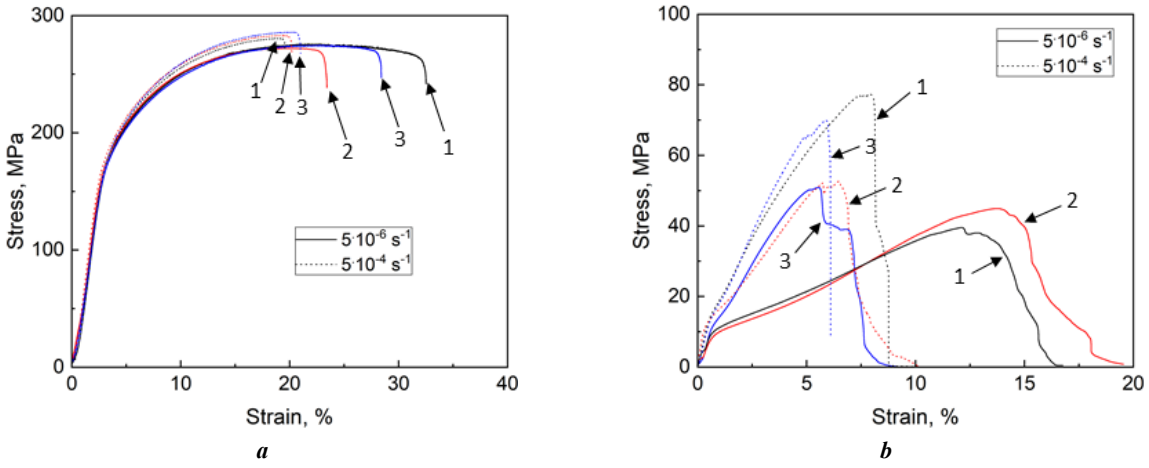

Fig. 2. *The effect of strain rate on the stress-strain diagrams of the AZ31 alloy specimens (**a**) and technically pure magnesium specimens (**b**) in different states: 1 – reference state; 2 – after the pre-exposure to a corrosive medium; 3 – after the pre-exposure to a corrosive medium and the removal of corrosion products*

Рис. 2. *Влияние скорости деформирования на диаграммы растяжения образцов сплава AZ31 (**a**) и технически чистого магния (**b**) в разных состояниях: 1 – исходном; 2 – после предварительной выдержки в коррозионной среде; 3 – после предварительной выдержки в коррозионной среде и удаления продуктов коррозии*

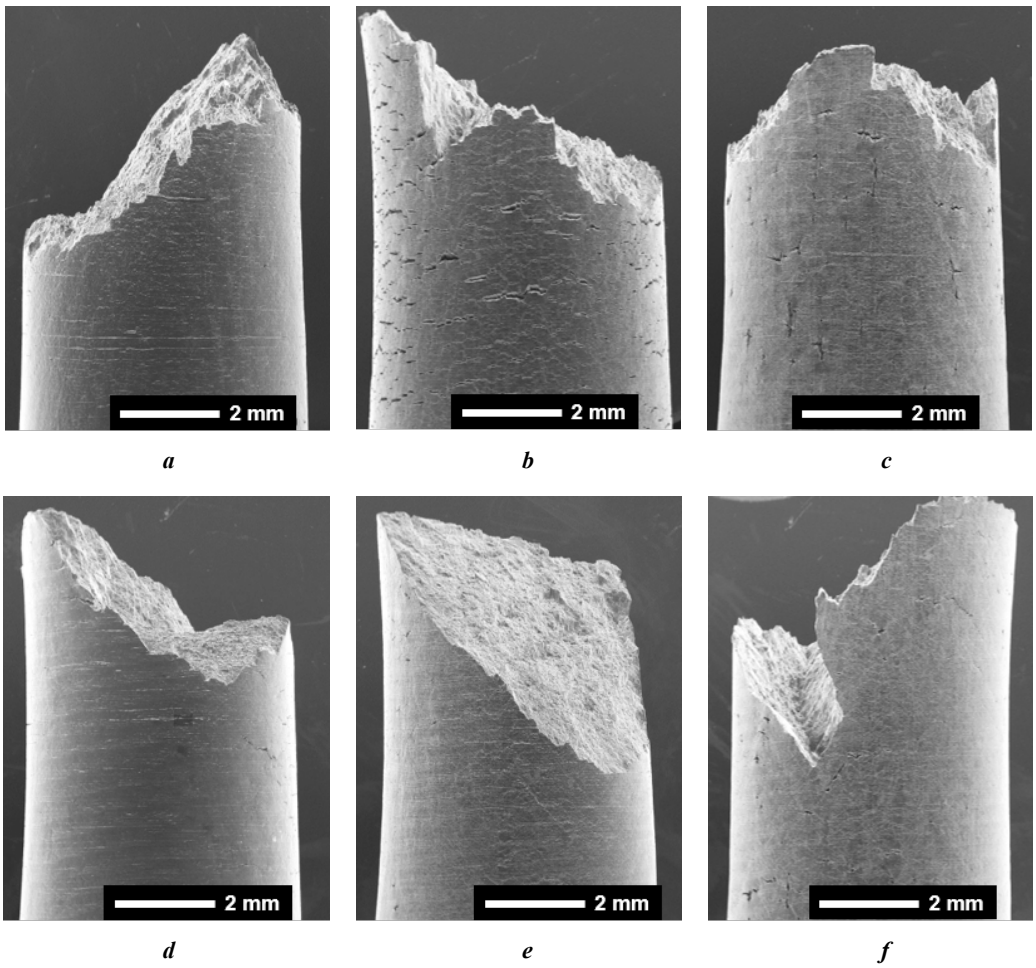

Fig. 3. *The appearance of the side surface of the AZ31 alloy specimens tensile-tested in air:* ***a***, ***d*** *– in the reference state;* ***b***, ***e*** *– after the pre-exposure to a corrosive medium;* ***c***, ***f*** *– after the pre-exposure to a corrosive medium and the removal of corrosion products:* ***a–c*** *– at a low ($5 \cdot 10^{-6}$ s^{-1}) strain rate;* ***d–f*** *– at a high ($5 \cdot 10^{-4}$ s^{-1}) strain rate. Images are obtained by SEM*

Рис. 3. *Внешний вид боковой поверхности образцов сплава AZ31, испытанных на растяжение на воздухе:* ***a***, ***d*** *– в исходном состоянии;* ***b***, ***e*** *– после выдержки в коррозионной среде;* ***c***, ***f*** *– после выдержки в коррозионной среде и удаления продуктов коррозии при:* ***a–c*** *– низкой ($5 \cdot 10^{-6}$ $с^{-1}$);* ***d–f*** *– высокой ($5 \cdot 10^{-4}$ $с^{-1}$) скоростях деформирования. Снимки получены при помощи СЭМ*

The fracture surface of all pure magnesium samples has a similar structure, regardless of the strain rate and the type of samples (Fig. 8). In all cases, the fracture is represented mainly by the facets with a fluted relief. Smooth facets without clearly defined relief are occasionally found.

DISCUSSION

The results obtained in the work showed that the loss of the AZ31 alloy mechanical properties as a result of PESCC can be completely eliminated when increasing the strain rate by two orders of magnitude, from $5 \cdot 10^{-6}$ to $5 \cdot 10^{-4}$ s^{-1}. A similar result was previously obtained for the ZK60 alloy [16] when exposing it to a medium of the same composition and at the same strain rates as in the present work. Usually, such behavior of mechanical characteristics depending on the strain rate is explained by the embrittling effect of diffusible hydrogen, which weakens with an increase in the strain rate.

A negative strain rate dependence of the ductility loss was identified in many metallic hydrogen-saturated materials, for example, in steels [18] and aluminum-based alloys [17]. In these works, such behavior of ductility depending on the strain rate can only be explained by the effect of hydrogen dissolved in the bulk of the metal, since hydrogenation was carried out without corrosion participation. However, when discussing the nature of the negative strain rate dependence of the loss of ductility of magnesium alloys embrittled as a result of interaction with a corrosive medium, it is necessary, along with the possible hydrogen dissolution in the bulk of the metal, to consider other factors, for example, the presence of corrosion products on the surface of samples, which may contain both hydrogen and residual corrosive medium in liquid form.

Indeed, the results of the present study for the AZ31 alloy, as well as of the previous studies for the ZK60 alloy, show that the removal of a layer of corrosion products from the surface of samples before tensile testing eliminates both the embrittlement caused by preliminary exposure to a corrosive environment and the negative strain rate sensitivity of ductility loss associated with this embrittlement. In this case, the loss of ductility of samples with the removed corrosion products either increases with an increase in the strain rate (ZK60 alloy) or does not depend on the latter (AZ31 alloy).

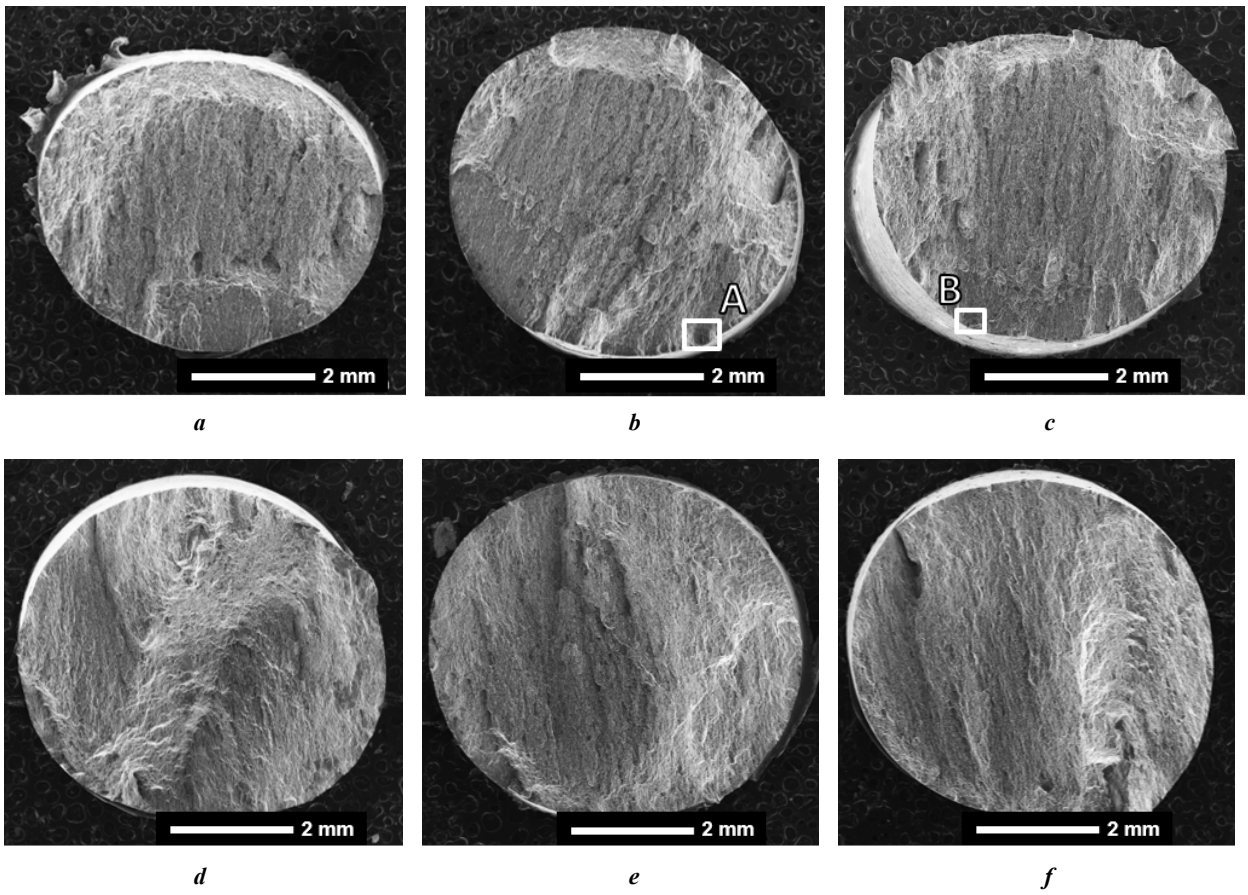

a *b* *c*

d *e* *f*

Fig. 4. *The appearance of the fracture surface of the AZ31 alloy specimens tensile- tested in air:* ***a***, ***d*** *– in the reference state;* ***b***, ***e*** *– after the pre-exposure to a corrosive medium;* ***c***, ***f*** *– after the pre-exposure to a corrosive medium and the removal of corrosion products:* ***a–c*** *– at a low ($5 \cdot 10^{-6}$ s^{-1}) strain rate;* ***d–f*** *– at a high ($5 \cdot 10^{-4}$ s^{-1}) strain rate. Images are obtained by SEM. The blocked "A" and "B" areas are shown in Figure 5*

Рис. 4. *Внешний вид изломов образцов сплава AZ31, испытанных на растяжение на воздухе:* ***a***, ***d*** *– в исходном состоянии;* ***b***, ***e*** *– после выдержки в коррозионной среде;* ***c***, ***f*** *– после выдержки в коррозионной среде и удаления продуктов коррозии при:* ***a–c*** *– низкой ($5 \cdot 10^{-6}$ $с^{-1}$); **d–f** – высокой ($5 \cdot 10^{-4}$ $с^{-1}$) скоростях деформирования. Снимки получены при помощи СЭМ. Выделенные области «А», «В» представлены на рис. 5*

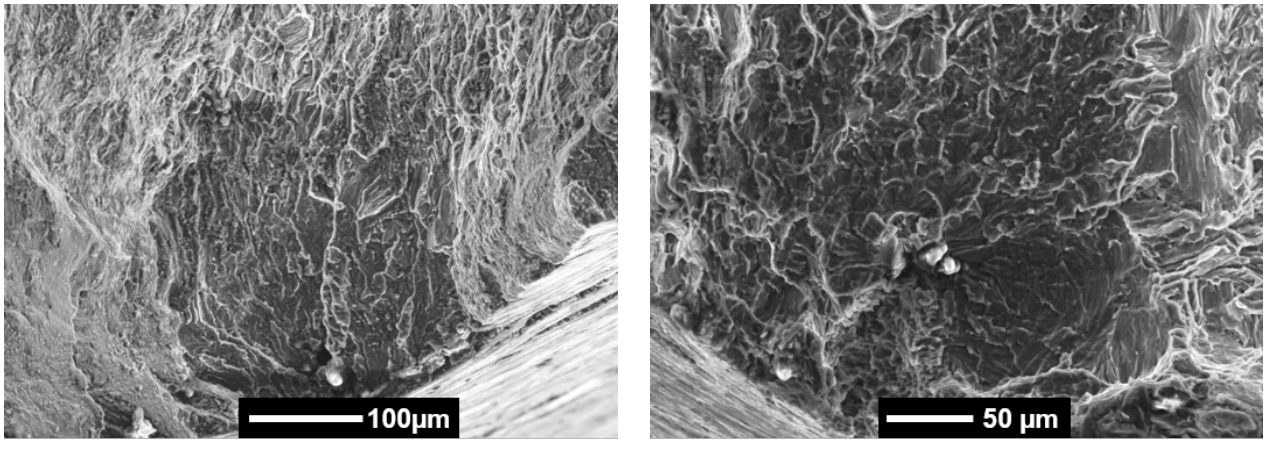

a *b*

Fig. 5. *The magnified fracture surface areas blocked in the frames in fig. 4 b and 4 c, respectively:* ***a*** *– "A" area;* ***b*** *– "B" area, containing the regions of brittle fracture in the peripheral part of the fracture surfaces of the AZ31 alloy specimens tested at a low strain rate immediately after the pre-exposure to a corrosive medium (**a**) and after the removal of corrosion products (**b**). Images are obtained by SEM*

Рис. 5. *Увеличенные области поверхности разрушения, обведенные рамками на рис. 4 b и 4 с соответственно:* ***a*** *– область «А»;* ***b*** *– область «В», содержащие участки хрупкого разрушения в периферийной части излома образцов сплава AZ31. Образцы испытывались при низкой скорости деформирования сразу после выдержки в коррозионной среде (**a**) и после удаления продуктов коррозии (**b**). Снимки получены при помощи СЭМ*

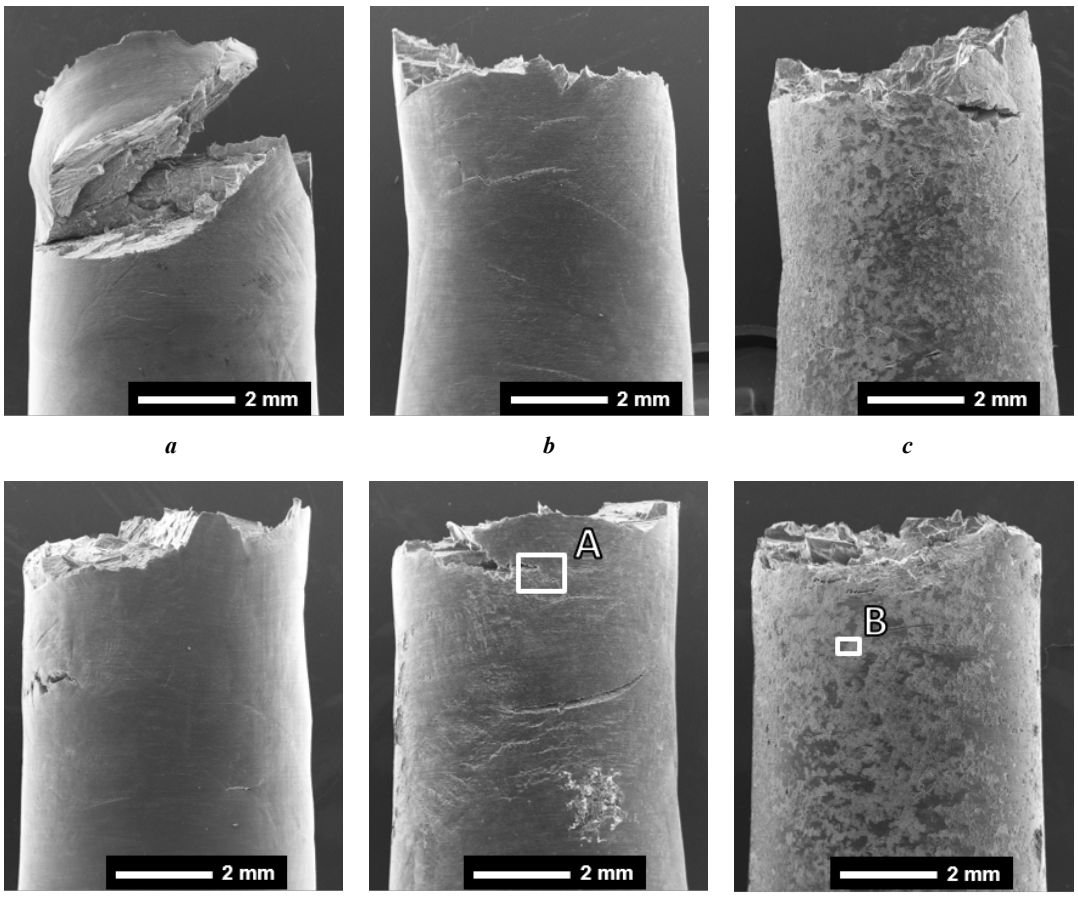

Fig. 6. *The appearance of the side surface of the technically pure magnesium specimens tensile-tested in air:* ***a***, ***d*** *– in the reference state;* ***b***, ***e*** *– after the pre-exposure to a corrosive medium;* ***c***, ***f*** *– after the pre-exposure to a corrosive medium and the removal of corrosion products:* ***a–c*** *– at a low ($5 \cdot 10^{-6}$ s^{-1}) strain rate;* ***d–f*** *– at a high ($5 \cdot 10^{-4}$ s^{-1}) strain rate. Images are obtained by SEM. The blocked "A" and "B" areas are shown in Figure 7*

Рис. 6. *Внешний вид боковой поверхности образцов технически чистого магния, испытанных на растяжение на воздухе:* ***a***, ***d*** *– в исходном состоянии;* ***b***, ***e*** *– после выдержки в коррозионной среде;* ***c***, ***f*** *– после выдержки в коррозионной среде и удаления продуктов коррозии при:* ***a–c*** *– низкой ($5 \cdot 10^{-6}$ $с^{-1}$); **d–f** – высокой ($5 \cdot 10^{-4}$ $с^{-1}$) скоростях деформирования. Снимки получены при помощи СЭМ. Выделенные области «А», «В» представлены на рис. 7*

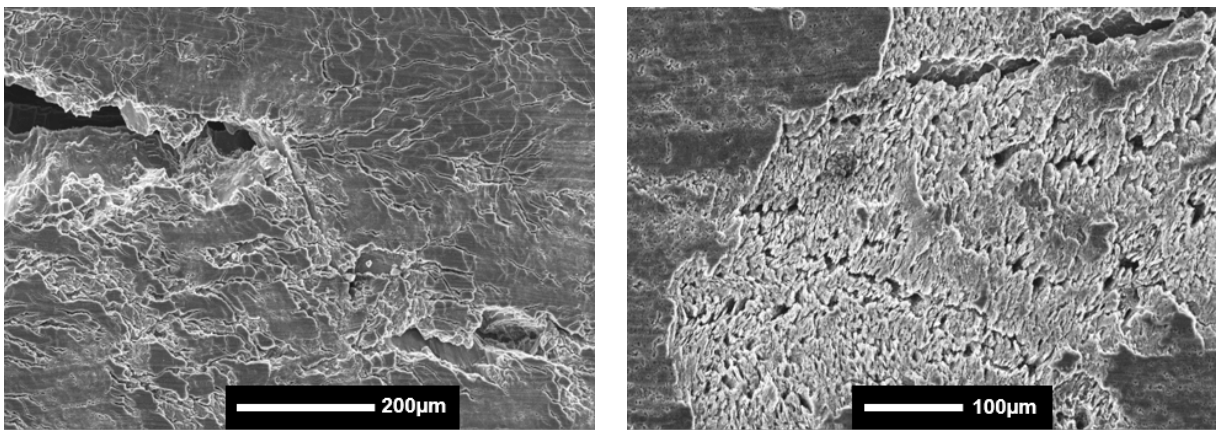

Fig. 7. *The magnified side surface areas blocked in the frames in fig. 6 e and 6 f respectively:* ***a*** *– "A" area;* ***b*** *– "B" area, illustrating the brittle cracks net (**a**) and corrosion pits (**b**) on the surface of technically pure magnesium specimens tested at the low strain rate right after pre-exposure to corrosive medium –* ***a****; as well as after the removal of corrosion products –* ***b****. The images are obtained by SEM*

Рис. 7. *Увеличенные области боковой поверхности, обведенные рамками на рис. 6 е и 6 f соответственно:* ***a*** *– область «А»;* ***b*** *– область «В», иллюстрирующие сетку хрупких трещин (**a**) и коррозионные язвы (**b**) на поверхности образцов технически чистого магния. Образцы испытывались при высокой скорости деформирования сразу после выдержки в коррозионной среде (**a**) и после удаления продуктов коррозии (**b**). Снимки получены при помощи СЭМ*

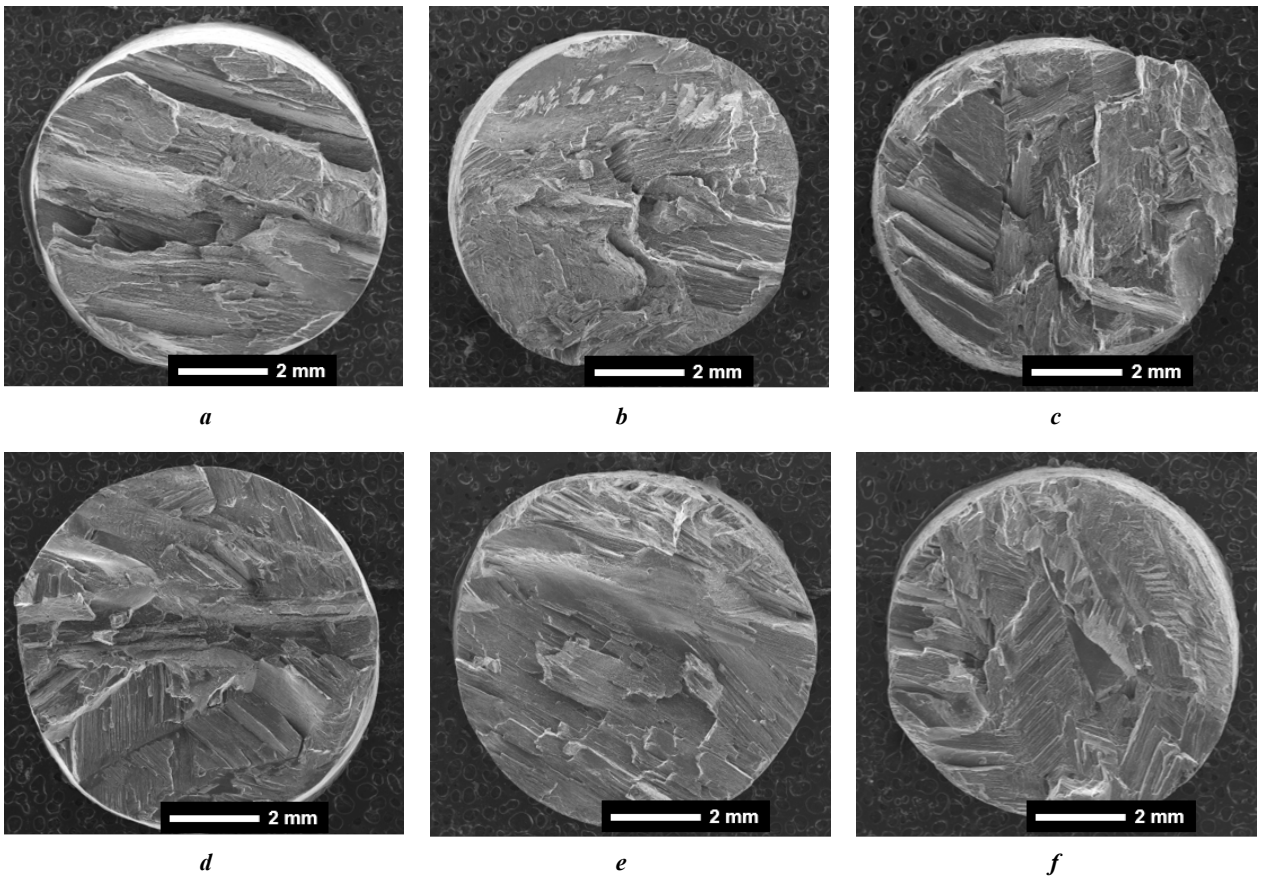

Fig. 8. *The appearance of the fracture surface of the technically pure magnesium specimens tensile-tested in air:* ***a***, ***d*** *– in the reference state;* ***b***, ***e*** *– after the pre-exposure to a corrosive medium;* ***c***, ***f*** *– after the pre-exposure to a corrosive medium and the removal of corrosion products:* ***a–c*** *– at a low ($5 \cdot 10^{-6}$ s^{-1}) strain rate;* ***d–f*** *– at a high ($5 \cdot 10^{-4}$ s^{-1}) strain rate. Images are obtained by SEM*

Рис. 8. *Внешний изломов образцов технически чистого магния, испытанных на растяжение на воздухе:* ***a***, ***d*** *– в исходном состоянии;* ***b***, ***e*** *– после выдержки в коррозионной среде;* ***c***, ***f*** *– после выдержки в коррозионной среде и удаления продуктов коррозии при:* ***a–c*** *– низкой ($5 \cdot 10^{-6}$ $с^{-1}$);* ***d–f*** *– высокой ($5 \cdot 10^{-4}$ $с^{-1}$) скоростях деформирования. Снимки получены при помощи СЭМ*

The suppression of the AZ31 alloy embrittlement as a result of the removal of corrosion products is confirmed, firstly, by the restoration of mechanical properties at a low strain rate, and secondly, by a significant decrease in the number of large brittle cracks on the side surface of samples, as well as the areas with the brittle fracture morphology on the fracture surfaces of these samples. In fairness, it should be noted that a small quantity of cracks and brittle fracture areas in the AZ31 alloy samples is still present even after the removal of corrosion products. Hypothetically, this may be associated with the incomplete removal of corrosion products. The work [7] showed that C.5.4 solution used in the present and previous works is noticeably less effective in removing corrosion products from the AZ31 alloy than from the ZK60 alloy. It can be assumed that hydrogen still partially penetrates into the metal surface layer. However, it is not clear why this does not occur in the ZK60 alloy, which, all other things being equal, as a result of soaking in a corrosive environment, is embrittled much more strongly than the AZ31 alloy, but does not show any signs of embrittlement after the removal of corrosion products [7]. It can be concluded that the key role in the PESCC mechanism of the AZ31 alloy is played by the layer of corrosion products, which presumably contains the "embrittling agents" such as hydrogen and residual corrosive environment. Probably, the participation of these agents in the mechanism of crack initiation and growth, including their diffusion from the sample surface to the crack tip, leads to the appearance of a negative rate sensitivity of ductility. At the same time, as shown by previous studies, the hydrogen penetration directly into the bulk of the magnesium matrix almost does not occur during the corrosion process [5; 7].

In view of the above reasoning, it is interesting that technically pure magnesium is actually not subject to the PESCC process – at least in the as-cast coarse-grained state and when exposed to a corrosive solution of the 4 % NaCl + 4 % $K_2Cr_2O_7$ composition. At the same time, in the literature, there is evidence that fine-grained magnesium suffers embrittlement after soaking in the 10^{-3} M Na_2SO_4 solution [8]. Coarse-grained magnesium is also distinguished by the almost complete absence of ductility strain rate sensitivity both in the reference state and after pre-exposure to a corrosive environment.

In spite of the fact that the actual reason for the high resistance of this material to PESCC has yet to be investigat-

ed, at the moment two possible explanations for this phenomenon can be proposed. Firstly, the presence of secondary phases in the structure can be a critical factor affecting the stability of a particular magnesium alloy. It is known that particles of almost all secondary phases in magnesium alloys act as a cathode in relation to the magnesium matrix and, therefore, serve as the sites for the initiation of corrosion pits [21], which subsequently act as the crack nuclei during SCC [1]. Consequently, the absence of such particles in pure magnesium can favorably affect its resistance to PESCC and SCC. Secondly, one can assume that the pure magnesium immunity to PESCC is associated with its low strength. The pure magnesium plastic deformation begins at very low stresses, so even if brittle cracks have time to nucleate, they quickly become blunted due to the plastic flow at their tips and propagate mainly by a ductile mechanism. Indeed, numerous small brittle cracks were found on the lateral surface of magnesium specimens kept in a corrosive medium. However, the fractures of these samples, as well as of samples in the reference state, are mainly represented by facets with a characteristic fluted pattern, which is formed due to the formation and ductile merging of tubular pores [22], which indicates a ductile mechanism of crack propagation in this material.

It is important to note that pure magnesium samples, from which the corrosion products were removed after soaking in a corrosive medium, have noticeably lower ductility than samples, from which corrosion products were not removed. Probably, it is associated with the presence of corrosion pits, which were identified on the side surface of the samples after the removal of corrosion products. Apparently, the standard C.5.4 solution for removing corrosion products can lead to corrosion damage to pure magnesium, although this was not observed when interacting with the AZ31 and ZK60 alloys. Currently, it is unclear whether this effect depends on the presence and type of corrosion products on the surface of pure magnesium.

CONCLUSIONS

1. An increase in the strain rate from $5 \cdot 10^{-6}$ to $5 \cdot 10^{-4}$ s^{-1} leads to a complete elimination of the AZ31 alloy embrittlement caused by preliminary exposure to an aqueous solution of the 4 % NaCl + 4 % $K_2Cr_2O_7$ composition for 24 h.

2. The removal of corrosion products using the standard C.5.4 (20 % CrO_3 + 1 % $AgNO_3$) solution from the surface of the AZ31 alloy pre-exposed to a corrosive environment leads to a complete elimination of the loss of ductility caused by PESCC, but does not completely suppress brittle cracking.

3. Technically pure magnesium in the as-cast coarse-grained condition is not susceptible to PESCC after soaking in an aqueous solution of the 4 % NaCl + 4 % $K_2Cr_2O_7$ composition for 24 h.

4. An increase in the strain rate from $5 \cdot 10^{-6}$ to $5 \cdot 10^{-4}$ s^{-1} has no significant effect on the mechanical properties of technically pure magnesium in the as-cast coarse-grained state, regardless of whether preliminary exposure to a corrosive medium was carried out before the tensile tests or not.

REFERENCES

1. Yu Z., Chen J., Yan H., Xia W., Su B., Gong X., Guo H. Degradation, stress corrosion cracking behavior and cytocompatibility of high strain rate rolled Mg-Zn-Sr alloys. *Materials Letters*, 2020, vol. 260, article number 126920. DOI: 10.1016/j.matlet.2019.126920.
2. Zhang X., Wu W., Fu H., Li J. The effect of corrosion evolution on the stress corrosion cracking behavior of mooring chain steel. *Corrosion Science*, 2022, vol. 203, article number 110316. DOI: 10.1016/j.corsci.2022.110316.
3. Song Y., Liu Q., Wang H., Zhu X. Effect of Gd on microstructure and stress corrosion cracking of the AZ91-extruded magnesium alloy. *Materials and Corrosion*, 2021, vol. 72, no. 7, pp. 1189–1200. DOI: 10.1002/maco.202112294.
4. Peron M., Bertolini R., Ghiotti A., Torgersen J., Bruschi S., Berto F. Enhancement of stress corrosion cracking of AZ31 magnesium alloy in simulated body fluid thanks to cryogenic machining. *Jounal of the Mechanical Behavior of Biomedical Materials*, 2020, vol. 101, article number 103429. DOI: 10.1016/j.jmbbm.2019.103429.
5. Merson E., Myagkikh P., Poluyanov V., Merson D., Vinogradov A. On the role of hydrogen in stress corrosion cracking of magnesium and its alloys: Gas-analysis study // *Materials Science and Engineering A*. 2019. Vol. 748. P. 337-346. DOI: 10.1016/j.msea.2019.01.107.
6. Chakrapani D.G., Pugh E.N. Hydrogen embrittlement in a Mg-Al alloy. *Metallurgical Transactions A*, 1976, vol. 7, no. 2, pp. 173–178. DOI: 10.1007/BF02644454.
7. Merson E., Poluyanov V., Myagkikh P., Merson D., Vinogradov A. On the role of pre-exposure time and corrosion products in stress-corrosion cracking of ZK60 and AZ31 magnesium alloys. *Materials Science and Engineering A*, 2021, vol. 806, article number 140876. DOI: 10.1016/j.msea.2021.140876.
8. Stampella R.S., Procter R.P.M., Ashworth V. Environmentally-induced cracking of magnesium. *Corrosion Science*, 1984, vol. 24, no. 4, pp. 325–341. DOI: 10.1016/0010-938X(84)90017-9.
9. Choudhary L., Singh Raman R.K. Magnesium alloys as body implants: Fracture mechanism under dynamic and static loadings in a physiological environment. *Acta Biomaterialia*, 2012, vol. 8, no. 2, pp. 916–923. DOI: 10.1016/j.actbio.2011.10.031.
10. Bobby Kannan M., Dietzel W. Pitting-induced hydrogen embrittlement of magnesium-aluminium alloy. *Materials and Design*, 2012, vol. 42, pp. 321–326. DOI: 10.1016/j.matdes.2012.06.007.
11. Jafari S., Raman R.K.S., Davies C.H.J. Stress corrosion cracking of an extruded magnesium alloy (ZK21) in a simulated body fluid. *Engineering Fracture Mechanics*, 2018, vol. 201, pp. 47–55. DOI: 10.1016/j.engfracmech.2018.09.002.
12. Cai C., Song R., Wen E., Wang Y., Li J. Effect of microstructure evolution on tensile fracture behavior of

Mg-2Zn-1Nd-0.6Zr alloy for biomedical applications. *Materials and Design*, 2019, vol. 182, article number 108038. DOI: 10.1016/j.matdes.2019.108038.
13. Jiang P., Blawert C., Bohlen J., Zheludkevich M.L. Corrosion performance, corrosion fatigue behavior and mechanical integrity of an extruded Mg4Zn0.2Sn alloy. *Journal of Materials Science and Technology*, 2020, vol. 59, pp. 107–116. DOI: 10.1016/j.jmst.2020.04.042.
14. Prabhu D.B., Nampoothiri J., Elakkiya V., Narmadha R., Selvakumar R., Sivasubramanian R., Gopalakrishnan P., Ravi K.R. Elucidating the role of microstructural modification on stress corrosion cracking of biodegradable Mg–4Zn alloy in simulated body fluid. *Materials Science and Engineering C*, 2020, vol. 106, article number 110164. DOI: 10.1016/j.msec.2019.110164.
15. Chen K., Lu Y., Tang H., Gao Y., Zhao F., Gu X., Fan Y. Effect of strain on degradation behaviors of WE43, Fe and Zn wires. *Acta Biomaterialia*, 2020, vol. 113, pp. 627–645. DOI: 10.1016/j.actbio.2020.06.028.
16. Merson E., Poluyanov V., Myagkikh P., Merson D., Vinogradov A. Effect of strain rate and corrosion products on pre-exposure stress corrosion cracking in the ZK60 magnesium alloy. *Materials Science and Engineering A*, 2022, vol. 830, article number 142304. DOI: 10.1016/j.msea.2021.142304.
17. Safyari M., Moshtaghi M., Kuramoto S. Effect of strain rate on environmental hydrogen embrittlement susceptibility of a severely cold-rolled Al–Cu alloy. *Vacuum*, 2020, vol. 172, article number 109057. DOI: 10.1016/j.vacuum.2019.109057.
18. Momotani Y., Shibata A., Terada D., Tsuji N. Effect of strain rate on hydrogen embrittlement in low-carbon martensitic steel. *International journal of hydrogen energy*, 2017, vol. 42, no. 5, pp. 3371–3379. DOI: 10.1016/j.ijhydene.2016.09.188.
19. Kappes M., Iannuzzi M., Carranza R.M. Pre-exposure embrittlement and stress corrosion cracking of magnesium alloy AZ31B in chloride solutions. *Corrosion*, 2014, vol. 70, no. 7, pp. 667–677. DOI: 10.5006/1172.
20. Merson E., Poluyanov V., Myagkikh P., Merson D., Vinogradov A. Effect of Air Storage on Stress Corrosion Cracking of ZK60 Alloy Induced by Preliminary Immersion in NaCl-Based Corrosion Solution. *Materials*, 2022, vol. 15, no. 21, article number 7862. DOI: 10.3390/ma15217862.
21. Atrens A., Shi Z., Mehreen S.U., Johnston S., Song G.L., Chen X., Pan F. Review of Mg alloy corrosion rates. *Journal of magnesium and alloys*, 2020, vol. 8, no. 4, pp. 989–998. DOI: 10.1016/j.jma.2020.08.002.
22. Lynch S.P., Trevena P. Stress corrosion cracking and liquid metal embrittlement in pure magnesium. *Corrosion*, 1988, vol. 44, no. 2, pp. 113–124. DOI: 10.5006/1.3583907.

СПИСОК ЛИТЕРАТУРЫ

1. Yu Z., Chen J., Yan H., Xia W., Su B., Gong X., Guo H. Degradation, stress corrosion cracking behavior and cytocompatibility of high strain rate rolled Mg-Zn-Sr alloys // Materials Letters. 2020. Vol. 260. Article number 126920. DOI: 10.1016/j.matlet.2019.126920.
2. Zhang X., Wu W., Fu H., Li J. The effect of corrosion evolution on the stress corrosion cracking behavior of mooring chain steel // Corrosion Science. 2022. Vol. 203. Article number 110316. DOI: 10.1016/j.corsci.2022.110316.
3. Song Y., Liu Q., Wang H., Zhu X. Effect of Gd on microstructure and stress corrosion cracking of the AZ91-extruded magnesium alloy // Materials and Corrosion. 2021. Vol. 72. № 7. P. 1189–1200. DOI: 10.1002/maco.202112294.
4. Peron M., Bertolini R., Ghiotti A., Torgersen J., Bruschi S., Berto F. Enhancement of stress corrosion cracking of AZ31 magnesium alloy in simulated body fluid thanks to cryogenic machining // Jounal of the Mechanical Behavior of Biomedical Materials. 2020. Vol. 101. Article number 103429. DOI: 10.1016/j.jmbbm.2019.103429.
5. Merson E., Myagkikh P., Poluyanov V., Merson D., Vinogradov A. On the role of hydrogen in stress corrosion cracking of magnesium and its alloys: Gas-analysis study // Materials Science and Engineering A. 2019. Vol. 748. P. 337-346. DOI: 10.1016/j.msea.2019.01.107.
6. Chakrapani D.G., Pugh E.N. Hydrogen embrittlement in a Mg-Al alloy // Metallurgical Transactions A. 1976. Vol. 7. № 2. P. 173–178. DOI: 10.1007/BF02644454.
7. Merson E., Poluyanov V., Myagkikh P., Merson D., Vinogradov A. On the role of pre-exposure time and corrosion products in stress-corrosion cracking of ZK60 and AZ31 magnesium alloys // Materials Science and Engineering A. 2021. Vol. 806. Article number 140876. DOI: 10.1016/j.msea.2021.140876.
8. Stampella R.S., Procter R.P.M., Ashworth V. Environmentally-induced cracking of magnesium // Corrosion Science. 1984. Vol. 24. № 4. P. 325–341. DOI: 10.1016/0010-938X(84)90017-9.
9. Choudhary L., Singh Raman R.K. Magnesium alloys as body implants: Fracture mechanism under dynamic and static loadings in a physiological environment // Acta Biomaterialia. 2012. Vol. 8. № 2. P. 916–923. DOI: 10.1016/j.actbio.2011.10.031.
10. Bobby Kannan M., Dietzel W. Pitting-induced hydrogen embrittlement of magnesium-aluminium alloy // Materials and Design. 2012. Vol. 42. P. 321–326. DOI: 10.1016/j.matdes.2012.06.007.
11. Jafari S., Raman R.K.S., Davies C.H.J. Stress corrosion cracking of an extruded magnesium alloy (ZK21) in a simulated body fluid // Engineering Fracture Mechanics. 2018. Vol. 201. P. 47–55. DOI: 10.1016/j.engfracmech.2018.09.002.
12. Cai C., Song R., Wen E., Wang Y., Li J. Effect of microstructure evolution on tensile fracture behavior of Mg-2Zn-1Nd-0.6Zr alloy for biomedical applications // Materials and Design. 2019. Vol. 182. Article number 108038. DOI: 10.1016/j.matdes.2019.108038.
13. Jiang P., Blawert C., Bohlen J., Zheludkevich M.L. Corrosion performance, corrosion fatigue behavior and mechanical integrity of an extruded Mg4Zn0.2Sn alloy //

Journal of Materials Science and Technology. 2020. Vol. 59. P. 107–116. DOI: 10.1016/j.jmst.2020.04.042.
14. Prabhu D.B., Nampoothiri J., Elakkiya V., Narmadha R., Selvakumar R., Sivasubramanian R., Gopalakrishnan P., Ravi K.R. Elucidating the role of microstructural modification on stress corrosion cracking of biodegradable Mg–4Zn alloy in simulated body fluid // Materials Science and Engineering C. 2020. Vol. 106. Article number 110164. DOI: 10.1016/j.msec.2019.110164.
15. Chen K., Lu Y., Tang H., Gao Y., Zhao F., Gu X., Fan Y. Effect of strain on degradation behaviors of WE43, Fe and Zn wires // Acta Biomaterialia. 2020. Vol. 113. P. 627–645. DOI: 10.1016/j.actbio.2020.06.028.
16. Merson E., Poluyanov V., Myagkikh P., Merson D., Vinogradov A. Effect of strain rate and corrosion products on pre-exposure stress corrosion cracking in the ZK60 magnesium alloy // Materials Science and Engineering A. 2022. Vol. 830. Article number 142304. DOI: 10.1016/j.msea.2021.142304.
17. Safyari M., Moshtaghi M., Kuramoto S. Effect of strain rate on environmental hydrogen embrittlement susceptibility of a severely cold-rolled Al–Cu alloy // Vacuum. 2020. Vol. 172. Article number 109057. DOI: 10.1016/j.vacuum.2019.109057.
18. Momotani Y., Shibata A., Terada D., Tsuji N. Effect of strain rate on hydrogen embrittlement in low-carbon martensitic steel // International journal of hydrogen energy. 2017. Vol. 42. № 5. P. 3371–3379. DOI: 10.1016/j.ijhydene.2016.09.188.
19. Kappes M., Iannuzzi M., Carranza R.M. Pre-exposure embrittlement and stress corrosion cracking of magnesium alloy AZ31B in chloride solutions // Corrosion. 2014. Vol. 70. № 7. P. 667–677. DOI: 10.5006/1172.
20. Merson E., Poluyanov V., Myagkikh P., Merson D., Vinogradov A. Effect of Air Storage on Stress Corrosion Cracking of ZK60 Alloy Induced by Preliminary Immersion in NaCl-Based Corrosion Solution // Materials. 2022. Vol. 15. № 21. Article number 7862. DOI: 10.3390/ma15217862.
21. Atrens A., Shi Z., Mehreen S.U., Johnston S., Song G.L., Chen X., Pan F. Review of Mg alloy corrosion rates // Journal of magnesium and alloys. 2020. Vol. 8. № 4. P. 989–998. DOI: 10.1016/j.jma.2020.08.002.
22. Lynch S.P., Trevena P. Stress corrosion cracking and liquid metal embrittlement in pure magnesium // Corrosion. 1988. Vol. 44. № 2. P. 113–124. DOI: 10.5006/1.3583907.

Влияние скорости деформирования на механические свойства и характер разрушения сплава AZ31 и технически чистого магния, предварительно выдержанных в коррозионной среде

© 2023

Мерсон Евгений Дмитриевич*[1], кандидат физико-математических наук,
старший научный сотрудник НИИ прогрессивных технологий
Полуянов Виталий Александрович[2], кандидат технических наук,
младший научный сотрудник НИИ прогрессивных технологий
Мягких Павел Николаевич[3], младший научный сотрудник НИИ прогрессивных технологий
Мерсон Дмитрий Львович[4], доктор физико-математических наук, профессор,
директор НИИ прогрессивных технологий
Тольяттинский государственный университет, Тольятти (Россия)

***E-mail: Mersoned@gmail.com**

[1]ORCID: https://orcid.org/0000-0002-7063-088X
[2]ORCID: https://orcid.org/0000-0002-0570-2584
[3]ORCID: https://orcid.org/0000-0002-7530-9518
[4]ORCID: https://orcid.org/0000-0001-5006-4115

Поступила в редакцию 15.11.2022 *Принята к публикации 02.12.2022*

Аннотация: Магниевые сплавы являются перспективными материалами для использования в авиации, автомобилестроении и медицине, однако, вследствие низкой стойкости к коррозионному растрескиванию под напряжением (КРН), область их применения ограничена. Для создания сплавов, обладающих высокой стойкостью к КРН, требуется всестороннее изучение природы этого явления. Ранее было высказано предположение, что важную роль в механизме КРН может играть диффузионно-подвижный водород и продукты коррозии, образующиеся на поверхности магния. Однако вклад каждого из этих факторов в охрупчивание магния и его сплавов, вызванное КРН, мало изучен. Поскольку влияние диффузионно-подвижного водорода на механические свойства металлов усиливается с уменьшением скорости деформирования, актуальной задачей является исследование скоростной чувствительности восприимчивости сплавов магния к КРН. В настоящей работе исследовались технически чистый магний в литом состоянии и сплав AZ31: изучалось влияние скорости деформирования в диапазоне от $5 \cdot 10^{-6}$ до $5 \cdot 10^{-4}$ $с^{-1}$ на механические свойства, состояние боковой поверхности и излома материалов до и после выдержки в коррозионной среде и после удаления продуктов коррозии. Установлено, что предварительная выдержка в коррозионной среде приводит к охрупчиванию сплава AZ31, но не влияет на механические свойства и характер

разрушения чистого магния. Обнаружено, что охрупчивание сплава AZ31, вызванное предварительной выдержкой в коррозионной среде, проявляется в полной мере только при низкой скорости деформирования и только в том случае, если на поверхности образцов присутствует слой продуктов коррозии. Показано, что изменение скорости деформирования оказывает незначительное влияние на свойства чистого магния. Сделан вывод о том, что основной причиной охрупчивания сплава AZ31 после выдержки в коррозионной среде является слой продуктов коррозии, который, предположительно, содержит охрупчивающие агенты, такие как водород и остаточная коррозионная среда.

Ключевые слова: магниевые сплавы; AZ31; магний; коррозионное растрескивание под напряжением; коррозия; скорость деформирования; механические свойства.

Благодарности: Исследование выполнено при финансовой поддержке РНФ в рамках научного проекта № 18-19-00592.

Для цитирования: Мерсон Е.Д., Полуянов В.А., Мягких П.Н., Мерсон Д.Л. Влияние скорости деформирования на механические свойства и характер разрушения сплава AZ31 и технически чистого магния, предварительно выдержанных в коррозионной среде // Frontier Materials & Technologies. 2023. № 3. С. 71–82. DOI: 10.18323/2782-4039-2023-3-65-7.

doi: 10.18323/2782-4039-2023-3-65-8

The kinetics of $L1_0$ superstructure formation in the Cu–56Au alloy (at. %): resistometric study

© 2023

Polina O. Podgorbunskaya*[1,2], student, laboratory assistant of Strength Laboratory
Dmitry A. Zgibnev[1,2], student, laboratory assistant of Strength Laboratory
Alyona A. Gavrilova[1,2], student, laboratory assistant of Strength Laboratory
Oksana S. Novikova[2,3], PhD (Physics and Mathematics), senior researcher of Strength Laboratory
Aleksey Yu. Volkov[2,4], Doctor of Sciences (Engineering), Head of Strength Laboratory
[1]*Ural Federal University named after the first President of Russia B.N. Yeltsin, Yekaterinburg (Russia)*
[2]*M.N. Mikheev Institute of Metal Physics of Ural Branch of RAS, Yekaterinburg (Russia)*

***E-mail: podgorbunskaua@imp.uran.ru, polina.podgorbunskaya@yandex.ru**
[3]ORCID: https://orcid.org/0000-0003-0474-8991
[4]ORCID: https://orcid.org/0000-0002-0636-6623

Received 06.06.2023 *Accepted 19.07.2023*

Abstract: Due to the improved strength properties compared to the equiatomic Cu–50 at. % Au alloy, non-stoichiometric Cu–56 at. % Au alloy can be used both in dentistry and as a corrosion-resistant conductor of weak electrical signals in tool engineering. The work studies the kinetics of the disorder→order phase transformation in the Cu–56Au alloy, during which the disordered fcc lattice ($A1$-phase) is rearranged into an atomically ordered one with the $L1_0$ superstructure. The initial disordered state of the alloy was obtained in two ways: applying plastic deformation by 90 % or quenching at a temperature of above 600 °C (i. e., from the region of the $A1$-phase existence). To form the $L1_0$ superstructure, annealing was carried out at temperatures of 200, 225, and 250 °C. The annealing duration ranged from 1 h to 2 months. Resistometry was chosen as the main technique to study the kinetics of the disorder→order transformation. The temperature dependences of the electrical resistivity of the alloy in various structural states are obtained. The authors constructed the graphs of the electrical resistance dependence on the annealing time logarithm, based on which, the rate of the new phase formation was estimated. To evaluate the structural state of the alloy at various transformation stages, the authors used X-ray diffraction analysis (XRD). The crystal structure rearrangement during the transformation is shown by the example of splitting the initial cubic $A1$-phase peak (200) into two tetragonal ordered $L1_0$ phase peaks – (200) and (002). Based on the resistometry and X-ray diffraction analysis data, the authors carried out a quantitative assessment of the rate of the disorder→order phase transformation in the alloy under the study. It is established that the values of the transformed volume fraction (resistometry) and the long-range order degree (X-ray diffraction analysis) are close. The study shows that in the temperature range of 200–250 °C, the rate of atomic ordering according to the $L1_0$ type in the nonstoichiometric alloy Cu–56 at. % Au is maximum at 250 °C. It is identified that the disorder→order transformation in the initially quenched specimens of the investigated alloy proceeds approximately an order of magnitude faster than in preliminarily deformed specimens.

Keywords: Cu–56 at. % Au; Cu-Au alloys; atomic ordering; resistometry; superstructural X-ray reflections; order degree evaluation.

Acknowledgments: The work was financially supported by the Russian Science Foundation (grant No. 21-13-00135).

The paper was written using the reports of the participants of the XI International School of Physical Materials Science (SPM-2023), Togliatti, September 11–15, 2023.

For citation: Podgorbunskaya P.O., Zgibnev D.A., Gavrilova A.A., Novikova O.S., Volkov A.Yu. The kinetics of L_10 superstructure formation in the Cu–56Au alloy (at. %): resistometric study. *Frontier Materials & Technologies*, 2023, no. 3, pp. 83–94. DOI: 10.18323/2782-4039-2023-3-65-8.

INTRODUCTION

The formation of an atomically ordered crystal lattice was discovered by Russian scientists more than 100 years ago, when studying the structure formed in a gold-copper alloy as a result of slow cooling from high temperature [1]. Since then, the formation of the structure and properties in the system of gold – copper alloys has been repeatedly studied in detail using various research techniques [2–4]. In the work [2], the authors studied the diffraction patterns, and obtained the concentration dependence of the specific electrical resistivity of the equiatomic CuAu alloy in various structural states. The formation of a lamellar structure in the CuAuI alloy in the temperature range of 270–370 °C was recorded in [3]. The lamellar structure consists of colonies of lamellar c-domains, where within one colony, the domains are in a twin orientation relative to the plane of their boundary {110}. As [5] shows, planes of this particular type are the planes of optimal conjugation in the fcc→fct transition. In [6], using the molecular dynamics method, computer experiments were carried out for the estimated block of an ordered CuAuI alloy with the $L1_0$ superstructure. It was shown that during thermal activation, if there are single vacancies in the alloy, they will tend to form vacancy complexes, for example, divacancies. The EBSD analysis of the CuAu alloy microstructure, was successfully used, to study the $L1_0$ phase orientations in the $A1$ matrix and showed the following orientation relationships:

(101)$L1_0$//{110}$A1$ and [010]$L1_0$//[010]$A1$ [7]. The lamellar structure is also observed during the formation of a long-period ordered phase of the CuAuII type [4]. A rather detailed analysis of the features of atomic ordering in the system of Cu–Au alloys is given in [8], which also presents an improved phase diagram and gives a crystallographic description of the formed ordered structures. The increased interest in these alloys is caused not only by the need to clarify the crystallography of the transformation of a disordered crystal lattice into an atomically ordered one. The fact is that gold-copper alloys are the basis of materials for various practical applications: this is both jewellery or dentistry and corrosion-resistant alloys for tool engineering [5; 9]. A detailed description of all areas of application of gold–copper alloys with references to relevant sources is given in [10].

According to the phase diagram of the Cu–Au system, upon cooling from high temperatures, several structural-phase transformations occur in alloys close to the equiatomic composition. First, near 400 °C, in the disordered fcc structure ($A1$-phase), an orthorhombic ordered CuAuII phase is formed, which, upon further cooling, rearranges into the ordered CuAuI phase. There are coexistence regions between these phases: ($A1$+CuAuII) and (CuAuI+CuAuII) [8]. A schematic view of the crystal lattice ordered according to the CuAuI-phase type is shown in Fig. 1. The orthorhombic CuAuII phase crystal lattice can be represented as 10 CuAuI phase crystal lattices, arranged together along the *a*-axis with an antiphase shear-type boundary in the middle.

The (100) type planes of the CuAuI phase crystal lattice are periodically filled with either gold or copper atoms (Fig. 1). Therefore, the initial fcc lattice becomes tetragonal as a result of atomic ordering, and the tetragonal *c*-axis is perpendicular to the lamination direction. At the same time, the lattice parameter slightly increases along the *a* and *b* axes, and decreases along the *c* axis. Such a rearrangement leads to the fact that the disorder→order phase transition in gold-copper alloys is accompanied by a decrease in the crystal lattice volume by approximately 1 % causing strong internal stresses. Shape distortion or even spontaneous destruction of jewellery due to atomic ordering, has been described in the literature [9; 11] many times. The scientific basis for solving problems with distortion or cracking of gold products, is given in [5] using the example of a detailed study of the structure and properties of the equiatomic Cu–50Au alloy in various structural states.

Previously, the equiatomic Cu–50Au (at. %) alloy was studied in most detail. Fewer works study alloys with a small deviation from stoichiometry. In the work [12], high-temperature *in situ* X-ray diffraction and mechanical spectroscopy, were applied to study phase transitions in the Au–25 wt. % Cu alloy when heating and cooling at a rate of 1 K/min (note that this composition corresponds with high accuracy to the equiatomic Cu–50Au alloy). Upon continuous heating, the following sequence of phase transitions was recorded: $A1$→AuCuI→AuCuII→$A1$, and upon subsequent cooling: $A1$→$A1$+AuCuI+AuCuII→AuCuI+AuCuII→AuCuI. In [13], the influence of plastic deformation on the ordered and disordered jewellery "red gold" alloy of the Cu–Au–Ag composition is described. It was identified that preliminary deformation reduces the temperature of the ordering process onset. However, this result can be explained by the influence of silver precipitation on the transformation acceleration [14]. In the work [15], the authors studied a method for determining the phase composition on the Cu (9.38%)–Au (90.62%) and Au (74.11%)–Cu (25.89%) alloys using laser-induced breakdown spectroscopy. Using the molecular dynamics method, the work [16] presents the results of computer simulation of the synthesis of binary Cu–Au nanoclusters, upon condensation from a high-temperature gaseous medium of Cu_3Au, CuAu, Cu90Au10, and Cu60Au40 chemical compositions. The theoretical possibility of the formation of binary Cu–Au clusters of a certain size with a certain predetermined chemical composition from the gas phase was established.

There are practically no publications dealing with the study of the structure and properties of gold-copper alloys with a deviation from stoichiometry of more than 5 %. Meanwhile, such alloys are of interest for various technical applications, for example, for the production of conductors of weak electrical signals operating in highly corrosive media. For example, the Cu–56Au alloy (at. %) is mass-produced under the ZlM-80 brand. However, the kinetics of the disorder→order transition in this alloy has been barely studied. It was found in [17] that the maximum rate of atomic ordering in the Cu–56Au (at. %) alloy falls within the temperature range of 300–350 °C,

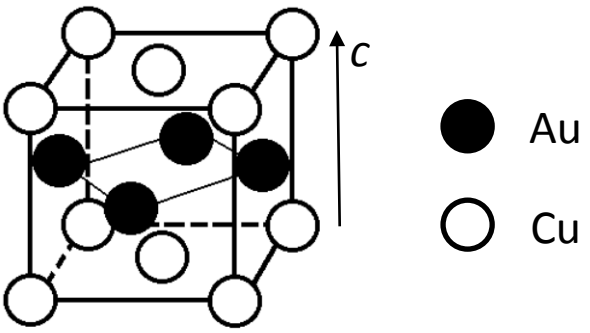

Fig. 1. *Schematic view of the crystal lattice of the ordered CuAuI phase*
Рис. 1. *Схематическое изображение кристаллической решетки атомно-упорядоченной фазы CuAuI*

and the orthorhombic ordered CuAuII phase is formed in this case. The work [14] shows that the rate of the Cu–56Au alloy ordering is much lower than that of the equiatomic CuAu alloy. It was established that slow (at a rate of 12 deg/h) cooling from 600 °C to room temperature is the fastest way to form an ordered state in the Cu–56Au alloy. However, as a result of such treatment, the high-temperature CuAuII phase appears in the alloy and not the equilibrium CuAuI phase, which is expected on the basis of the phase diagram. It is shown that the orthorhombic ordered CuAuII phase formed in the alloy has a high thermal stability, and is retained even after long-term low-temperature annealing. Thus, the kinetics of the formation of the low-temperature ordered CuAuI phase in the Cu–56Au alloy has not yet been studied in detail.

The purpose of this work is to find out the rate of atomic ordering of the $L1_0$ type in the Cu–56Au alloy in the temperature range of 200–250 °C.

METHODS

For the study, an alloy was taken, which contains 56 at. % of gold and 44 at. % of copper (or 80 wt. % Au and 20 wt. % Cu). According to the Cu–Au system phase diagram [8], the disorder→order phase transition in the alloy under study occurs at temperatures below 375 °C. Therefore, the initial, disordered state in the alloy samples was formed by quenching from a temperature of 600 °C after annealing for 1 h. Moreover, the authors studied the influence of preliminary plastic deformation on the kinetics of atomic ordering. In this case, the initial disordered state was formed by the deformation of the samples by 90 %.

The study of the transformation kinetics in this work was carried out in the temperature range of 200–250 °C. The duration of heat treatments during the study ranged from 1 h to 2 months. All heat treatments were carried out in evacuated glass or quartz ampoules.

As the main research technique in our work, resistometry was chosen. Electrical resistivity at room temperature was measured, using the standard four-probe method on long wire samples with a diameter of 0.25 mm at a constant current I=20 mA. The measurement accuracy was $\pm 0.04 \cdot 10^{-8}$ Ohm·m. Moreover, the temperature dependences of the electrical resistivity during heating and cooling of the samples at a constant rate of 120 deg/h were constructed.

Based on the resistometry data, the authors estimated the relative volume of the new phase using the formula

$$\eta = \frac{\rho_{dis} - \rho_t}{\rho_{dis} - \rho_{LRO}},$$

where η is the transformed volume fraction;
ρ_{dis} and ρ_{LRO} are the specific electrical resistivity values of samples in the state of disorder and long-range order (LRO), respectively;
ρ_t is the specific electrical resistivity of the sample at a certain stage of heat treatment.

X-ray diffraction analysis (hereinafter referred to as XRD) was carried out on the alloy plates 0.3 mm thick using a PANalytical Empyrean Series 2 diffractometer in Cu-Kα radiation. To determine the LRO degree, the ratio of the integral intensities of the superstructural and fundamental peaks was calculated using known formulas [18; 19]. Calculations were carried out for several pairs of reflections, after which the average value was determined. Such an approach is necessary to minimise the influence of texture effects on the result. X-ray diffraction calculations were carried out only after annealings of maximum duration.

RESULTS

Fig. 2 shows the Temperature dependences of electrical resistivity obtained during heating of initially deformed (Fig. 2 a) or quenched (Fig. 2 b) samples of the Cu–56Au alloy after annealings of various durations (from 1 h to 2 months) at a temperature of 250 °C. Note that some of the temperature dependences we obtained are not shown in Fig. 2: at long exposure times, the electrical resistivity of the samples changes insignificantly, so the curves begin to overlap each other.

The electrical resistivity of the Cu–56Au alloy disordered by quenching is $\rho=14.29 \cdot 10^{-8}$ Ohm·m. An alloy disordered by severe plastic deformation (90 %) has a lower electrical resistivity – $\rho=14.06 \cdot 10^{-8}$ Ohm·m.

Comparison of temperature dependences given in Fig. 2 shows that the decrease in electrical resistivity caused by atomic ordering occurs somewhat faster, in the quenched sample. For example, when an initially deformed sample is heated, the dependence remains almost linear up to 200 °C. In turn, in the quenched sample, a slight drop in electrical resistivity begins at about 150 °C. Continued heating leads to a gradual decrease in electrical resistivity. The electrical resistivity minimum values are achieved at a temperature of ~320 °C regardless of the initial state of the samples. Further heating causes a rather sharp increase in electrical resistivity, which is caused by a change in the alloy phase composition: CuAuI→CuAuII→$A1$. At temperatures above 380 °C, the alloy becomes single-phase and disordered, which results in a linear dependence of the electrical resistivity.

All the transformations described above are quite clearly identified on the graphs of the temperature derivatives of the corresponding electrical resistivity dependences (Fig. 3). In Fig. 3 a, two peaks are revealed in the temperature range of 300–400 °C. The first of them, with a maximum at about 350 °C, corresponds to the CuAuI→CuAuII transformation. The second peak, whose maximum falls at ~380 °C, corresponds to the CuAuII→$A1$ transformation. When comparing the dependencies in Fig. 3 a, it is well seen that in the pre-quenched sample, these peaks are clearly separated and have a higher intensity.

Fig. 2 clearly shows that after annealings of the same duration, the specific electrical resistivity of pre-quenched samples is always lower. After annealing of the quenched alloy for 2 months at a temperature of 250 °C, its specific electrical resistivity decreases to $\rho=7.04 \cdot 10^{-8}$ Ohm·m. As follows from Fig. 2, after annealing of the same duration, the initially deformed sample has a significantly higher value of electrical resistivity. Consequently, a LRO state has not yet formed in this sample. What calls attention is the fact that after annealings of the maximum duration, clearly pronounced steps are observed in the temperature dependences of the electrical resistivity (shown in the insets in Fig. 2 a and 2 b). They are especially visible after annealing of pre-quenched samples. The difference, in reaction rates at different temperatures, is clearly seen in the graphs of

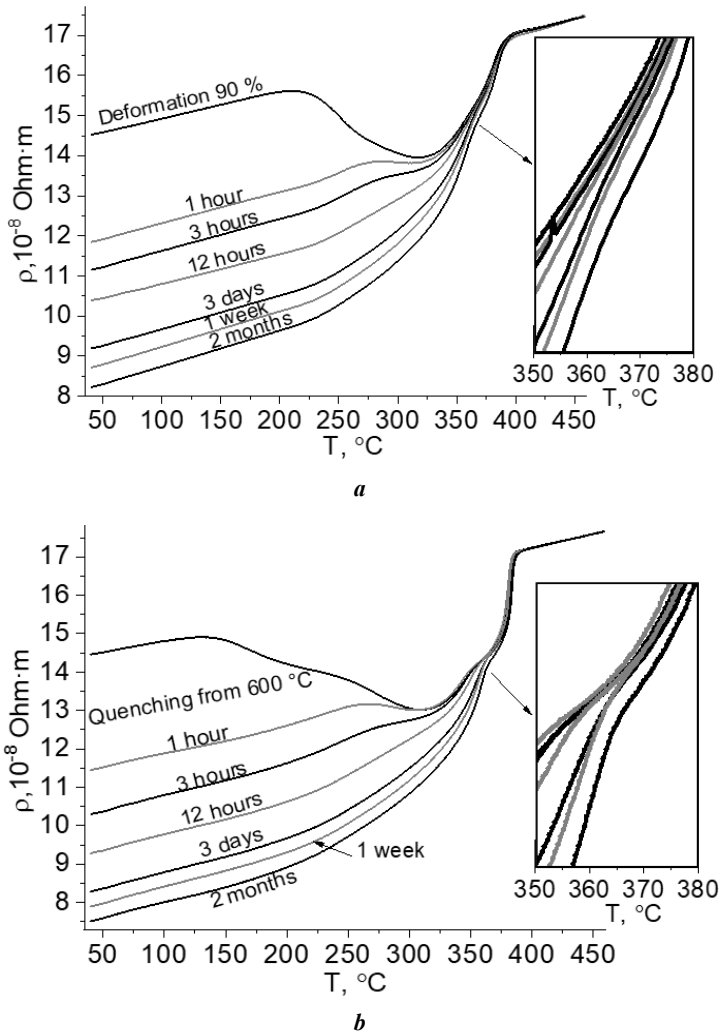

Fig. 2. *Temperature dependences of electrical resistivity obtained when heating the deformed (**a**) and quenched (**b**) specimens of the Cu–56Au alloy, which were annealed at a temperature of 250 °C from 1 h to 2 months. The insets show the regions where the step change in the electrical resistance is observed*

Рис. 2. *Температурные зависимости электросопротивления, полученные при нагреве деформированных (**а**) и закаленных (**b**) образцов сплава Cu–56Au, которые отжигались при температуре 250 °C от 1 ч до 2 мес. На вставках показаны участки, на которых наблюдается ступенчатое изменение электросопротивления*

temperature derivatives (Fig. 3 b). The narrow and intense peaks in the graphs of the temperature derivatives of the electrical resistivity, once again confirm the higher degree of atomic order achieved as a result of annealing of the pre-quenched alloy.

Fig. 4 shows XRD patterns of samples in two initial states, as well as after their annealing for 1 h and 2 months at 250 °C.

According to the data obtained, the lattice parameter of the 90 % deformed Cu–56Au alloy is a=0.3912 nm. The X-ray peaks of the deformed alloy are quite wide, which is caused by elastic stresses and a large number of nonequilibrium boundaries [20]. Annealing at a high temperature relieves stress, and reduces the structure defect, as a result of which the crystal lattice parameter of the quenched alloy decreases to a=0.3901 nm. Compared to the deformed state, the X-ray peaks of the quenched alloy are very narrow and have a high intensity (one can compare XRD patterns 1 in Fig. 4 a and 4 b).

The ordered arrangement of atoms in the crystal lattice changes the conditions for X-ray reflection, as a result of which the number of peaks in the diffraction patterns of annealed samples increases significantly. Peaks (001), (011), etc. appear, which are forbidden for the fcc structure. Such additional peaks are called superstructural, and the ordered lattice itself is called a superstructure. Moreover, additional fundamental peaks appear in the XRD patterns of the $L1_0$ superstructure. For example, the original fundamental peak (200) is split into two peaks – (200) and (002). This is caused by the rearrangement of the initial disordered fcc lattice into an ordered tetragonal structure (Fig. 1). According to the obtained XRD data, annealing of the quenched alloy for 2 months at a temperature of 250 °C leads to the formation of an $L1_0$ superstructure, the crystal lattice of which has the following parameters: a=0.3963 nm and c=0.3671 nm.

Since the crystal lattice parameter along the a and b axes slightly increases during atomic ordering, the reflections

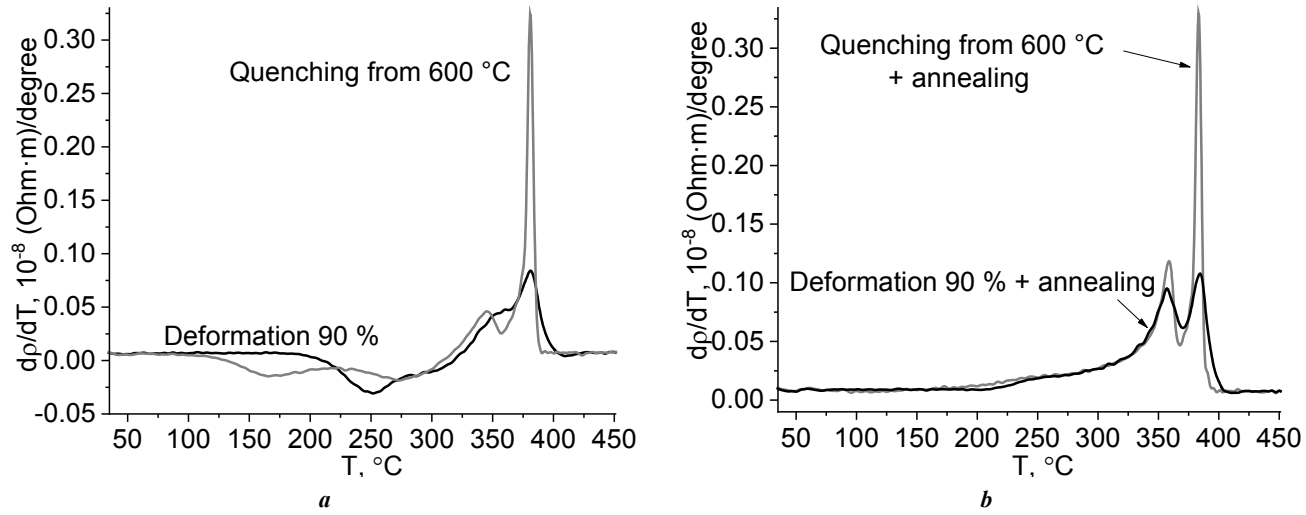

Fig. 3. *Temperature derivatives of the electrical resistivity dependences (Fig. 2) obtained when heating specimens of the Cu–56Au alloy in two initial states* ***(a)*** *and after annealing of these specimens at a temperature of 250 °C during 2 months* ***(b)***
Рис. 3. *Температурные производные зависимостей электросопротивления (рис. 2), полученные при нагреве образцов сплава Cu–56Au в двух исходных состояниях* ***(a)*** *и после отжигов этих образцов при температуре 250 °C в течение 2 мес.* ***(b)***

from these planes shift to the left of the original peak. In turn, the new peak (002) is a reflection from the planes, the interplane distance between which (along the *c*-axis) is less than the original one, in consequence of which this peak is formed to the right of the original one. Obviously, in the equilibrium state, the intensity of the (200)$L1_0$ peak should be two times higher than that of the (002)$L1_0$ peak. In Fig. 4, this condition is practically met only for the sample that was annealed after preliminary quenching. In full accordance with the resistometric data, annealing of the sample, initially deformed for 2 months at 250 °C does not lead to a diffraction pattern corresponding to a well-ordered state.

The curves in Fig. 5 show the change in the electrical resistivity of the alloy under study during long-term heat treatments in the selected temperature range. Due to differences in the mechanisms of formation of an ordered structure, these dependences are plotted separately for the initially deformed and pre-quenched states of the alloy. At the annealing temperature of 250 °C, the left points (i.e., at room temperature) on the corresponding temperature dependences of the electrical resistivity were taken to construct these graphs (Fig. 2).

As follows from the graphs in Fig. 5, regardless of the initial state, the rate of decrease in electrical resistivity during annealing is maximum at a temperature of 250 °C. Based on this, one can make an unambiguous conclusion that the rate of the disorder→order phase transition at this temperature is maximal as well. In turn, the rate of decrease in electrical resistivity at a temperature of 200 °C is minimal.

Fig. 6 shows XRD patterns obtained from samples that were held for 2 months at temperatures of 200, 225, and 250 °C. Note that, regardless of the annealing temperature, diffraction patterns with more intense peaks correspond to pre-quenched samples. A quenched sample annealed at a temperature of 250 °C has the clearest pattern of X-ray reflections, fully corresponding to a LRO structure with the $L1_0$ type. Thus, the conclusions made based on the resistometry data are again well confirmed by the X-ray diffraction data.

Fig. 6 clearly shows that the XRD patterns from the samples annealed at 200 °C, do not have some peaks typical of the ordered state (for example, (002)). This means that the phase transition at this temperature is still far from completion. Such a slow phase transition rate allows tracing the initial stages of the rearrangement of the disordered fcc structure into the $L1_0$ ordered one. Fig. 7 shows the initial (200)$A1$ peak splitting into two peaks – (200)$L1_0$ and (002)$L1_0$ (in the range of 2θ angles from 44 to 50°), which gives the clearest picture of the ordered structure formation. Previously, similar experiments were carried out on the equiatomic CuAu alloy [21]. However, the high transition rate did not allow observing all the structural rearrangement stages.

As follows from the data shown in Fig. 7, a shoulder appears on the left side of the initial peak (200) at the first stage of ordering. Therefore, *a* and *b* planes of the ordered phase, which have a larger interplanar spacing compared to the disordered matrix, are first formed. The (002)$L1_0$ peak, which is formed from tetragonal *c*-planes with a smaller parameter, becomes clearly visible only after 1 month of annealing at a temperature of 200 °C. In Fig. 7, the different rates of the ordered structure formation in the deformed and quenched samples again are clearly revealed. Here, one can also compare the different widths of X-ray reflections from heavily deformed or quenched samples.

The set of results obtained in this work allows quantifying the rate of the disorder→order phase transition in the alloy under study in the temperature range of 200–250 °C (Fig. 8).

Moreover, the LRO degree *(S)*, averaged over the sample, can be estimated based on the XRD-data in Fig. 6. Note that both considered parameters (η and *S*) have the same physical

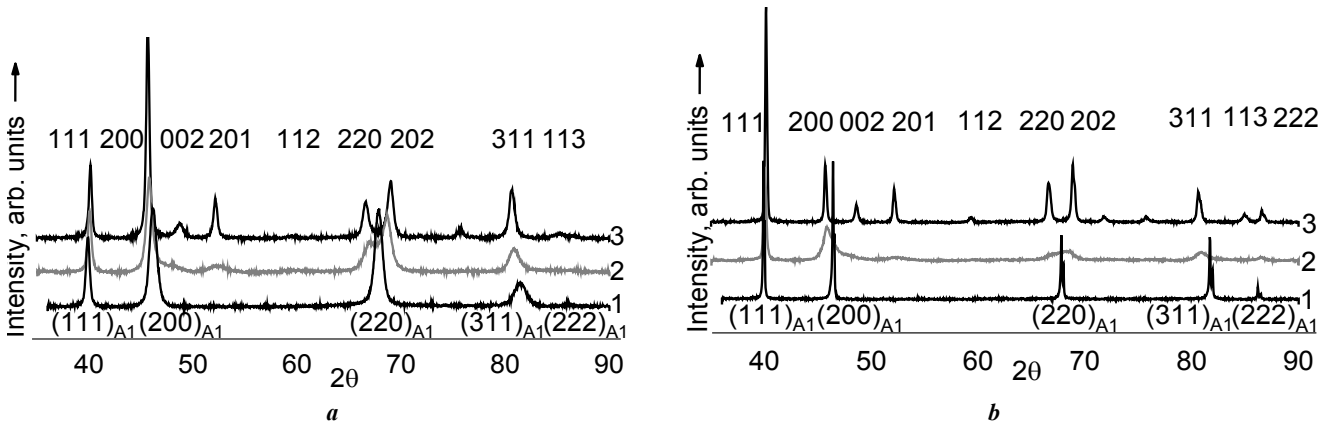

Fig. 4. *The results of XRD analysis of specimens of the deformed (**a**) and quenched (**b**) alloy in the initial states (1), after annealing during 1 h (2) and 2 months (3) at 250 °C*

Рис. 4. *Результаты РСА-исследования образцов деформированного (**a**) и закаленного (**b**) сплава в исходных состояниях (1), после отжига в течение 1 ч (2) и 2 мес. (3) при 250 °C*

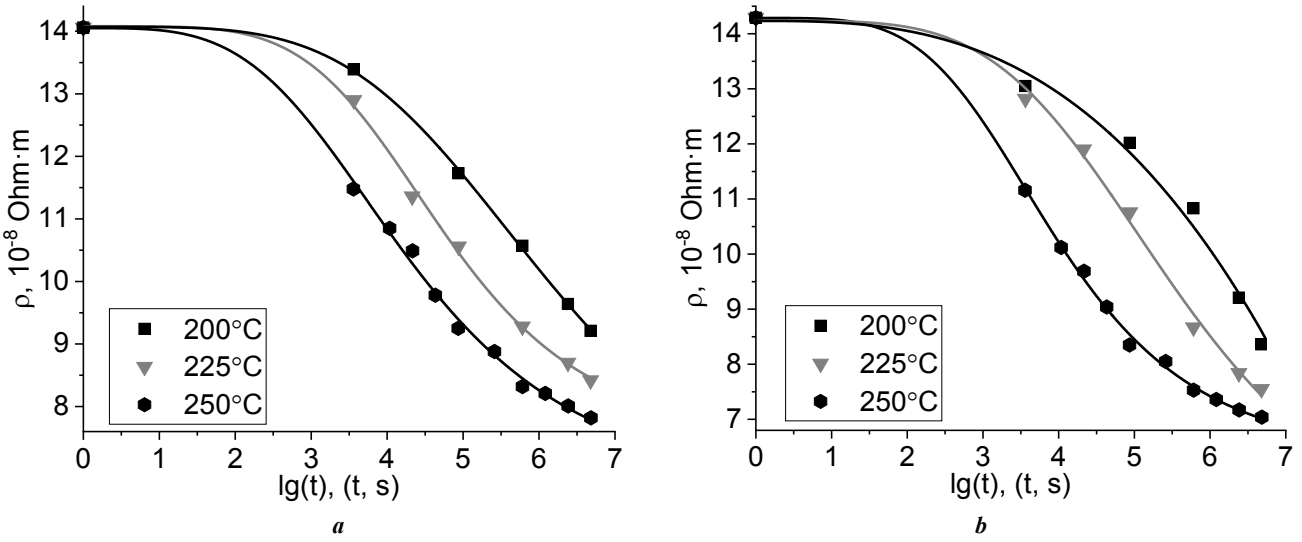

Fig. 5. *Change in the specific electrical resistance of the initially deformed (**a**) and quenched (**b**) specimens of the alloy under study in the process of annealing at temperatures of 200, 225, and 250 °C*

Рис. 5. *Изменение удельного электросопротивления исходно деформированных (**a**) и закаленных (**b**) образцов исследуемого сплава в процессе отжигов при температурах 200, 225 и 250 °C*

significance, and differ only in the method on the basis of which they were obtained. The values of the LRO degree determined, based on the XRD-data, are shown by points in Fig. 8. Moreover, due to the insufficient number of superstructural peaks, we failed to estimate the fraction of the transformed volume after annealing of the deformed sample at temperatures of 200 and 225 °C.

DISCUSSION

Previously, we assumed [14] that annealing at 250 °C is optimal for the $L1_0$ superstructure formation in the Cu–56Au alloy. It was found as well that holding at this temperature for 1 week is far from sufficient for the formation of a well-ordered state in this alloy. The study completely confirmed the previously obtained conclusions, and showed that to complete the disorder→order phase transition, it is necessary to anneal the nonstoichiometric Cu–56Au alloy for at least 2 months at 250 °C. Lowering the processing temperature significantly, slows down the transition rate. In addition, it was reliably identified that the atomic ordering rate depends heavily on how the initial, disordered state was formed in the alloy: by quenching from high temperature or by plastic deformation.

All the obtained results indicate that the rate of ordering of pre-quenched samples is higher in the studied temperature range. This seems unusual, since plastic deformation significantly increases the rate of diffusion reactions [22]. For example, the rate of ordering of preliminarily deformed alloys is higher, as a rule [18; 23]. Thus, the phenomenon of a decrease in the ordering rate after preliminary deformation observed in the Cu–56Au alloy requires an explanation.

As was shown in [24], by high-resolution electron microscopy, clusters 2–3 nm in size with a high LRO degree,

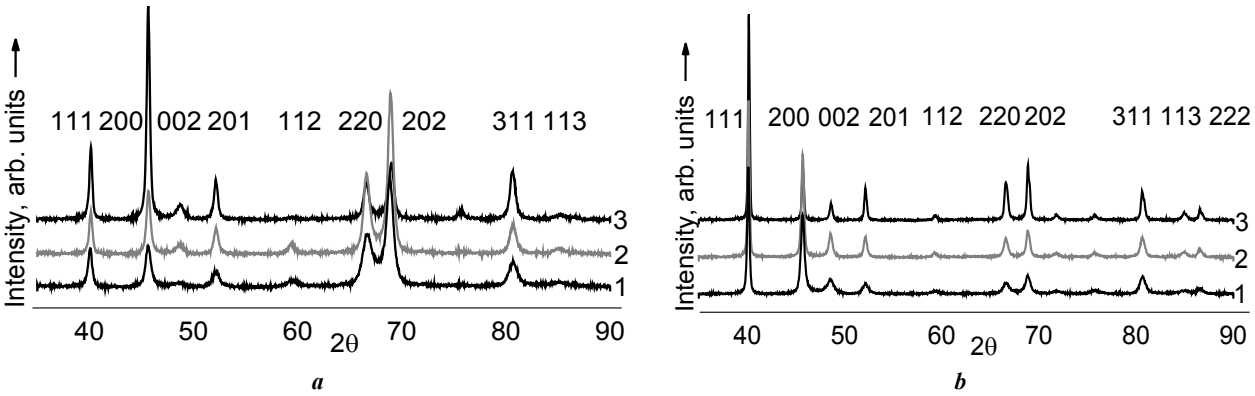

Fig. 6. *X-ray diffraction patterns obtained from the initially deformed (**a**) and quenched (**b**) specimens annealed during 2 months at temperatures of 200 (1), 225 (2), and 250 °C (3)*

Рис. 6. *Рентгеновские дифрактограммы, полученные с исходно деформированных (**a**) и закаленных (**b**) образцов, отожженных в течение 2 мес. при температурах 200 (1), 225 (2) и 250 °C (3)*

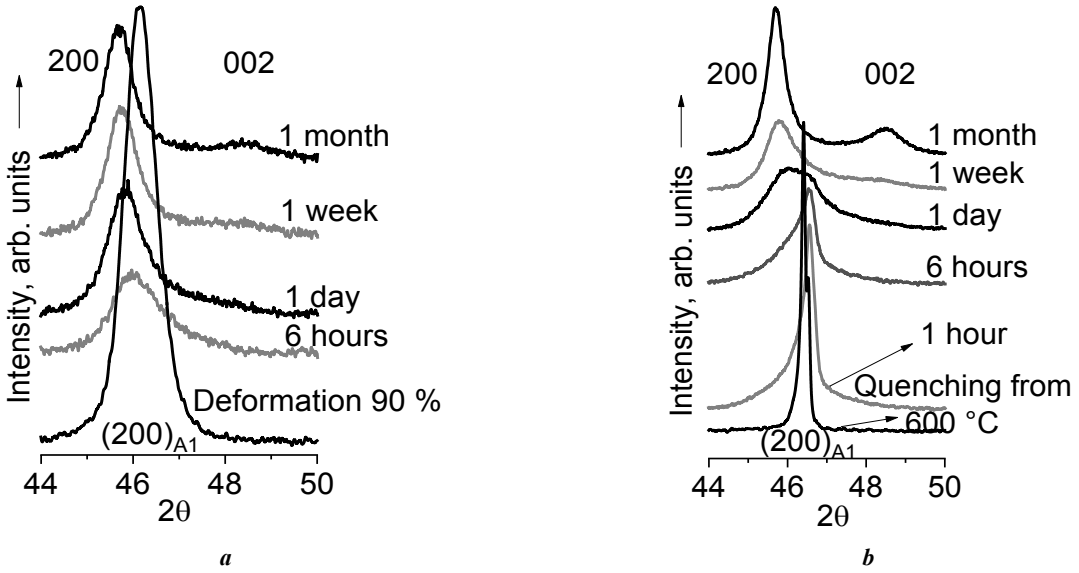

Fig. 7. *X-ray reflection (200) evolution during atomic ordering at a temperature of 200 °C of the initially deformed (**a**) and quenched (**b**) specimens*

Рис. 7. *Эволюция рентгеновского отражения (200) в ходе атомного упорядочения при температуре 200 °C исходно деформированных (**a**) и закаленных (**b**) образцов*

are formed in gold-copper alloys even during quenching. The number of these clusters is determined by the temperature and quenching rate. Cases when quenching of gold-copper alloys led to the formation of a strong short-range order in them have been described in the literature many times. In this case, in addition to strong reflections from the disordered fcc phase, the XRD patterns show the extended maxima at the positions of superstructural reflections (as an example, see Fig. 1 a in [12]). The formation of ordered nanoclusters in the alloy, during quenching, also leads to a significant increase in electrical resistivity (initial points in Fig. 2 a and 2 b). Plastic deformation destroys these clusters, as a result of which the alloy electrical resistivity decreases [23; 25].

In turn, in a strongly deformed alloy, a combined reaction occurs: the atomic ordering process is accompanied by recrystallisation. The paper [26] describes the possible options: either ordering and recrystallisation are implemented jointly, or one of these solid-state reactions overtakes the other. Most often, the boundary of a growing recrystallised grain is simultaneously an interphase boundary [27]. The progress of recrystallisation can be judged from the decrease in the width of X-ray peaks during annealing of the deformed alloy. Indeed, it is clearly seen in Fig. 7 a that when increasing the duration of heat treatment of the initially deformed alloy, the broad peak (200) gradually becomes narrower.

Thus, the difference in the rates of disorder→order transition is caused by the difference in the mechanisms of the ordered state formation in quenched or deformed samples of the same alloy. Even a slight heating of a quenched sample leads to the fact that the ordered clusters in it become the nuclei of a new phase. In turn, to initiate the phase transition in a deformed alloy, it must be heated to the recrystallisation temperature.

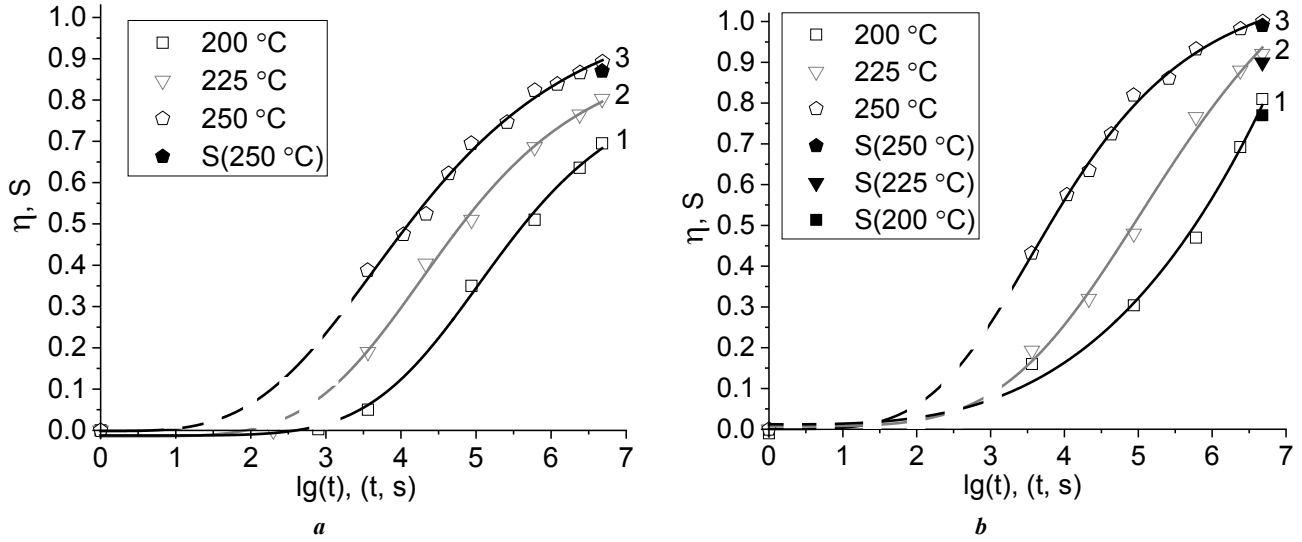

Fig. 8. *The transformed fraction as a function of the annealing time of the deformed (**a**) and quenched (**b**) specimens of the Cu–56Au alloy at temperatures of: 200 (1), 225 (2), and 250 °C (3) built according to the resistometry data. Evaluation based on the XRD-results was carried out after maximum duration annealing and is shown by points*

Рис. 8. *Изменение доли превращенного объема от продолжительности отжига деформированных (**а**) и закаленных (**b**) образцов сплава Cu–56Au при температурах: 200 (1), 225 (2) и 250 °C (3), построенные по данным резистометрии. Оценки на основе РСА-результатов проводились после отжигов максимальной продолжительности и показаны точками*

Of course, the results obtained during resistometry of the alloy samples after maximum duration annealings are of special interest. As mentioned above, the minimum electrical resistivity of the Cu–56Au alloy achieved in this work is $\rho=7.04\cdot10^{-8}$ Ohm·m. It was obtained by annealing of a quenched alloy for 2 months at a temperature of 250 °C. To verify the result obtained, an additional annealing of this sample was carried out for another 2 months. This processing slightly influenced the value of electrical resistivity, which amounted to $\rho=6.98\cdot10^{-8}$ Ohm·m. This allows concluding that to complete the disorder→order phase transition in the Cu–56Au alloy at a temperature of 250 °C, annealing for 2 months is required. Note that the electrical resistivity values obtained during the study are quite lower than the known literature data. Previously, we have already concluded that the generally accepted concentration dependence of the electrical resistivity of the Cu–Au system alloys (see Fig. 46 in [9]) needs to be refined [28].

The results of the XRD study of the nonstoichiometric Cu–56Au alloy obtained in our work can be compared with the literature data [29] given for the stoichiometric Cu–50Au alloy. For example, the crystal lattice parameters of an equiatomic alloy ordered after the $L1_0$ type (a=0.3958 nm, c=0.3666 nm) are somewhat smaller than those under study. However, the tetragonality degrees of the ordered lattices of both alloys are equal and amount to c/a=0.926. This is a rather interesting result that will allow reasoning about the structure of a nonstoichiometric alloy at the atomic level. Indeed, when deviating from stoichiometry, the question always arises: how the excess number of atoms (in this case, gold) is redistributed during the superlattice formation. If we assume that some of the gold atoms are embedded in the copper sublattice, this should lead to a difference in the tetragonality degrees of the crystal lattices of the alloys. Most likely, in the process of atomic ordering, an excess amount of gold atoms is displaced onto defects and boundaries of various nature (for example, c-domain boundaries, thermal antiphase domain boundaries (APBs), shear-type APBs, grain boundaries, etc.). This is indirectly confirmed by the higher strength (by ~15 %) of the ordered nonstoichiometric alloy compared to the equiatomic one. This hypothesis was put forward for the first time and requires verification using structural research methods (for example, high-resolution electron microscopy).

The study showed that the results of a quantitative assessment of the phase transition rate ($A1\rightarrow L1_0$) based on the resistometry and XRD data are close (Fig. 8). This makes it possible, using two methods, to compare the rate of atomic ordering of nonstoichiometric alloy samples in different initial states. For example, the fraction of the transformed volume after the deformed alloy annealing at a temperature of 250 °C for 2 months is η=0.89 (according to resistometric data) or S=0.87 (according to X-ray diffraction data). In the initially quenched alloy, similar values of the transformed volume fraction are achieved after annealing for ~4 days (i.e., an order of magnitude faster).

CONCLUSIONS

1. It was established that the formation of the $L1_0$ superstructure in the initially quenched nonstoichiometric Cu–56Au alloy, occurs approximately an order of magnitude faster than in the pre-deformed alloy.

2. It was identified that in the temperature range of 200–250 °C the maximum rate of ordering of the nonstoichiometric Cu–56Au alloy is observed at 250 °C; however, even in this case 2 months' exposure is necessary to form a LRO state with $L1_0$ superstructure.

3. It was suggested that during the disorder→order phase transition, excess (compared to stoichiometry) gold atoms are not built into the copper sublattice, but are displaced onto domain walls and other defects.

4. Based on the obtained data, for the first time for the Cu–56Au alloy, kinetic *C*-curves can be plotted and the thermodynamic *n* and *k* constants calculated in the temperature range of 200–250 °C for the disorder→order transition ($A1 \rightarrow L1_0$).

REFERENCES

1. Kurnakov N., Zemczuzny S., Zasedatelev M. Transformations in Alloys of Gold with Copper. *Journal of the Institute of Metals*, 1916, vol. 15, pp. 305–331.
2. Jogansson C.H., Linde J.O. Röntgenographische und elektrische Untersuchungen der CuAu-Systems. *Annalen der Physik*, 1936, vol. 417, no. 1, pp. 1–48. DOI: 10.1002/andp.19364170102.
3. Hirabayashi M. Stress-Ordering Effect on Thermal Expansion of CuAu Single Crystals. *Journal of the Physical Society of Japan*, 1959, vol. 14, pp. 149–152. DOI: 10.1143/JPSJ.14.149.
4. Van Tendeloo G., Amelinckx S., Jeng S.J., Wayman C.M. The initial stages of ordering in CuAuI and CuAuII. *Journal of Materials Science*, 1986, vol. 21, pp. 4395–4402. DOI: 10.1007/BF01106562.
5. Getov L.A., ed. *Khudozhestvennoe litye iz dragotsennykh metallov* [Artistic casting from precious metals]. Leningrad, Mashinostroenie Publ., 223 p.
6. Popova L.A. Structural and energy properties of bivacansions in CuAu alloy. *Yugra state university bulletin*, 2022, vol. 66, no. 3, pp. 145–151. DOI: 10.18822/byusu202203145-151.
7. Larcher M., Cayron C., Blatter A., Soulignac R., Logé R.E. Electron backscatter diffraction study of variant selection during ordering phase transformation in $L1_0$-type red gold alloy. *Journal of Applied Crystallography*, 2019, vol. 52, pp. 1202–1213. DOI: 10.1107/S1600576719011890.
8. Fedorov P.P., Volkov S.N. Au-Cu phase diagram. *Russian journal of inorganic chemistry*, 2016, vol. 61, no. 6, pp. 809–812. DOI: 10.7868/S0044457X16060061.
9. Malyshev V.M., Rumyantsev D.V. *Zoloto* [Gold]. Moscow, Metallurgiya Publ., 1979. 288 p.
10. Trong D.N., Long V.C., Saraç U., Quoc V.D., Ţălu Ş. First-Principles Calculations of Crystallographic and Electronic Structural Properties of Au-Cu Alloys. *Journal of Composites Science*, 2022, vol. 6, no. 12, pp. 383. DOI: https://doi.org/10.3390/jcs6120383.
11. Volkov A.Y., Kazantsev V.A. Impact of the initial state on the structure and properties of the ordered CuAu alloy. *The physics of metals and metallography*, 2012, vol. 113, no. 1, pp. 66–76. DOI: 10.1134/S0031918X12010127.
12. Lamiri I., Martinez-Blanco D., Abdelbaky M.S.M., Mari D., Hamana D., García-Granda S. Investigation of the order-disorder phase transition series in AuCu by in-situ temperature XRD and mechanical spectroscopy. *Journal of Alloys and Compounds*, 2019, vol. 770, pp. 748–754. DOI: 10.1016/j.jallcom.2018.08.094.
13. Garcia-Gonzalez M., Van Petegem S., Baluc N., Hocine S., Dupraz M., Lalire F., Van Swygenhoven H. Enhanced precipitate growth at reduced temperatures during chemical ordering in deformed red gold alloys. *Scripta Materialia*, 2019, vol. 170, pp. 129–133. DOI: 10.1016/j.scriptamat.2019.05.038.
14. Volkov A.Yu., Antonova O.V., Glukhov A.V., Komkova D.A., Antonov B.D., Kostina A.E., Livinets A.A., Generalova K.N. Features of the disorder-order phase transition in non-stoichiometric Cu-56at%Au alloy. *Journal of Alloys and Compounds*, 2022, vol. 891, p. 161938. DOI: 10.1016/j.jallcom.2021.161938.
15. Farooq Z., Ali R., Ahmed N., Fahad M., Ahmad A., Yaseen M., Mahmood M.H.R., Hussain S., Rehan I., Zubair Khan M., Jan T., Qayyum M.A., Afzal M., Mahr M.S., Shafique M. Determination of the Gold Alloys Composition by Laser-Induced Plasma Spectroscopy Using an Algorithm for Matching Experimental and Calculated Values of Electron Number Density. *Journal of Applied Spectroscopy*, 2023, vol. 90, pp. 126–136. DOI: 10.1007/s10812-023-01513-x.
16. Gafner Y.Y., Gafner S.L., Golovenko Z.V. Analysis of the size distribution of binary Cu-Au nanoparticles during synthesis from a gaseous medium. *Letters on Materials*, 2020, vol. 10, no. 1, pp. 33–37. DOI: 10.22226/2410-3535-2020-1-33-37.
17. Generalova K.N., Glukhov A.V., Volkov A.Y. Kinetics of atomic ordering by $L1_0$-type in non-stoichiometric copper-gold alloy: X-ray analysis. *Bulletin of Perm national research polytechnic university. Mechanical engineering, materials science*, 2018, vol. 20, no. 2, pp. 75–85. DOI: 10.15593/2224-9877/2018.2.09.
18. Volkov A.Yu., Novikova O.S., Antonov B.D. The kinetics of ordering in an equiatomic CuPd alloy: A resistometric study. *Journal of Alloys and Compounds*, 2013, vol. 581, pp. 625–631. DOI: 10.1016/j.jallcom.2013.07.132.
19. Glezer A.M., Timshin I.A., Shchetinin I.V., Gorshenkov M.V., Sundeev R.V., Ezhova A.G. Unusual behavior of long-range ordered parameter in Fe_3Al superstructure under severe plastic deformation in Bridgman anvils. *Journal of Alloys and Compounds*, 2018, vol. 744, pp. 791–796. DOI: 10.1016/j.jallcom.2018.02.124.
20. Valiev R.Z., Aleksandrov I.V. *Nanostrukturnye materialy, poluchennye intensivnoy plasticheskoy deformatsiey* [Nanostructured materials obtained by severe plastic deformation]. Moscow, Logos Publ., 2000. 271 p.
21. Malis O., Ludwig K.F. Kinetics of phase transitions in equiatomic CuAu. *Physical Review B*, 1999, vol. 60, no. 21, pp. 14675–14682. DOI: 10.1103/PhysRevB.60.14675.
22. Christian J.W. *Teoriya prevrashcheniy v metallakh i splavakh* [The theory of transformation in metals and alloys]. Vol. 1. Moscow, Mir Publ., 1978. 806 p.
23. Kim M.J., Flanagan W.F. The effect of plastic deformation on the resistivity and Hall Effect of copper-palladium and gold-palladium alloys. *Acta Metallurgica*, 1967, vol. 15, pp. 735–745. DOI: 10.1016/0001-6160(67)90354-9.

24. Garcia-Gonzalez M., Van Petegem S., Baluc N., Dupraz M., Honkimaki V., Lalire F., Van Swygenhoven H. Influence of thermo-mechanical history on the ordering kinetics in 18 carat Au alloys. *Acta Materialia*, 2020, vol. 191, pp. 186–197. DOI: 10.1016/j.actamat.2020.03.032.
25. Volkov A.Yu., Antonova O.V., Komkova D.A., Glukhov A.V., Volkova E.G., Livinets A.A., Podgorbunskaya P.O., Antonov B.D. Effect of moderate plastic deformation on structure and properties of the ordered Cu-56Au (at.%) alloy. *Materials Science and Engineering A*, 2023, vol. 865, p. 144626. DOI: 10.1016/j.msea.2023.144626.
26. Cahn R.W. Recovery, Strain-Age-Hardening and Recrystallization in Deformed Intermetallics. *High Temperature Aluminides and Intermetallics* / eds. Whang S.H. et al. The Minerals, Metals & Materials Society, 1990, p. 245–270.
27. Grinberg B.A., Ivanov M.A. *Intermetallidy Ni_3Al i TiAl: mikrostruktura, leformatsionnoe povedenie* [Intermetallics Ni3Al and TiAl: microstructure, deformation behavior]. Ekaterinburg, UrO RAN Publ., 2002. 359 p.
28. Volkov A.Yu., Podgorbunskaya P.O., Novikova O.S., Valiullin A.I., Glukhov A.V., Kruglikov N.A. Atomic ordering kinetics of Cu-56at.%Au alloy at a temperature of 250 °C. *Inorganic Materials*. 2023 (In print).
29. Grinberg B.A., Cyutkina V.I. *Novye metody uprochneniya uporyadochennykh splavov* [New methods for strengthening ordered alloys]. Moscow, Metallurgiya Publ., 1985. 175 p.

СПИСОК ЛИТЕРАТУРЫ

1. Kurnakov N., Zemczuzny S., Zasedatelev M. Transformations in Alloys of Gold with Copper // Journal of the Institute of Metals. 1916. Vol. 15. P. 305–331.
2. Jogansson C.H., Linde J.O. Röntgenographische und elektrische Untersuchungen der CuAu-Systems // Annalen der Physik. 1936. Vol. 417. № 1. P. 1–48. DOI: 10.1002/andp.19364170102.
3. Hirabayashi M. Stress-Ordering Effect on Thermal Expansion of CuAu Single Crystals // Journal of the Physical Society of Japan. 1959. Vol. 14. P. 149–152. DOI: 10.1143/JPSJ.14.149.
4. Van Tendeloo G., Amelinckx S., Jeng S.J., Wayman C.M. The initial stages of ordering in CuAuI and CuAuII // Journal of Materials Science. 1986. Vol. 21. P. 4395–4402. DOI: 10.1007/BF01106562.
5. Художественное литье из драгоценных металлов / под общ. ред. Л.А. Гутова. Л.: Машиностроение, 1988. 223 с.
6. Попова Л.А. Структурно-энергетические свойства бивакансий в сплаве CuAu I // Вестник Югорского государственного университета. 2022. Т. 66. № 3. С. 145–151. DOI: 10.18822/byusu202203145-151.
7. Larcher M., Cayron C., Blatter A., Soulignac R., Logé R.E. Electron backscatter diffraction study of variant selection during ordering phase transformation in $L1_0$-type red gold alloy // Journal of Applied Crystallography. 2019. Vol. 52. P. 1202–1213. DOI: 10.1107/S1600576719011890.
8. Федоров П.П., Волков С.Н. Фазовая диаграмма системы Au-Cu // Журнал неорганической химии. 2016. Т. 61. № 6. С. 809–812. DOI: 10.7868/S0044457X16060064.
9. Малышев В.М., Румянцев Д.В. Золото. М.: Металлургия, 1979. 288 с.
10. Trong D.N., Long V.C., Saraç U., Quoc V.D., Ţălu Ş. First-Principles Calculations of Crystallographic and Electronic Structural Properties of Au-Cu Alloys // Journal of Composites Science. 2022. Vol. 6. № 12. P. 383. DOI: https://doi.org/10.3390/jcs6120383.
11. Волков А.Ю., Казанцев В.А. Влияние исходного состояния на формирование структуры и свойств упорядоченного сплава CuAu // Физика металлов и металловедение. 2012. Т. 113. № 1. С. 66–76. DOI: 10.1134/S0031918X12010127.
12. Lamiri I., Martinez-Blanco D., Abdelbaky M.S.M., Mari D., Hamana D., García-Granda S. Investigation of the order-disorder phase transition series in AuCu by in-situ temperature XRD and mechanical spectroscopy // Journal of Alloys and Compounds. 2019. Vol. 770. P. 748–754. DOI: 10.1016/j.jallcom.2018.08.094.
13. Garcia-Gonzalez M., Van Petegem S., Baluc N., Hocine S., Dupraz M., Lalire F., Van Swygenhoven H. Enhanced precipitate growth at reduced temperatures during chemical ordering in deformed red gold alloys // Scripta Materialia. 2019. Vol. 170. P. 129–133. DOI: 10.1016/j.scriptamat.2019.05.038.
14. Volkov A.Yu., Antonova O.V., Glukhov A.V., Komkova D.A., Antonov B.D., Kostina A.E., Livinets A.A., Generalova K.N. Features of the disorder-order phase transition in non-stoichoimetric Cu-56at%Au alloy // Journal of Alloys and Compounds. 2022. Vol. 891. P. 161938. DOI: 10.1016/j.jallcom.2021.161938.
15. Farooq Z., Ali R., Ahmed N., Fahad M., Ahmad A., Yaseen M., Mahmood M.H.R., Hussain S., Rehan I., Zubair Khan M., Jan T., Qayyum M.A., Afzal M., Mahr M.S., Shafique M. Determination of the Gold Alloys Composition by Laser-Induced Plasma Spectroscopy Using an Algorithm for Matching Experimental and Calculated Values of Electron Number Density // Journal of Applied Spectroscopy. 2023. Vol. 90. P. 126–136. DOI: 10.1007/s10812-023-01513-x.
16. Gafner Y.Y., Gafner S.L., Golovenko Z.V. Analysis of the size distribution of binary Cu-Au nanoparticles during synthesis from a gaseous medium // Letters on Materials. 2020. Vol. 10. № 1. P. 33–37. DOI: 10.22226/2410-3535-2020-1-33-37.
17. Генералова К.Н., Глухов А.В., Волков А.Ю. Рентгеноструктурный анализ кинетики атомного упорядочения по типу $L1_0$ в нестехиометрическом медно-золотом сплаве // Вестник Пермского национального исследовательского политехнического университета. Машиностроение, материаловедение. 2018. Т. 20. № 2. С. 75–85. DOI: 10.15593/2224-9877/2018.2.09.
18. Volkov A.Yu., Novikova O.S., Antonov B.D. The kinetics of ordering in an equiatomic CuPd alloy: A resistometric study // Journal of Alloys and Compounds. 2013. Vol. 581. P. 625–631. DOI: 10.1016/j.jallcom.2013.07.132.
19. Glezer A.M., Timshin I.A., Shchetinin I.V., Gorshenkov M.V., Sundeev R.V., Ezhova A.G. Unusual behavior

of long-range ordered parameter in Fe_3Al superstructure under severe plastic deformation in Bridgman anvils // Journal of Alloys and Compounds. 2018. Vol. 744. P. 791–796. DOI: 10.1016/j.jallcom.2018.02.124.
20. Валиев Р.З., Александров И.В. Наноструктурные материалы, полученные интенсивной пластической деформацией. М.: Логос, 2000. 271 с.
21. Malis O., Ludwig K.F. Kinetics of phase transitions in equiatomic CuAu // Physical Review B. 1999. Vol. 60. № 21. P. 14675–14682. DOI: 10.1103/PhysRevB.60.14675.
22. Кристиан Дж. Теория превращений в металлах и сплавах. Т. 1. М.: Мир, 1978. 806 с.
23. Kim M.J., Flanagan W.F. The effect of plastic deformation on the resistivity and Hall Effect of copper-palladium and gold-palladium alloys // Acta Metallurgica. 1967. Vol. 15. P. 735–745. DOI: 10.1016/0001-6160(67)90354-9.
24. Garcia-Gonzalez M., Van Petegem S., Baluc N., Dupraz M., Honkimaki V., Lalire F., Van Swygenhoven H. Influence of thermo-mechanical history on the ordering kinetics in 18 carat Au alloys // Acta Materialia. 2020. Vol. 191. P. 186–197. DOI: 10.1016/j.actamat.2020.03.032.
25. Volkov A.Yu., Antonova O.V., Komkova D.A., Glukhov A.V., Volkova E.G., Livinets A.A., Podgorbunskaya P.O., Antonov B.D. Effect of moderate plastic deformation on structure and properties of the ordered Cu-56Au (at.%) alloy // Materials Science and Engineering A. 2023. Vol. 865. P. 144626. DOI: 10.1016/j.msea.2023.144626.
26. Cahn R.W. Recovery, Strain-Age-Hardening and Recrystallization in Deformed Intermetallics // High Temperature Aluminides and Intermetallics / eds. Whang S.H. et al. Indianapolis: The Minerals, Metals & Materials Society, 1990. P. 245–270.
27. Гринберг Б.А., Иванов М.А. Интерметаллиды Ni_3Al и TiAl: микроструктура, деформационное поведение. Екатеринбург: УрО РАН, 2002. 359 с.
28. Волков А.Ю., Подгорбунская П.О., Новикова О.С., Валиуллин А.И., Глухов А.В., Кругликов Н.А. Кинетика атомного упорядочения сплава Cu-56ат.%Au при температуре 250 °C // Неорганические материалы. 2023 (в печати).
29. Гринберг Б.А., Сюткина В.И. Новые методы упрочнения упорядоченных сплавов. М.: Металлургия, 1985. 175 с.

Кинетика формирования сверхструктуры $L1_0$ в сплаве Cu–56Au (ат. %): резистометрическое исследование

© 2023

Подгорбунская Полина Олеговна*[1,2], студент, лаборант лаборатории прочности
Згибнев Дмитрий Александрович[1,2], студент, лаборант лаборатории прочности
Гаврилова Алена Антоновна[1,2], студент, лаборант лаборатории прочности
Новикова Оксана Сергеевна[2,3], кандидат физико-математических наук, старший научный сотрудник лаборатории прочности
Волков Алексей Юрьевич[2,4], доктор технических наук, заведующий лабораторией прочности
[1]*Уральский федеральный университет имени первого Президента России Б.Н. Ельцина, Екатеринбург (Россия)*
[2]*Институт физики металлов имени М.Н. Михеева Уральского отделения РАН, Екатеринбург (Россия)*

***E-mail: podgorbunskaua@imp.uran.ru, polina.podgorbunskaya@yandex.ru**
[3]ORCID: https://orcid.org/0000-0003-0474-8991
[4]ORCID: https://orcid.org/0000-0002-0636-6623

Поступила в редакцию 06.06.2023 *Принята к публикации 19.07.2023*

Аннотация: Благодаря повышенным прочностным свойствам в сравнении с эквиатомным сплавом Cu–50 ат. % Au, нестехиометрический сплав Cu–56 ат. % Au может найти применение не только в стоматологии, но и в качестве коррозионностойкого проводника слабых электрических сигналов для приборостроения. Работа посвящена изучению кинетики фазового превращения беспорядок→порядок в сплаве Cu–56Au, в ходе которого неупорядоченная ГЦК-решетка ($A1$-фаза) перестраивается в атомно-упорядоченную со сверхструктурой $L1_0$. Исходное разупорядоченное состояние сплава получали двумя способами: применением пластической деформации на 90 % или закалкой от температуры 600 °C (т. е. из области существования $A1$-фазы). Отжиги для формирования сверхструктуры $L1_0$ проводили при температурах 200, 225 и 250 °C. Продолжительность отжигов составляла от 1 ч до 2 мес. В качестве основной методики исследования кинетики превращения беспорядок→порядок была выбрана резистометрия. Получены температурные зависимости удельного электросопротивления сплава в различных структурных состояниях. Построены графики зависимости удельного электросопротивления от логарифма времени отжига, на основе которых проведена оценка скорости образования новой фазы. Для аттестации структурного состояния сплава на различных этапах превращения использовался рентгеноструктурный анализ (РСА). Перестройка кристаллической структуры в ходе превращения показана на примере расщепления пика (200) кубической исходной $A1$-фазы на два пика – (200) и (002) тетрагональной упорядоченной $L1_0$-фазы. По данным резистометрии и РСА проведена количественная оценка скорости фазового превращения беспорядок→порядок в исследуемом сплаве. Установлено, что значения доли превращенного объема (резистометрия) и степени дальнего

порядка (рентгеноструктурный анализ) близки. Показано, что в температурном интервале 200–250 °C скорость атомного упорядочения по типу $L1_0$ в нестехиометрическом сплаве Cu–56 ат. % Au максимальна при 250 °C. Установлено, что превращение беспорядок→порядок в исходно закаленных образцах исследованного сплава протекает приблизительно на порядок быстрее по сравнению с предварительно деформированными образцами.

Ключевые слова: Cu–56 ат. % Au; сплавы Cu–Au; атомное упорядочение; резистометрия; сверхструктурные рентгеновские отражения; оценка степени порядка.

Благодарности: Работа выполнена при финансовой поддержке Российского научного фонда (грант № 21-13-00135).

Статья подготовлена по материалам докладов участников XI Международной школы «Физическое материаловедение» (ШФМ-2023), Тольятти, 11–15 сентября 2023 года.

Для цитирования: Подгорбунская П.О., Згибнев Д.А., Гаврилова А.А., Новикова О.С., Волков А.Ю. Кинетика формирования сверхструктуры $L1_0$ в сплаве Cu–56Au (ат. %): резистометрическое исследование // Frontier Materials & Technologies. 2023. № 3. С. 83–94. DOI: 10.18323/2782-4039-2023-3-65-8.

doi: 10.18323/2782-4039-2023-3-65-9

Determination of the volume fraction of primary carbides in the microstructure of composite coatings using semantic segmentation

© 2023

Natalia N. Soboleva*[1,2,3], PhD (Engineering), senior researcher
Aleksandr N. Mushnikov[1,4], PhD (Engineering), researcher
[1]*Institute of Engineering Science of the Ural Branch of RAS, Yekaterinburg (Russia)*
[2]*M.N. Mikheev Institute of Metal Physics of the Ural Branch of RAS, Yekaterinburg (Russia)*

***E-mail: soboleva@imach.uran.ru, natashasoboleva@list.ru**

[3]ORCID: https://orcid.org/0000-0002-7598-2980
[4]ORCID: https://orcid.org/0000-0001-7073-6476

Received 14.06.2023 *Accepted 15.08.2023*

Abstract: In the process of formation of composite coatings, partial dissolution of strengthening particles (most often carbides) in the matrix is possible; therefore, in some cases, the material creation mode is chosen taking into account the volume fraction of primary carbides not dissolved during coating deposition. The methods currently widely used for calculating the volume fraction of carbides in the structure of composite coatings (manual point method and programs implementing classical computer vision methods) have limitations in terms of the possibility of automation. It is expected that performing semantic segmentation using convolutional neural networks will improve both the performance of the process and the accuracy of carbide detection. In the work, multiclass semantic segmentation was carried out including the classification on the image of pores and areas that are not a microstructure. The authors used two neural networks based on DeepLab-v3 trained with different loss functions (IoU Loss and Dice Loss). The initial data were images of various sizes from electron and optical microscopes, with spherical and angular carbides darker and lighter than the matrix, in some cases with pores and areas not related to the microstructure. The paper presents mask images consisting of four classes, created manually and by two trained neural networks. The study shows that the networks recognize pores, areas not related to the microstructure, and perfectly segment spherical carbides in images, regardless of their color relative to the matrix and the presence of pores in the structure. The authors compared the proportion of carbides in the microstructure of coatings determined by two neural networks and a manual point method.

Keywords: composite coatings; carbides; optical microscopy; scanning electron microscopy; semantic segmentation; neural networks.

Acknowledgements: The work was carried out within the state assignment to the Institute of Engineering Science, UB RAS on the topics No. AAAA-A18-118020790147-4 and No. AAAA-A18-118020790148-1 and the Institute of Metal Physics, UB RAS on the topic “Additivity” No. 121102900049-1.

Microscopic images were obtained using the equipment of the “Plastometry” Core Facility Center of the IES UB RAS.

The paper was written on the reports of the participants of the XI International School of Physical Materials Science (SPM-2023), Togliatti, September 11–15, 2023.

For citation: Soboleva N.N., Mushnikov A.N. Determination of the volume fraction of primary carbides in the microstructure of composite coatings using semantic segmentation. *Frontier Materials & Technologies*, 2023, no. 3, pp. 95–102. DOI: 10.18323/2782-4039-2023-3-65-9.

INTRODUCTION

At present, the industry is imposing increasingly strict requirements to strength, wear resistance, durability, and other working properties of machine parts and tools. To solve the problem of improving the tribological properties of products, new wear-resistant materials and coatings, including composite ones, are constantly being developed [1]. One of the most promising coatings for operation under abrasive wear conditions are “carbide – metal matrix” composite materials [2–4].

For the effective composite coating formation, it is necessary that the matrix has a relatively low melting point, and the carbides have a high one [5]. Thus, when creating a material, a wear-resistant filler will be provided in the form of initial primary particles not dissolved in the matrix. However, carbides can partially dissolve in the matrix when creating composite coatings [6–8], thereby reducing their wear resistance [9]. In this regard, in a number of cases, when developing a coating technology for the resulting prototypes, both the composition and effective properties are studied, and the volume of coarse primary strengthening particles in the microstructural material is determined.

Currently, the standardised method for determining the phase volume fraction is the manual point method according to ASTM E 562-02, which is a labour-intensive process. Simplification of the process is possible by using programs implementing classical computer vision methods, such as Siams, Thixomet, ImageJ, JMicroVision, etc. [10; 11]. However, it was shown in [12] that the use of classical computer vision methods has a number of limitations, that make it difficult to automate the process.

The application of neural networks for segmentation of images of composite materials is a possible problem solution. In this case, semantic segmentation, the process of understanding images at the pixel level [13], is performed, which allows dividing images into the areas corresponding to the semantic class in a predetermined list. A neural

network studies the features of the classes using pre-prepared masks – images marked by different colours. Semantic segmentation combines object detection, shape recognition, and classification.

The use of convolutional neural networks makes it possible to significantly improve the semantic segmentation performance [14]. Over the past few years, many semantic segmentation models, based on convolutional neural networks have demonstrated good performance in the image segmentation tasks, such as FCN, SegNet, RefineNet, U-net, PSPNet, and DeepLab [13; 15; 16]. To produce segmentation maps, the DeepLab model implements an architecture based on a convolutional neural network. In addition to conventional convolutions, discharged convolution kernels are used, which allow considering, more spatial information without increasing the number of parameters [17]. A more advanced DeepLab-v3 version is characterised by the improved performance at high segmentation accuracy [18].

In the work [12], WC tungsten carbide particles were segmented in the structure of NiCrBSi coatings using U-net and LinkNet networks. At the same time, the task of one-class segmentation was solved: pixels were identified, which belonged and did not belong to carbides. The authors of the work note that the trained models had a tendency for incorrect classification of pores, related to the class of carbides.

The present work aims to determine the volume fraction of primary carbides in the microstructure of composite materials, using trained neural networks, based on DeepLab-v3 for semantic segmentation. An implementation feature is multiclass segmentation including classification by image of pores and domains that are not a microstructure.

METHODS

The initial data were images of the microstructure of composite coatings based on nickel and iron with coarse primary tungsten, titanium, and chromium carbides, obtained using a Tescan VEGA II XMU scanning electron microscope and the optical system of a Shimadzu HMV-G21DT microhardness tester. The use of two different methods allowed obtaining images with different characteristics: different sizes (768×840 and 640×480 pixels), TIFF/JPG formats, carbides in microphotographs are lighter and darker than the matrix, the presence/absence of areas that are not a microstructure (areas with shooting parameters and a scale bar). Moreover, the images obtained by both methods were characterised by the presence of pores on some of them, as well as the presence of two types of carbides: spherical and angular. The number of original images was 41.

For convenience, all files were converted to the PNG format. The data set was marked manually in MS Paint (obtaining masks – ground truth images), using four colours: dark gray on the mask image – carbides, black – pores, white – the rest of the microstructure, light gray – the area that is not a microstructure.

The implementation of the deeplabv3_resnet101 model from the torchvision library was taken as a neural network. As the base for the deeplabv3_resnet101 model, the ResNet image classification network of the resnet101 version pre-trained on the Imagenet dataset was used. By default, the number of recognisable classes in the DeepLab-v3 network is 21. In the work, the head of the network was re-trained, with the replacement of the number of output layers in the last convolution by 4 – according to the number of identifiable classes. At the network output, a float tensor with the size of (*B, C, H, W*) is obtained, where *B* is the batch size, *C* is the number of classes, *H* is the image height, and *W* is the image width.

To train the network, the authors used the Adam optimizer. According to the results of preliminary tests, from the traditional range of learning rates for Adam from 10^{-4} to 10^{-3}, a learning rate of $3 \cdot 10^{-4}$ was chosen. The batch size was equal to 32. At the same time, 80 training and 20 testing iterations were performed at each training epoch. The number of epochs was 20.

Two networks were created with the same parameters except for the loss function. For one network, the loss function was based on the Jaccard distance metric, known as IoU (Intersection over Union), and for the other, on the Sörensen–Dice metric (Dice) [19].

Five images with different features were selected for the test set. The remaining 36 images were subjected to the following processing. Since it is preferable to train a neural network using images of the same size, a size of 224×224 pixels was chosen, corresponding to the recommended size for the ResNet network, on the basis of which the selected DeepLab-v3 model is built. Fragments of 224×224 pixels were cut out from the original images and masks with a random step from 50 to 65 pixels along each axis. Then the original images were reduced twice, and the procedure was repeated for the reduced images. The division of the obtained 3148 images into training and testing sets was performed randomly with a ratio of 0.8:0.2.

The trained model allows building a mask from a photograph of a microstructure of arbitrary resolution. To do this, the program cuts the original image into fragments of 224×224 pixels. If the size (width or height) of the original image is not a multiple of 224, the last (in horizontal or vertical direction) square may have an intersection with the penultimate one. The network processes each fragment separately, and then the mask of the entire image is assembled in reverse order. The mask obtained as a result of the neural network operation allows calculating the volume fraction of the content of carbides (dark gray pixels) in the microstructure image as a percentage. In this case, areas not related to the microstructure (light gray pixels) are subtracted from the calculation of the total area occupied by the microstructure.

Comparison of the proportion of carbides, in the microstructure, determined using artificial intelligence was carried out, applying a manual point method for determining the volume fraction of phases according to ASTM E 562. To do this, a 100-points grid was applied to the test images (Fig. 1). The volume fraction of carbides was calculated as the ratio of the number of grid points fell on the carbide to the total number of points. In the case of a point hitting the "carbide-matrix" boundary, it was considered as belonging to both phases, so its contribution to the calculation of the proportion of carbides was 0.5.

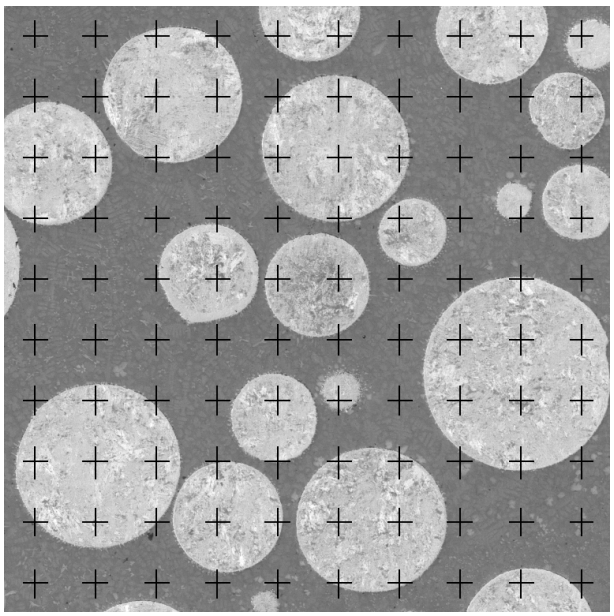

Fig. 1. *An example of determining the fraction of carbides in the microstructure according to ASTM E 562 test method*
Рис. 1. *Пример расчета доли карбидов в микроструктуре по ASTM E 562*

RESULTS

Table 1 shows the microstructure images used as test, as well as image masks using four assigned colours generated by a human (manual marking) and two neural networks trained with different loss functions: IoU Loss and Dice Loss.

It can be observed that the neural networks had no problems when segmenting the areas not occupied by the microstructure (light gray in images 1, 2 and 5). The networks also recognise pores (black in images 4 and 5), and if in image 5 the carbides are lighter than the matrix, and the pore visually differs significantly from them in colour, then in image 4 the carbides are darker than the matrix and, similar to the pore, is spherical. Therefore, adequate pore recognition in this image was not predictable. It can be observed, however, that the network with Dice Loss mistook a small part of the pore for a carbide part.

Artificial intelligence segmentation of carbides, occupying a large volume in images and are characterised by various visual features, was expectedly performed with some errors. Among them is the recognition of carbides in the places of their absence (highlighted by a dashed circle in the image 1 of the network with Dice Loss) and, conversely, the non-recognition of a part of the carbide (highlighted by a dashed circle in images 2, 4, and 5), which was recorded by both networks in the same places. The analysis of this error showed that it is related to cutting the original images into squares of 224×224 pixels, and processing them separately. In this case, a small edge of the carbide appeared in another image, and the network did not recognise it. Probably for the same reason, image 3 is segmented with the largest error, since in some sliced images, large carbide occupied most of the frame.

In general, one can note good recognition of pores by trained neural networks and excellent segmentation in images of spherical carbides, regardless of their colour relative to the matrix and the presence of pores in the structure.

Table 2 calculates the volume fraction of carbides in the microstructure of coatings in test images. It can be observed that the calculation according to ASTM showed good results, compared to the reference calculation according to manual marking, the difference is from 0.5 to 1.3 % of the volume fraction of carbides. The neural network with IoU Loss, showed a difference with the ground truth images from 0.1 to 1.1 %, and the network with Dice Loss – from 0.1 to 0.6 % of carbides. Table 3 shows the mean square error of calculating the fraction of carbides over the entire test set. The calculation by the network with Dice Loss was characterised by the smallest value of the mean square error (0.14), and the calculation according to ASTM – by the largest one (0.80).

However, the mean square error of calculating the fraction of carbides does not fully reflect the quality of the neural network, since it does not consider the "two-sided" errors of the network: finding carbides where they are absent, and not finding where they should be. Therefore, the IoU, Dice, and MeanIoU metrics, the values of which can range from 0 to 1 and tend to 1 in the case of the smallest error in the segmentation of areas, were also defined for neural networks. Despite the less accurate determination of the volume fraction of carbides in percent (Table 2), the network with IoU Loss is characterised by the maximum values of all three metrics (Table 3), which is associated with its smaller inaccuracies (compared to the network with Dice Loss), in the segmentation of the most "problematic" image No. 3 (Table 1).

DISCUSSION

The use of artificial intelligence has a number of disadvantages, in particular, the necessity of collecting and preparing a large amount of data for training a neural network

Table 1. *Microstructure images from test set and imaging of masks created manually and by two neural networks*
Таблица 1. *Изображения микроструктуры из тестового набора и отображение масок, сформированных вручную и двумя нейронными сетями*

No.	Microstructure image	Manual marking	Network with Loss=(1−IoU)	Network with Loss=(1−Dice)
1	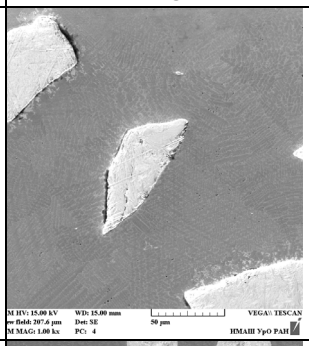	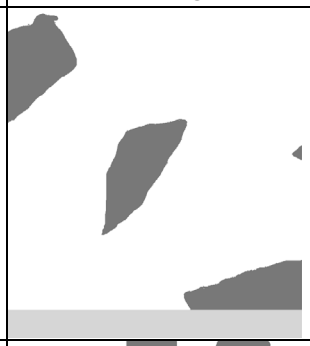	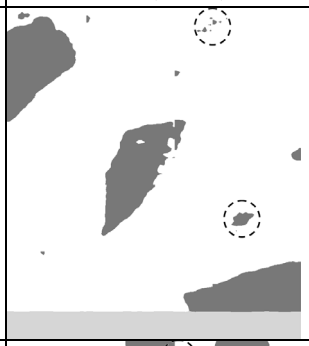	
2	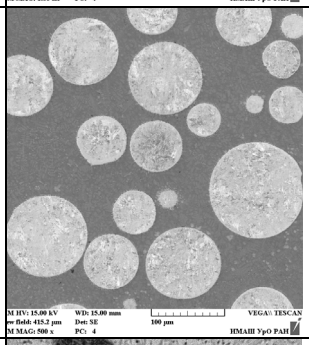	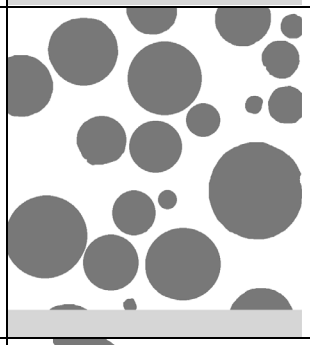	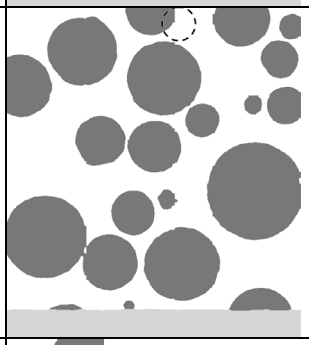	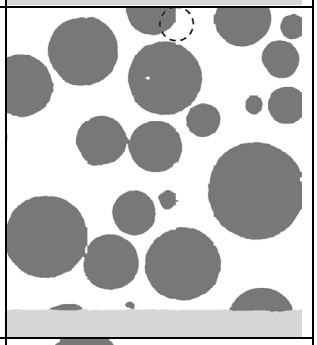
3	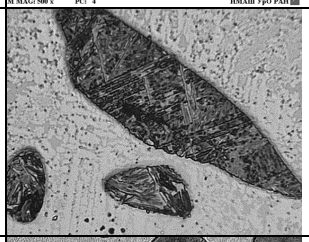			
4	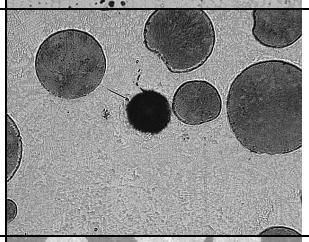	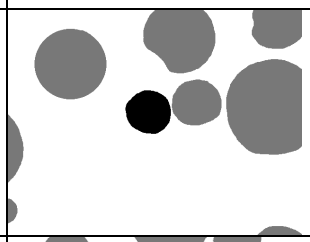	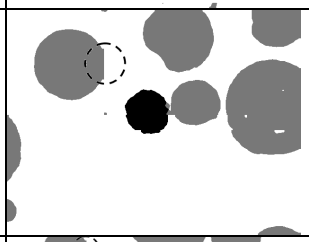	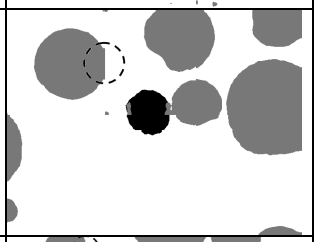
5	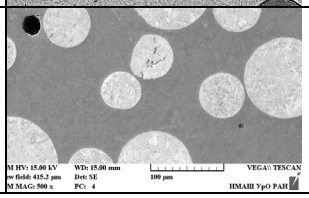	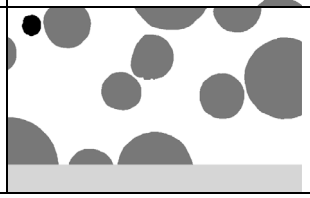	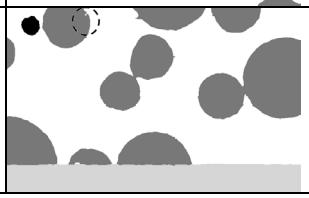	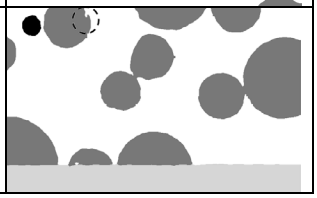

[20], as well as selecting training parameters for more accurate network operation, and many of them are selected only experimentally [21]. Thus, training a neural network and reducing the segmentation error of carbides takes a long time. However, in the future, the network will determine the volume fraction of carbides in images in the split seconds. The calculation, using the manual method according to ASTM, takes less time than training the neural network, but much more than the calculation by the network after training, and there are no prerequisites for reducing the time of this operation. Moreover, the "step" for determining the volume fraction according to ASTM, in the case of a 100-points grid, is 0.5 %, and in the case of high-quality neural network training, the accuracy will be higher. In the case of using neural networks, the statistical error in determining the average carbide content over the entire coverage area can also be reduced, since fast calculation allows increasing the number of analysed fields of vision.

The networks trained in this work are characterised by good pore recognition, and excellent segmentation of spherical

Table 2. *The fraction of carbides in the microstructure of coatings determined by different methods, %*
Таблица 2. *Доля карбидов в микроструктуре покрытий, определенная различными методами, %*

No. of image	Manual marking	Calculation according to ASTM	Network with IoU Loss	Network with Dice Loss
1	15.8	16.5	15.7	15.6
2	48.4	49.0	48.5	48.5
3	36.6	35.5	37.7	37.2
4	28.5	28.0	27.9	28.3
5	36.2	37.5	36.6	36.7

Table 3. *Mean square error, IoU, Dice, and MeanIoU metrics for different methods of determining the fraction of carbides*
Таблица 3. *Среднеквадратическая ошибка, метрики IoU, Dice и MeanIoU для разных методов определения доли карбидов*

Methods of determining the fraction of carbides	Mean square error	IoU	Dice	MeanIoU
Calculation according to ASTM	0.80	–	–	–
Network with IoU Loss	0.37	0.958	0.979	0.952
Network with Dice Loss	0.14	0.956	0.977	0.945

carbides, regardless of the imaging method (optical/electron microscope), and can now be successfully applied to estimate the volume fraction of spherical carbides in the microstructure of coatings.

There are some problems with segmentation of angular carbides, which may be related both to the lower number of images with this type of carbides in the network training set, and to the fact that such carbides were large (relative to the total image area) in the tested images and therefore not adequately estimated by networks trained on small (224×224 pixels) image fragments.

The solution to these problems can be either expanding the dataset, in particular adding images with angular carbides, and situations where the carbide takes up most of the frame, or changing the network training parameters: training on larger images, testing other loss functions, varying the size of the batch size, learning rate, etc.

CONCLUSIONS

The study shows the principal possibility of using two neural networks based on DeepLab-v3 trained with different loss functions (IoU Loss and Dice Loss) for semantic segmentation of carbides in the microstructure of composite coatings and subsequent calculation of their volume fraction. The networks recognise pores, areas not related to the microstructure and perfectly segment spherical carbides in images, regardless of their colour relative to the matrix and the presence of pores in the structure.

The values of the volume fraction of carbides determined by both networks differed from the reference values by smaller amounts than the values calculated by the manual point method according to ASTM. The network with IoU Loss is characterised by the maximum values of all IoU, Dice, and MeanIoU metrics compared to the network with Dice Loss, which indicates a smaller error in the segmentation of areas.

The main problem of the networks was the segmentation of a large angular carbide, which can be solved by expanding the dataset and changing the neural network training parameters.

REFERENCES

1. Savrai R.A., Gladkovsky S.V., Lepikhin S.V., Kolobylin Yu.M. Approaches to the development of wear-resistant laminated metal composites. *Diagnostics, Resource and Mechanics of materials and structures*, 2021, no. 5, pp. 24–35. DOI: 10.17804/2410-9908.2021.5.24-35.
2. Soboleva N.N., Nikolaeva E.P., Makarov A.V., Malygina I.Yu. The influence of chromium carbide additive on the structure and abrasive wear resistance of the NiCrBSi coating formed by laser cladding. *Vektor nauki Tolyattinskogo gosudarstvennogo universiteta*, 2020, no. 1, pp. 68–76. DOI: 10.18323/2073-5073-2020-1-68-76.
3. Pribytkov G.A., Kalita V.I., Komlev D.I. et al. Hardness and wear resistance of plasma coatings sprayed by SHS-

TiC + Ti-binder composite powders. *Uprochnyayushchie tekhnologii i pokrytiya*, 2019, vol. 15, no. 8, pp. 359–364. EDN: MROUSQ.
4. Makarov A.V., Soboleva N.N., Malygina I.Yu., Osintseva A.L. The tribological performances of a NiCrBSi – TiC laser-clad composite coating under abrasion and sliding friction. *Diagnostics, Resource and Mechanics of materials and structures*, 2015, no. 3, pp. 83–97. DOI: 10.17804/2410-9908.2015.3.083-097.
5. Nurminen J., Näkki J., Vuoristo P. Microstructure and properties of hard and wear resistant MMC coatings deposited by laser cladding. *International Journal of Refractory Metals and Hard Materials*, 2009, vol. 27, no. 2, pp. 472–478. DOI: 10.1016/j.ijrmhm.2008.10.008.
6. Enrici T.M., Dedry O., Boschini F., Tchuindjang J.T., Mertens A. Microstructural and Thermal Characterization of 316L+WC Composite Coatings obtained by Laser Cladding. *Advanced Engineering Materials*, 2020, vol. 22, no. 12, article number 2000291. DOI: 10.1002/adem.202000291.
7. Deschuyteneer D., Petit F., Gonon M., Cambier F. Processing and characterization of laser clad NiCrBSi/WC composite coatings – Influence of microstructure on hardness and wear. *Surface and Coatings Technology*, 2015, vol. 283, pp. 162–171. DOI: 10.1016/j.surfcoat.2015.10.055.
8. Zhang Z., Liu H.X., Zhang X.W., Ji S.W., Jiang Y.H. Dissolution Behavior of WC Reinforced Particles on Carbon Steel Surface during Laser Cladding Process. *Advanced Materials Research*, 2012, vol. 430-432, pp. 137–141. DOI: 10.4028/www.scientific.net/AMR.430-432.137.
9. Xu H., Huang H. Plasma remelting and injection method for fabricating metal matrix composite coatings reinforced with tungsten carbide. *Ceramics International*, 2022, vol. 48, no. 2, pp. 2645–2659. DOI: 10.1016/j.ceramint.2021.10.048.
10. Kazakov A.A., Kiselev D. Industrial Application of Thixomet Image Analyzer for Quantitative Description of Steel and Alloy's Microstructure. *Metallography, Microstructure, and Analysis*, 2016, vol. 5, pp. 294–301. DOI: 10.1007/s13632-016-0289-6.
11. Schneider C.A., Rasband W.S., Eliceiri K.W. NIH Image to ImageJ: 25 years of image analysis. *Nature Methods*, 2012, vol. 9, pp. 671–675. DOI: 10.1038/nmeth.2089.
12. Rose D., Forth J., Henein H., Wolfe T., Qureshi A.J. Automated semantic segmentation of NiCrBSi-WC optical microscopy images using convolutional neural networks. *Computational Materials Science*, 2022, vol. 210, article number 111391. DOI: 10.1016/j.commatsci.2022.111391.
13. Wang M., Wu F., Zhao J. A Comprehensive Research and Strategy of Transfer Learning for Image Segmentation. *Lecture Notes on Data Engineering and Communications Technologies book series*, 2021, vol. 88, pp. 1394–1406. DOI: 10.1007/978-3-030-70665-4_152.
14. Benjdira B., Bazi Y., Koubaa A., Ouni K. Unsupervised domain adaptation using generative adversarial networks for semantic segmentation of aerial images. *Remote Sensing*, 2019, vol. 11, no. 11, article number 1369. DOI: 10.3390/rs11111369.
15. Chen L.C., Papandreou G., Kokkinos I., Murphy K., Yuille A.L. DeepLab: Semantic Image Segmentation with Deep Convolutional Nets, Atrous Convolution, and Fully Connected CRFs. *IEEE Transactions on Pattern Analysis and Machine Intelligence*, 2018, vol. 40, pp. 834–848. DOI: 10.1109/TPAMI.2017.2699184.
16. Long J., Shelhamer E., Darrell T. Fully convolutional networks for semantic segmentation. *Proceedings of the IEEE Conference on Computer Vision and Pattern Recognition*, 2015, pp. 3431–3440. DOI: 10.1109/CVPR.2015.7298965.
17. Emelyanov A.V. Analysis of image semantic segmentation methods based on neural networks. *Matematicheskie metody v tekhnike i tekhnologiyakh – MMTT*, 2019, vol. 12-1, pp. 195–201. EDN: GCGRLL.
18. Chen L.C., Papandreou G., Schroff F., Adam H. Rethinking Atrous Convolution for Semantic Image Segmentation. *arXiv:1706.05587*, 2017. DOI: 10.48550/arXiv.1706.05587.
19. Xu H., He H., Zhang Y., Ma L., Li J. A comparative study of loss functions for road segmentation in remotely sensed road datasets. *International Journal of Applied Earth Observations and Geoinformation*, 2023, vol. 116, article number 103159. DOI: 10.1016/j.jag.2022.103159.
20. Rastorguev D.A., Sevastyanov A.A. Development of turning process digital twin based on machine learning. *Vektor nauki Tolyattinskogo gosudarstvennogo universiteta*, 2021, no. 1, pp. 32–41. DOI: 10.18323/2073-5073-2021-1-32-41.
21. Vik K.V., Druki A.A., Grigorev D.S., Spitsyn V.G. Application of deep learning neural networks for solving the problem of forest fire segmentation on satellite images. *Vestnik Tomskogo gosudarstvennogo universiteta. Upravlenie, vychislitelnaya tekhnika i informatika*, 2021, no. 55, pp. 18–25. DOI: 10.17223/19988605/55/3.

СПИСОК ЛИТЕРАТУРЫ

1. Savrai R.A., Gladkovsky S.V., Lepikhin S.V., Kolobylin Yu.M. Approaches to the development of wear-resistant laminated metal composites // Diagnostics, Resource and Mechanics of materials and structures. 2021. № 5. P. 24–35. DOI: 10.17804/2410-9908.2021.5.24-35.
2. Соболева Н.Н., Николаева Е.П., Макаров А.В., Малыгина И.Ю. Влияние добавки карбида хрома на структуру и абразивную износостойкость NiCrBSi покрытия, сформированного лазерной наплавкой // Вектор науки Тольяттинского государственного университета. 2020. № 1. С. 68–76. DOI: 10.18323/2073-5073-2020-1-68-76.
3. Прибытков Г.А., Калита В.И., Комлев Д.И. и др. Твердость и износостойкость плазменных покрытий, напыленных СВС-композиционными порошками TiC + Ti-связка // Упрочняющие технологии и покрытия. 2019. Т. 15. № 8. С. 359–364. EDN: MROUSQ.
4. Makarov A.V., Soboleva N.N., Malygina I.Yu., Osintseva A.L. The tribological performances of a NiCrBSi – TiC laser-clad composite coating under abrasion and sliding friction // Diagnostics, Resource and Mechanics of materials and structures. 2015. № 3. P. 83–97. DOI: 10.17804/2410-9908.2015.3.083-097.

5. Nurminen J., Näkki J., Vuoristo P. Microstructure and properties of hard and wear resistant MMC coatings deposited by laser cladding // International Journal of Refractory Metals and Hard Materials. 2009. Vol. 27. № 2. P. 472–478. DOI: 10.1016/j.ijrmhm.2008.10.008.
6. Enrici T.M., Dedry O., Boschini F., Tchuindjang J.T., Mertens A. Microstructural and Thermal Characterization of 316L+WC Composite Coatings obtained by Laser Cladding // Advanced Engineering Materials. 2020. Vol. 22. № 12. Article number 2000291. DOI: 10.1002/adem.202000291.
7. Deschuyteneer D., Petit F., Gonon M., Cambier F. Processing and characterization of laser clad NiCrBSi/WC composite coatings – Influence of microstructure on hardness and wear // Surface and Coatings Technology. 2015. Vol. 283. P. 162–171. DOI: 10.1016/j.surfcoat.2015.10.055.
8. Zhang Z., Liu H.X., Zhang X.W., Ji S.W., Jiang Y.H. Dissolution Behavior of WC Reinforced Particles on Carbon Steel Surface during Laser Cladding Process // Advanced Materials Research. 2012. Vol. 430-432. P. 137–141. DOI: 10.4028/www.scientific.net/AMR.430-432.137.
9. Xu H., Huang H. Plasma remelting and injection method for fabricating metal matrix composite coatings reinforced with tungsten carbide // Ceramics International. 2022. Vol. 48. № 2. P. 2645–2659. DOI: 10.1016/j.ceramint.2021.10.048.
10. Kazakov A.A., Kiselev D. Industrial Application of Thixomet Image Analyzer for Quantitative Description of Steel and Alloy's Microstructure // Metallography, Microstructure, and Analysis. 2016. Vol. 5. P. 294–301. DOI: 10.1007/s13632-016-0289-6.
11. Schneider C.A., Rasband W.S., Eliceiri K.W. NIH Image to ImageJ: 25 years of image analysis // Nature Methods. 2012. Vol. 9. P. 671–675. DOI: 10.1038/nmeth.2089.
12. Rose D., Forth J., Henein H., Wolfe T., Qureshi A.J. Automated semantic segmentation of NiCrBSi-WC optical microscopy images using convolutional neural networks // Computational Materials Science. 2022. Vol. 210. Article number 111391. DOI: 10.1016/j.commatsci.2022.111391.
13. Wang M., Wu F., Zhao J. A Comprehensive Research and Strategy of Transfer Learning for Image Segmentation // Lecture Notes on Data Engineering and Communications Technologies book series. 2021. Vol. 88. P. 1394–1406. DOI: 10.1007/978-3-030-70665-4_152.
14. Benjdira B., Bazi Y., Koubaa A., Ouni K. Unsupervised domain adaptation using generative adversarial networks for semantic segmentation of aerial images // Remote Sensing. 2019. Vol. 11. № 11. Article number 1369. DOI: 10.3390/rs11111369.
15. Chen L.C., Papandreou G., Kokkinos I., Murphy K., Yuille A.L. DeepLab: Semantic Image Segmentation with Deep Convolutional Nets, Atrous Convolution, and Fully Connected CRFs // IEEE Transactions on Pattern Analysis and Machine Intelligence. 2018. Vol. 40. P. 834–848. DOI: 10.1109/TPAMI.2017.2699184.
16. Long J., Shelhamer E., Darrell T. Fully convolutional networks for semantic segmentation // Proceedings of the IEEE Conference on Computer Vision and Pattern Recognition. 2015. P. 3431–3440. DOI: 10.1109/CVPR.2015.7298965.
17. Емельянов А.В. Анализ методов семантической сегментации изображений на основе нейронных сетей // Математические методы в технике и технологиях – ММТТ. 2019. Т. 12-1. С. 195–201. EDN: GCGRLL.
18. Chen L.C., Papandreou G., Schroff F., Adam H. Rethinking Atrous Convolution for Semantic Image Segmentation // arXiv:1706.05587. 2017. DOI: 10.48550/arXiv.1706.05587.
19. Xu H., He H., Zhang Y., Ma L., Li J. A comparative study of loss functions for road segmentation in remotely sensed road datasets // International Journal of Applied Earth Observations and Geoinformation. 2023. Vol. 116. Article number 103159. DOI: 10.1016/j.jag.2022.103159.
20. Расторгуев Д.А., Севастьянов А.А. Разработка цифрового двойника процесса точения на основе машинного обучения // Вектор науки Тольяттинского государственного университета. 2021. № 1. С. 32–41. DOI: 10.18323/2073-5073-2021-1-32-41.
21. Вик К.В., Друки А.А., Григорьев Д.С., Спицын В.Г. Применение нейронных сетей глубокого обучения для решения задачи сегментации лесных пожаров на спутниковых снимках // Вестник Томского государственного университета. Управление, вычислительная техника и информатика. 2021. № 55. С. 18–25. DOI: 10.17223/19988605/55/3.

Определение объемной доли первичных карбидов в микроструктуре композиционных покрытий с применением семантической сегментации

© 2023

Соболева Наталья Николаевна*[1,2,3], кандидат технических наук, старший научный сотрудник
Мушников Александр Николаевич[1,4], кандидат технических наук, научный сотрудник
[1]*Институт машиноведения имени Э.С. Горкунова Уральского отделения РАН, Екатеринбург (Россия)*
[2]*Институт физики металлов имени М.Н. Михеева Уральского отделения РАН, Екатеринбург (Россия)*

***E-mail: soboleva@imach.uran.ru, natashasoboleva@list.ru**

[3]ORCID: https://orcid.org/0000-0002-7598-2980
[4]ORCID: https://orcid.org/0000-0001-7073-6476

Поступила в редакцию 14.06.2023 *Принята к публикации 15.08.2023*

Аннотация: В процессе формирования композиционных покрытий возможно частичное растворение упрочняющих частиц (чаще всего карбидов) в матрице, поэтому в ряде случаев выбор режима создания материала осуществляется с учетом объемной доли первичных, не растворившихся при нанесении покрытий карбидов. Широко используемые в настоящее время методы расчета объемной доли карбидов в структуре композиционных покрытий (ручной точечный метод и программы, реализующие классические методы машинного зрения) имеют ограничения по возможности автоматизации. Ожидается, что выполнение семантической сегментации с использованием сверточных нейронных сетей повысит как производительность процесса, так и точность определения карбидов. В работе проводилась многоклассовая семантическая сегментация, включающая классификацию на изображении пор и областей, не являющихся микроструктурой. Использовались две нейронные сети на основе DeepLab-v3, обученные с разными функциями потерь (IoU Loss и Dice Loss). Исходными данными были изображения различных размеров с электронного и оптического микроскопов, с карбидами сферической и угловатой формы темнее и светлее матрицы, в ряде случаев – с порами и областями, не относящимися к микроструктуре. В работе представлены изображения-маски, состоящие из четырех классов, созданные вручную и двумя обученными нейронными сетями. Показано, что сети распознают поры, области, не относящиеся к микроструктуре, и отлично сегментируют на изображениях карбиды сферической формы, независимо от их цвета относительно матрицы и наличия пор в структуре. Проведено сравнение доли карбидов в микроструктуре покрытий, определенной двумя нейронными сетями и ручным точечным методом.

Ключевые слова: композиционные покрытия; карбиды; оптическая микроскопия; растровая электронная микроскопия; семантическая сегментация; нейронные сети.

Благодарности: Работа выполнена в рамках государственных заданий ИМАШ УрО РАН по темам № АААА-А18-118020790147-4 и № АААА-А18-118020790148-1 и ИФМ УрО РАН по теме «Аддитивность» № 121102900049-1.

Микроскопические изображения получены с использованием оборудования ЦКП «Пластометрия» ИМАШ УрО РАН.

Статья подготовлена по материалам докладов участников XI Международной школы «Физическое материаловедение» (ШФМ-2023), Тольятти, 11–15 сентября 2023 года.

Для цитирования: Соболева Н.Н., Мушников А.Н. Определение объемной доли первичных карбидов в микроструктуре композиционных покрытий с применением семантической сегментации // Frontier Materials & Technologies. 2023. № 3. С. 95–102. DOI: 10.18323/2782-4039-2023-3-65-9.

doi: 10.18323/2782-4039-2023-3-65-10

Concerning the selection of areas with a dominant type of dependence when analyzing production control data

© 2023

Victoria V. Timoshenko[1], postgraduate student
Ekaterina S. Budanova[2], graduate student
Davronjon F. Kodirov[3], postgraduate student
Elina A. Sokolovskaya[4], PhD (Engineering), Associate Professor,
assistant professor of Chair of Materials Science and Strength Physics
Aleksandr V. Kudrya*[5], Doctor of Sciences (Engineering), Professor,
professor of Chair of Materials Science and Strength Physics
University of Science and Technology MISIS, Moscow (Russia)

***E-mail: AVKudrya@misis.ru**

[1]ORCID: https://orcid.org/0009-0008-7671-0291
[2]ORCID: https://orcid.org/0009-0003-4055-9298
[3]ORCID: https://orcid.org/0009-0003-5380-5558
[4]ORCID: https://orcid.org/0000-0001-9381-9223
[5]ORCID: https://orcid.org/0000-0002-0339-2391

Received 06.06.2023 *Accepted 16.06.2023*

Abstract: The formation of representative databases determines the interest in forecasting and managing the quality of metal based on data mining using special software products often based on regression analysis and not always taking into account the statistical nature of an object of study itself. This can lead to misinterpretation of the results or incomplete extracted information reducing the efficiency of statistical processing. Based on the analysis of the production database of the technology for producing 13G1S-U sheet steel, the authors evaluated the possibilities of multiple linear regression for predicting the quality of a steel sheet. The study shows that the type of distribution of the values of control parameters, the distribution nature of which was estimated based on the determination of the skewness and kurtosis coefficients, limits the regression forecast depth. Due to the great deviation of the predicted models from the experimental values in the right tail area of the distribution of the impact strength values, in this work, the authors developed the methods for separating data arrays and proposed criteria to compare the obtained results. To assess the accuracy of the results obtained, arrays with a deliberately asymmetric distribution were selected from the initial sample, against which the statistical characteristics were also compared. Based on the proposed techniques, the authors identified the dominant chemical elements that contribute to the difference in the distribution of the values of acceptance properties existing within the same standard technology. The study shows that the proposed separation method can be used as a variation of cognitive graphics techniques to identify areas with a dependence dominant type based on the correlation of skewness and kurtosis coefficients.

Keywords: analysis of production control data; metal product quality control; quality forecast in metallurgy; cognitive graphics techniques; production data mining; 13G1S-U steel.

For citation: Timoshenko V.V., Budanova E.S., Kodirov D.F., Sokolovskaya E.A., Kudrya A.V. Concerning the selection of areas with a dominant type of dependence when analyzing production control data. *Frontier Materials & Technologies*, 2023, no. 3, pp. 103–114. DOI: 10.18323/2782-4039-2023-3-65-10.

INTRODUCTION

The high level of fitting of metallurgical enterprises with digital tools of intermediate control, and information collection, allows obtaining representative databases of production in a short period. This determines the interest in a post-event analysis of such data arrays for identifying the reasons for the heterogeneity of the quality of metal products, and developing sound principles for managing them [1; 2]. When analysing such information, a passive experiment is implemented [3; 4]. The costs of which are justified within the current, well-functioning technology, when the high quality of the metal is achieved for a part of the product (usually from half of its volume or less), and it is necessary to solve the problem of "improving the low-performers" to the advanced level [5].

Traditional approaches to solving such problems are based, in particular, on the analysis of the stability of process and product parameters, for example, using Shewhart control charts[1]. Their main disadvantage is the assumption of normalcy of distributions and a single space of process and product parameters, which can lead to poor forecasting performance [6]. In fact, a deep post-event analysis will be more informative, revealing both the presence of direct links between significant control parameters and properties and their manifold influence, taking into account existing

[1] *GOST R ISO 7870-1-2022. Statistical Methods. Control Charts. Part 1. General guidelines. M.: Russian Standardization Institute, 2022. 19 p.*

GOST R ISO 7870-2-2015. Statistical Methods. Control Charts. Part 2. Shewhart Control Charts. M.: Standartinform, 2016. 41 p.

GOST R ISO 7870-3-2013. Statistical Methods. Control Charts. Part 3. Acceptance Control Charts. M.: Standartinform, 2014. 18 p.

areas with one or another type of dependence, the boundaries of which can be determined, for example, using cognitive graphics techniques. [7].

Recently, to solve the problem of quality control of metal products (including end-to-end – from smelting to acceptance tests), machine learning algorithms are increasingly used. Among them, methods based on decision trees [8–12], neural networks, etc. [13–19] have become widespread. In a number of cases, their application allowed creating models, the prediction of which was higher against the conventional regression, for example, when developing a digital laser cladding model [9]. Random forest algorithms were also used when predicting the structure (in particular, the interlamellar distance of precipitated phases), and mechanical properties for alloys with a relatively short production chain [11; 12]. The application of methods, based on decision trees, showed its effectiveness when predicting the consequences at individual stages of the production cycle.

There is a wide interest in software solutions built on the basis of neural networks, for example, for predicting mechanical (during tensile and impact tests [14], as well as measuring hardness [15]), and processing characteristics (hardenability [16]) depending on chemical composition. Moreover, the use of neural networks was tested in the production of slabs, to predict the cast structure, depending on the variation in the values of technological parameters of production [17]. Neural networks were also applied to predict metal defects in the manufacturing process [5]. Neural networks are actively used when recognizing the structure objects, for example, when detecting sulfide inclusions [18] or classifying structural components [19]. Despite their "independence" in work, it is obvious that the effectiveness of the functioning of neural network software products will be largely determined at the stage of their training by highly skilled representatives of the expert community.

In this regard, in particular, it is important to consider issues related to specifying the role of the statistical nature of objects in metallurgy, when applying both classical and developed algorithms. Obviously, it is also important to determine the boundaries of areas with a dominant dependence type, the patterns of their interaction, which will allow justifying the choice of appropriate statistical procedures and criteria. When developing IT solutions in relation to metallurgy, these circumstances are not always given the necessary attention, which, at least, follows from the analysis of relevant publications.

The purpose of this work is to determine the procedure for selecting samples (with the asymmetric nature of the distribution histograms of the values of the 13G1S-U sheet steel acceptance characteristics), to identify areas of change in technological parameters with a dominant dependence type.

METHODS

The study object was the database of production control of the process and product of the technology for producing rolled 13G1S-U steel with a sheet thickness of 12 mm and consisting of 1021 heats. The impact strength values at test temperatures of 0 and −40 °C (KCV^0 and KCU^{-40}, respectively) were chosen as quality characteristics.

Regression analysis was performed using multiple linear regression. The parameters identified were the multiple regression coefficients b_i, the standard error of the regression coefficients σ_b, the correlation coefficients R, and the significance level of the Fisher test F. The removal of insignificant coefficients was carried out when the regression coefficient was equal to zero within the error and the Student's risk level was equal to 0.05.

The main calculated characteristics of the samples were the average value x_{av}, the standard error of the sample σ, the skewness A_s and kurtosis E_x coefficients.

RESULTS

Initial sample analysis

Fig. 1 shows the distribution histograms of the impact strength values for 13G1C-U sheet steel.

The available samples have an asymmetric distribution, while the skewness coefficients are equal to 1.44 and 1.26, and the kurtosis coefficients are equal to 2.53 and 2.38 for the impact strength values KCV^0 and KCU^{-40}, respectively (if the error in their determination for the skewness coefficient is 0.23 and for kurtosis is 0.76).

Regression models were obtained to predict impact strength, with respect to chemical composition, the characteristics of which (b_i is the regression coefficient; σ_b is the standard error of the regression coefficient; R is the correlation coefficient; F is the Fisher criterion significance level) are shown in Table 1.

The regression models obtained are significant proceeding from the Fisher criterion significance level. Fig. 2 presents the graphs illustrating the correspondence of the model to the actual values.

The resulting models predict the desired mechanical properties at a low level. At the same time, clearly outlying values of impact strength are noticeable in the region of its high values, which correspond to the right tails of the histograms determining the deviation of the distribution as a whole from the normal one. This deviation may be the result of the joint action of independent disturbances of approximately equal strength, which determines the nature of its distribution (close to normal). Therefore, there is an interest in dividing the initial sample of impact strength values into two sub-arrays.

Dividing the sample into two data arrays

The initial histograms of impact strength values with pronounced asymmetry were divided into two distributions (with signs of normal one), based on the selection of the largest sample of values (basic sample) as a data array, where the statistical outliers are absent, if the values of the skewness A_s and kurtosis E_x coefficients approach zero as much as possible [20]. The remaining impact strength values (from the right tail of the primary sample distribution) were selected into a separate array (selected sample) and supplemented with values from the basic sample (drawn at random from the right tail of its histogram), also until the values of skewness A_s and kurtosis E_x coefficients (outliers) approach zero as much as possible. The values of technological parameters (chemical composition) corresponding to the two formed samples of impact strength were also separated into paired data arrays.

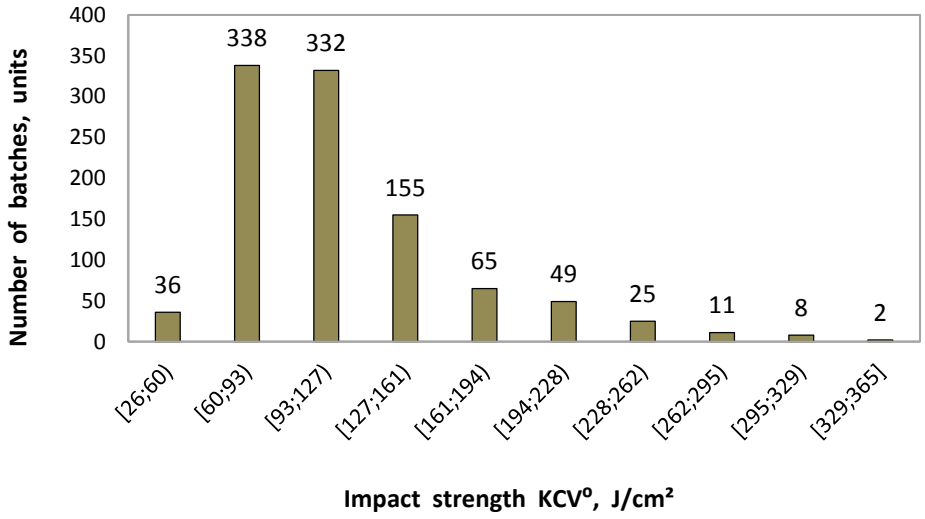

a

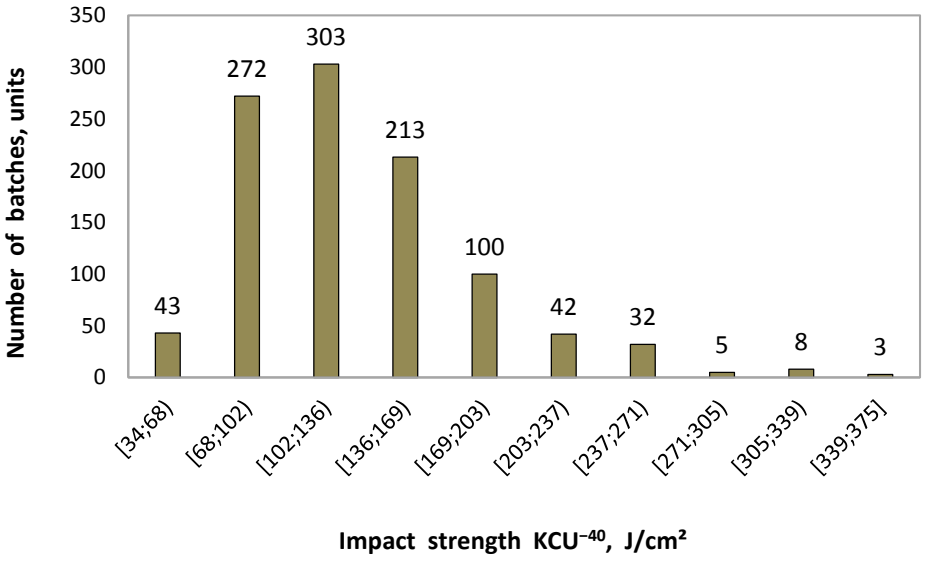

b

Fig. 1. *Histograms of distributions of impact strength of 13G1S-U steel:*
a *– test temperature 0 °C, V-cut;*
b *– test temperature −40 °C, U-cut*
Рис. 1. *Гистограммы распределений ударной вязкости стали 13Г1С-У:*
a *– температура испытания 0 °C, V-надрез;*
b *– температура испытания −40 °C, U-надрез*

Table 1. *Characteristics of the "chemical composition – property" regression model for impact strength of 13G1S-U steel*
Таблица 1. *Характеристики регрессионной модели «химический состав – свойство» для ударной вязкости листовой стали 13Г1С-У*

Property	Equation parameters $\left(\frac{b_i}{\sigma_b}\right)$									*R*	*F*
	Mo	**Nb**	**Cu**	**Cr**	**S**	**Mn**	**Si**	**C**	**0**		
KCU⁻⁴⁰	−1374 403	1485 270	−252 73	132 42	−9425 557	−123 33	−106 29	−833 214	485 62	0.53	$2\cdot10^{-6}$
KCV⁰	–	–	–	–	−9412 521	–	−174 23	–	255 12	0.49	$4\cdot10^{-4}$

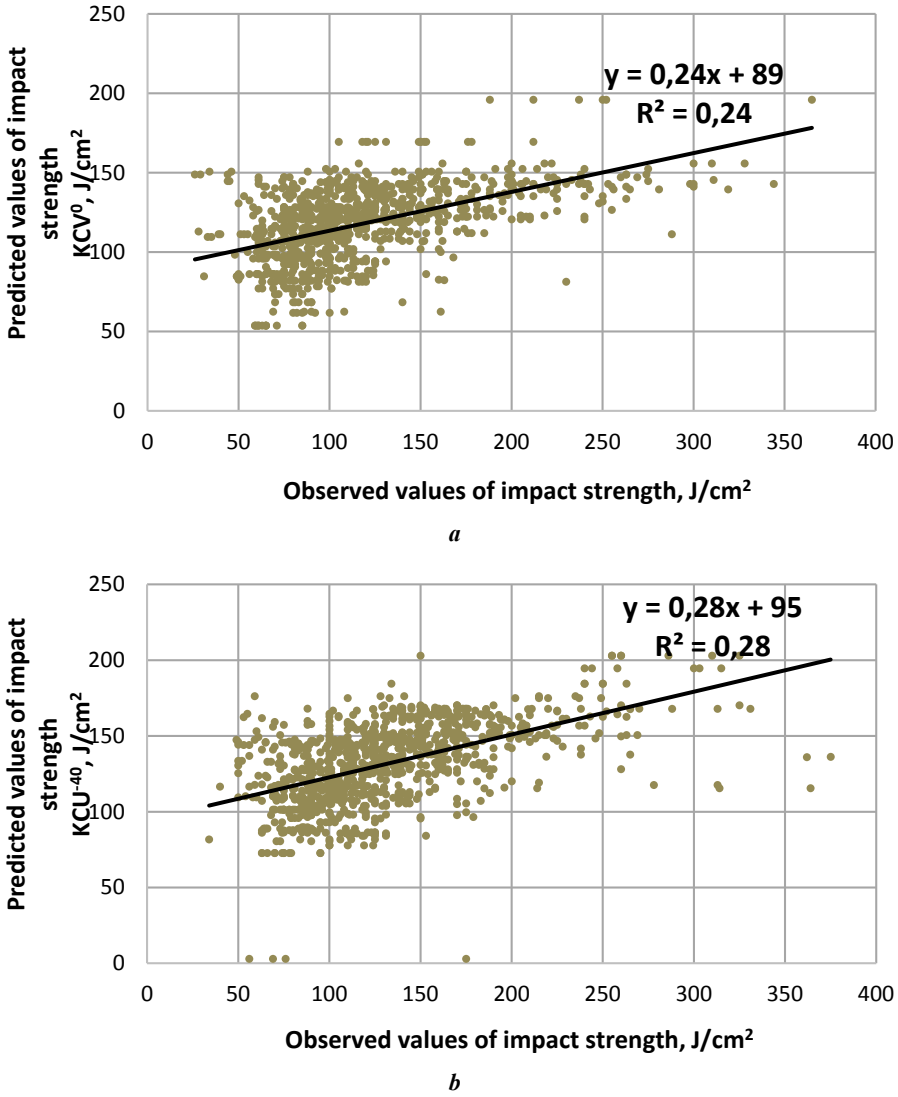

Fig. 2. *Correspondence of predicted and observed values of impact strength of 13G1S-U steel:* ***a*** *– test temperature 0 °C, V-cut;* ***b*** *– test temperature −40 °C, U-cut*

Рис. 2. *Соответствие предсказанных и наблюдаемых значений ударной вязкости стали 13Г1С-У:* ***а*** *– температура испытания 0 °С, V-надрез;* ***b*** *– температура испытания −40 °С, U-надрез*

Fig. 3 shows diagrams for separated impact strength arrays, and Table 2 represents the statistical characteristics of the obtained distributions: x_{av} average values, their σ determination error, skewness and kurtosis coefficients. At the same time, the number of values in the main sample and outliers was 878 and 143 batches for the KCU^{-40} impact strength and 858 and 163 for the KCV^{0} impact strength, respectively.

According to the appearance of the diagrams, and the values of the skewness and kurtosis coefficients, it follows that the distribution of the obtained samples is close to normal.

Table 3 presents the statistical characteristics of the chemical composition samples according to the division into sub-arrays with a normal distribution of KCU^{-40}, and KCV^{0} impact strength values. Differences between the types of distribution of the corresponding chemical composition samples were estimated based on a comparison of the values of the skewness and kurtosis coefficients for the main sample and selected within the error. Therefore, for example, if the difference between the coefficients was greater than the sum of their errors, then this confirmed the validity of the hypothesis about the difference between the samples.

One should note that following the results presented in Table 3, it is not possible to identify differences between the samples based on the average values of the content of the chemical composition constituents. However, for some arrays of values of the content of chemical elements in the basic and selected samples, there is a difference in the form of their distribution: the values of their skewness and kurtosis coefficients differ significantly. Thus, for two samples of impact strength at −40 °C, differences were revealed in the form of corresponding distributions of the content of sulphur, nickel, titanium, vanadium, niobium, boron, and molybdenum; for two samples of impact strength at 0 °C – for the content of nickel (by the value of the kurtosis coefficient only), titanium, vanadium, niobium, and molybdenum. In both cases, the difference in the titanium distribution was revealed by the kurtosis coefficient only. This means, that particular, these parameters contribute the most to the difference between the normally distributed samples shown in Fig. 3.

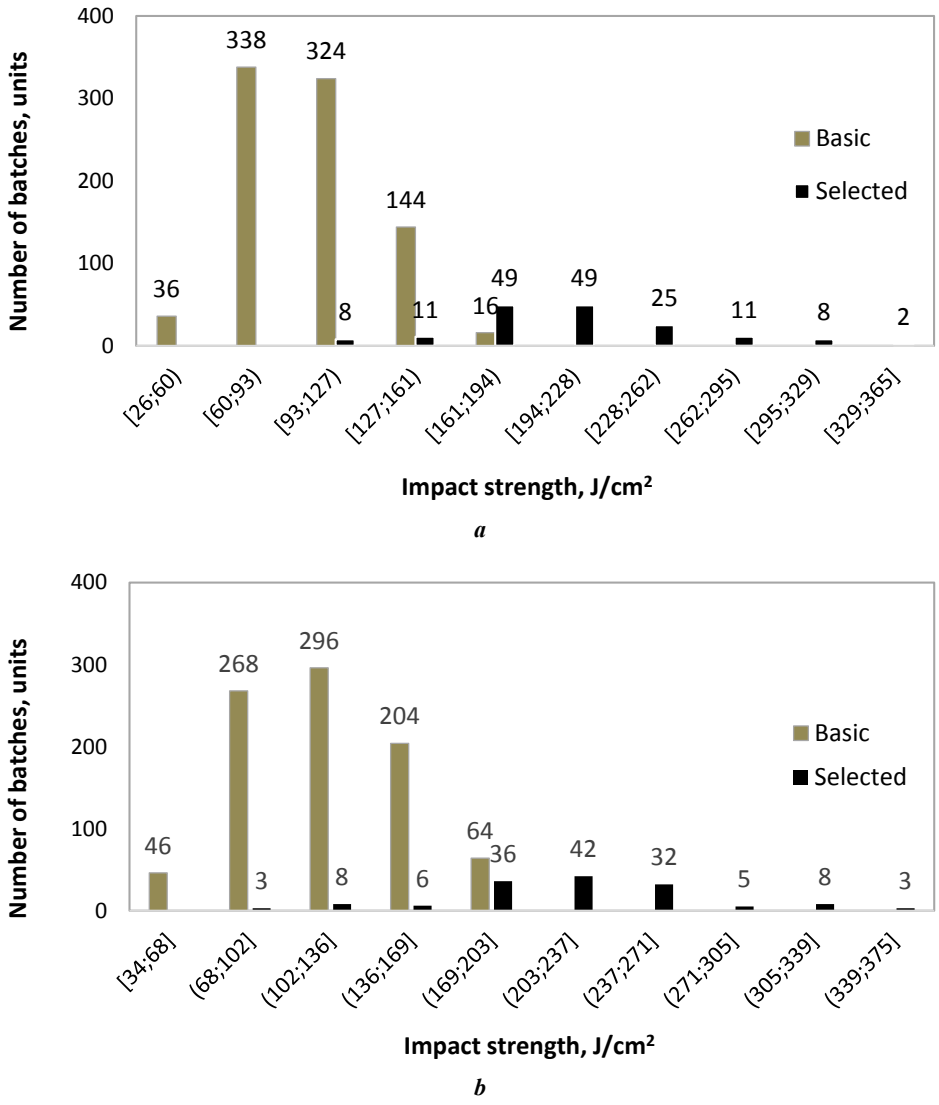

Fig. 3. *Distribution diagrams for the impact strength values of 13G1S-U steel when dividing the initial array into two sub-arrays:*
a *– test temperature 0 °C, V-cut;* ***b*** *– test temperature −40 °C, U-cut*
Рис. 3. *Диаграммы распределения значений ударной вязкости стали 13Г1С-У при разделении исходного массива на два подмассива:*
а *– температура испытания 0 °C, V-надрез;* ***b*** *– температура испытания −40 °C, U-надрез*

Table 2. *Statistical characteristics of divided arrays of the impact strength values of 13G1S-U sheet steel*
Таблица 2. *Статистические характеристики разделенных массивов значений ударной вязкости листовой стали 13Г1С-У*

Property	Sample type	x_{av}, J/cm²	σ, J/cm²	A_s	E_x
KCV^0	Basic	101	29	0.25±0.25	−0.46±0.83
	Selected	205	51	0.19±0.57	0.64±1.83
KCU^{-40}	Basic	118	34	0.24±0.25	−0.54±0.82
	Selected	214	58	0.12±0.60	0.45±1.94

Identification of areas of change in the values of control parameters with a dominant dependence type

The assessment of the influence of certain technology parameters on the quality deviation based on the traditional comparison of their average values over the sample is complicated by some factors, for example, due to the lack of a normal distribution of control parameter values. Regression is also usually ineffective due to the lack of a single space of process and product parameters. Obviously, the influence of certain technology parameters (mainly joint) on the properties of metal products, both positive and negative, is most pronounced, when the level of properties

Table 3. *Statistical characteristics of samples corresponding to the distribution of the content of the 13G1S-U steel chemical composition elements, which conform to the basic and selected arrays of the impact strength values (KCU^{-40} and KCV^{0})*
Таблица 3. *Статистические характеристики выборок, отвечающих распределению содержания элементов химического состава стали 13Г1С-У, соответствующих основному и выделенному массивам значений ударной вязкости (KCU^{-40} и KCV^{0})*

Parameter	Relevant to the array of the KCU^{-40} values				Relevant to the array of the KCV^{0} values			
	x_{av}, % wt.	σ, % wt.	A_s	E_x	x_{cp}, % wt.	σ, % wt.	A_s	E_x
C	0.13*	0.01	−1.34	2.02	0.13	0.01	−1.36	1.97
	0.13	0.01	−0.99	0.13	0.13	0.01	−1.13	0.81
Si	0.49	0.06	−2.28	6.46	0.48	0.06	−2.28	6.12
	0.47	0.08	−2.48	4.99	0.48	0.07	−2.81	7.80
Mn	1.41	0.06	1.57	3.19	1.41	0.06	1.60	3.14
	1.41	0.05	1.68	4.38	1.41	0.05	1.19	3.49
P	0.014	0.003	1.24	2.18	0.014	0.003	1.22	2.17
	0.014	0.003	0.95	1.42	0.014	0.003	1.06	1.35
S*	0.006	0.003	**1.29**	**2.82**	0.006	0.003	1.39	3.37
	0.004	0.003	**3.23**	**15.09**	0.004	0.002	1.07	1.06
Cr	0.10	0.03	1.60	4.33	0.10	0.03	1.63	4.35
	0.11	0.04	1.43	3.04	0.10	0.03	1.27	2.80
Ni*	0.09	0.02	**1.89**	**7.01**	0.09	0.02	1.76	**6.36**
	0.13	0.02	**0.18**	**−0.32**	0.09	0.02	2.12	**9.11**
Cu	0.13	0.02	0.82	1.08	0.13	0.02	0.78	0.97
	0.13	0.02	0.18	−0.32	0.13	0.02	0.76	1.40
Ti*	0.006	0.005	3.38	**10.05**	0.006	0.005	3.18	**8.78**
	0.006	0.005	2.73	**6.88**	0.005	0.004	3.95	**15.96**
Al	0.03	0.006	−0.03	0.42	0.03	0.006	−0.04	0.46
	0.03	0.006	−0.13	−0.05	0.03	0.006	−0.04	−0.19
V*	0.003	0.009	**5.40**	**29.12**	0.004	0.009	**5.11**	**25.87**
	0.007	0.014	**2.85**	**6.42**	0.005	0.013	**3.48**	**10.49**
N	0.009	0.002	0.13	−0.93	0.009	0.002	0.13	−0.92
	0.008	0.002	0.42	−0.16	0.008	0.002	0.36	−0.42
As	0.017	$2\cdot10^{-16}$	1.00	−2.00	0.017	$2\cdot10^{-16}$	1.00	−2.00
	0.017	$5\cdot10^{-17}$	1.01	−2.03	0.017	$6\cdot10^{-17}$	1.01	−2.03

Continue table 3

Parameter	Relevant to the array of the KCU^{-40} values				Relevant to the array of the KCV^0 values			
	x_{av}, % wt.	σ, % wt.	A_s	E_x	x_{cp}, % wt.	σ, % wt.	A_s	E_x
Nb*	0.043	0.007	**2.57**	**6.78**	0.043	0.007	**2.50**	**6.31**
	0.044	0.005	**1.28**	**2.24**	0.043	0.005	**0.85**	**−1.30**
B*	0.001	0.0001	**−3.12**	**11.54**	0.001	0.0001	−2.93	10.19
	0.001	0.0002	**−2.11**	**5.60**	0.001	0.0001	−2.90	10.75
Mo*	0.008	0.004	**6.18**	**47.60**	0.008	0.004	**6.34**	**51.04**
	0.008	0.001	**0.35**	**−1.05**	0.008	0.003	**7.56**	**75.76**

Note. The basic sample is in the upper line of a cell, the selected sample of the impact strength values of the initial array is in the lower line of a cell.

** Chemical composition elements for which the differences in the form of the distribution of values of their content in the basic and selected samples are identified (the corresponding coefficients are highlighted in bold).*

Примечание. В верхней строке ячейки основная, в нижней – выделенная выборка значений ударной вязкости исходного массива.

** Элементы химического состава, для которых выявлены различия в виде распределения значений их содержания в основной и выделенной выборках (соответствующие коэффициенты выделены полужирным начертанием).*

is close to either the upper or lower limits of the sample of their distribution. The selection of the relevant data subarrays, from the production control database can be effective for the subsequent determination of the areas of change in the technology parameters with the dominant dependence type – corresponding, for example, to high and low (positive and negative signs, respectively) values of impact strength. For this purpose, a two-dimensional display of the areas of existence of objects in the form of a "cloud of points" on different planes of x_i–x_m parameters is useful [21]. If the cloud splits into two, then, obviously, there is some objective reason. Usually, the division of arrays is carried out either by selecting an equal number of left and right columns of the histogram of the distribution of the output parameter values (if the sample of n measurements is divided into the number of digits $n^{1/3}$ and the values in the extreme digit numbers are near-equal). However, the correspondence of the values in the left and right tails of the histogram is more often observed with a symmetrical distribution, and in the presence of more or less pronounced asymmetry, such a condition is rather difficult to fulfill. In this case, it is not easy to substantiate even the boundaries of the selection of the distribution "long" tail to identify subsequently the reasons for its formation. In this regard, the variant of considering it as a separate disturbance with a normal distribution proposed in the paper, can be useful as one of the methods of cognitive graphics used to separate data arrays.

Table 4 presents the statistical characteristics of the distributions of the content of the 13G1S-U sheet steel chemical composition elements corresponding to the impact strength (KCU^{-40} and KCV^0) values of the basic and selected samples (obtained by splitting the initial distribution histograms of the impact strength values with right-hand asymmetry according to the proposed procedure).

Table 4. *Statistical characteristics of samples corresponding to the distribution of the content of the 13G1S-U steel chemical composition elements, which conform to the left and right tails of the distribution of the impact strength values (KCU^{-40} and KCV^0)*

Таблица 4. *Статистические характеристики выборок, отвечающих распределению содержания элементов химического состава стали 13Г1С-У, соответствующих левым и правым хвостам распределения значений ударной вязкости (KCU^{-40} и KCV^0)*

Parameter	Relevant to the array of the KCU^{-40} values				Relevant to the array of the KCV^0 values			
	x_{av}, % wt.	σ, % wt.	A_s	E_x	x_{cp}, % wt.	σ, % wt.	A_s	E_x
C	0.13	0.01	−0.78	−0.33	0.14	0.01	−0.90	−0.12
	0.13	0.01	−0.60	−0.73	0.13	0.01	−0.83	−0.29
Si	0.48	0.07	−1.85	2.85	0.46	0.08	−1.25	−0.15
	0.46	0.09	−2.20	3.40	0.46	0.08	−2.45	4.65

Continue table 4

Parameter	Relevant to the array of the KCU^{-40} values				Relevant to the array of the KCV^{0} values			
	x_{av}, % wt.	σ, % wt.	A_s	E_x	x_{cp}, % wt.	σ, % wt.	A_s	E_x
Mn	1.42	0.05	1.35	2.02	1.44	0.08	1.12	−0.07
	1.40	0.04	−0.14	−0.69	1.41	0.04	0.09	0.24
P	0.015	0.003	0.77	−0.21	0.016	0.003	0.29	−0.73
	0.014	0.003	1.23	4.86	0.014	0.003	1.57	3.95
S*	0.007	0.004	1.50	2.50	0.008	0.005	0.98	**0.33**
	0.003	0.001	1.34	0.61	0.003	0.001	2.36	**6.57**
Cr	0.12	0.05	1.51	2.18	0.10	0.04	1.26	0.78
	0.11	0.04	1.34	3.04	0.11	0.05	1.38	1.58
Ni	0.09	0.02	0.69	0.34	0.09	0.02	1.30	1.37
	0.13	0.02	0.25	−0.49	0.08	0.01	0.93	0.90
Cu	0.13	0.02	0.62	0.31	0.13	0.02	0.40	0.73
	0.13	0.02	0.25	−0.49	0.12	0.02	0.10	−0.28
Ti*	0.007	0.007	1.94	2.26	0.010	0.010	1.05	**−0.81**
	0.006	0.005	1.82	1.56	0.006	0.005	2.59	**5.78**
Al	0.029	0.006	0.59	0.76	0.031	0.006	0.43	−0.61
	0.028	0.006	−0.75	−0.21	0.027	0.006	−0.19	0.18
V*	0.005	0.012	4.32	**18.29**	0.005	0.009	**4.99**	**29.27**
	0.008	0.016	2.40	**3.94**	0.007	0.016	**2.63**	**5.24**
N	0.009	0.002	0.57	−0.64	0.008	0.002	0.37	−1.15
	0.008	0.001	0.22	−0.42	0.008	0.001	0.05	−0.70
As	0.017	10^{-17}	−1.03	−2.09	0.017	10^{-17}	−1.04	−2.10
	0.017	10^{-17}	−1.03	−2.09	0.017	10^{-17}	−1.03	−2.09
Nb*	0.044	0.008	**2.40**	**5.43**	0.050	0.011	0.98	−0.47
	0.045	0.005	**0.17**	**−2.06**	0.044	0.005	0.46	−1.87
B	0.001	0.0002	−2.18	6.03	0.001	0.0003	−0.85	0.21
	0.001	0.0002	−2.04	2.42	0.001	0.0002	−2.47	4.54
Mo*	0.008	0.001	−0.24	−0.28	0.009	0.005	**5.68**	**35.79**
	0.008	0.002	0.47	−1.15	0.007	0.001	**0.79**	**−0.62**

Note. The sample of low values is in the upper line of a cell, the sample of high values of the impact strength of the initial arrays corresponding to left and right distribution tails is in the lower line of a cell.

** Chemical composition elements for which the differences in the form of the distribution of values of their content in the samples corresponding to the impact strength values at the lower and upper limits of initial histograms of their distribution are identified (the corresponding coefficients are highlighted in bold).*

Примечание. В верхней строке ячейки – выборка из низких значений, в нижней – высоких значений ударной вязкости исходных массивов, соответствующие левым и правым хвостам распределения.

** Элементы химического состава, для которых выявлены различия в виде распределения значений их содержания в выборках, соответствующих значениям ударной вязкости на нижнем и верхнем пределах исходных гистограмм их распределения (соответствующие коэффициенты выделены полужирным начертанием).*

From the results obtained, it is possible to identify the elements of the steel 13G1S-U chemical composition, in particular, niobium and vanadium, as well as molybdenum, vanadium, titanium, and sulfur, which determine the spread in the values of KCU^{-40} and KCV^{0} impact strength, respectively.

DISCUSSION

The low level of predicting when using regression models is primarily related to the difference in the distribution type of the initial samples of values of the technology control parameters, and the lack of a single space of process and product parameters. One of the main statistical criteria for accepting and rejecting a hypothesis about the regression coefficient significance is the risk of accepting the hypothesis, calculated using the Student's distribution. The desired Student's coefficient, in turn, depends on the standard error of the found regression coefficient. The standard error in the presence of an asymmetric or bimodal distribution of control parameter values is a characteristic describing the parameter with a "large margin", which brings the multiple regression coefficients into an insignificant region, due to which the coefficient corresponding to the parameter is removed from the best model. However, the work shows that variants of the asymmetric distribution of the values of control parameters, for example, the content of elements in 13G1S-U steel, are rather the norm than a deviation from it.

In this regard, one should not rely on predictive production control models based on regression analysis of the entire sample. Another approach, is the analysis of the distributions of technological parameters with predetermined boundaries: on the example of dividing the samples according to the criterion of normality, or the choice of obviously different areas using other methods of cognitive graphics.

The results obtained will be useful when developing IT solutions in metallurgy for forecasting and managing the quality of metal products (within the standard technology without changing it in essence).

CONCLUSIONS

The study showed the multiple regression inefficiency when identifying the technology parameters, limiting the 13G1S-U sheet steel impact strength inhomogeneity and discussed the reasons for this: the discrepancy between the distributions of the values of the technology control parameters and the normal type of distribution and the absence of a single space of process and product parameters. A procedure for selecting samples with an asymmetric nature of distribution histograms is proposed, which is important for an objective selection of technology parameters (or their combinations) that determine their appearance. This can be used as one of the methods of cognitive graphics for the subsequent selection of areas of change in technological parameters with a dominant dependence type.

REFERENCES

1. Vyboyshchik M.A., Ioffe A.V. Scientific basis of development and the methodology of creation of steels for the production of oilfield casing and tubular goods with the increased strength and corrosion resistance. *Vektor nauki Tolyattinskogo gosudarstvennogo universiteta*, 2019, no. 1, pp. 13–20. DOI: 10.18323/2073-5073-2019-1-13-20.
2. Vlasov S.A., Genkin A.L., Nikulina I.V., Koynov T.A., Shatalov R.L., Kravtsov S.V. Computer-integrated control of metallurgical complexes using forecasting simulation. *IFAC Proceedings Volumes*, 2009, vol. 42, no. 4, pp. 1832–1837. DOI: 10.3182/20090603-3-ru-2001.0321.
3. Kudrya A.V., Sokolovskaya E.A., Kodirov D.F., Bosov E.V., Timoshenko V.V. Possibilities of "data mining" of production control in metallurgy for prediction of strength, ductility and toughness of metal products. *Deformatsiya i razrushenie materialov*, 2023, no. S3, pp. 31–40. EDN: UBYQIQ.
4. Chaykin A.V. *Nauchnye osnovy innovatsionnykh tekhnologiy pechnoy i vnepechnoy obrabotki chugunov i staley dlya otlivok otvetstvennogo naznacheniya* [Scientific foundations of innovative technologies for furnace and out-of-furnace processing of cast irons and steels for critical castings]. Sankt Petersburg, Naukoemkie tekhnologii Publ., 2022. 245 p.
5. Wang G., Ledwoch A., Hasani R.M., Grosu R., Brintrup A. A generative neural network model for the quality prediction of work in progress products. *Applied Soft Computing*, 2019, vol. 85, article number 105683. DOI: 10.1016/j.asoc.2019.105683.
6. Kudrya A.V., Sokolovskaya E.A., Kodirov D.F., Bosov E.V., Kotishevskiy G.V. On necessity of taking into account statistical nature of the objects using Big Data in metallurgy. *CIS Iron and Steel Review*, 2022, no. 1, pp. 105–112. DOI: 10.17580/cisisr.2022.01.19.
7. Kudrya A.V., Sokolovskaya E.A., Trachenko V.A., Korotneva K.V. Contribution of the technological heredity into appearance of viscosity nonhomogeneity in constructional steel. *Vektor nauki Tolyattinskogo gosudarstvennogo universiteta*, 2013, no. 3, pp. 202–204. EDN: SBOZDD.
8. Zhukov P.I., Glushchenko A.I., Fomin A.V. Prediction model of temperature of cast billet based on its heating retrospection using boosting "random forest" structure. *Vestnik Novosibirskogo gosudarstvennogo universiteta. Seriya: Informatsionnye tekhnologii*, 2020, vol. 18, no. 4, pp. 11–27. DOI: 10.25205/1818-7900-2020-18-4-11-27.
9. Kolobov A.V., Malyshev K.V., Varfolomeev I.A., Ivanov D.A., Bogachev D.V. Effectiveness increasing of rolling mill operation due to prediction of uninterruptedly-casted block defects. *Proizvodstvo prokata*, 2017, no. 9, pp. 39–42. EDN: ZFPZKT.
10. Zenisek J., Gröning H., Wild N., Huskic A., Affenzeller M. Machine Learning based Data Stream Merging in Additive Manufacturing. *Procedia Computer Science*, 2022, vol. 200, pp. 1422–1431. DOI: 10.1016/j.procs.2022.01.343.
11. Jain R., Lee U., Samal S., Park N. Machine-Learning-Guided Phase Identification and Hardness Prediction of Al-Co-Cr-Fe-Mn-Nb-Ni-V Containing High Entropy Alloys. *Journal of Alloys and Compounds*, 2023, vol. 956, article number 170193. DOI: 10.1016/j.jallcom.2023.170193.

12. Narula P., Kumar P.A., Vanaja J., Prasad Reddy G.V., Rao G.V.S. Machine learning assisted prediction of creep data of India specific reduced activation ferritic martensitic steel. *Materials Today Communications*, 2023, vol. 35, article number 106165. DOI: 10.1016/j.mtcomm.2023.106165.
13. Doroganov V.S., Pimonov A.G. Methods of statistical analysis and neural network technologies for prediction of metallurgical coke quality. *Vestnik Kemerovskogo gosudarstvennogo universiteta*, 2014, no. 4-3, pp. 123–129. EDN: TELNMP.
14. Saoudi A., Fellah M., Hezil N., Lerari D., Khamouli F., Atoui L., Bachari K., Morozova J., Obrosov A., Samad M.A. Prediction of mechanical properties of welded steel X70 pipeline using neural network modelling. *International Journal of Pressure Vessels and Piping*, 2020, vol. 186, article number 104153. DOI: 10.1016/j.ijpvp.2020.104153.
15. Li C., Yin C., Xu X. Hybrid optimization assisted deep convolutional neural network for hardening prediction in steel. *Journal of King Saud University – Science*, 2021, vol. 33, no. 6, article number 101453. DOI: 10.1016/j.jksus.2021.101453.
16. Gao X., Qi K., Deng T., Qiu C., Zhou P., Du X. Application of Artificial Neural Network to Predicting Hardenability of Gear Steel. *Journal of Iron and Steel Research International*, 2006, vol. 13, no. 6, pp. 71–73. DOI: 10.1016/S1006-706X(06)60114-3.
17. Jiang L., Wang A., Tian N., Zhang W., Fan Q. BP Neural Network of Continuous Casting Technological Parameters and Secondary Dendrite Arm Spacing of Spring Steel. *Journal of Iron and Steel Research International*, 2011, vol. 18, no. 8, pp. 25–29. DOI: 10.1016/S1006-706X(11)60099-X.
18. De Oliveira Filho M.F., Caradec P.D.B., Calsaverini R., Spinelli J.E., Ishikawa T.T. Neural network for classification of MnS microinclusions in steels. *Journal of Materials Research and Technology*, 2023, vol. 24, pp. 8522–8532. DOI: 10.1016/j.jmrt.2023.05.101.
19. Gola J., Britz D., Staudt T., Winter M., Schneider A.S., Ludovici M., Mücklich F. Advanced microstructure classification by data mining methods. *Computational Materials Science*, 2018, vol. 148, pp. 324–335. DOI: 10.1016/j.commatsci.2018.03.004.
20. Gmurman V.E. *Teoriya veroyatnostey i matematicheskaya statistika* [Probability Theory and Mathematical Statistics]. Moscow, YuRAYT Publ., 2009. 478 p.
21. Kudrya A.V., Sokolovskaya E.A. Prediction of the Destruction of Materials with an Inhomogeneous Structures. *Fizika metallov i metallovedenie*, 2022, vol. 123, no. 12, pp. 1334–1346. EDN: DROJHB.

СПИСОК ЛИТЕРАТУРЫ

1. Выбойщик М.А., Иоффе А.В. Научные основы разработки и методология создания сталей для производства нефтепромысловых труб повышенной прочности и коррозионной стойкости // Вектор науки Тольяттинского государственного университета. 2019. № 1. С. 13–20. DOI: 10.18323/2073-5073-2019-1-13-20.
2. Vlasov S.A., Genkin A.L., Nikulina I.V., Koynov T.A., Shatalov R.L., Kravtsov S.V. Computer-integrated control of metallurgical complexes using forecasting simulation // IFAC Proceedings Volumes. 2009. Vol. 42. № 4. P. 1832–1837. DOI: 10.3182/20090603-3-ru-2001.0321.
3. Кудря А.В., Соколовская Э.А., Кодиров Д.Ф., Босов Е.В., Тимошенко В.В. Возможности «раскопок данных» производственного контроля в металлургии для прогноза прочности, пластичности и вязкости металлопродукции // Деформация и разрушение материалов. 2023. № S3. С. 31–40. EDN: UBYQIQ.
4. Чайкин А.В. Научные основы инновационных технологий печной и внепечной обработки чугунов и сталей для отливок ответственного назначения. СПб.: Наукоемкие технологии, 2022. 245 с.
5. Wang G., Ledwoch A., Hasani R.M., Grosu R., Brintrup A. A generative neural network model for the quality prediction of work in progress products // Applied Soft Computing. 2019. Vol. 85. Article number 105683. DOI: 10.1016/j.asoc.2019.105683.
6. Kudrya A.V., Sokolovskaya E.A., Kodirov D.F., Bosov E.V., Kotishevskiy G.V. On necessity of taking into account statistical nature of the objects using Big Data in metallurgy // CIS Iron and Steel Review. 2022. № 1. P. 105–112. DOI: 10.17580/cisisr.2022.01.19.
7. Кудря А.В., Соколовская Э.А., Траченко В.А., Коротнева К.В. Вклад технологической наследственности в появление неоднородности вязкости конструкционных сталей // Вектор науки Тольяттинского государственного университета. 2013. № 3. С. 202–204. EDN: SBOZDD.
8. Жуков П.И., Глущенко А.И., Фомин А.В. Модель для прогнозирования температуры заготовки по ретроспекции ее нагрева на основе бустинга структуры // Вестник Новосибирского государственного университета. Серия: Информационные технологии. 2020. Т. 18. № 4. С. 11–27. DOI: 10.25205/1818-7900-2020-18-4-11-27.
9. Колобов А.В., Малышев К.В., Варфоломеев И.А., Иванов Д.А., Богачев Д.В. Повышение эффективности работы прокатного стана за счет прогнозирования дефектов непрерывнолитой заготовки // Производство проката. 2017. № 9. С. 39–42. EDN: ZFPZKT.
10. Zenisek J., Gröning H., Wild N., Huskic A., Affenzeller M. Machine Learning based Data Stream Merging in Additive Manufacturing // Procedia Computer Science. 2022. Vol. 200. P. 1422–1431. DOI: 10.1016/j.procs.2022.01.343.
11. Jain R., Lee U., Samal S., Park N. Machine-Learning-Guided Phase Identification and Hardness Prediction of Al-Co-Cr-Fe-Mn-Nb-Ni-V Containing High Entropy Alloys // Journal of Alloys and Compounds. 2023. Vol. 956. Article number 170193. DOI: 10.1016/j.jallcom.2023.170193.
12. Narula P., Kumar P.A., Vanaja J., Prasad Reddy G.V., Rao G.V.S. Machine learning assisted prediction of creep data of India specific reduced activation ferritic martensitic steel // Materials Today Communications. 2023. Vol. 35. Article number 106165. DOI: 10.1016/j.mtcomm.2023.106165.

13. Дороганов В.С., Пимонов А.Г. Методы статистического анализа и нейросетевые технологии для прогнозирования показателей качества металлургического кокса // Вестник Кемеровского государственного университета. 2014. № 4-3. С. 123–129. EDN: TELNMP.
14. Saoudi A., Fellah M., Hezil N., Lerari D., Khamouli F., Atoui L., Bachari K., Morozova J., Obrosov A., Samad M.A. Prediction of mechanical properties of welded steel X70 pipeline using neural network modelling // International Journal of Pressure Vessels and Piping. 2020. Vol. 186. Article number 104153. DOI: 10.1016/j.ijpvp.2020.104153.
15. Li C., Yin C., Xu X. Hybrid optimization assisted deep convolutional neural network for hardening prediction in steel // Journal of King Saud University – Science. 2021. Vol. 33. № 6. Article number 101453. DOI: 10.1016/j.jksus.2021.101453.
16. Gao X., Qi K., Deng T., Qiu C., Zhou P., Du X. Application of Artificial Neural Network to Predicting Hardenability of Gear Steel // Journal of Iron and Steel Research International. 2006. Vol. 13. № 6. P. 71–73. DOI: 10.1016/S1006-706X(06)60114-3.
17. Jiang L., Wang A., Tian N., Zhang W., Fan Q. BP Neural Network of Continuous Casting Technological Parameters and Secondary Dendrite Arm Spacing of Spring Steel // Journal of Iron and Steel Research International. 2011. Vol. 18. № 8. P. 25–29. DOI: 10.1016/S1006-706X(11)60099-X.
18. De Oliveira Filho M.F., Caradec P.D.B., Calsaverini R., Spinelli J.E., Ishikawa T.T. Neural network for classification of MnS microinclusions in steels // Journal of Materials Research and Technology. 2023. Vol. 24. P. 8522–8532. DOI: 10.1016/j.jmrt.2023.05.101.
19. Gola J., Britz D., Staudt T., Winter M., Schneider A.S., Ludovici M., Mücklich F. Advanced microstructure classification by data mining methods // Computational Materials Science. 2018. Vol. 148. P. 324–335. DOI: 10.1016/j.commatsci.2018.03.004.
20. Гмурман В.Е. Теория вероятностей и математическая статистика. М.: ЮРАЙТ, 2009. 478 с.
21. Кудря А.В., Соколовская Э.А. Прогноз разрушения материалов с неоднородной структурой // Физика металлов и металловедение. 2022. Т. 123. № 12. С. 1334–1346. EDN: DROJHB.

О выборе областей с доминирующим типом зависимости при анализе данных производственного контроля

© 2023

Тимошенко Виктория Владимировна[1], аспирант
Буданова Екатерина Сергеевна[2], магистрант
Кодиров Давронжон Фарходжон Угли[3], аспирант
Соколовская Элина Александровна[4], кандидат технических наук, доцент, доцент кафедры металловедения и физики прочности
Кудря Александр Викторович*[5], доктор технических наук, профессор, профессор кафедры металловедения и физики прочности
Университет науки и технологий МИСИС, Москва (Россия)

***E-mail: AVKudrya@misis.ru**

[1]ORCID: https://orcid.org/0009-0008-7671-0291
[2]ORCID: https://orcid.org/0009-0003-4055-9298
[3]ORCID: https://orcid.org/0009-0003-5380-5558
[4]ORCID: https://orcid.org/0000-0001-9381-9223
[5]ORCID: https://orcid.org/0000-0002-0339-2391

Поступила в редакцию 06.06.2023 *Принята к публикации 16.06.2023*

Аннотация: Формирование представительных баз данных определяет интерес к прогнозированию и управлению качеством металла на основе раскопок данных с использованием специальных программных продуктов, зачастую основанных на регрессионном анализе и не всегда учитывающих статистическую природу самого объекта исследования. Это может привести к ошибочной трактовке результатов или к неполноте извлекаемой информации, снижая эффективность статистической обработки. На основе анализа производственной базы данных технологии получения листовой стали 13Г1С-У были оценены возможности множественной линейной регрессии для прогноза качества листа. Показано, что глубина прогноза регрессии ограничена видом распределения значений управляющих параметров, характер распределения которых оценивали на основе определения коэффициентов асимметрии и эксцесса. В связи с сильным отклонением прогнозируемых моделей от экспериментальных значений в области правого хвоста распределений значений ударной вязкости, в данной работе были развиты методы разделения массивов данных и предложены критерии сравнения получаемых результатов. Для оценки корректности получаемых результатов из исходной выборки были выделены массивы с заведомо ассиметричным распределением, относительно которых также проведено сравнение статистических характеристик. На основе предлагаемых методов выявлены доминирующие химические элементы, которые вносят вклад в различие распределения значений приемо-сдаточных свойств, существующих в рамках одной и той же штатной технологии. Показано, что

предложенный метод разделения может быть использован как вариация приемов когнитивной графики для выделения областей с доминирующим типом зависимости на основе соотношения коэффициентов асимметрии и эксцесса.

Ключевые слова: анализ данных производственного контроля; управление качеством металлопродукции; прогноз качества в металлургии; приемы когнитивной графики; раскопки производственных данных; сталь 13Г1С-У.

Для цитирования: Тимошенко В.В., Буданова Е.С., Кодиров Д.Ф., Соколовская Э.А., Кудря А.В. О выборе областей с доминирующим типом зависимости при анализе данных производственного контроля // Frontier Materials & Technologies. 2023. № 3. С. 103–114. DOI: 10.18323/2782-4039-2023-3-65-10.

doi: 10.18323/2782-4039-2023-3-65-11

Features of microstructure formation in the AK4-1 and AK12D aluminum alloys after their joint friction stir processing

© 2023

Gulnara R. Khalikova*[1,2,3], PhD (Engineering), senior researcher,
assistant professor of Chair "Technological Machines and Equipment",
assistant professor of Chair "Metal Technology in Oil-and-Gas Mechanical Engineering"
Regina A. Basyrova[1], research assistant
Vadim G. Trifonov[1,2,4], PhD (Engineering), leading researcher,
assistant professor of Chair "Metal Technology in Oil-and-Gas Mechanical Engineering"
[1]*Institute for Metals Superplasticity Problems of RAS, Ufa (Russia)*
[2]*Ufa State Petroleum Technological University, Ufa (Russia)*

***E-mail: gulnara.r.khalikova@gmail.com**

[3]ORCID: https://orcid.org/0000-0002-6712-8469
[4]ORCID: https://orcid.org/0000-0002-8187-1355

Received 14.06.2023 *Accepted 21.08.2023*

Abstract: Friction stir processing is one of the modern methods of local modification of the surface of aluminum alloys in the solid-phase state, which provides the dispersion of structural components. In heat-hardened aluminum alloys with a matrix type structure, heat treatment following after friction stir processing can lead to abnormal grain growth in the stir zone. However, in alloys with the structure close to microduplex type, a fine-grained structure can be formed after friction stir processing and heat treatment. This work is aimed at evaluating the possibility of increasing the microstructure thermal stability of the AK4-1 (Al–Cu–Mg–Fe–Si–Ni) matrix-type aluminum alloy. For this purpose, AK12D (Al–Si–Cu–Ni–Mg) aluminum alloy with the structure close to microduplex type was locally mixed into the studied alloy by friction stir processing. Subsequent T6 heat treatment was carried out according to the standard mode for the AK4-1 alloy. Studies showed that the stir zone had an elliptical shape with an onion-ring structure. This structure comprised alternating rings with different amounts and sizes of excess phases. At the same time, in the stir zone center, the width of rings and the average area of excess phases were larger compared to the stir zone periphery, where the width of rings and the average area of particles were smaller. The average area of excess phases in the rings with their higher content was smaller than in the rings with their lower content. This distribution of excess phases leads to the formation of a fine-grained microstructure, where the average size of grains depends on the interparticle distance in the α-Al solid solution.

Keywords: aluminum alloys; AK4-1; AK12D; friction stir processing; heat treatment; thermal stability; structure of onion rings; onion-ring structure.

Acknowledgements: Friction stir processing, macrostructure study, and alloy microstructure quantitative estimation were financially supported by the grant No. 22-29-01318 of the Russian Science Foundation. Energy-dispersive spectroscopy analysis was supported within the program of fundamental research and state assignment of the Ministry of Science and Higher Education of the Russian Federation.

Microstructural research using scanning electron microscopes was carried out on the equipment of Collaborative Access Center "Structural and Physical-Mechanical Research of Materials" of IMSP RAS.

For citation: Khalikova G.R., Basyrova R.A., Trifonov V.G. Features of microstructure formation in the AK4-1 and AK12D aluminum alloys after their joint friction stir processing. *Frontier Materials & Technologies*, 2023, no. 3. pp. 115–124. DOI: 10.18323/2782-4039-2023-3-65-11.

INTRODUCTION

Friction stir processing (FSP), as one of the methods of surface hardening of solid-phase aluminum alloys, has perspectives for development in various industries, since, compared to other traditional methods of surface treatment, it is free of such disadvantages as agglomeration of additive particles, formation of unwanted phases, and interphase reactions due to the high processing temperature, the necessity of using additional processing methods and complex technological equipment, low processing efficiency, etc. [1]. This method of local surface modification of alloys, based on the physical principles of friction stir welding is caused by severe plastic deformation at elevated temperatures, and provides the formation of a fine-grained structure due to the mechanisms of dynamic recrystallisation and recovery [2]. Such a structure often leads to an optimal combination of strength and ductility [3–5].

In heat-hardened aluminum alloys, the strength characteristics are largely determined by coherent dispersed particles, the formation of which occurs due to precipitation hardening during heat treatment, which includes quenching and subsequent artificial aging [6]. However, a significant temperature gradient occurs during friction stir processing/welding [7]. In this case, particles of secondary phases in the processed alloy can undergo complex transformations, which can lead to degradation of strength characteristics. For example, in the thermo-mechanically affected zone, which is subjected to a relatively low temperature effect (≈0.7–0.6 Tmelt, Tmelt is the homologous melting temperature), as a rule, coagulation of excess phases is observed, which can lead to a coherence breakdown at

the interphase boundaries [8]. In the stir zone heated to high temperatures (≈0.9–0.75 Tmelt), particles of secondary phases usually dissolve in the aluminum matrix. Moreover, depending on the deformation temperature during FSP, upon subsequent cooling of the alloy to room temperature, dispersoids can partially precipitate from the α-Al solid solution [9–11], contributing to a partial restoration of the strength characteristics.

The required level of mechanical properties of aluminum alloys after friction stir processing can be achieved by subsequent re-quenching and artificial ageing. In this case, a relatively uniform release of hardening particles is provided in different areas of the treatment zone. However, high temperature treatment often leads to abnormal grain growth in the stir zone, which was observed in various aluminum alloys with a matrix type structure [12–14]. Doping of aluminum alloys with high-strength second-phase particles, such as SiC Al_2O_3, B_4C, SiO_2, TiC, fullerene, carbon nanotubes, graphene, etc., followed by the formation of aluminum-matrix composites, does not always lead to the suppression of abnormal grain growth [15]. Abnormal grain growth is usually described in terms of so-called Humphrey's "cellular model" [16; 17], according to which the anomalous nature of grain growth is associated either with an increased content of low-angle boundaries, or with a relatively low concentration of particles of secondary phases. Nevertheless, it was shown in [18] that a fine-grained structure, with an average grain size of about 3.3±0.1 μm is formed in the AK12D aluminum alloy after FSP and T6 heat treatment. This alloy is characterized by a structure close to that of the microduplex type and consisting of an α-Al matrix, and a large number of excess phases, including the eutectic silicon particles [6]. In this case, a large proportion of dispersed excess phases hindered the migration rate of grain boundaries under the action of the Zener retarding force [19].

Since doping of aluminum matrix alloys, with the second-phase particles does not always help to suppress the anomalous nature of grain growth. It was suggested that a local increase in particles of excess phases due to the mixing of a microduplex-type aluminum alloy into it, can lead to the formation of a fine-grained structure after high-temperature treatment.

The purpose of this work is to evaluate the possibility of increasing the thermal stability of the AK4-1 aluminum alloy microstructure by the local mixing of the AK12D alloy into it by friction stir processing, and subsequent T6 heat treatment.

METHODS

In this work, the authors considered an commercial heat-resistant aluminum alloy AK4-1 with the following chemical composition: Al–1.97%Cu–1.73%Mg–1.01%Fe–0.98%Si–0.96%Ni–0.24%Co (wt. %). From a hot-pressed AK4-1 alloy bar Ø140 mm, plates were cut in the transverse direction, which were machined with a surface roughness of 0.6 Ra. The final thickness of the plates was 7 mm. Grooves 2 mm wide and 2 mm deep were cut out in the surfaces of these plates. As a reinforcing material, the industrial heat-resistant aluminum alloy AK12D with the following chemical composition was used: Al–12.8%Si–1.67%Cu–1.03%Ni–0.84%Mg–0.33%Mn–0.23%Co–0.24%Fe (wt. %). Inserts in the form of rectangular parallelepipeds made of AK12D alloy 2 mm wide and 2 mm high were placed in the grooves of AK4-1 alloy plates. The blank part was attached to the table of a modernized universal milling machine. In order for the inserts in the grooves not to move during the FSP process, the surface of this area was "rubbed" with hangers. In this case, the tool was advanced along the blank surface normal.

Then, a single-pass friction stir processing was performed. A processing tool with a cylindrical pin Ø6 mm and a height of 4 mm with a left-hand thread was used. The processing tool was introduced into the alloy under study at an angle of α=2° to the surface of the blank part, until its shoulders came into contact with the surface to be subjected to FSP. The speed modes of the processing tool were the following: rotation speed ω – 1000 rpm, feed rate ν – 30 mm/min. T6 heat treatment of all studied compositions of aluminum alloys was carried out according to the following mode: quenching at a temperature of 530±5 °C, artificial aging at 190±2 °C for 10 h.

Structural changes were evaluated in the initial heat-treated state, as well as in the state after FSP and subsequent T6 heat treatment. The cross sections of the processed blank parts were prepared for macro- and microstructural analysis. To study the macrostructure and the grain structure, the samples were etched in a solution of the following composition: H_2O (60 ml), HNO_3 (35 ml), HF (5 ml).

Macrostructural analysis of the cross sections of the samples was carried out using a ZEISS Axio Scope.A1 optical microscope (OM). Microstructural studies were carried out on a Tescan Mira 3LMH scanning electron microscope (SEM) using secondary electron (SE), and backscattered electron (BSE) detectors. Energy-dispersive spectral analysis (EDS) was performed on a Tescan Vega 3SBH SEM. Quantification of the average area (*S*) of particles of primary excess intermetallic phases (Pr) and silicon particles (Si), was carried out on the polished surface of the samples, using computer analysis techniques by graphical selection of a group of particles of each of the studied phases. For each treatment zone, quantitative measurements were carried out on the regions equal in area. The average grain size was estimated by the random linear intercept method in five fields of vision. When assessing the primary excess phases and the grain structure, at least 300 structural elements were measured. Processing of research results was carried out with a confidence level of 95 %.

RESULTS

Initial microstructure

A typical microstructure of the AK4-1 aluminum alloy after T6 heat treatment consists of an α-Al solid solution, and a certain amount of excess intermetallide phases located in the direction of material flow during hot deformation (Fig. 1 a). According to [6], the following primary phases of crystallization origin can be present in the Al–Cu–Mg–Ni–Fe system alloys: Al_9FeNi, Mg_2Si, Al_7Cu_2Fe, and Al_2CuMg. After hardening heat treatment, metastable secondary hardening Al_2CuMg phases are formed in these alloys [6]. In the initial heat-treated state, a grain structure recrystallized with an average grain size of 78.6±8.0 μm is observed in the alloy.

A typical microstructure of the AK12D aluminum alloy after T6 heat treatment contains a certain amount of primary

intermetallide phases and silicon, as well as a certain amount of secondary hardening phases (Fig. 1 b). In the Al–Si–Cu–Ni–Mg–Mn–Fe system alloys rich in silicon, in addition to the (Al+Si) eutectics, the presence of the following primary phases of crystallization origin can be expected: Al_5FeSi, Al_8Fe_2Si, $Al_{15}(Fe, Mn)_2Si$, $FeNiAl_9$, $Al_8FeMg_3Si_6$, Al_3Ni, Al_7Cu_4Ni, $Al_3(Ni, Cu)_2$, Al_2Cu, Mg_2Si, $Al_6Cu_2Mg_8Si_5$ [6]. When using T6 heat treatment, the formation of metastable secondary hardening phases, such as Al_2Cu, Mg_2Si, $Al_5Cu_2Mg_8Si_6$, Al_2CuMg, is possible [6]. Hardening heat treatment of the alloy leads to the formation of a grain microstructure with an average grain size of 11.5±0.4 μm.

Macrostructure after FSP

Fig. 3 shows a typical macrostructure of the AK4-1 aluminum alloy at local mixing of the AK12D alloy into it by friction stir processing. It can be observed that a defect-free processing area is formed. A stir zone consisting of a mixture of AK12D and AK4-1 alloys, a thermo-mechanical effect zone, and the base material zone corresponding to the AK4-1 alloy are visible in the structure (Fig. 2). In the near-surface region between the stir zone and the area of contact of the processing tool with a blank part, a coarse-grained microstructure of the AK4-1 alloy is observed. The stir zone has an elliptical shape with concentric circles progressively decreasing in radius, referred to as the "onion-ring" structure.

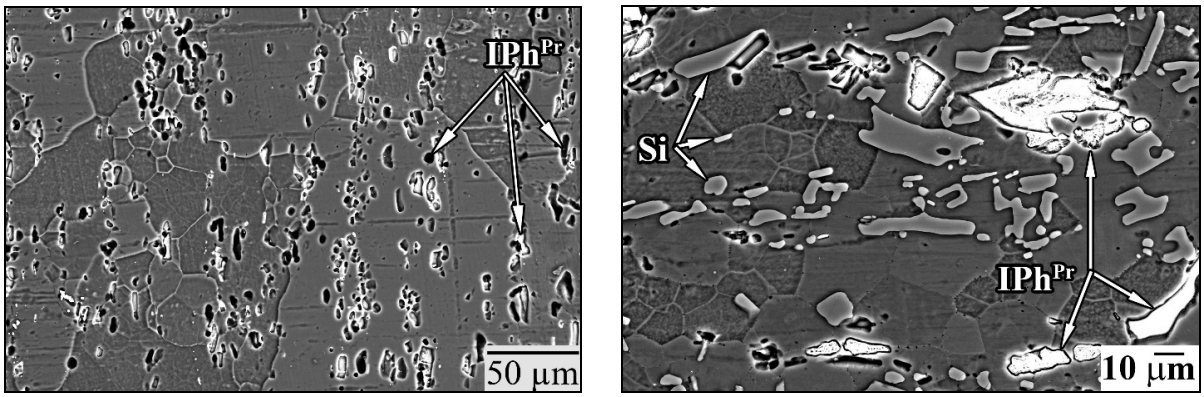

Fig. 1. *Typical microstructure of the AK4-1 (**a**) and AK12D (**b**) alloys in the initial heat-treated state. IPh^{Pr} – primary intermetallic phases, Si – silicon particles. BSE mode SEM images*
Рис. 1. *Типичная микроструктура сплавов АК4-1 (**а**) и АК12Д (**b**) в исходном термообработанном состоянии. IPh^{Pr} – первичные интерметаллидные фазы, Si – частицы кремния. BSE-режим съемки*

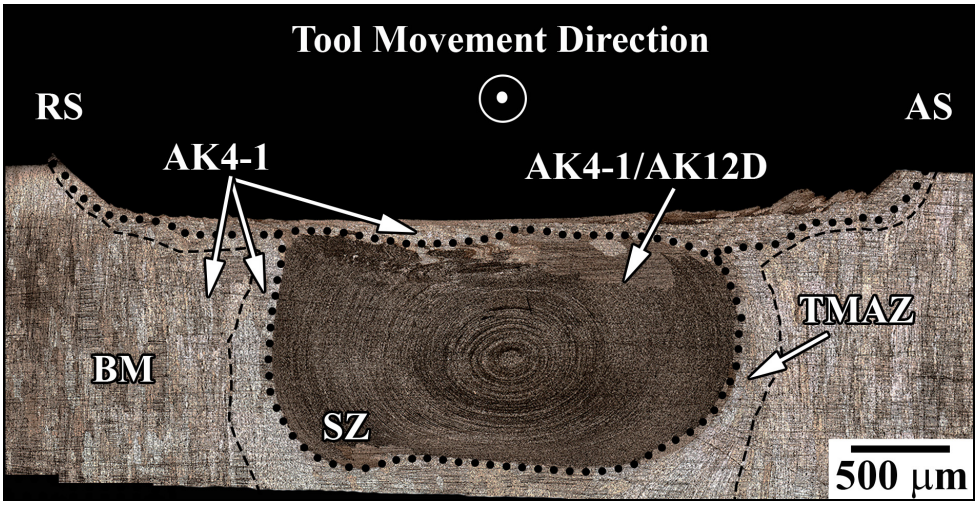

Fig. 2. *Macrostructure of the AK4-1 aluminum alloy after mixing into it the AK12D alloy via friction stir processing at the ω=1000 rpm and v=30 mm/min. AS – advancing side, RS – retreating side, SZ – stir zone, TMAZ –thermo-mechanical affected zone, BM – base metal (initial alloy). Optical metallography*
Рис. 2. *Макростроение алюминиевого сплава АК4-1 после замешивания в него сплава АК12Д обработкой трением с перемешиванием при скоростях деформации ω=1000 об/мин и v=30 мм/мин. AS – наступающая сторона, RS – отступающая сторона, SZ – зона перемешивания, TMAZ – зона термомеханического влияния, BM – основной металл (исходный сплав). Оптическая металлография*

Microstructure after FSP

The "onion rings" structure is heterogeneous over the cross section of the stir zone, and represents alternating rings with different amounts and sizes of excess phases (Fig. 3). The width of the rings decreases from the stir zone center to the periphery. Friction stir processing leads to intense crushing of particles of excess phases. A quantitative assessment of the alloy microstructure is given in Table 1. The average area of particles in rings with a higher content of excess phases is smaller than in rings where the number of phases is lower. It should be noted that eutectic silicon particles are concentrated in rings with a higher content of primary phases (Fig. 4). This is also evidenced by the EDS analysis results. The corresponding distribution maps for the main alloying elements are shown in Fig. 5.

The study of the grain structure showed that after FSP, and T6 heat treatment, a fine-grained microstructure is formed in the stir zone (Fig. 6), the average grain size (Table 1) of which depends on the amount of excess phases located in different parts of the stir zone.

DISCUSSION

As a rule, the stir zone shape depends on the processing tool geometry, the technological parameters of processing, the thermal conductivity of the material, and the temperature of the blank part [20; 21]. The stir zone shape is much determined by the temperature of the heated alloy in the near-surface regions, during friction between the processing tool shoulders and the blank part. During friction stir processing, a stir zone typically assumes a basin-like shape with a widening at the blank part surface or an elliptical shape [20; 21].

According to findings presented in [21], a stir zone with a basin-like shape is created during low-speed tool rotation. In this case, the alloy yield strength is higher due to the low temperature of the heated material, and consequently, its volume subjected to deformation (caused by the pin motion) is smaller. With an increase in the rotation velocity of the tool, the temperature of the heated alloy increases, contributing to a decrease in the yield strength. An increase in the volume of the material that is involved in the deformation process, and the formation of an elliptical stir zone (Fig. 3). The formation of the "onion rings" structure occurs due to a periodic change in the stress state in the three-dimensional flow of a plastically deformable alloy, which is caused by the movement of the processing tool (shoulders and pins) [22–24]. As a result, the stir zone structure exhibits a periodically changing average grain size [25], alternating bands (rings) enriched in excess phases [26], different grain orientations [27], and texture changes [28]. Moreover, the temperature of deformation during the FSP process is non-uniform over the cross section of the stir zone [29–31]. Therefore, in the structure of the treatment zone, rings are observed, the width of which decreases from its center to the periphery.

As noted earlier, subsequent T6 heat treatment (including solution heat treatment and artificial aging) can lead to abnormal grain growth in the treatment area, which presumably indicates a low thermal stability of the microstructure. The AK12D alloy, in contrast to the AK4-1 alloy, is characterized by a structure close to that of the microduplex type [6]. The formation of a fine-grained microstructure during mixing of the AK12D alloy into the AK4-1 alloy by friction stir processing and subsequent T6 heat treatment occurs due to the fact that a large number of excess phase particles of both alloys, has a retarding effect on the migration of grain boundaries. In areas where the number of excess phases is greater, the average grain size is smaller. This is related to the smaller distance between the excess phase particles in the α-Al solid solution.

CONCLUSIONS

The authors studied the structure of the AK4-1 aluminum alloy, in which the AK12D alloy was locally mixed by friction stir processing, and subsequent T6 heat treatment carried out according to the standard mode for the AK4-1 alloy.

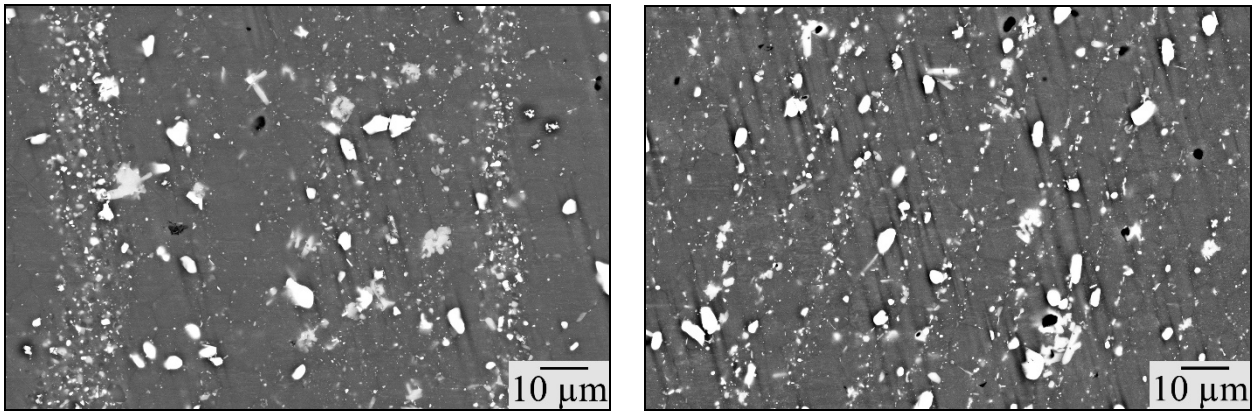

a ***b***

Fig. 3. *Typical microstructure of the polished stir zone surface.*
*Ring fragments in the center (**a**) and on the periphery of stir zone (**b**) are shown. BSE mode SEM images*
Рис. 3. *Типичная микроструктура полированной поверхности зоны перемешивания.*
*Приведены фрагменты колец в центре (**a**) и на периферии зоны перемешивания (**b**). BSE-режим съемки*

Table 1. *Quantitative estimation of the AK4-1 aluminum alloy microstructure after mixing the AK12D alloy into it via friction stir processing*

Таблица 1. *Количественная оценка микроструктуры алюминиевого сплава АК4-1 после замешивания в него сплава АК12Д обработкой трением с перемешиванием*

Microstructural elements of alloys			State					
			Initial state		Friction stir treatment			
					Stir zone AK4-1/AK12D			
			АК4-1	АК12D	Center		Periphery	
					SZ	SZ-1	SZ	SZ-1
S	IPh	μm^2	12.8±1.0	39.9±4.0	13.5±0.4	0.17±0.01	10.3±0.3	0.13±0.01
	Si	μm^2	–	45.9±5.7	–	2.2±0.1	–	1.2±0.1
d		μm	78.6±8.0	11.5±0.4	7.1±0.2	3.0±0.1	4.0±0.1	

Note. SZ – rings with a low content of excess phases;
SZ-1 – rings with a higher content of excess phases;
S – average area of primary intermetallic phases (IPh) and Si particles;
d – average grain size. For comparison, a quantitative estimation of the structure in the initial heat-treated state of the AK4-1 and AK12D alloys is given.

Примечание. SZ – кольца с малым содержанием избыточных фаз;
SZ-1 – кольца с бóльшим содержанием избыточных фаз;
S – средняя площадь первичных интерметаллидных фаз IPh и частиц Si;
d – средний размер зерен. Для сравнения приведена количественная оценка структуры в исходном термообработанном состоянии сплавов АК4-1 и АК12Д.

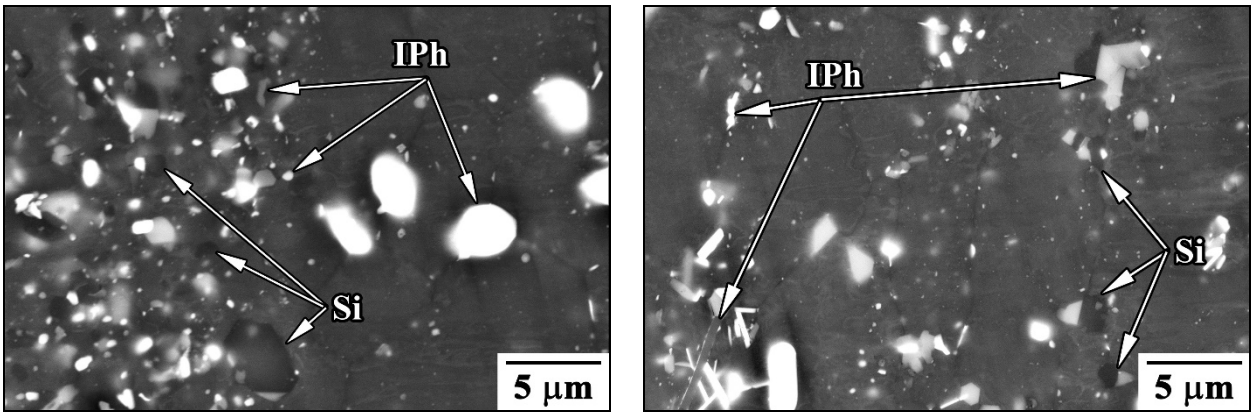

a ***b***

Fig. 4. *Typical microstructure of the polished stir zone surface. Fragments of the boundaries between the rings with varying degrees of excess phases in the center (**a**) and on the periphery (**b**) of the stir zone are shown. IPh – intermetallic phases, Si – silicon particles. BSE mode SEM images*

Рис. 4. *Типичная микроструктура полированной поверхности зоны перемешивания. Приведены фрагменты границ между кольцами с бóльшим и меньшим количеством избыточных фаз в центре (**а**) и на периферии (**b**) зоны перемешивания. IPh – интерметаллидные фазы, Si – частицы кремния. BSE-режим съемки*

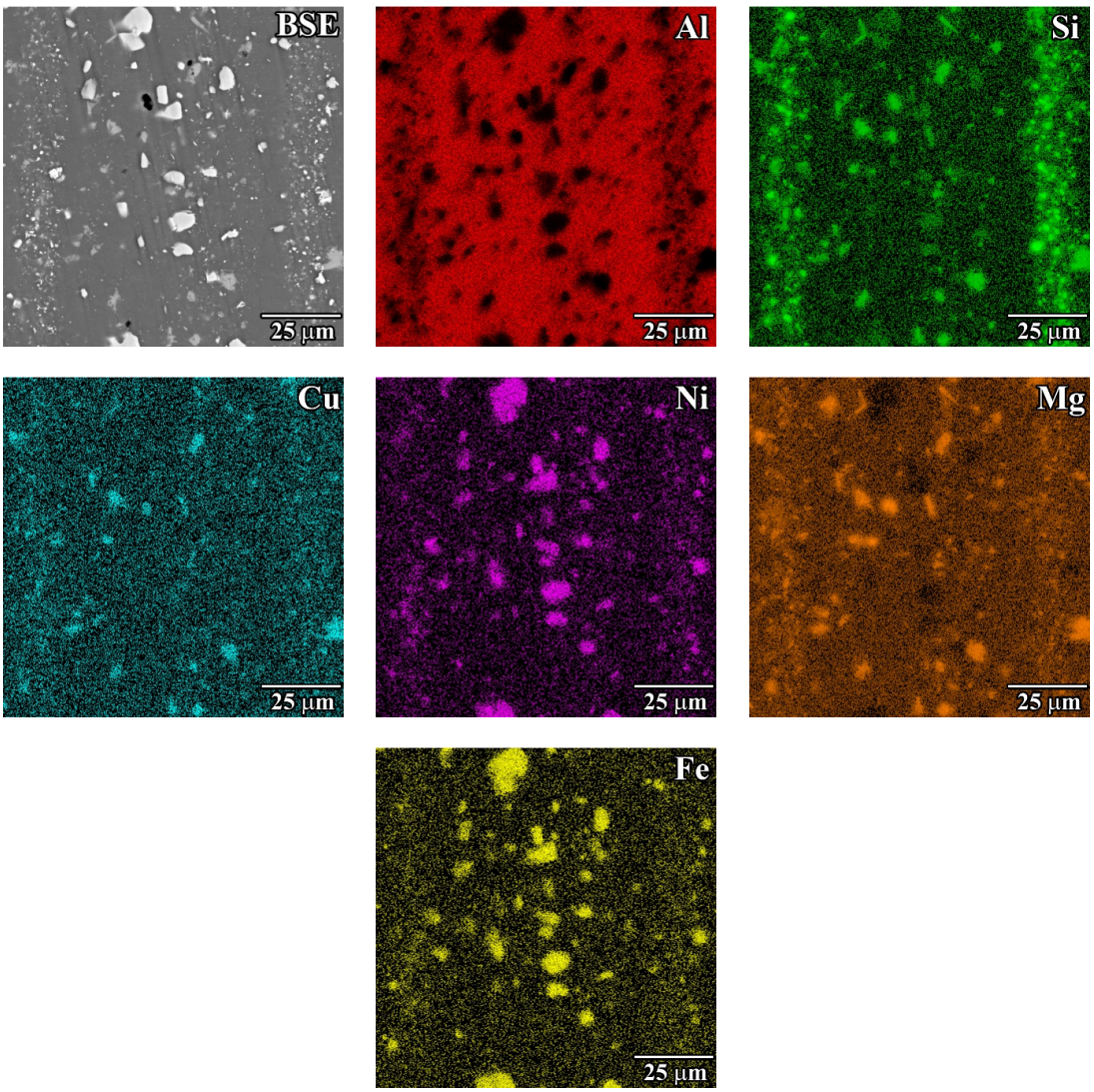

Fig. 5. *Distribution maps of the primary alloying elements in the center part of the polished stir zone surface. EDS analysis*
Рис. 5. *Карты распределения основных легирующих элементов в центральной части полированной поверхности зоны перемешивания. ЭДС-анализ*

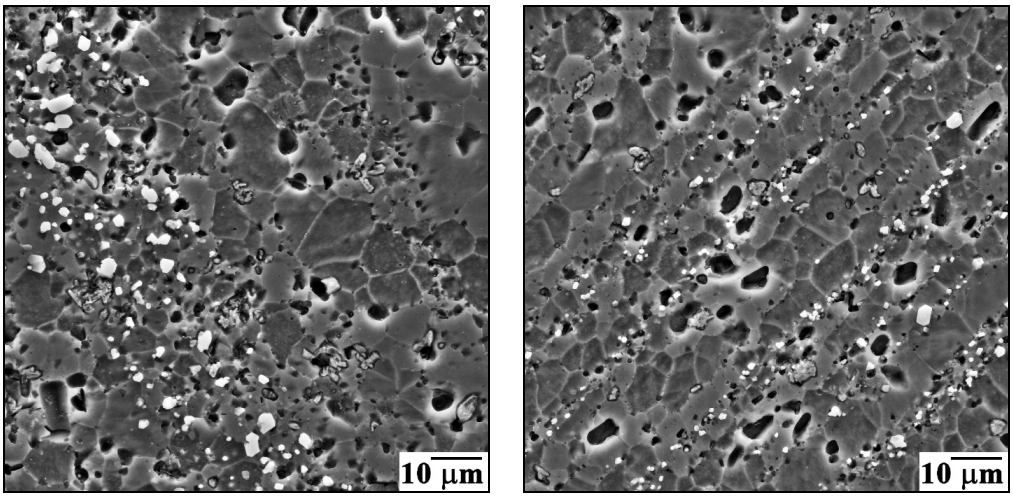

a ***b***

Fig. 6. *Typical grain microstructure in the center* ***(a)*** *and on the periphery* ***(b)*** *of the stir zone. SE mode SEM images*
Рис. 6. *Типичная зеренная микроструктура в центре* ***(а)*** *и на периферии* ***(b)*** *зоны перемешивания. SE-режим съемки*

It is shown that after FSP, a defect-free treatment area was formed, the stir zone of which had an elliptical shape with the "onion rings" structure. The width of these rings decreased from the stir zone center to the periphery. The onion structure consisted of alternating rings with different amounts and sizes of excess phases.

It was established that the friction stir processing led to intense crushing of the primary excess phases of both alloys. At the same time, the average area of particles in rings with a higher content of them is smaller than in rings where their number is lower. Moreover, eutectic silicon particles are concentrated in rings with a higher content of primary phases.

It was found that the nonuniform distribution of particles of excess phases led to the formation of a fine-grained microstructure, the average grain size of which depends on the interparticle distance in the α-Al solid solution. The minimum average grain size was observed in the stir zone center in rings with a higher content of excess phases and was 3.0±0.1 μm. The largest average grain size reached 7.1±0.2 μm and was formed in the stir zone center in rings with a low content of excess phases.

REFERENCES

1. Zykova A.P., Tarasov S.Yu., Chumaevskiy A.V., Kolubaev E.A. A Review of friction stir processing of structural metallic materials: process, properties, and methods. *Metals*, 2020, vol. 10, no. 6, article number 772. DOI: 10.3390/met10060772.
2. Mishra R.S., Ma Z.Y. Friction stir welding and processing. *Materials Science and Engineering: R: Reports*, 2005, vol. 50, no. 1-2, pp. 1–78. DOI: 10.1016/j.mser.2005.07.001.
3. Mirian Mehrian S.S., Rahsepar M., Khodabakhshi F., Gerlich A.P. Effects of friction stir processing on the microstructure, mechanical and corrosion behaviors of an aluminum-magnesium alloy. *Surface and Coatings Technology*, 2021, vol. 405, article number 126647. DOI: 10.1016/j.surfcoat.2020.126647.
4. Croteau J.R., Jung J.G., Whalen S.A. et al. Ultrafine-grained Al–Mg–Zr alloy processed by shear-assisted extrusion with high thermal stability. *Scripta Materialia*, 2020, vol. 186, pp. 326–330. DOI: 10.1016/j.scriptamat.2020.05.051.
5. He Ch., Li Y., Wei J., Zhang Zh., Tian N., Qin G., Zhao X. Enhancing the mechanical performance of Al–Zn–Mg alloy builds fabricated via underwater friction stir additive manufacturing and post-processing aging. *Journal of Materials Science and Technology*, 2022, vol. 108, pp. 26–36. DOI: 10.1016/j.jmst.2021.08.050.
6. Belov N.A. *Fazovyy sostav promyshlennykh i perspektivnykh alyuminievykh splavov* [Phase Composition of Industrial and Prospective Aluminium Alloys]. Moscow, MISiS Publ., 2010. 511 p.
7. Heidarzadeh A., Mironov S., Kaibyshev R. et al. Friction stir welding/processing of metals and alloys: a comprehensive review on microstructural evolution. *Progress in Materials Science*, 2021, vol. 117, article number 100752. DOI: 10.1016/j.pmatsci.2020.100752.
8. Feng X., Liu H., Lippold J.C. Microstructure characterization of the stir zone of submerged friction stir processed aluminum alloy 2219. *Materials Characterization*, 2013, vol. 82, pp. 97–102. DOI: 10.1016/j.matchar.2013.05.010.
9. Rhodes C.G., Mahoney M.W., Bingel W.H., Spurling R.A., Bampton C.C. Effects of friction stir welding on microstructure of 7075 aluminum. *Scripta Materialia*, 1997, vol. 36, no. 1, pp. 69–75. DOI: 10.1016/S1359-6462(96)00344-2.
10. Fonda R.W., Bingert J.F. Microstructural evolution in the heat-affected zone of a friction stir weld. *Metallurgical and Materials Transactions A*, 2004, vol. 35, pp. 1487–1499. DOI: 10.1007/s11661-004-0257-7.
11. Qin H., Zhang H., Wu H. The evolution of precipitation and microstructure in friction stir welded 2195-T8 Al–Li alloy. *Materials Science and Engineering: A*, 2015, vol. 626, pp. 322–329. DOI: 10.1016/j.msea.2014.12.026.
12. Zuiko I.S., Mironov S., Betsofen S., Kaibyshev R. Suppression of abnormal grain growth in friction-stir welded Al–Cu–Mg alloy by lowering of welding temperature. *Scripta Materialia*, 2021, vol. 196, article number 113765. DOI: 10.1016/j.scriptamat.2021.113765.
13. Charit I., Mishra R.S. Abnormal grain growth in friction stir processed alloys. *Scripta Materialia*, 2008, vol. 58, pp. 367–371. DOI: 10.1016/j.scriptamat.2007.09.052.
14. Kalinenko A., Vysotskiy I., Malopheyev S., Mironov S., Kaibyshev R. New insight into the phenomenon of the abnormal grain growth in friction-stir welded aluminum. *Materials Letters*, 2021, vol. 302, article number 130407. DOI: 10.1016/j.matlet.2021.130407.
15. Khodabakhshi F., Simchi A., Kokabi A.H., Gerlich A.P., Nosko M. Effects of post-annealing on the microstructure and mechanical properties of friction stir processed Al–Mg–TiO_2 nanocomposites. *Materials and Design*, 2014, vol. 63, pp. 30–41. DOI: 10.1016/j.matdes.2014.05.065.
16. Humphreys F.J. A unified theory of recovery, recrystallization and grain growth, based on the stability and growth of cellular microstructures – I. The basic model. *Acta Materialia*, 1997, vol. 45, no. 10, pp. 4231–4240. DOI: 10.1016/S1359-6454(97)00070-0.
17. Humphreys F.J. A unified theory of recovery, recrystallization and grain growth, based on the stability and growth of cellular microstructures – II. The effect of second-phase particles. *Acta Materialia*, 1997, vol. 45, no. 12, pp. 5031–5039. DOI: 10.1016/S1359-6454(97)00173-0.
18. Khalikova G.R., Zakirova G.R., Farkhutdinov A.I., Korznikova E.A., Trifonov V.G. Surface hardening of an Al–Si–Cu–Ni–Mg aluminum alloy by friction stir processing and T6 heat treatment. *Letters on Materials*, 2022, vol. 12, no. 3, pp. 255–260. DOI: 10.22226/2410-3535-2022-3-255-260.
19. Khodabakhshi F., Nosko M., Gerlich A.P. Dynamic restoration and crystallographic texture of a friction-stir processed Al–Mg–SiC surface nanocomposite. *Materials Science and Technology*, 2018, vol. 34, no. 14, pp. 1773–1791. DOI: 10.1080/02670836.2018.1490858.

20. Ma Z.Y., Sharma S.R., Mishra R.S. Microstructural modification of as-cast Al–Si–Mg alloy by friction stir processing. *Metallurgical and Materials Transactions A*, 2006, vol. 37, pp. 3323–3336. DOI: 10.1007/BF02586167.
21. Yang J., Wang D., Xiao B.L., Ni D.R., Ma Z.Y. Effects of rotation rates on microstructure, mechanical properties, and fracture behavior of friction stir-welded (FSW) AZ31 magnesium alloy. *Metallurgical and Materials Transactions A*, 2013, vol. 44, pp. 517–530. DOI: 10.1007/s11661-012-1373-4.
22. Cui G.R., Ma Z.Y., Li S.X. Periodical plastic flow pattern in friction stir processed Al–Mg alloy. *Scripta Materialia*, 2008, vol. 58, no. 12, pp. 1082–1085. DOI: 10.1016/j.scriptamat.2008.02.003.
23. Andrade D.G., Leitão C., Dialami N., Chiumenti M., Rodrigues D.M. Analysis of contact conditions and its influence on strain rate and temperature in friction stir welding. *International Journal of Mechanical Sciences*, 2021, vol. 191, article number 106095. DOI: 10.1016/j.ijmecsci.2020.106095.
24. Avettand-Fénoël M.-N., Taillard R., Laye J., Odiévre T. Experimental investigation of three-dimensional (3-D) material flow pattern in thick dissimilar 2050 friction-stir welds. *Metallurgical and Materials Transactions A*, 2014, vol. 45, pp. 563–578. DOI: 10.1007/s11661-013-2015-1.
25. Schneider J.A., Nunes A.C. Characterization of plastic flow and resulting microtextures in a friction stir weld. *Metallurgical and Materials Transactions B*, 2004, vol. 35, pp. 777–783. DOI: 10.1007/s11663-004-0018-4.
26. Yang B.C., Yan J.H., Sutton M.A., Reynolds A.P. Banded microstructure in AA2024-T351 and AA2524-T351 aluminum friction stir welds: Part I. Metallurgical studies. *Materials Science and Engineering: A*, 2004, vol. 364, no. 1-2, pp. 55–65. DOI: 10.1016/S0921-5093(03)00532-X.
27. Zhou Y.Z., Zhang W., Wang B.Q., Guo J.D. Ultrafine-grained microstructure in a Cu–Zn alloy produced by electropulsing treatment. *Journal of Materials Research*, 2003, vol. 18, pp. 1991–1997. DOI: 10.1557/JMR.2003.0276.
28. Xu S.W., Deng X.M. A study of texture patterns in friction stir welds. *Acta Materialia*, 2008, vol. 56, no. 6, pp. 1326–1341. DOI: 10.1016/j.actamat.2007.11.016.
29. Ma X., Xu Sh., Wang F., Zhao Y., Meng X., Xie Y., Wan L., Huang Y.Y. Effect of temperature and material flow gradients on mechanical performances of friction stir welded AA6082-T6 joints. *Materials*, 2022, vol. 15, no. 19, article number 6579. DOI: 10.3390/ma15196579.
30. Woo W., Choo H., Withers P.J., Feng Z. Prediction of hardness minimum locations during natural aging in an aluminum alloy 6061-T6 friction stir weld. *Journal of Materials Science*, 2009, vol. 44, pp. 6302–6309. DOI: 10.1007/s10853-009-3868-y.
31. Mehdi H., Mishra R.S. Effect of friction stir processing on mechanical properties and heat transfer of TIG welded joint of AA6061 and AA7075. *Defence Technology*, 2021, vol. 17, no. 3, pp. 715–727. DOI: 10.1016/j.dt.2020.04.014.

СПИСОК ЛИТЕРАТУРЫ

1. Zykova A.P., Tarasov S.Yu., Chumaevskiy A.V., Kolubaev E.A. A Review of friction stir processing of structural metallic materials: process, properties, and methods // Metals. 2020. Vol. 10. № 6. Article number 772. DOI: 10.3390/met10060772.
2. Mishra R.S., Ma Z.Y. Friction stir welding and processing // Materials Science and Engineering: R: Reports. 2005. Vol. 50. № 1-2. P. 1–78. DOI: 10.1016/j.mser.2005.07.001.
3. Mirian Mehrian S.S., Rahsepar M., Khodabakhshi F., Gerlich A.P. Effects of friction stir processing on the microstructure, mechanical and corrosion behaviors of an aluminum-magnesium alloy // Surface and Coatings Technology. 2021. Vol. 405. Article number 126647. DOI: 10.1016/j.surfcoat.2020.126647.
4. Croteau J.R., Jung J.G., Whalen S.A. et al. Ultrafine-grained Al–Mg–Zr alloy processed by shear-assisted extrusion with high thermal stability // Scripta Materialia. 2020. Vol. 186. P. 326–330. DOI: 10.1016/j.scriptamat.2020.05.051.
5. He Ch., Li Y., Wei J., Zhang Zh., Tian N., Qin G., Zhao X. Enhancing the mechanical performance of Al–Zn–Mg alloy builds fabricated via underwater friction stir additive manufacturing and post-processing aging // Journal of Materials Science and Technology. 2022. Vol. 108. P. 26–36. DOI: 10.1016/j.jmst.2021.08.050.
6. Белов Н.А. Фазовый состав промышленных и перспективных алюминиевых сплавов. М.: МИСиС, 2010. 511 с.
7. Heidarzadeh A., Mironov S., Kaibyshev R. et al. Friction stir welding/processing of metals and alloys: a comprehensive review on microstructural evolution // Progress in Materials Science. 2021. Vol. 117. Article number 100752. DOI: 10.1016/j.pmatsci.2020.100752.
8. Feng X., Liu H., Lippold J.C. Microstructure characterization of the stir zone of submerged friction stir processed aluminum alloy 2219 // Materials Characterization. 2013. Vol. 82. P. 97–102. DOI: 10.1016/j.matchar.2013.05.010.
9. Rhodes C.G., Mahoney M.W., Bingel W.H., Spurling R.A., Bampton C.C. Effects of friction stir welding on microstructure of 7075 aluminum // Scripta Materialia. 1997. Vol. 36. № 1. P. 69–75. DOI: 10.1016/S1359-6462(96)00344-2.
10. Fonda R.W., Bingert J.F. Microstructural evolution in the heat-affected zone of a friction stir weld // Metallurgical and Materials Transactions A. 2004. Vol. 35. P. 1487–1499. DOI: 10.1007/s11661-004-0257-7.
11. Qin H., Zhang H., Wu H. The evolution of precipitation and microstructure in friction stir welded 2195-T8 Al–Li alloy // Materials Science and Engineering: A. 2015. Vol. 626. P. 322–329. DOI: 10.1016/j.msea.2014.12.026.
12. Zuiko I.S., Mironov S., Betsofen S., Kaibyshev R. Suppression of abnormal grain growth in friction-stir welded Al–Cu–Mg alloy by lowering of welding temperature // Scripta Materialia. 2021. Vol. 196. Article number 113765. DOI: 10.1016/j.scriptamat.2021.113765.
13. Charit I., Mishra R.S. Abnormal grain growth in friction stir processed alloys // Scripta Materialia. 2008. Vol. 58. P. 367–371. DOI: 10.1016/j.scriptamat.2007.09.052.

14. Kalinenko A., Vysotskiy I., Malopheyev S., Mironov S., Kaibyshev R. New insight into the phenomenon of the abnormal grain growth in friction-stir welded aluminum // Materials Letters. 2021. Vol. 302. Article number 130407. DOI: 10.1016/j.matlet.2021.130407.
15. Khodabakhshi F., Simchi A., Kokabi A.H., Gerlich A.P., Nosko M. Effects of post-annealing on the microstructure and mechanical properties of friction stir processed Al–Mg–TiO_2 nanocomposites // Materials and Design. 2014. Vol. 63. P. 30–41. DOI: 10.1016/j.matdes.2014.05.065.
16. Humphreys F.J. A unified theory of recovery, recrystallization and grain growth, based on the stability and growth of cellular microstructures – I. The basic model // Acta Materialia. 1997. Vol. 45. № 10. P. 4231–4240. DOI: 10.1016/S1359-6454(97)00070-0.
17. Humphreys F.J. A unified theory of recovery, recrystallization and grain growth, based on the stability and growth of cellular microstructures – II. The effect of second-phase particles // Acta Materialia. 1997. Vol. 45. № 12. P. 5031–5039. DOI: 10.1016/S1359-6454(97)00173-0.
18. Khalikova G.R., Zakirova G.R., Farkhutdinov A.I., Korznikova E.A., Trifonov V.G. Surface hardening of an Al–Si–Cu–Ni–Mg aluminum alloy by friction stir processing and T6 heat treatment // Letters on Materials. 2022. Vol. 12. № 3. P. 255–260. DOI: 10.22226/2410-3535-2022-3-255-260.
19. Khodabakhshi F., Nosko M., Gerlich A.P. Dynamic restoration and crystallographic texture of a friction-stir processed Al–Mg–SiC surface nanocomposite // Materials Science and Technology. 2018. Vol. 34. № 14. P. 1773–1791. DOI: 10.1080/02670836.2018.1490858.
20. Ma Z.Y., Sharma S.R., Mishra R.S. Microstructural modification of as-cast Al–Si–Mg alloy by friction stir processing // Metallurgical and Materials Transactions A. 2006. Vol. 37. P. 3323–3336. DOI: 10.1007/BF02586167.
21. Yang J., Wang D., Xiao B.L., Ni D.R., Ma Z.Y. Effects of rotation rates on microstructure, mechanical properties, and fracture behavior of friction stir-welded (FSW) AZ31 magnesium alloy // Metallurgical and Materials Transactions A. 2013. Vol. 44. P. 517–530. DOI: 10.1007/s11661-012-1373-4.
22. Cui G.R., Ma Z.Y., Li S.X. Periodical plastic flow pattern in friction stir processed Al–Mg alloy // Scripta Materialia. 2008. Vol. 58. № 12. P. 1082–1085. DOI: 10.1016/j.scriptamat.2008.02.003.
23. Andrade D.G., Leitão C., Dialami N., Chiumenti M., Rodrigues D.M. Analysis of contact conditions and its influence on strain rate and temperature in friction stir welding // International Journal of Mechanical Sciences. 2021. Vol. 191. Article number 106095. DOI: 10.1016/j.ijmecsci.2020.106095.
24. Avettand-Fénoël M.-N., Taillard R., Laye J., Odiévre T. Experimental investigation of three-dimensional (3-D) material flow pattern in thick dissimilar 2050 friction-stir welds // Metallurgical and Materials Transactions A. 2014. Vol. 45. P. 563–578. DOI: 10.1007/s11661-013-2015-1.
25. Schneider J.A., Nunes A.C. Characterization of plastic flow and resulting microtextures in a friction stir weld // Metallurgical and Materials Transactions B. 2004. Vol. 35. P. 777–783. DOI: 10.1007/s11663-004-0018-4.
26. Yang B.C., Yan J.H., Sutton M.A., Reynolds A.P. Banded microstructure in AA2024-T351 and AA2524-T351 aluminum friction stir welds: Part I. Metallurgical studies // Materials Science and Engineering: A. 2004. Vol. 364. № 1-2. P. 55–65. DOI: 10.1016/S0921-5093(03)00532-X.
27. Zhou Y.Z., Zhang W., Wang B.Q., Guo J.D. Ultrafine-grained microstructure in a Cu–Zn alloy produced by electropulsing treatment // Journal of Materials Research. 2003. Vol. 18. P. 1991–1997. DOI: 10.1557/JMR.2003.0276.
28. Xu S.W., Deng X.M. A study of texture patterns in friction stir welds // Acta Materialia. 2008. Vol. 56. № 6. P. 1326–1341. DOI: 10.1016/j.actamat.2007.11.016.
29. Ma X., Xu Sh., Wang F., Zhao Y., Meng X., Xie Y., Wan L., Huang Y.Y. Effect of temperature and material flow gradients on mechanical performances of friction stir welded AA6082-T6 joints // Materials. 2022. Vol. 15. № 19. Article number 6579. DOI: 10.3390/ma15196579.
30. Woo W., Choo H., Withers P.J., Feng Z. Prediction of hardness minimum locations during natural aging in an aluminum alloy 6061-T6 friction stir weld // Journal of Materials Science. 2009. Vol. 44. P. 6302–6309. DOI: 10.1007/s10853-009-3868-y.
31. Mehdi H., Mishra R.S. Effect of friction stir processing on mechanical properties and heat transfer of TIG welded joint of AA6061 and AA7075 // Defence Technology. 2021. Vol. 17. № 3. P. 715–727. DOI: 10.1016/j.dt.2020.04.014.

Особенности формирования микроструктуры алюминиевых сплавов АК4-1 и АК12Д после их совместной обработки трением с перемешиванием

© 2023

Халикова Гульнара Рашитовна*[1,2,3], кандидат технических наук, старший научный сотрудник,
доцент кафедры «Технологические машины и оборудование»,
доцент кафедры «Технология металлов в нефтегазовом машиностроении»
Басырова Регина Айратовна[1], стажер-исследователь
Трифонов Вадим Геннадьевич[1,2,4], кандидат технических наук, ведущий научный сотрудник,
доцент кафедры «Технология металлов в нефтегазовом машиностроении»
[1]*Институт проблем сверхпластичности металлов РАН, Уфа (Россия)*
[2]*Уфимский государственный нефтяной технический университет, Уфа (Россия)*

***E-mail: gulnara.r.khalikova@gmail.com**

[3]ORCID: https://orcid.org/0000-0002-6712-8469
[4]ORCID: https://orcid.org/0000-0002-8187-1355

Поступила в редакцию 14.06.2023 *Принята к публикации 21.08.2023*

Аннотация: Обработка трением с перемешиванием – один из современных методов локального модифицирования поверхности алюминиевых сплавов в твердофазном состоянии, обеспечивающий диспергирование структурных составляющих. В термически упрочняемых алюминиевых сплавах со структурой матричного типа последующая после обработки трением с перемешиванием термообработка может приводить к аномальному росту зерен в зоне перемешивания. Однако в сплавах, структура которых близка к микродуплексному типу, после обработки трением с перемешиванием и термообработки может сформироваться мелкозернистая структура. Работа направлена на оценку возможности повышения термической стабильности микроструктуры алюминиевого сплава АК4-1 (Al–Cu–Mg–Fe–Si–Ni) матричного типа. Для этого в исследуемый сплав обработкой трением с перемешиванием локально замешивался алюминиевый сплав АК12Д (Al–Si–Cu–Ni–Mg) со структурой, близкой к микродуплексному типу. Последующая упрочняющая термообработка проводилась по стандартному режиму для сплава АК4-1. Исследования показали, что зона перемешивания имеет эллиптическую форму со структурой «луковичных колец». Такая структура представляет собой чередующиеся кольца с разным количеством и размером избыточных фаз. При этом в центре зоны перемешивания ширина колец и средняя площадь избыточных фаз больше по сравнению с периферией зоны перемешивания, где ширина колец и средняя площадь частиц меньше. Средняя площадь частиц избыточных фаз в кольцах с бóльшим их содержанием меньше по сравнению с кольцами, где их количество ниже. Такое распределение избыточных фаз приводит к формированию мелкозернистой микроструктуры, средний размер которой зависит от межчастичного расстояния в α-Al твердом растворе.

Ключевые слова: алюминиевые сплавы; АК4-1; АК12Д; обработка трением с перемешиванием; термообработка; термическая стабильность; структура луковичных колец; луковично-кольцевая структура

Благодарности: Обработка трением с перемешиванием, исследование макростроения и количественная оценка микроструктуры сплавов выполнены за счет гранта Российского научного фонда № 22-29-01318. Энергодисперсионный спектральный анализ поддержан в рамках программы фундаментальных исследований и государственного задания Министерства науки и высшего образования РФ.

Микроструктурные исследования на растровых электронных микроскопах выполнены на оборудовании Центра коллективного пользования «Структурные и физико-механические исследования материалов» ИПСМ РАН.

Для цитирования: Халикова Г.Р., Басырова Р.А., Трифонов В.Г. Особенности формирования микроструктуры алюминиевых сплавов АК4-1 и АК12Д после их совместной обработки трением с перемешиванием // Frontier Materials & Technologies. 2023. № 3. С. 115–124. DOI: 10.18323/2782-4039-2023-3-65-11.

OUR AUTHORS

Astafurov Sergey Vladimirovich, PhD (Physics and Mathematics),
senior researcher of "Physics of Hierarchical Structures of Metals and Alloys" Laboratory.
Address: Institute of Strength Physics and Materials Science of Siberian Branch of RAS,
634055, Russia, Tomsk, Akademichesky Prospekt, 2/4.
E-mail: svastafurov@gmail.com

Astafurova Elena Gennadyevna, Doctor of Sciences (Physics and Mathematics), Associate Professor,
chief researcher of "Physics of Hierarchical Structures of Metals and Alloys" Laboratory.
Address: Institute of Strength Physics and Materials Science of Siberian Branch of RAS,
634055, Russia, Tomsk, Akademichesky Prospekt, 2/4.
E-mail: elena.g.astafurova@gmail.com

Basyrova Regina Ayratovna, research assistant.
Address: Institute for Metals Superplasticity Problems of RAS,
450001, Russia, Ufa, Stepan Khalturin Street, 39.
E-mail: regina1296@yandex.ru

Bhuvaneswari Mohanrao Chembu, Bachelor of Engineering,
Regional Director (Sc 'F').
Address: RCMA (F&F), CEMILAC, Defence R&D Organization,
560037, India, Bangalore, Doddanekundi Main Rd.
E-mail: cm.cemilac@gov.in

Bobrovskij Igor Nikolaevich, Doctor of Sciences (Engineering), researcher.
Address: Togliatti State University,
445020, Russia, Togliatti, Belorusskaya Street, 14.
E-mail: bobri@yandex.ru

Boldyrev Denis Alekseevich, Doctor of Sciences (Engineering),
professor of Chair "Nanotechnologies, Materials Science, and Mechanics".
Address: Togliatti State University,
445020, Russia, Togliatti, Belorusskaya Street, 14.
E-mail: 10169@portal.ru

Budanova Ekaterina Sergeevna, graduate student.
Address: University of Science and Technology MISIS,
119049, Russia, Moscow, Leninskiy Prospekt, 4, block 1.
E-mail: EPastukh@edu.misis.ru

Denisenko Aleksandr Fedorovich, Doctor of Sciences (Engineering), Professor,
professor of Chair "Mechanical Engineering Technology, Machines and Tools".
Address: Samara State Technical University,
443100, Russia, Samara, Molodogvardeyskaya Street, 244.
E-mail: sammortor@yandex.ru

Gavrilova Alyona Antonovna, student,
laboratory assistant of Strength Laboratory.
Address 1: Ural Federal University named after the first President of Russia B.N. Yeltsin,
620002, Russia, Yekaterinburg, Mira Street, 19.
Address 2: M.N. Mikheev Institute of Metal Physics of Ural Branch of RAS,
620108, Russia, Yekaterinburg, S. Kovalevskaya Street, 18.
E-mail: Gawrilowa.aliona2015@gmail.com

Kabaldin Yury Georgievich, Doctor of Sciences (Engineering),
professor of Chair "Technology and Equipment of Machine Building".
Address: R.E. Alekseev Nizhny Novgorod State Technical University,
603155, Russia, Nizhny Novgorod, Minin Street, 24.
E-mail: uru.40@mail.ru

Kale Shirish Sharad, Ph.D., Director (Sc ‘G’).
Address: RCMA (F&F), CEMILAC, Defence R&D Organization,
560037, India, Bangalore, Doddanekundi Main Rd.
E-mail: shirish.kale.cemilac@gov.in

Khalikova Gulnara Rashitovna, PhD (Engineering), senior researcher,
assistant professor of Chair “Technological Machines and Equipment”,
assistant professor of Chair “Metal Technology in Oil-and-Gas Mechanical Engineering”.
Address 1: Institute for Metals Superplasticity Problems of RAS,
450001, Russia, Ufa, Stepan Khalturin Street, 39.
Address 2: Ufa State Petroleum Technological University,
450062, Russia, Ufa, Kosmonavtov Street, 1.
E-mail: gulnara.r.khalikova@gmail.com

Klimov Aleksey Sergeevich, PhD (Engineering),
assistant professor of Chair “Welding, Pressure Material Treatment, and Allied Processes”.
Address: Togliatti State University,
445020, Russia, Togliatti, Belorusskaya Street, 14.
E-mail: klimov@tltsu.ru

Klimov Vitaly Sergeevich, PhD (Engineering),
assistant professor of Chair “Applied Mathematics and Informatics”.
Address: Togliatti State University,
445020, Russia, Togliatti, Belorusskaya Street, 14.
E-mail: klimovv@gmail.com

Kodirov Davronjon Farkhodzhon Ugli, postgraduate student.
Address: University of Science and Technology MISIS,
119049, Russia, Moscow, Leninskiy Prospekt, 4, block 1.
E-mail: DFKodirov@edu.misis.ru

Kolubaev Eugeny Aleksandrovich, Doctor of Sciences (Engineering), Professor,
Director.
Address: Institute of Strength Physics and Materials Science of Siberian Branch of Russian Academy of Sciences,
634055, Russia, Tomsk, Akademichesky Prospekt, 2/4.
E-mail: eak@ispms.ru

Krishnakumar Subbulakshmi, Bachelor of Engineering,
Technical Assistant.
Address: RCMA (F&F), CEMILAC, Defence R&D Organization,
560037, India, Bangalore, Doddanekundi Main Rd.
E-mail: krishna.ks0531@gmail.com

Kudinov Andrey Konstantinovich, senior lecturer of Chair “Industrial Electronics”.
Address: Togliatti State University,
445020, Russia, Togliatti, Belorusskaya Street, 14.
E-mail: akudinov@yandex.ru

Kudrya Aleksandr Viktorovich, Doctor of Sciences (Engineering), Professor,
professor of Chair of Materials Science and Strength Physics.
Address: University of Science and Technology MISIS,
119049, Russia, Moscow, Leninskiy Prospekt, 4, block 1.
E-mail: AVKudrya@misis.ru

Luchin Andrey Vladimirovich, postgraduate student,
research engineer of Laboratory “Physics of Hierarchical Structures of Metals and Alloys”.
Address: Institute of Strength Physics and Materials Science of Siberian Branch of RAS,
634055, Russia, Tomsk, Akademichesky Prospekt, 2/4.
E-mail: luchin250398@yandex.ru

Merson Dmitry Lvovich, Doctor of Sciences (Physics and Mathematics), Professor,
Director of the Research Institute of Advanced Technologies.
Address: Togliatti State University,
445020, Russia, Togliatti, Belorusskaya Street, 14.
E-mail: D.Merson@tltsu.ru

Merson Evgeny Dmitrievich, PhD (Physics and Mathematics),
senior researcher of the Research Institute of Advanced Technologies.
Address: Togliatti State University, 445020, Russia, Togliatti, Belorusskaya Street, 14.
E-mail: mersoned@gmail.com

Mushnikov Aleksandr Nikolaevich, PhD (Engineering), researcher.
Address: Institute of Engineering Science of the Ural Branch of RAS,
620049, Russia, Yekaterinburg, Komsomolskaya Street, 34.
E-mail: mushnikov@imach.uran.ru

Myagkikh Pavel Nikolaevich, junior researcher of the Research Institute of Advanced Technologies.
Address: Togliatti State University,
445020, Russia, Togliatti, Belorusskaya Street, 14.
E-mail: feanorhao@gmail.com

Novikova Oksana Sergeevna, PhD (Physics and Mathematics),
senior researcher of Strength Laboratory.
Address: M.N. Mikheev Institute of Metal Physics of Ural Branch of RAS,
620108, Russia, Yekaterinburg, S. Kovalevskaya Street, 18.
E-mail: novikova@imp.uran.ru

Podgorbunskaya Polina Olegovna, student,
laboratory assistant of Strength Laboratory.
Address 1: Ural Federal University named after the first President of Russia B.N. Yeltsin,
620002, Russia, Yekaterinburg, Mira Street, 19.
Address 2: M.N. Mikheev Institute of Metal Physics of Ural Branch of RAS,
620108, Russia, Yekaterinburg, S. Kovalevskaya Street, 18.
E-mail: podgorbunskaua@imp.uran.ru

Podkruglyak Lyubov Yurievna, postgraduate student
of Chair “Mechanical Engineering Technology, Machines and Tools”.
Address: Samara State Technical University,
443100, Russia, Samara, Molodogvardeyskaya Street, 244.
E-mail: podkruglak@mail.ru

Poluyanov Vitaly Aleksandrovich, PhD (Engineering),
junior researcher of the Research Institute of Advanced Technologies.
Address: Togliatti State University,
445020, Russia, Togliatti, Belorusskaya Street, 14.
E-mail: vitaliy.poluyanov@gmail.com

Praveen K.V., Bachelor of Engineering, Technical Assistant.
Address: RCMA (F&F), CEMILAC, Defence R&D Organization,
560037, India, Bangalore, Doddanekundi Main Rd.
E-mail: praveenkv61@gmail.com

Ram Prabhu Theagarajan, Ph.D., Joint Director (Sc ‘E’).
Address: RCMA (F&F), CEMILAC, Defence R&D Organization,
560037, India, Bangalore, Doddanekundi Main Rd.
E-mail: ramprabhu.t@gmail.com

Reunova Kseniya Andreevna, postgraduate student,
junior researcher of “Physics of Hierarchical Structures of Metals and Alloys” Laboratory.
Address: Institute of Strength Physics and Materials Science of Siberian Branch of RAS,
634055, Russia, Tomsk, Akademichesky Prospekt, 2/4.
E-mail: reunova.ksenya@mail.ru

Sablin Pavel Alekseevich, PhD (Engineering), Associate Professor,
assistant professor of Chair “Machine Building”.
Address: Komsomolsk-na-Amure State University,
681013, Russia, Komsomolsk-on-Amur, Lenin Street, 27.
E-mail: ikpmto@knastu.ru

Schetinin Vladimir Sergeevich, Doctor of Sciences (Engineering), Associate Professor,
professor of Chair “Machine Building”.
Address: Komsomolsk-na-Amure State University,
681013, Russia, Komsomolsk-on-Amur, Lenin Street, 27.
E-mail: schetynin@mail.ru

Soboleva Natalia Nikolaevna, PhD (Engineering), senior researcher.
Address 1: Institute of Engineering Science of the Ural Branch of RAS,
620049, Russia, Yekaterinburg, Komsomolskaya Street, 34.
Address 2: M.N. Mikheev Institute of Metal Physics of the Ural Branch of RAS,
620137, Russia, Yekaterinburg, Sofya Kovalevskaya Street, 18.
E-mail: soboleva@imach.uran.ru

Sokolovskaya Elina Aleksandrovna, PhD (Engineering), Associate Professor,
assistant professor of Chair of Materials Science and Strength Physics.
Address: University of Science and Technology MISIS,
119049, Russia, Moscow, Leninskiy Prospekt, 4, block 1.
E-mail: Sokolovskaya@misis.ru

Timoshenko Victoria Vladimirovna, postgraduate student.
Address: University of Science and Technology MISIS,
119049, Russia, Moscow, Leninskiy Prospekt, 4, block 1.
E-mail: VVTimoshenko@edu.misis.ru

Trifonov Vadim Gennadyevich, PhD (Engineering), leading researcher,
assistant professor of Chair “Metal Technology in Oil-and-Gas Mechanical Engineering”.
Address 1: Institute for Metals Superplasticity Problems of RAS,
450001, Russia, Ufa, Stepan Khalturin Street, 39.
Address 2: Ufa State Petroleum Technological University,
450062, Russia, Ufa, Kosmonavtov Street, 1.
E-mail: vadimt@imsp.ru

Vignesh Ponnusamy, PhD, Junior Specialist-1.
Address: RCMA (F&F), CEMILAC, Defence R&D Organization,
560037, India, Bangalore, Doddanekundi Main Rd.
E-mail: vigneshpt3532@gmail.com

Volkov Aleksey Yuryevich, Doctor of Sciences (Engineering),
Head of Strength Laboratory.
Address: M.N. Mikheev Institute of Metal Physics of Ural Branch of RAS,
620108, Russia, Yekaterinburg, S. Kovalevskaya Street, 18.
E-mail: volkov@imp.uran.ru.

Yeltsov Valery Valentinovich, Doctor of Sciences (Engineering),
professor of Chair “Welding, Pressure Material Treatment, and Allied Processes”.
Address: Togliatti State University,
445020, Russia, Togliatti, Belorusskaya Street, 14.
E-mail: VEV@tltsu.ru

Zagibalova Elena Andreevna, student,
engineer of “Physics of Hierarchical Structures of Metals and Alloys” Laboratory.
Address: Institute of Strength Physics and Materials Science of Siberian Branch of RAS,
634055, Russia, Tomsk, Akademichesky Prospekt, 2/4.
E-mail: zagibalova-lena99@mail.ru

Zgibnev Dmitry Aleksandrovich, student, laboratory assistant of Strength Laboratory.
Address 1: Ural Federal University named after the first President of Russia B.N. Yeltsin,
620002, Russia, Yekaterinburg, Mira Street, 19.
Address 2: M.N. Mikheev Institute of Metal Physics of Ural Branch of RAS,
620108, Russia, Yekaterinburg, S. Kovalevskaya Street, 18.
E-mail: ske4study@gmail.com

НАШИ АВТОРЫ

Астафуров Сергей Владимирович, кандидат физико-математических наук,
старший научный сотрудник лаборатории физики иерархических структур в металлах и сплавах.
Адрес: Институт физики прочности и материаловедения Сибирского отделения РАН,
634055, Россия, г. Томск, Академический пр-т, 2/4.
E-mail: svastafurov@gmail.com

Астафурова Елена Геннадьевна, доктор физико-математических наук, доцент,
главный научный сотрудник лаборатории физики иерархических структур в металлах и сплавах.
Адрес: Институт физики прочности и материаловедения Сибирского отделения РАН,
634055, Россия, г. Томск, Академический пр-т, 2/4.
E-mail: elena.g.astafurova@gmail.com

Басырова Регина Айратовна, стажер-исследователь.
Адрес: Институт проблем сверхпластичности металлов РАН,
450001, Россия, г. Уфа, ул. Степана Халтурина, 39.
E-mail: regina1296@yandex.ru

Бобровский Игорь Николаевич, доктор технических наук, научный сотрудник.
Адрес: Тольяттинский государственный университет,
445020, Россия, г. Тольятти, ул. Белорусская, 14.
E-mail: bobri@yandex.ru

Болдырев Денис Алексеевич, доктор технических наук,
профессор кафедры «Нанотехнологии, материаловедение и механика».
Адрес: Тольяттинский государственный университет,
445020, Россия, г. Тольятти, ул. Белорусская, 14.
E-mail: 10169@portal.ru

Буданова Екатерина Сергеевна, магистрант.
Адрес: Университет науки и технологий МИСИС,
119049, Россия, г. Москва, Ленинский пр-т, 4, стр. 1.
E-mail: EPastukh@edu.misis.ru

Бхуванесвари Моханрао Чембу, бакалавр технических наук,
региональный директор (сектор ‘F’).
Адрес: Региональный центр военной полетопригодности (F&F),
Центр боевой полетопригодности и сертификации, Организация оборонных исследований и разработок,
560037, Индия, г. Бангалор, Додданекунди Мейн Роад.
E-mail: cm.cemilac@gov.in

Вигнеш Поннусами, доктор наук, младший специалист-1.
Адрес: Региональный центр военной полетопригодности (F&F),
Центр боевой полетопригодности и сертификации, Организация оборонных исследований и разработок,
560037, Индия, г. Бангалор, Додданекунди Мейн Роад.
E-mail: vigneshpt3532@gmail.com

Волков Алексей Юрьевич, доктор технических наук,
заведующий лабораторией прочности.
Адрес: Институт физики металлов имени М.Н. Михеева Уральского отделения РАН,
620990, Россия, г. Екатеринбург, ул. С. Ковалевской, 18.
E-mail: volkov@imp.uran.ru.

Гаврилова Алена Антоновна, студент, лаборант лаборатории прочности.
Адрес 1: Уральский федеральный университет имени первого Президента России Б.Н. Ельцина,
620002, Россия, г. Екатеринбург, ул. Мира, 19.
Адрес 2: Институт физики металлов имени М.Н. Михеева Уральского отделения РАН,
620990, Россия, г. Екатеринбург, ул. С. Ковалевской, 18.
E-mail: Gawrilowa.aliona2015@gmail.com

Денисенко Александр Федорович, доктор технических наук, профессор,
профессор кафедры «Технология машиностроения, станки и инструменты».
Адрес: Самарский государственный технический университет,
443100, Россия, г. Самара, ул. Молодогвардейская, 244.
E-mail: sammortor@yandex.ru

Ельцов Валерий Валентинович, доктор технических наук,
профессор кафедры «Сварка, обработка материалов давлением и родственные процессы».
Адрес: Тольяттинский государственный университет,
445020, Россия, г. Тольятти, ул. Белорусская, 14.
E-mail: VEV@tltsu.ru

Загибалова Елена Андреевна, студент,
инженер лаборатории физики иерархических структур в металлах и сплавах.
Адрес: Институт физики прочности и материаловедения Сибирского отделения РАН,
634055, Россия, г. Томск, Академический пр-т, 2/4.
E-mail: zagibalova-lena99@mail.ru

Згибнев Дмитрий Александрович, студент, лаборант лаборатории прочности.
Адрес 1: Уральский федеральный университет имени первого Президента России Б.Н. Ельцина,
620002, Россия, г. Екатеринбург, ул. Мира, 19.
Адрес 2: Институт физики металлов имени М.Н. Михеева Уральского отделения РАН,
620990, Россия, г. Екатеринбург, ул. С. Ковалевской, 18.
E-mail: ske4study@gmail.com

Кабалдин Юрий Георгиевич, доктор технических наук, профессор,
профессор кафедры «Технология и оборудование машиностроения».
Адрес: Нижегородский государственный технический университет им. Р.Е. Алексеева,
603155, Россия, г. Нижний Новгород, ул. Минина, 24.
E-mail: uru.40@mail.ru

Кейл Шириш Шарад, доктор наук, директор (сектор ‘G’).
Адрес: Региональный центр военной полетопригодности (F&F),
Центр боевой полетопригодности и сертификации, Организация оборонных исследований и разработок,
560037, Индия, г. Бангалор, Доддanекунди Мейн Роад.
E-mail: shirish.kale.cemilac@gov.in

Климов Алексей Сергеевич, кандидат технических наук,
доцент кафедры «Сварка, обработка материалов давлением и родственные процессы».
Адрес: Тольяттинский государственный университет,
445020, Россия, г. Тольятти, ул. Белорусская, 14.
E-mail: klimov@tltsu.ru

Климов Виталий Сергеевич, кандидат технических наук,
доцент кафедры «Прикладная математика и информатика».
Адрес: Тольяттинский государственный университет,
445020, Россия, г. Тольятти, ул. Белорусская, 14.
E-mail: klimovv@gmail.com

Кодиров Давронжон Фарходжон Угли, аспирант.
Адрес: Университет науки и технологий МИСИС,
119049, Россия, г. Москва, Ленинский пр-т, 4, стр. 1.
E-mail: DFKodirov@edu.misis.ru

Колубаев Евгений Александрович, доктор технических наук,
профессор, директор.
Адрес: Институт физики прочности и материаловедения Сибирского отделения РАН,
634055, Россия, г. Томск, Академический пр-т, 2/4.
E-mail: eak@ispms.ru

Кришнакумар Суббулакшми, бакалавр технических наук, технический помощник.
Адрес: Региональный центр военной полетопригодности (F&F),
Центр боевой полетопригодности и сертификации, Организация оборонных исследований и разработок,
560037, Индия, г. Бангалор, Доддanекунди Мейн Роад.
E-mail: krishna.ks0531@gmail.com

Кудинов Андрей Константинович, старший преподаватель
кафедры «Промышленная электроника».
Адрес: Тольяттинский государственный университет,
445020, Россия, г. Тольятти, ул. Белорусская, 14.
E-mail: akudinov@yandex.ru

Кудря Александр Викторович, доктор технических наук, профессор,
профессор кафедры металловедения и физики прочности.
Адрес: Университет науки и технологий МИСИС,
119049, Россия, г. Москва, Ленинский пр-т, 4, стр. 1.
E-mail: AVKudrya@misis.ru

Лучин Андрей Владимирович, аспирант,
инженер-исследователь лаборатории физики иерархических структур в металлах и сплавах.
Адрес: Институт физики прочности и материаловедения Сибирского отделения РАН,
634055, Россия, г. Томск, Академический пр-т, 2/4.
E-mail: luchin250398@yandex.ru

Мерсон Дмитрий Львович, доктор физико-математических наук, профессор,
директор НИИ прогрессивных технологий.
Адрес: Тольяттинский государственный университет,
445020, Россия, г. Тольятти, ул. Белорусская, 14.
E-mail: D.Merson@tltsu.ru

Мерсон Евгений Дмитриевич, кандидат физико-математических наук,
старший научный сотрудник НИИ прогрессивных технологий.
Адрес: Тольяттинский государственный университет,
445020, Россия, г. Тольятти, ул. Белорусская, 14.
E-mail: mersoned@gmail.com

Мушников Александр Николаевич, кандидат технических наук,
научный сотрудник.
Адрес: Институт машиноведения имени Э.С. Горкунова Уральского отделения РАН,
620049, Россия, г. Екатеринбург, ул. Комсомольская, 34.
E-mail: mushnikov@imach.uran.ru

Мягких Павел Николаевич, младший научный сотрудник НИИ прогрессивных технологий.
Адрес: Тольяттинский государственный университет,
445020, Россия, г. Тольятти, ул. Белорусская, 14.
E-mail: feanorhao@gmail.com

Новикова Оксана Сергеевна, кандидат физико-математических наук,
старший научный сотрудник лаборатории прочности.
Адрес: Институт физики металлов имени М.Н. Михеева Уральского отделения РАН,
620990, Россия, г. Екатеринбург, ул. С. Ковалевской, 18.
E-mail: novikova@imp.uran.ru

Подгорбунская Полина Олеговна, студент, лаборант лаборатории прочности.
Адрес 1: Уральский федеральный университет имени первого Президента России Б.Н. Ельцина,
620002, Россия, г. Екатеринбург, ул. Мира, 19.
Адрес 2: Институт физики металлов имени М.Н. Михеева Уральского отделения РАН,
620990, Россия, г. Екатеринбург, ул. С. Ковалевской, 18.
E-mail: podgorbunskaua@imp.uran.ru

Подкругляк Любовь Юрьевна, аспирант
кафедры «Технология машиностроения, станки и инструменты».
Адрес: Самарский государственный технический университет,
443100, Россия, г. Самара, ул. Молодогвардейская, 244.
E-mail: podkruglak@mail.ru

Полуянов Виталий Александрович, кандидат технических наук,
младший научный сотрудник НИИ прогрессивных технологий.
Адрес: Тольяттинский государственный университет,
445020, Россия, г. Тольятти, ул. Белорусская, 14.
E-mail: vitaliy.poluyanov@gmail.com

Правин К.В., бакалавр технических наук, технический помощник.
Адрес: Региональный центр военной полетопригодности (F&F),
Центр боевой полетопригодности и сертификации, Организация оборонных исследований и разработок,
560037, Индия, г. Бангалор, Додданекунди Мейн Роад.
E-mail: praveenkv61@gmail.com

Рам Прабху Тэгараджан, доктор наук, содиректор (сектор ‘E’).
Адрес: Региональный центр военной полетопригодности (F&F),
Центр боевой полетопригодности и сертификации, Организация оборонных исследований и разработок,
560037, Индия, г. Бангалор, Додданекунди Мейн Роад.
E-mail: ramprabhu.t@gmail.com

Реунова Ксения Андреевна, аспирант,
младший научный сотрудник лаборатории физики иерархических структур в металлах и сплавах.
Адрес: Институт физики прочности и материаловедения Сибирского отделения РАН,
634055, Россия, г. Томск, Академический пр-т, 2/4.
E-mail: reunova.ksenya@mail.ru

Саблин Павел Алексеевич, кандидат технических наук, доцент,
доцент кафедры «Машиностроение».
Адрес: Комсомольский-на-Амуре государственный университет,
681013, Россия, г. Комсомольск-на-Амуре, ул. Ленина, 27.
E-mail: ikpmto@knastu.ru

Соболева Наталья Николаевна, кандидат технических наук,
старший научный сотрудник.
Адрес 1: Институт машиноведения имени Э.С. Горкунова Уральского отделения РАН,
620049, Россия, г. Екатеринбург, ул. Комсомольская, 34.
Адрес 2: Институт физики металлов имени М.Н. Михеева Уральского отделения РАН,
620137, Россия, г. Екатеринбург, ул. Софьи Ковалевской, 18.
E-mail: soboleva@imach.uran.ru

Соколовская Элина Александровна, кандидат технических наук, доцент,
доцент кафедры металловедения и физики прочности.
Адрес: Университет науки и технологий МИСИС,
119049, Россия, г. Москва, Ленинский пр-т, 4, стр. 1.
E-mail: Sokolovskaya@misis.ru

Тимошенко Виктория Владимировна, аспирант.
Адрес: Университет науки и технологий МИСИС,
119049, Россия, г. Москва, Ленинский пр-т, 4, стр. 1.
E-mail: VVTimoshenko@edu.misis.ru

Трифонов Вадим Геннадьевич, кандидат технических наук,
ведущий научный сотрудник, доцент кафедры «Технология металлов в нефтегазовом машиностроении».
Адрес 1: Институт проблем сверхпластичности металлов РАН,
450001, Россия, г. Уфа, ул. Степана Халтурина, 39.
Адрес 2: Уфимский государственный нефтяной технический университет,
450064, Россия, г. Уфа, ул. Космонавтов, 1.
E-mail: vadimt@imsp.ru

Халикова Гульнара Рашитовна, кандидат технических наук,
старший научный сотрудник, доцент кафедры «Технологические машины и оборудование», доцент кафедры «Технология металлов в нефтегазовом машиностроении».
Адрес 1: Институт проблем сверхпластичности металлов РАН,
450001, Россия, г. Уфа, ул. Степана Халтурина, 39.
Адрес 2: Уфимский государственный нефтяной технический университет,
450064, Россия, г. Уфа, ул. Космонавтов, 1.
E-mail: gulnara.r.khalikova@gmail.com

Щетинин Владимир Сергеевич, доктор технических наук, доцент,
профессор кафедры «Машиностроение».
Адрес: Комсомольский-на-Амуре государственный университет,
681013, Россия, г. Комсомольск-на-Амуре, ул. Ленина, 27.
E-mail: schetynin@mail.ru

On the cover: SEM image of the fracture AlSi10Mg powder material. Authors of the photo: Vignesh P., Praveen K.V., Krishnakumar S., Bhuvaneswari M.C., Kale S.S., Ram Prabhu T. (RCMA (F&F), CEMILAC, Defence R&D Organization, Bangalore, India).

На обложке: РЭМ-изображение порошкового материала AlSi10Mg. Авторы фото: П. Вигнеш, К.В. Правин, С. Кришнакумар, М.Ч. Бхуванесвари, Ш.Ш. Кейл, Т. Рам Прабху (Региональный центр военной полетопригодности (F&F), Центр боевой полетопригодности и сертификации, Организация оборонных исследований и разработок, Бангалор, Индия).